

SEISMIC CORRECTION IN THE WAVELET DOMAIN

Thesis by

Andrew A Chanerley

In Partial Fulfilment of the Requirements
for the Degree of
Doctor of Philosophy (by Publication)

UNIVERSITY OF EAST LONDON

May 2014

CONTENTS

Acknowledgments	4
Abstract	5
List of Figures	6
List of Symbols	8
Preface	9

Chapter 1

De-coupling of the Instrument Response from Legacy Records

1 Introduction	12
Some Theoretical Background to Seismic Instruments	
2.1 A simple accelerometer model	14
2.2 Some Instrument Parameters	15
2.3 Digital accelerometers	17
3 Instrument de-convolution with standard methods	20
3.2 Time domain de-convolution of instrument response	21
3.2 Frequency domain de-convolution of instrument response	23
3.3 Pre-filtering the Convolved Data	25
4.0 De-convolution of unknown instrument characteristics using adaptive algorithms	28
4.1 Summary of De-Convolution with the QR-RLS and the TLS algorithms	30
Inverse QR-Recursive Least Squares (QR-RLS) algorithm	30
The Total Least Squares (TLS)	31
4.2 Some Results for the QR-RLS and the TLS	33

Chapter 2

The Recovery of Velocity and Displacement from the Acceleration Time-Series and the Localisation in Time and Removal of the Baseline Error

5.0 Introduction	37
5.1 De-noising overlapping spectra using a threshold	38
5.2 A note on the un-decimated wavelet transform	40

6 Results	41
6.1 Some results from Chi-Chi Event, Taiwan (1999), stations TCU052, TCU068 and TCU129	41
6.2 Station TCU129 Chi-Chi Event (1999)	46
6.3 Some Permanent Displacement and tilt estimate summaries	51
7 Conclusions	53
References	54
APPENDIX I	
Pseudo code for the un-decimated wavelet transform with de-noising	60
APPENDIX II	
61	
1. Chanerley, A. A., Alexander, N. A. “Using a Total Least Squares approach for Seismic Correction of Accelerometer Data”, <i>Advances in Engineering Software</i> . Volume 39, Issue 10, pp 849-860, ISSN: 0965-9978, 2008	
2. Chanerley, A. A., Alexander, N.A. “Correcting Data from an unknown Accelerometer using Recursive Least Squares and Wavelet De-noising”, <i>Computers and Structures</i> , Issue 21-22, 85 1679-1692, Nov 2007	
3. Chanerley, A. A., Alexander, N. A. “Novel Seismic Correction approaches without instrument data, using adaptive methods and de-noising”, 13 th World Conference on Earthquake Engineering, Vancouver, Canada, paper 2664, August 1 st -6 th , 2004.	
4. Chanerley, A. A., Alexander, N.A. “An Approach to Seismic Correction which includes Wavelet de-noising”, <i>Proc of the 6th International Conference on Computational Structures Technology</i> ISBN 0-948749-81-4, , Prague, Czech Republic, paper 44, 4-6 th Sept, 2002. doi:10.4203/ccp.75.44	
5. Chanerley, A. A., Alexander, N.A., Berrill, J., Avery, H., Halldorsson, B., and Sigbjornsson, R. “Concerning baseline errors in the form of acceleration transients when recovering displacements from strong motion records using the undecimated wavelet transform”, <i>Bulletin of the Seismological Society of America</i> , vol. 103, pp. 283-295, February, 2013, doi: 10.1785/0120110352	
6. Chanerley, A. A., Alexander, N.A., ”Obtaining estimates of the low-frequency ‘fling’, instrument tilts and displacement time series using wavelet decomposition”, <i>Bulletin of European Earthquake Engineering</i> , vol. 8, pp231-255, 2010 http://dx.doi.org/10.1007/s10518-009-9150-5	

7. Chanerley A. A., Alexander, N A, Halldorsson, B, 'On fling and baseline correction using quadrature mirror filters', *12th International Conference on Civil, Structural and Environmental Engineering Computing*, paper 177, Madeira, Portugal, 1-4 September, 2009 " [doi:10.4203/ccp.91.177](https://doi.org/10.4203/ccp.91.177)

8. Chanerley A. A., Alexander, N A., 'Automated Baseline Correction, Fling and Displacement Estimates from the Chi-Chi Earthquake using the Wavelet Transform' *9th International Conference on Computational Structures Technology* Athens, Greece, 2-5th Sept., 2008 <http://dx.doi.org/10.4203/ccp.88.197>

Abstracts of Published Papers

61 to End

Acknowledgements

This study and research would have not been possible were it not for the support of a list of people, both internal and external to the University.

To the Grace of God, the Lord Jesus Christ, that I survived two major and life-threatening operations during this research and study period, lived to tell the tale and to complete the publications.

To my wife for her love, support and encouragement.

Dr Nicholas Alexander, Civil Engineering Dept., University of Bristol, colleague, friend and mentor with whom the whole study began, over a lunch and some discussions on the processing of seismic data.

Dr Wada Hosny, my Director of Studies at UEL, whose constant encouragement and support along the way is gratefully acknowledged and appreciated

Professor Ragnar Sigbjornsson, Dr Benedikt Halldorsson, Dr Simon Olafsson, of the Earthquake Engineering Research Centre (EERC), in Selfoss, Iceland. In particular for their warm welcome during my visits to the EERC and the many useful and informative discussions over lunch in the Cafe Krús. In particular though the sharing of data after the $M_w6.3$, 29th May, 2008 earthquake in the SISZ, which produced conference papers and a journal paper based in part on the $M_w6.3$, 29th May data.

Dr John Berrill, Dr Hamish Avery from the Canterbury University Seismic Project (CUSP) for generously providing information on their CUSP seismograph. Their seismograph made an impact in harnessing a wealth of data from the $M_w7.1$, September 4th 2010, Darfield Event in Christchurch, New Zealand. The many email exchanges, the sharing of data, all of which made possible both conference and journal papers

Abstract

This thesis summarises novel approaches and methods in the wavelet domain employed and published in the literature by the author for the correction and processing of time-series data from recorded seismic events, obtained from strong motion accelerographs. Historically, the research developed to first de-convolve the instrument response from legacy analogue strong-motion instruments, of which there are a large number. This was to make available better estimates of the acceleration ground motion before the more problematic part of the research that of obtaining ground velocities and displacements. The characteristics of legacy analogue strong-motion instruments are unfortunately in most cases not available, making it difficult to de-couple the instrument response. Essentially this is a system identification problem presented and summarised therein with solutions that are transparent to this lack of instrument data. This was followed by the more fundamental and problematic part of the research that of recovering the velocity and displacement from the recorded data. In all cases the instruments are tri-axial, i.e. translation only. This is a limiting factor and leads to distortions manifest by dc shifts in the recorded data as a consequence of the instrument pitching, rolling and yawing during seismic events. These distortions are embedded in the translation acceleration time-series, their contributions having been recorded by the same tri-axial sensors. In the literature this is termed ‘baseline error’ and it effectively prevents meaningful integration to velocity and displacement. Sophisticated methods do exist, which recover estimates of velocity and displacement, but these require a good measure of expertise and do not recover all the possible information from the recorded data. A novel, automated wavelet transform method developed by the author and published in the earthquake engineering literature is presented. This surmounts the problem of obtaining the velocity and displacement and in addition recovers both a low-frequency pulse called the ‘fling’, the displacement ‘fling-step’ and the form of the baseline error, both inferred in the literature, but hitherto never recovered. Once the acceleration fling pulse is recovered meaningful integration becomes a reality. However, the necessity of developing novel algorithms in order to recover important information emphasises the weakness of modern digital instruments in that they are all tri- rather than sext-axial instruments.

List of Figures

Figure 1 CUSP 3B Digital Accelerograph, Canterbury Seismic Instruments Ltd	18
Figure 2 Frequency response curves for Instrument correction methods	22
Figure 3 Classical Single Degree of Freedom System (SDOF) instrument characteristics. The bold line is a typical value for the instrument SMA-1, with an instrument damping ratio $\gamma = 0.6$	24
Figure 4: Comparison of estimate displacement time-series (for 1999 Chi-Chi event, station TCU068N) using various correction schemes	27
Figure 6 Adaptive RLS diagram	29
Figure 7 Comparison of QR-RLS recovered filters and original "unknown" FIR test filter (Kanai-Tajimi accelerogram)	33
Figure 8 Comparison of extracted instrument characteristic from the El-Centro (1940) event using (i) QR-RLS adaptive filter and wavelet pre-denoising (ii) SDOF instrument response ($f = 10$ Hz, $\xi = 0.552$)	34
Figure 9 Frequency and phase response plots for a 7-coefficient TLS inverse filter. The event is TAI03.150N from the SMART-1 Array in Taiwan.	36
Figure 10 Frequency and phase response plots for a 9-coefficient TLS inverse filter. The event is TAI03.150N from the SMART-1 Array in Taiwan	36
Figure 11 A 4- channel, analysis (decomposition) wavelet filter bank showing sub-band	40
Figure 12 TCU052NS LFS, fling, which shows results before (red, green) and after (blue) baseline correction, wavelet used is the <i>bior1.3</i>	42
Figure 13 TCU052EW low-frequency sub-band, fling, which shows results before (red) and after baseline correction (blue). The wavelet used is the <i>bior1.3</i>	43
Figure 14 Recovered tilt $g\theta$ acceleration, velocity and displacement response of instrument A900 for the TCU052 component	44
Figure 15 The resultant plots for TCU052EW after the corrected low frequency sub-band (LFS) are added to the high frequency sub-band (HFS)	44
Figure 16 TCU068NS low-frequency sub-band	45
Figure 17 Acceleration Tilt transient for TCU068NS	46
Figure 18 TCU129EW, low-frequency sub-band fling	47
Figure 19 Recovered tilt $g\theta$ acceleration, velocity and displacement	47
Figure 20 low frequency sub-bands using <i>bior1.3</i> for TCU129EW	48

Figure 21 low and high frequency sub-bands for TCU129NS	49
Figure 22 low frequency sub-band vertical component TCU129V	50
Figure 23 LFS, HFS, and Corrected for TCU129V	50
Table 1 Some typical analogue and digital instrument characteristics	17
Table 2 Summary of zero velocity points employed and estimated peak tilt acceleration	51
Table 3 Comparison of residual displacement (wavelet method) vs GPS	52
Table 4 Comparison of residual displacement (wavelet method) vs GPS	52
Table 5 Displacements for station TCU068, Chi-Chi event 1999	52

List of Symbols

$u(t)$: signal in time

$H(\omega)$ or $H(f)$: Fourier transform of $h(t)$

$U(\omega)$: Fourier transform of $u(t)$

$E(\omega)$: Fourier transform of 'noise'

DR: Dynamic Range

x : recorded instrument response

ω : natural frequency

γ : critical damping

ψ_i : angle of rotation of ground surface about x, y, and z {i=1,2,3}

a_g : ground acceleration

T : sampling interval

\underline{h} : vector of filter coefficients

\underline{d} : vector of a desired signal

\underline{a} : recorded acceleration

\underline{R} : upper triangular matrix

Q : unitary matrix (also used for Householder Matrix)

$\underline{0}$: null matrix

\underline{P} : inverse correlation matrix

λ : 'forgetting' factor

$\xi(n)$: a priori estimation error

$h(n)$: updated filter coefficients

$\underline{Ax} = \underline{b}$: system of equations

$[\underline{A}|\underline{b}]$: extended matrix

Sgn : signum (sign) function

σ : standard deviation

Preface

This thesis is based on a summary of the papers published below in international scientific journals or in the proceedings of international conferences. The list is not exhaustive, but contains the papers as summarised in this thesis.

The structure of the thesis is in three chapters and its approach follows a historical description. Chapter 1 begins with the first part of the research, which was to obtain better estimates of ground motion from recorded seismic data by de-coupling the instrument response, where unfortunately and in most cases, the instrument characteristics were not available to facilitate the de-coupling. The approach was to treat the problem as one of system identification applying adaptive algorithms which iterated to an optimal description of the inverse instrument response.

Chapter 2 then continues on to the main part of the research with a summary of the wavelet transform method developed to recover the low-frequency acceleration fling pulse such that integration can proceed to the velocity pulse and the displacement fling-step. The novel method uses the undecimated wavelet transform with de-noising which is effective in removing low-frequency noise, but without removing the low-frequency signal. This is one of the key issues that render the method a success.

Chapter 3 is a collection of some of the important papers published by the author. There are two key journal papers (papers 1 and 2) which support Chapter 1 and present the methods implemented in order to obtain an optimal estimate of the recorded acceleration after de-convolution. Chapter 1 is also supported by publications from proceedings (papers 3 and 4), where these methods and implementations were first presented. Furthermore there are two key journal papers (papers 5 and 6) in support of Chapter 2 which present the novel wavelet transform algorithm with de-noising and which demonstrate the recovery of velocity and displacement and additionally the acceleration and velocity fling pulses and the displacement fling-step and the form of the baseline error. These too are supported by conference proceedings where these ideas, methods and implementations were presented.

The link between the chapters and papers is broadly the limitation of the various instruments used with which to record the seismic data. These limitations therefore have required the development of novel algorithms with which to overcome some of the problems associated with instrument inadequacy in order to extract useful data. This thesis addresses some of the problems and summarises the formulated novel solutions.

The author of this thesis is the principal author of the papers listed below.

1. Chanerley, A. A., Alexander, N. A. “Using a Total Least Squares approach for Seismic Correction of Accelerometer Data”, *Advances in Engineering Software*. Volume 39, Issue 10, pp 849-860, ISSN: 0965-9978, 2008

2. Chanerley, A. A., Alexander, N.A. “Correcting Data from an unknown Accelerometer using Recursive Least Squares and Wavelet De-noising”, *Computers and Structures*, Issue 21-22, 85 1679-1692, Nov 2007

3. Chanerley, A. A., Alexander, N. A. “Novel Seismic Correction approaches without instrument data, using adaptive methods and de-noising”, 13th World Conference on Earthquake Engineering, Vancouver, Canada, paper 2664, August 1st-6th, 2004.

4. Chanerley, A. A., Alexander, N.A. “An Approach to Seismic Correction which includes Wavelet De-noising”, *Proc of The Sixth International Conference on Computational Structures Technology* ISBN 0-948749-81-4, Prague, Czech Republic, paper 44, 4-6th September, 2002 [doi:10.4203/ccp.75.44](https://doi.org/10.4203/ccp.75.44)

5. Chanerley, A. A., Alexander, N.A., Berrill, J., Avery, H., Halldorsson, B., and Sigbjornsson, R. “Concerning baseline errors in the form of acceleration transients when recovering displacements from strong motion records using the undecimated wavelet transform”, *Bulletin of the Seismological Society of America*, vol. 103, pp. 283-295, February, 2013, [doi: 10.1785/0120110352](https://doi.org/10.1785/0120110352)

6. Chanerley, A. A., Alexander, N.A., "Obtaining estimates of the low-frequency 'fling', instrument tilts and displacement time series using wavelet decomposition", *Bulletin of European Earthquake Engineering*, vol. 8, pp231-255, 2010

<http://dx.doi.org/10.1007/s10518-009-9150-5>

7. Chanerley A. A., Alexander, N A, Halldorsson, B, 'On fling and baseline correction using quadrature mirror filters', *12th International Conference on Civil, Structural and Environmental Engineering Computing*, paper 177, Madeira, Portugal, 1-4 September, 2009 " [doi:10.4203/ccp.91.177](https://doi.org/10.4203/ccp.91.177)

8. Chanerley A. A., Alexander, N A., 'Automated Baseline Correction, Fling and Displacement Estimates from the Chi-Chi Earthquake using the Wavelet Transform' *9th International Conference on Computational Structures Technology* Athens, Greece, 2-5th Sept., 2008 <http://dx.doi.org/10.4203/ccp.88.197>

Chapter 1 De-coupling of the Instrument Response from Legacy Records

1 Introduction

The structural/geotechnical engineering analyst/designer needs a complete set of boundary conditions (i.e. ground accelerations, velocities and displacements) at every location a structural artefact makes contact with the ground. A full spatiotemporal ground motion description is required rather than just ground accelerations at a single point. For this however a statistically significant sample of strong motion records is needed so that behaviour can be confidently predicted for unknown and critical future seismic events. However a statistically significant sample is the first problem we face i.e. the dearth of data, we do not have all the ground motion data we need. That is to say we do not have enough recordings for every location type and magnitude combination. There is insufficient good quality data so as not to neglect some of the older time histories recorded with analogue instruments. There are now arrays of instruments in the USA and Japan, but of course the problem is still with us because clearly the earthquake still has to occur within range of the instruments provided.

Data of ground motion acceleration recorded during seismic events is important to the process of developing models of system behaviour. Reliable, error free, experimental data is a major factor in the scientific method of developing and validating theoretical models. In the case of earthquake engineering ground motion times-series are used to predict the performance of structural systems to seismic events. As computational power increases the employment of non-linear time-history analysis of structural artefacts, e.g. buildings, bridges, etc. has become more feasible and widespread. These very challenging numerical models are subject to many unknowns; such as non-linear material behaviours. However, the greatest of these unknowns come from the loading, i.e. the ground motion, acceleration time-series, velocity pulses in the near and far field and displacement fling steps.

The second problem is that both legacy (analogue) and modern (digital) strong motion accelerographs, to date, only measure ground motion acceleration and then only the 3 translational component accelerations; i.e. they do not measure the rotational degrees

of freedom nor do they record velocities or displacements. The advent of satellite global positioning means that if accelerographs are coupled with GPS then it is possible to obtain some information about ground displacements. However, the sampling rate and dynamic range associated with GPS is generally low so this limits the frequency bandwidth of information that can be obtained. Nevertheless, more information is always required and a bonus.

Classically, structural engineers have avoided the problem of ground motion displacements by formulating their analyses in terms of a moving coordinate frame. That is we consider structural accelerations, velocities and displacements relative to the moving ground [17]. In this formulation the resulting equations of motion can be written in terms of ground motion acceleration alone. Nevertheless, for the most part, we still neglect the unrecorded ground rotational accelerations. This approach is reasonable for the case where the structure is small, i.e. less than 25m in length horizontally, [18]. Observed wavelengths of ground motion displacement may not impose any significant differential displacement on small structures. For longer, larger structures, i.e. very large buildings, bridges, tunnels, pipelines and dams, differential seismic displacements are more credible.

However, as has been already stated, we do not directly record ground motion displacement time-series. At first glance it appears that acceleration can be simply integrated twice to obtain displacement. While this is true in principle, in practice noise in the recording is the problem. Low frequency noise caused by the unrecorded ground rotations destroys any reasonable estimate of the true ground motion displacement time-series obtained by double integration. This is in part due to modern digital instruments not being 6-axis instruments, so a complete picture of ground motion acceleration, velocity and displacement at a point is not possible.

This issue has to some extent been neglected in databases of strong motion records, such as [19] where low frequency filtering of accelerograms effectively removes much of the ground motion displacement. Standard filtering processes will eliminate a key feature of a seismic event, namely the acceleration pulse known as the 'fling' and the displacement known as the 'fling-step'. This arises as a very low-frequency acceleration pulse, which can give rise to residual ground displacement. This very low

frequency (i.e. less than 0.1Hz) fling pulse is buried in low-frequency noise. Thus, it is difficult to remove the low frequency noise without removing the low-frequency ‘fling’ when applying standard filtering methods. In [3, 20] the reported permanent displacement of the ground during the Chi-Chi, Taiwan (1999) event was some 10m (reported by GPS). Compare this with an estimated (imposed) zero value in permanent displacement obtained by using a low-cut filter “correction”. Clearly low-cut filtering can produce very large errors in estimated ground displacements.

In this thesis we review published procedures for processing and correcting accelerograph data. The generic theoretical background to both analogue and digital instruments is considered as are the sources of noise/error along with the effect of ground rotations on accelerograph performance. The thesis reviews various techniques for noise/error reduction. The thesis also discusses the vexed problem of obtaining estimates of ground motion displacement time-series from accelerograph data.

2 Some Theoretical Background to Seismic Instruments

2.1 A simple accelerometer model

A strong motion instrument, commonly termed an accelerograph, is one that can be viewed as a generic process $h(t)$ that transforms an input signal (e.g. the actual ground motion) $u(t)$ into some output signal (e.g. the recorded ground motion) $v(t)$, thus

$$v(t) = \int_{-\infty}^{\infty} h(\tau)u(t-\tau)d\tau + \varepsilon(t) \quad (1)$$

where $\varepsilon(t)$ is some “error” or noise added to the convolution integral. This noise can be thought of as resulting from either instrument behaviour, processing of recorded data and/or background vibrations from non-seismic sources. Some of this noise may have been convoluted through the instrument. However, we separate it in equation (1)

for mathematical simplicity. This equation (1) can be re-expressed in the frequency domain as following linear equation

$$V(\omega) = H(\omega)U(\omega) + E(\omega) \quad (2)$$

where $U(\omega)$, $V(\omega)$ and $E(\omega)$ are the Fourier transforms of $u(t)$, $v(t)$ and $\varepsilon(t)$ respectively and $H(\omega)$ is the Fourier transform of $h(t)$. Any instrument should record the signal $v(t)$, which should be a very good estimate of $u(t)$ i.e. ideally $H(\omega)$ would equal one and $E(\omega)$ zero.

2.2 Some Instrument Parameters

The first Strong motion recordings were obtained in Long Beach in 1933, [21]. The first accelerographs were optical-mechanical instruments that produced traces of ground acceleration on paper or film. These were analogue instruments, for example such as Kinematic's SMA-1 used in USA, SMA-C and DC-2 accelerographs used in Japan, these were widespread until the mid 1980s when digital instruments began to be used. In fact these instruments were still in situ in the late 1990s because they were considered relatively maintenance free and up front purchase costs had already been met. The problems with these analogue instruments and their subsequent legacy recordings were:

- (i) The *dynamic range* of analogue accelerographs was relatively low. The dynamic range DR where:

$$DR = 20 \log(\max |v(t)| / \min |v(t)|), \quad (3)$$

Where $\min |v(t)|$ and $\max |v(t)|$ are the smallest and largest amplitudes that can be recorded. Usually the dynamic range is usually expressed in decibels (dB):

$$DR_{dB} = 20 \log(\max |v(t)| / \min |v(t)|) \quad (4)$$

For analogue instruments this dynamic range was limited by the breadth of the recording paper/film and the width of the trace line, for example recordings made on recording paper have a maximum amplitude of about 10cm and a minimum resolution of 0.1mm, i.e. a $DR_{dB} = 60\text{dB}$, or 3 orders of magnitude. Thus, these instruments are subject to large quantization errors [23] and this was particularly a problem for very small events where little of the dynamic range was employed. Full scale on analogue accelerographs, $\max |v(t)|$, was typically 1g and this is a problem in the case of very large seismic events as it resulted in clipping of peaks (similar to arithmetic saturation in digital instruments) of the signal.

- (ii) The frequency bandwidth of analogue accelerographs was low. The bandwidth was limited by the instruments natural frequency. The optical-mechanical instruments behaved like a low-pass filter, attenuating all components of the recorded signal a little above the instruments natural frequency. In the 1930-40's the operation frequency bandwidth was $\sim 0\text{-}20\text{Hz}$ that improved over time to $\sim 0\text{-}80\text{Hz}$ [24]. The bandwidth was in practice never down to DC as low frequency, so called baseline, errors were difficult to eliminate. This was because digitization of analogue paper/film records resulted in low frequency noise that was difficult to eliminate, though often attempted [6].

- (iii) The analogue accelerographs characteristic was not completely flat in the operational range. The optical-mechanical system could be theoretically modelled like a simple pendulum with natural frequency and damping. Large ratios of critical damping were incorporated (using electro-mechanical, air or oil pistons) into the instrument to flatten out the pass-band frequency characteristics of the accelerographs. However, it was difficult to have both a large and a completely flat frequency operational range thus some compromise in design of such devices was required [5]. These analogue accelerographs characteristics, namely the critical damping and natural frequency, were not necessarily known precisely after many years in situ.

- (iv) The threshold acceleration (the trigger) used to start the recording meant that all data ‘pre-trigger’ was normally lost. This sometimes resulted in the P wave arrival time being lost by this time delay.
- (v) Digitization of analogue paper/film records resulted in much lower signal to noise ratio (SNR) than that of modern digital instruments. The so called baseline errors caused by low frequencies resulted in very large problems in the accurate determination of low frequency ground displacements time-series. In some legacy recordings erroneous spikes are found caused by errors in the automated digitization process. This was highlighted in [11] and shown to have a significant effect of derived acceleration response spectra.

It is clear therefore that there are number of problems surrounding legacy recording. Correction of these records is discussed in later sections of the paper but it worth noting that some care should be taken when employing these recording in engineering analysis.

Table 1: Some typical analogue and digital instrument characteristics

Name	Dynamic Range	Full Scale Range	Signal to Noise Ratio	Operational Bandwidth	Ref.
CUSP 3B	80 dB	4g	91 dB	DC to 80Hz	[25]
CUSP 3E	120dB	3g	130dB	DC to 80Hz	[25]
130-SMA	113dB	4g	~166dB	DC to 100Hz	[26]
ETNA	108 dB	4g	~114dB	DC to 200Hz	[27]
SMA-1	40-55dB	1g	-	~0 to 25Hz	

2.3 Digital accelerometers

Digital instruments are superior to the older analogue instruments in terms of performance. For example the digital recording system at each ICEARRAY station in

Iceland (Figure 1) and the stations in CanNet, New Zealand, comprises a low-cost, single unit, CUSP-3Clp strong-motion accelerographs manufactured by Canterbury University Seismic Project in New Zealand, for the Canterbury Seismic Network in New Zealand. The units are equipped with 24-bit, tri-axial, low-noise ($\sim 70 \mu\text{g rms}$) Micro-Electro-Mechanical (MEM) accelerometers with a high maximum range ($\pm 2.5 \text{ g}$) and a wide-frequency pass-band (0-80 Hz at a 200 Hz sampling frequency) [63, 64]. These instruments have an amplifier, an anti-alias filter, a 24-bit A/D convertor and memory. Table 1 gives typical examples of dynamic range, full scale range, SNR's and operational bandwidths of some modern digital accelerometers with a SMA-1 analogue accelerometer as a comparison. The dynamic range of the 24-bit digitizer is $6.02 \times 23 \approx 139\text{dB}$, each additional bit increasing the dynamic range by $20\log_{10}(2)$.



Figure 1: CUSP 3B Digital Accelerograph, Canterbury Seismic Instruments Ltd

The clipping limit of such digital instruments can be up to $\pm 4\text{g}$ (39.24m/sec^2) up to their corner frequencies, as shown in Table 1. They have a flat instrument response in the frequency bandwidth of operation, problems of instrument calibration, triggering, and digitization are all much reduced. The signal-to-noise ratios are well above the dynamic range suggesting that noise is unlikely to affect anything other than the least significant bit. In addition these instruments can be synchronized to a common time

base (for the case where a large array of instruments are deployed [28]) and are coupled with GPS sensors that are able to determine position before and after a seismic event.

While digital accelerometers are superior to their analogue counterparts they are still only 3 axis instruments. Moreover some of the earlier digital instruments had internal filters, which removed the low frequency noise, but also removed any low-frequency, pulse-like accelerations, which cause the displacement fling-steps. That is to say they only record translational accelerations and not rotational accelerations. The assumption being that ground rotations (the commonly referred to tilts – pitch, roll and yaw) are small enough to be neglected. These are small in most cases, but in fact their effects can be considerable when velocity and displacement need to be recovered.

The effects of tilting are discussed in [2, 4, 13, 44, and 45] in particular in the long period which leads to dc shifts in velocity and offsets in the final displacement. Moreover [1] has demonstrated displacement offsets by using numerical simulations, a tilt of 0.1° (1.75mrad) is added to the Hector Mine seismic data. This gave displacement offsets similar to those obtained in the seismic data analysed and published and shown in this thesis for the TCU068NS station of the Chi-Chi (1999) event. The simulations in [1] showed a similar permanent displacement when Hector Mine was contaminated by a simulated tilt as that for the actual data from the recorded TCU068 station. It is shown in [3, 4] above that after operating on the seismic data using the wavelet transform method, the angle of tilt can be estimated.

The approximate equations [1, 3] which describe small tilt angles are as follows:

$$\text{Longitudinal} \quad \ddot{x}_1 + 2\omega_1\gamma_1\dot{x}_1 + \omega_1^2 x_1 = -a_{g1} + g\psi_1 \quad (5)$$

$$\text{Transverse} \quad \ddot{x}_2 + 2\omega_2\gamma_2\dot{x}_2 + \omega_2^2 x_2 = -a_{g2} + g\psi_2 \quad (6)$$

$$\text{Vertical} \quad \ddot{x}_3 + 2\omega_3\gamma_3\dot{x}_3 + \omega_3^2 x_3 = -a_{g3} \quad (7)$$

where x = recorded response of instrument,

ω = natural frequency,

γ = critical damping,
 g = acceleration due to gravity,
 ψ = rotation of the ground surface about x axis
 a_g = ground acceleration.

The conclusions from the above equations are that the two horizontal sensors are responding to horizontal acceleration and tilts and that the vertical sensor is responding to vertical acceleration only. Clearly there is an “error” in the recorded horizontal ground motion that is present even for the case of digital instruments. This error is an unknown, time varying, function $g\psi_i$, where $i = \{1,2\}$ are the horizontal translational components and $i = 3$ is the vertical component. [3] suggested that this error produces a signal to noise ratio, for the 1999 Chi-Chi TCU068 record, of around 31dB. This value is clearly far lower than the instrument signal to noise ratio as in Table 1. As an example of the effect tilts can have on the double time integration of the acceleration record then a displacement offset of 100cm over 100sec, requires a tilt angle of 20.4×10^{-6} radians. Chapter 2 of the thesis dealing with recovery of displacements shows the considerable offsets created by small and abrupt changes in acceleration.

3 Instrument de-convolution with standard methods

In many of the corrected data records available, instrument correction is not applied because the header of the original data does not provide any information on useful instrument parameters or indeed the type of instrument used. In a lot of cases the seismic data analysed did not, after processing without instrument de-convolution, produce marked differences in outputs when processed with instrument de-convolution. However, with some data analysed the differences in outputs, in particular for the acceleration response spectra were clear and not insignificant. In most of the older records the accelerograms recorded the characteristics of strong-motion earthquakes with single-degree-of-freedom, stiff and highly damped transducers whose relative displacement $x(t)$ is approximately proportional to the ground acceleration $a_g(t)$. To obtain estimates of the ground acceleration from the

recorded relative displacement response, an instrument correction can be applied as follows:

$$a_g(t) = -\ddot{x}(t) - 2\gamma\omega\dot{x}(t) - \omega^2x(t) \quad (8)$$

where γ is the viscous damping ratio, ω is the transducer's natural frequency and $a_g(t)$ is the ground acceleration. The above expression (8) can be used to de-convolve the recorded motion from the ground acceleration in either the time [6,9,29] or frequency domain [7,61].

3.1 Time domain de-convolution of instrument response

Analogue instruments such as the SMA-1 have their own dynamic response characteristics that affect their recording. This instrument response is classically modelled by a single degree of freedom system [7] (i.e. a simple small oscillation pendulum) as shown in equation (1). One way to de-convolve the instrument response is to do so in the time domain as follows below.

Applying the central difference [6, 9] to equation (8) and using the approximation [9] that the values of the acceleration of the uncorrected accelerograms are $-\omega_n^2x(t)$ gives a 3-tap FIR convolver for $-(\omega^2T^2)a_g(t)$, where T is the sampling rate of the digitised accelerograms, as:

$$y = -4\omega^2T^2a_g = (1 + 4\gamma\omega T + 4\omega^2T^2)a_i - (2 + 4\gamma\omega T)a_{i-2} + a_{i-4} \quad (9)$$

where now $a_{i-n} = -\omega^2x_{i-n}$ are the discrete values of the instrument acceleration output of the uncorrected accelerograms. For values of $\gamma=0.6$, $f = 25\text{Hz}$ and $T = 1/600$ the expression becomes:

$$y = -0.10432a_g = 0.72386a_i - a_{i-2} + 0.38046a_{i-4} \quad (10)$$

The backward difference approximation gives a similar expression:

$$y = -\omega^2 T^2 a_g = (1 + 2\gamma\omega T + \omega^2 T^2)a_i - 2(1 + \gamma\omega T)a_{i-1} + a_{i-2} \quad (11)$$

For values of $\gamma = 0.6$, $f = 25\text{Hz}$ and $T = 1/600$ the expression becomes:

$$y = -0.2962a_g = 0.5975a_i - a_{i-1} + 0.43211a_{i-2} \quad (12)$$

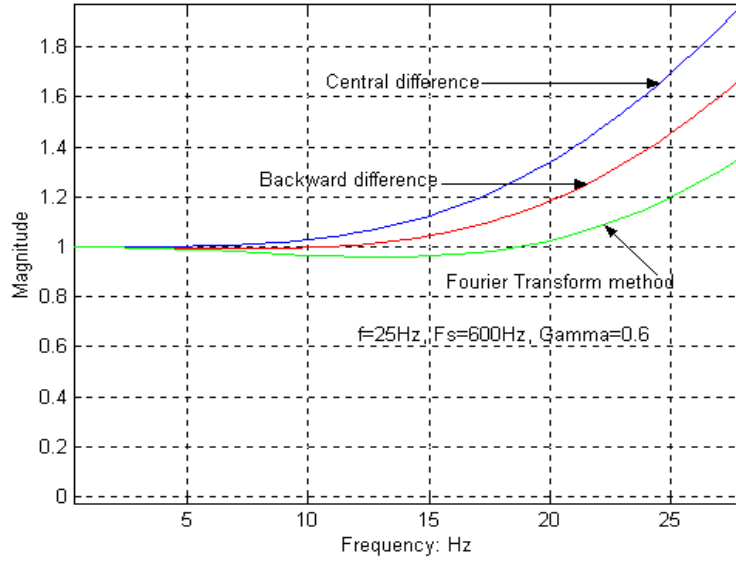


Figure 2: Frequency response curves for Instrument correction methods

The frequency response using [9] central and backward difference is shown in Figure 2. It vindicates the conclusions in [6, 9] in respect of the central difference correction, at sampling rates greater than 4 times the instrument response frequency. The frequency response at a lower sampling rate in this case at $T = 0.02\text{sec}$, using central difference doesn't however exhibit suppression at higher frequencies, nor does it exhibit the same degree of linearity up to 6Hz as reported in [6, 60]. The frequency responses at $T = 1/600$ in Figure 2 also indicate that the backward difference is approximately linear up to 12Hz, compared to 6Hz for the central difference. The strong-motion, unevenly spaced data has an average sampling rate of approximately 600Hz, which is then interpolated to give an evenly spaced data at 600Hz or a Nyquist rate of 300Hz.

3.2 Frequency domain de-convolution of instrument response

Equation (8) can also be transformed into the frequency domain [7, 29] by applying the Fourier transformation

$$\ddot{X}_g = -H(f)A(f) \quad \text{where} \quad H(f) = \left\{ \left(1 - \frac{f}{f_i} \right) + i \left(2\gamma \frac{f}{f_i} \right) \right\} \quad (13)$$

where the approximate acceleration output of the instrument is $A(f) = \omega^2 X(f)$. The ground acceleration in time can therefore be recovered from the inverse Fourier transform of the ground acceleration $\ddot{X}_g(f)$, obtained from the Fourier transform of the relative displacement $X(f)$. Figure 2 compares these most popular three methods used in correcting for the instrument response. It shows that over a limited range the responses are almost the same with the backward difference demonstrating a flat response up to approximately 12Hz, therefore over this range it can be inferred that the acceleration is approximately equal to the ground acceleration. At higher frequencies further corrections must be applied. However Figure 2 also demonstrates that using frequency domain de-convolution the response is approximately flat up to 20Hz; therefore results presented in [59] have been processed using this method.

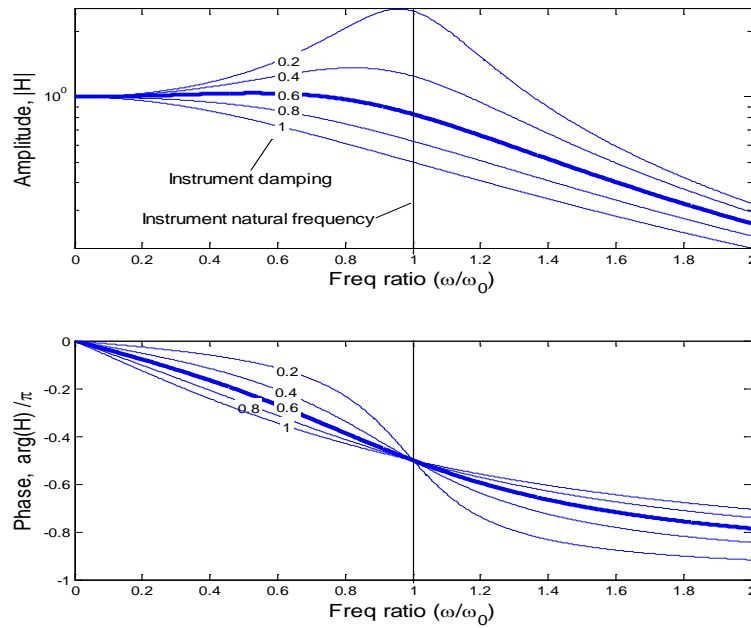


Figure 3 Classical Single Degree of Freedom System (SDOF) instrument characteristics. The bold line is a typical value for the instrument SMA-1, with an instrument damping ratio $\gamma = 0.6$

This instrument characteristic (nonlinear frequency response function) is displayed in the above Figure 3. As the instrument's ratio of critical damping increases the effect of the instrument resonance attenuates, so producing a flatter instrument response. Consider the bold line highlighted in the figure that corresponds to 60% percent of critical damping. This instrument's characteristic is relatively flat for frequencies below the instruments natural frequency ω_0 . The phase of $H_i(\omega)$ is also displayed and appears almost linear for frequencies below the instruments natural frequency ω_0 at this value of damping. A linear phase change results in a constant time-shift in the time-domain was considered fairly neutral. Thus, is easy to understand the choice of ratio of critical damping of 0.6 that was used for SMA-1. However, by modern standards this response is far from flat and the phase distortion (though almost linear) does require some correction. This correction can be achieved in the time-domain as suggested by [7] or simply by using the FFT, IFFT and equations (13) and as suggested by [10].

It should be noted that the instrument response is effectively a low-pass filter i.e. it attenuates the high-frequency components (i.e. those higher than the instrument's

natural frequency). Recovering the true ground acceleration requires de-convolution therefore in correcting for the instrument characteristic we end up amplifying the higher frequency terms (as shown in the frequency responses of Figure 2) that have been attenuated by the instrument. Therefore high frequency noise and alias errors, together with higher frequency signal components, will be amplified. Instrument correction in this case should be followed by a high cut filter to attenuate again the high frequency noise/signal.

3.3 Pre-filtering the Convolved Data

Any process that converts an analogue signal into a digital one runs the risk of introducing aliasing errors. Discrete sampling of a continuous signal at a sampling rate f results in a digital signal is unable to distinguish components above the Nyquist frequency $f/2$ [23]. Furthermore, frequency components above this Nyquist limit may produce errors in the sampled signal cause by high frequency components folding back power below the Nyquist frequency. So aliasing error is an issue whether an A/D converter is used (for digital seismographs) or some optical-mechanical digitization (for analogue seismographs). To mitigate this error, an anti-alias filter is employed in the case of digital seismographs and this filter is a simple high-cut filter that seeks to remove frequency components above the Nyquist frequency, this filter precedes the A/D converter. Unfortunately for the case of an analogue seismograph the aliasing errors have already been introduced through the optical-mechanical digitization device. Therefore, a high-cut filter appears unnecessary as it cannot remove the aliasing errors after they have been folded back into the low frequency bandwidth. Nevertheless, this high-cut filter may still have utility. If it is employed after the instrument correction (as in [8, 10]) it can mitigate the amplification of instrument noise at frequencies above the natural frequency of the instrument. This effectively removes the least reliable part of the signal.

On the other hand digitization of paper/film records from analogue instruments is thought to introduce low frequency errors due to small misalignments of these analogue paper/film records in the optical-mechanical digitizers. These errors were termed ‘baseline errors’ by [8, 10]. The suggested solution was either (i) linear or

quadratic de-trending of the data (i.e. finding the least square linear or quadratic fit and then subtracting this from the recording) or (ii) to use of some low-cut filter. These two processes are qualitatively similar as both are, in effect, low-cut filters. If a low-cut filter is to be employed we would favour one that has known and designed filter characteristics i.e. one with a known corner frequency, flat pass-band and zero/linear phase characteristic and so method (ii) rather than (i) is preferable.

Many digital accelerometer transducers are reliable down to DC so technically there should not be any baseline error. Once the true ground motion acceleration time-series is obtained it is typical to try and obtain both the ground velocity and displacement time-series.

However, the very low frequency components are amplified exponentially and this produces a resulting displacement time-series that are often swamped by error. This is demonstrated in Figure 4 where the ground motion acceleration time-series is double integrated to obtain an estimated permanent final displacement of the ground (in the northerly direction) of -16.22m. This compares with a value of +5.56m from the wavelet based method proposed in [3] that is very near to the recorded GPS value. In this case the error in displacement, caused by low frequency noise, is nearly 22m.

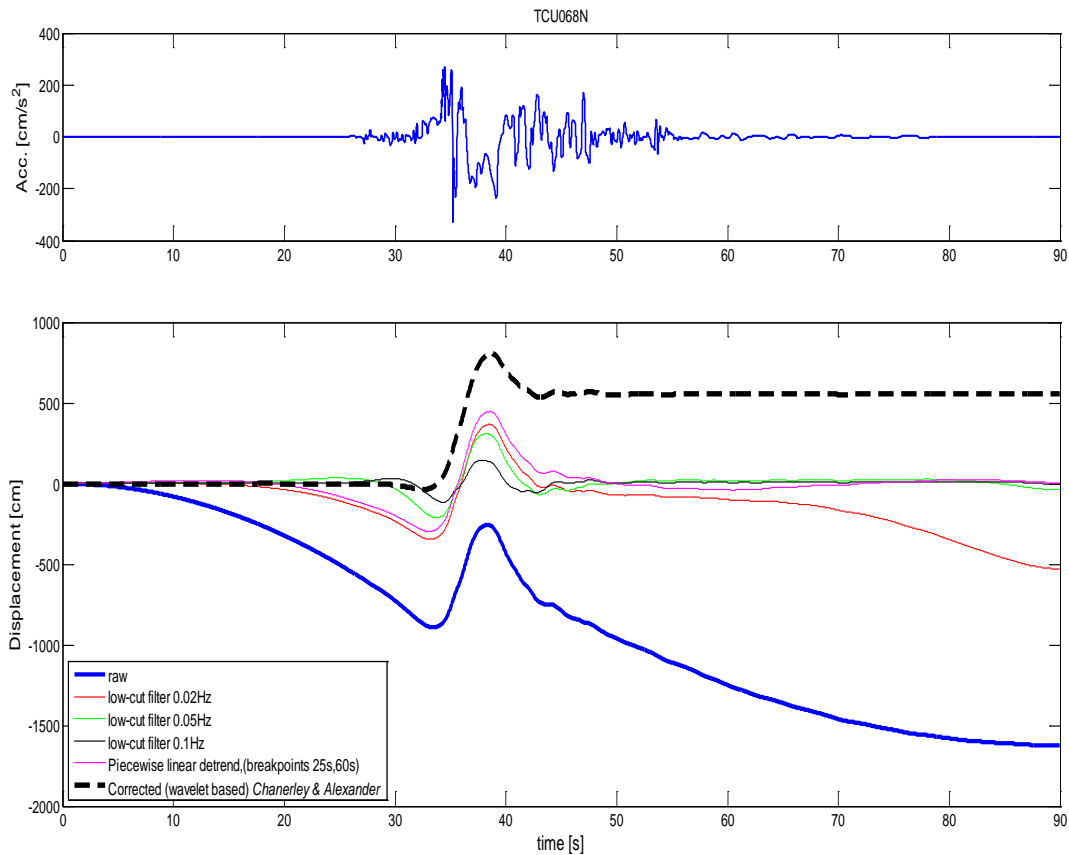


Figure 4: Comparison of estimate displacement timeseries (for 1999 chi-chi event, station TCU068N) using various correction schemes

This problem of amplification of low frequency noise (by a double-time integration filter) was well known and tackled almost universally by some low-cut filter with a cut-off frequency < 0.25 Hz, e.g. the Ormsby filter [30], which is a Finite Impulse response filter (FIR) [31, 32], was a popular filter to use in the early days of correction procedures. The corrected records in the PEER strong motion database [19] filters it's data. The trouble with this approach is that it eliminates signal components with the noise at the very low frequency. Figure demonstrates how sensitive this low-cut filtering can be. There are clear differences in the estimated ground displacement obtained by a Butterworth zero-phase (IIR) [31, 32] filter at 0.02Hz, 0.05Hz and 0.1Hz (cut-off frequency).

In addition to removing the low-frequency noise, these low-cut filters remove from the record the low-frequency 'fling' or permanent DC (shift that results in a residual

displacement) that is present after the strong ground motion. That is to say that often the estimated residual displacement from a low-cut filter record is often near to zero. Thus, it implies that there is never any residual ground deformation after an earthquake and GPS readings have shown this to be clearly incorrect.

Obtaining reliable ground displacement estimates from older analogue data is very problematic because of the presence of large noise (caused by misalignments in paper/film processing) so low-cut filtering here is only to stabilise the acceleration time-series. For these cases, the displacement time-series thus obtained are highly questionable. For modern recordings (from digital instruments) the removal of the very low frequency of the time-series is also questionable as it removes important parts of the signal. This problem is considered in Chapter 2 of the thesis.

4.0 De-convolution of unknown instrument characteristics using adaptive algorithms [12, 13, 55, 57, 58, 59]

The de-convolution of legacy instrument response (i.e. its non-flat frequency response) discussed in the beginning of section 3 makes a number of assumptions. Firstly, we assume to form of the instrument response (filter), in this it is defined by a single degree of freedom system (for these optical-mechanical instruments). Secondly, we need to know the instrument parameters, namely its natural frequency and ratio of critical damping. Some legacy recordings have been obtained from accelerographs that may no longer exist and so it is not possible to validate either of these two assumptions exactly. Thus, we are left with a system identification problem i.e. the determination of the characteristic or footprint that the instrument leaves imposed on the time-series. Once obtained the resulting inverse filter can be applied to the data in order to de-convolve the instrument response. The actual ground acceleration \underline{a}_g and the accelerometer system \underline{g} are unknown, and the adaptive algorithm estimates an optimal system to improve the ground motion estimate, see Figure 6.

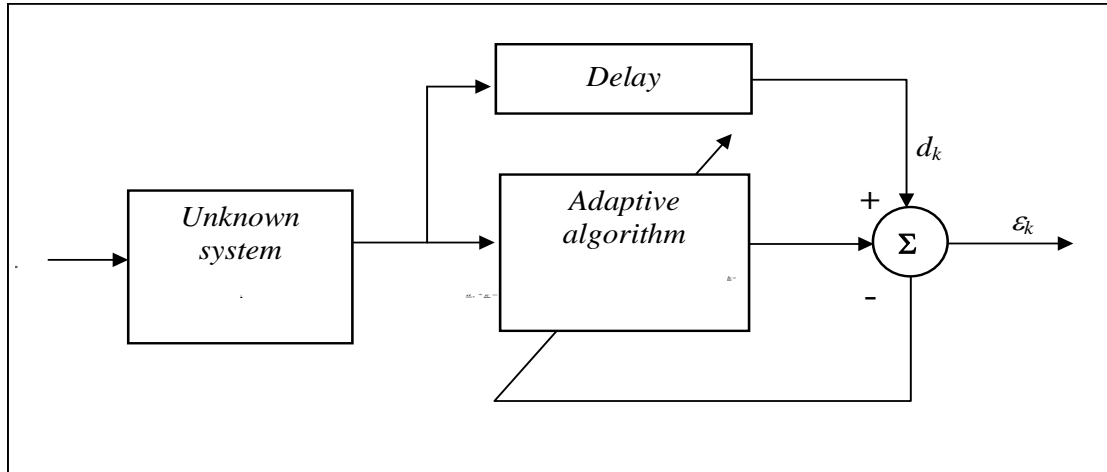


Figure 6 Adaptive RLS diagram

In the time domain, the actual ground acceleration \underline{a}_g is convolved “*” with the filter function of the accelerometer \underline{g} to give the recorded signal \underline{a} .

$$\underline{a} = \underline{a}_g * \underline{g} \quad (14)$$

In this thesis, the implementation of the adaptive algorithm attempts to find a solution to the inverse problem, equation (2) where ideally the inverse filter \underline{h} is such that $\underline{h} = \underline{g}^{-1}$ and then the desired signal \underline{d} equals the actual ground motion \underline{a}_g .

$$\underline{a} * \underline{h} = \underline{d} \quad (15)$$

Solution of this problem, in general, is not possible; however under certain limited condition it is possible to produce an estimate of \underline{h} from the recorded signal \underline{a} . The conditions for the application of the recursive least squares method is that \underline{a} and \underline{a}_g are similar and the amplitude of noise is low, i.e. the signal to noise ratio is high. The Telecoms example, described previously, is an example of the implementation of this approach.

4.1 Summary of De-Convolution with the QR-RLS and the TLS algorithms

There are many different, but related, least squares algorithm for obtaining a system identification. The Least Mean Square (LMS) algorithm [42] is the simplest and easiest adaptive algorithm to implement. However, its performance, in terms of computational cost and fidelity, is not as good as the Recursive Least Square (RLS) [43] and Square Root RLS algorithms (QR-RLS) [12, 43]. There also exists the total least square (TLS) [13]. The QR-RLS and TLS successfully obtained estimates of the instrument response from just the output of the accelerograph during earthquakes in Taiwan and Iceland. The basis for the QR-RLS algorithm and the TLS are summarised.

Inverse QR-Recursive Least Squares (QR-RLS) algorithm

QR-decomposition-based RLS algorithm is derived from the square-root Kalman filter counterpart Haykin [42], Sayed [43]. The ‘square-root’ is in fact a Cholesky factorization of the inverse correlation matrix. The derivation of this algorithm depends on the use of an orthogonal triangulation process known as QR decomposition.

$$QA = \begin{bmatrix} R \\ 0 \end{bmatrix} \quad (16)$$

Where 0 is the null matrix, R is upper triangular and Q is a unitary matrix. The QR decomposition of a matrix requires that certain elements of a vector be reduced to zero. The unitary matrix used in the algorithm is based on a Givens rotation or a Householder reflection, which zero’s out the elements of the input data vector and modifies the square root of the inverse correlation matrix. The QR-RLS is as follows in equation (17) below.

$$\begin{bmatrix} 1 & \lambda^{-1/2} u^H P^{1/2}(n-1) \\ 0 & \lambda^{-1/2} P^{1/2}(n-1) \end{bmatrix} U(n) = \begin{bmatrix} \gamma^{-1/2}(n) & 0 \\ k(n)\gamma^{-1/2}(n) & P^{1/2}(n) \end{bmatrix} \quad (17)$$

Where P = the inverse correlation matrix, λ = *forgetting* factor, γ = a scalar and the gain vector is determined from the 1st column of the post-array. $U(n)$ is a unitary transformation which operates on the elements of $\lambda^{-1/2}u^H(n)P^{1/2}(n-1)$ in the pre-array zeroing out each one to give a zero-block entry in the post-array. The filter coefficients are then updated commencing with equation (18), which is the gain vector. This is followed by equation (19) the a priori estimation error.

$$k(n) = \left[k(n)\gamma^{-1/2}(n) / \gamma^{-1/2}(n) \right] \quad (18)$$

$$\varepsilon(n) = d(n) - h^H(n-1)u(n) \quad (19)$$

$$h(n) = h(n-1) + k(n)\varepsilon(n) \quad (20)$$

This in turn, leads to the updating of the least-squares weight vector, $h(n)$, in equation (9). These inverse-filter weights are an estimate of the inverse transfer function of the instrument and these are then convoluted with the original seismic data in order to obtain an estimate of the true ground motion.

The Total Least Squares (TLS)

The Total Least Squares [13, 62] has a history of applications in de-convolution in medicine and spectroscopy. It was applied to the de-convolution [13] of seismic data in order to obtain an estimate of the instrument response. This method of de-convolution has the advantage that it includes the error in the sensitivity matrix as well as the data vector. Essentially the problem is given by equation (21):

$$\text{minimise} \left(\|Ax - b\|^2 \right) \quad (21)$$

In some practical engineering situations the matrix A is in fact a function of the measured data, as is the case here. Therefore we need to take into account that noise measurements occur on both sides of the matrix equation. This is essentially a total least squares problem, where we have the matrix A plus noise and the matrix b plus noise, $[A + E]$ and $[b + r]$.

The Total Least Squares (TLS) problem is formulated as follows:

$$[A + E] \underline{\hat{x}} = [b + r] \quad (22)$$

Equation (22) can be re-written as:

$$([A|b] + [E|r]) [\underline{\hat{x}}^T, -1]^T = 0 \quad (23)$$

The solution is obtained by first finding the SVD of $[A|b] \in \mathbb{R}^{m \times p}$ as in (26); where $A \in \mathbb{R}^{m \times n}$, $p = n + 1$

$$[A|b] = U \Lambda V^T \quad (24)$$

$$U = [\underline{u}_1 \ \underline{u}_2 \ \dots \ \underline{u}_m], \quad V = [\underline{v}_1 \ \underline{v}_2 \ \dots \ \underline{v}_p], \quad \Lambda = [diag(\sigma_1, \sigma_2, \dots, \sigma_r)] \quad (25)$$

where $U \in \mathbb{R}^{m \times m}$ and $V \in \mathbb{R}^{p \times p}$ are square orthogonal matrices, diagonal matrix $\Sigma \in \mathbb{R}^{m \times p}$ with non-negative number on the diagonal; it is the same size as $[A|b]$. One way to obtain a solution is to find a Householder matrix Q such that

$$VQ = \begin{bmatrix} W & \underline{y} \\ \underline{0}^T & \alpha \end{bmatrix} \quad (26)$$

then the minimum norm solution is given by

$$\underline{\hat{x}} = -\underline{y} / \alpha \quad (27)$$

The solution $\underline{\hat{x}}$ are the filter coefficients. In general then the TLS algorithm demonstrates that it can be used effectively to de-convolute the instrument response from the seismic data. The TLS provides a reasonable tool for de-convoluting the instrument response providing an inverse filter, with which to de-couple the instrument to obtain an estimate of the ground motion.

4.2 Some Results for the QR-RLS and the TLS

Figure 7 demonstrates the performance of the QR-RLS in recovering the frequency response of an “unknown filter” embedded in a simulation of an earthquake using the Kanai-Tajimi model. The simulation shows a reasonable estimate, in particular over the key flat region of the frequency response.

The plots of Figure 8 show that at low frequencies to approximately 40Hz for the El-Centro Eastern component the QR-RLS inverse filter show an approximately flat response (0dB) in the region of interest. The El-Centro Northern component is approximately flat to about 75Hz and the phase plots are approximately linear.

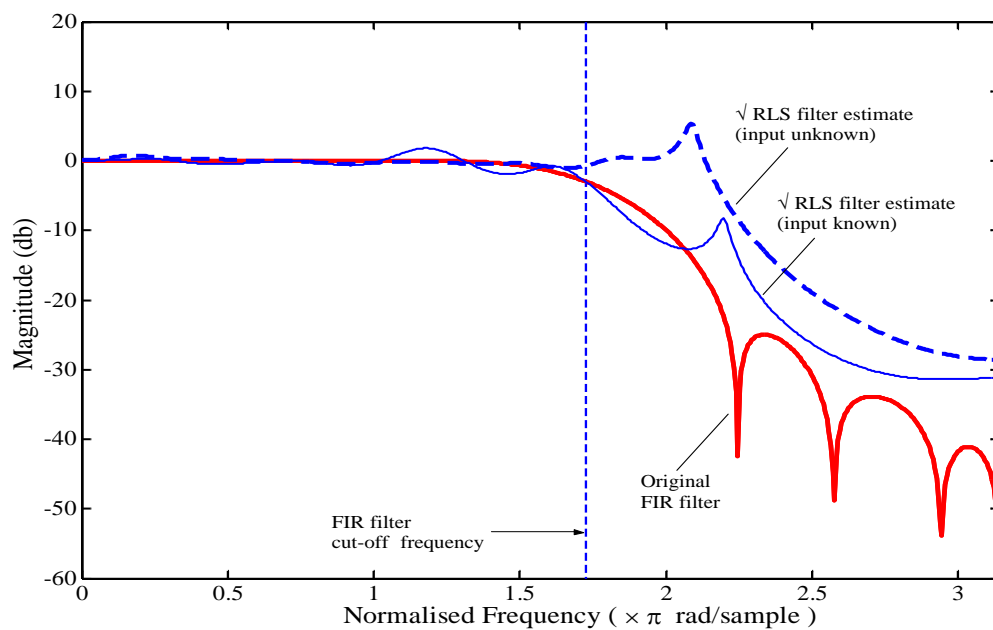


Figure 7 Comparison of QR-RLS recovered filters and original "unknown" FIR test filter (Kanai-Tajimi accelerogram)

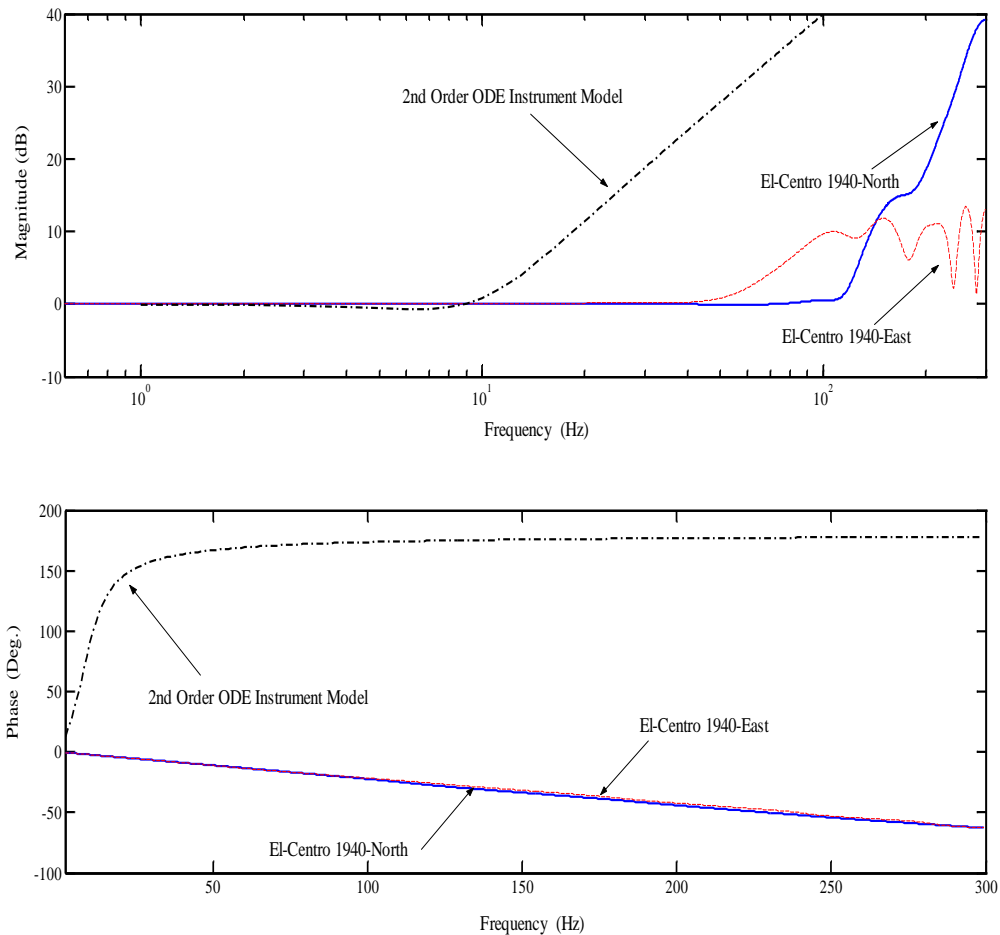


Figure 8 Comparison of extracted instrument characteristic from El-Centro (1940) event using (i) QR-RLS adaptive filter and wavelet pre-denoising (ii) SDOF instrument response ($f = 10 \text{ Hz}$, $\xi = 0.552$)

There is of course an element of uncertainty in both models, in particular given the instruments' years in situ, whether the calibration parameters were in fact correct. The QR-RLS approach does perform quite well in the pass band region, which is, for the engineering, the region of interest. The RLS therefore provides a reasonable indication of instrument performance. These results demonstrate the usefulness of using the QR-RLS in order to de-convolve the instrument response without any prior knowledge of the instrument parameters.

A useful test of the performance of the TLS algorithm comes from the results for the Taiwan earthquake recorded by the SMART-1 array. Two examples are shown in

Figure 9 and Figure 10 with 7- and 9-coefficients respectively, from station TAI03.150N (SA-3000 instrument) with a 25Hz anti-alias filter. Figure 9 and Figure 10 demonstrate that the TLS algorithm performs well and recovers the inverse response of the 5th order Butterworth, anti-alias filter, with a cut-off at 25Hz. The TLS algorithm secured the same cut-off frequency at 25Hz as shown in the frequency response plots for station TAI03.150N and also stations TAI03.149, TAI03.161 and the TAI03.170, all of which have the same anti-alias filter and showed similar performance and results. The phase plots are linear, which means that all the frequencies are impressed with a constant phase difference or the same time shift for all the data points in the time history. Once the inverse filter coefficients are recovered the data is then filtered through the same coefficients in order to obtain an estimate of the de-convoluted data. Results from events in Iceland using the SMA-1, A-700, DCA-333 and SSA-1 instruments with cut-off frequencies at 15Hz, 45Hz, 30Hz and 53Hz respectively as in [13] show that the performance of the TLS algorithm is provides good estimates of the cut-off frequencies in particular for the z-component, which is less sensitive to tilts than the x- and y- components.

The novel application [12, 13, 57, 58, 59] of these adaptive filters to de-couple the instrument response from seismic events has shown that the method of correcting seismic acceleration time-series obtains reasonable estimates of the inverse frequency response. Applying the filters to instruments where the natural frequency and damping ratio are unknown but some of the cut-off frequencies of anti-alias filters are known provides a good measure of the performance of the algorithm. Where standard instrument characteristics such as some of those described in section 2.2 and 2.3 are not available, in particular the instrument natural frequency and critical damping, which is the case for many legacy instruments, then the QR-RLS and the TLS adaptive algorithms, provide a means of obtaining estimates of a corrected acceleration time-series.

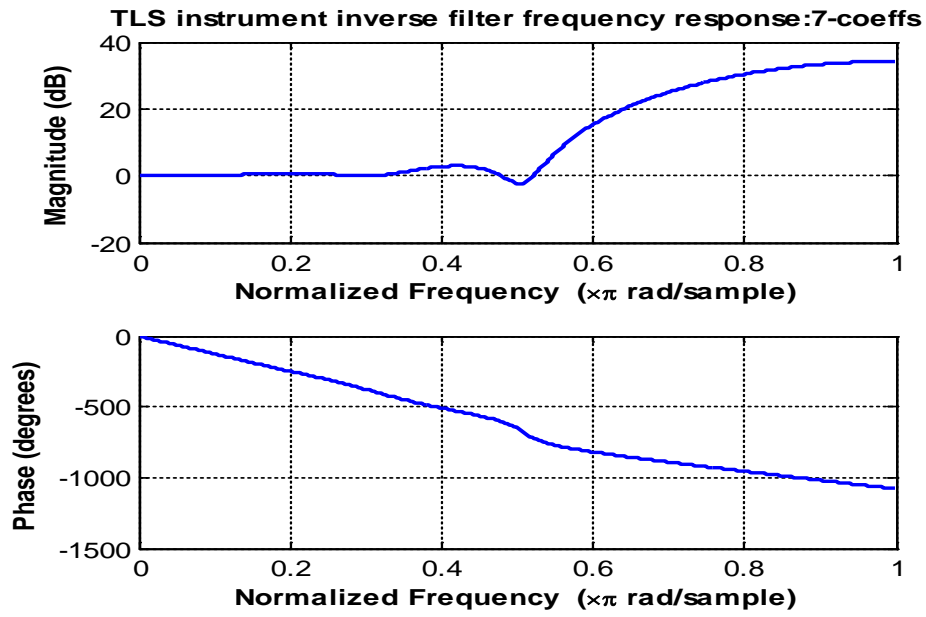


Figure 9 Frequency and phase response plots for a 7-coefficient TLS inverse filter. The event is TAI03.150N from the SMART-1 Array in Taiwan.

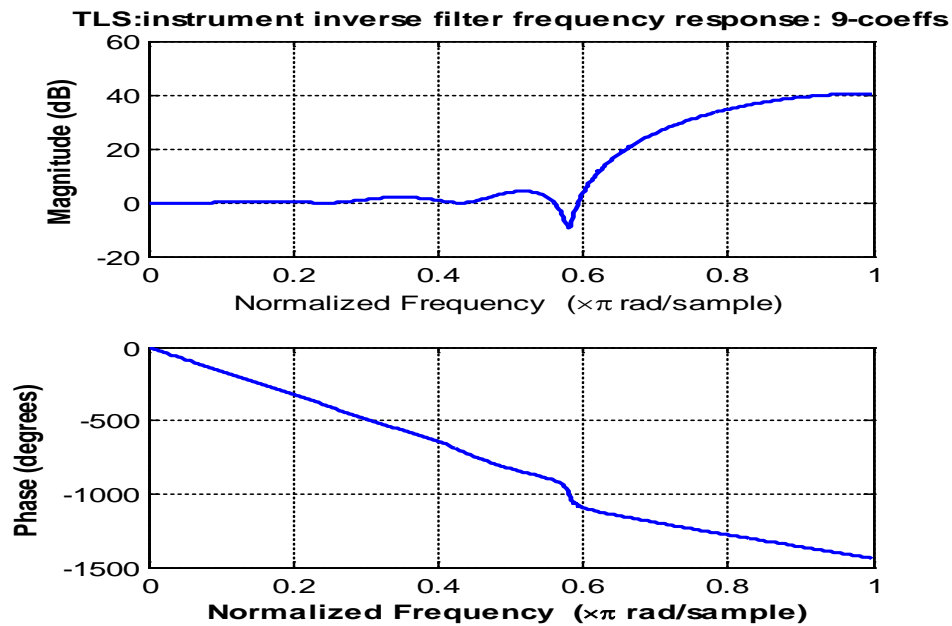


Figure 10 Frequency and phase response plots for a 9-coefficient TLS inverse filter. The event is TAI03.150N from the SMART-1 Array in Taiwan.

Chapter 2 The Recovery of Velocity and Displacement from the Acceleration Time-Series and the Localisation in Time and Removal of the Baseline Error

5.0 Introduction

Unfortunately recovering displacements from acceleration time-histories is not straight forward. Direct double integration does not yield a stable displacement time history as is shown in Figure 3. The displacement time histories in Figure 3 demonstrate the sort of linear and quadratic trends obtained from double integrating after filtering with standard low-cut filters with differing cut-off frequencies.

Sophisticated methods exist for correcting baseline errors and obtaining stable double time integration. Grazier [1,2,44,45] was the first to advocate a baseline correction procedure by obtaining and fitting a straight line to a segment of the velocity. Chiu in [46] high-pass filtered before integration, Iwan *et al* in [47] removed pulses and steps by locating the time points which exceeded a pre-defined acceleration, later generalized by Boore *et al* in [11,15,48,49]. Boore and Akkar [50] by added further time points and made the time point's t_1 and t_2 free of any acceleration thresholds, the accumulated effects of these baseline changes represented by average offsets in the baseline. Wu in [51] also used a modified a method due to [47] on the Chi-Chi event and defined t_1 at the beginning of the ground motion, and defined t_2 on the basis of a flatness coefficient and defined a further parameter t_3 , the time at which the displacement had reached a final value. Wang, *et al* [52] removed pulses and steps fitted with amplitudes which gave the same areas as the slope of the displacement to achieve stable double integration. Pillet and Vireaux in [53] on the other hand, using data from station TCU068 from the 1999 Chi-Chi earthquake, recovered a baseline error as an average acceleration from a linear trend in the velocity and removed it at the time points where the velocity crossed the zero axes. Chen and Loh in [54] also used a wavelet transform method, which applied the decimating discrete wavelet transform, using an FIR filter approximation to the Meyer wavelet. Their method however does not use a de-noising scheme, nor does their method or that of other schemes recover the fling time history. Indeed the recovery of the low-frequency

‘fling’ pulse in time by the wavelet transform algorithm, is novel, never before having been recovered, though always inferred from some strong-motion time-series and modelled as a sinusoidal pulse.

The undecimated wavelet algorithm, described in detail in papers [3, 4, 20 and 56] uses the undecimated wavelet transform, with a de-noising scheme, which is the key to its success. The advantage of using the un-decimated transform with de-noising is that it is automated and it recovers the low-frequency ‘fling’ time history, locates an acceleration transient i.e. the baseline error and permits stable integration to displacement.

Generally the ‘fling’ contains an acceleration transient (‘spike’), which on integration shifts the DC level of the velocity and causes linear trends in displacement. It has been shown that the vertical component is insensitive to tilts, therefore any ‘spikes’ in the vertical direction in the acceleration time history are usually attributed to instrument noise and indeed are usually small when compared with the ‘spikes’ of the horizontal components, which are attributed to ground rotation. This use of the undecimated wavelet transform recovers the residual displacement and extracts and then removes ground rotation acceleration transients that are a cause of double-time integration problems. This shows its usefulness and flexibility in being able to provide not only displacements, but in addition information on the rotational acceleration transients, hitherto always inferred, but never located. We begin this chapter with de-noising

5.1 De-noising overlapping spectra using a threshold

De-noising is a non-linear method of removing unwanted signals, it’s advantageous because spectra (of signal and noise) can overlap, whereas when filtering they should not. It’s the amplitude to which a threshold is applied, it has been applied together with the undecimated wavelet transform in Chanerley *et al* [3, 4 12, 13] to seismic events when de-convolving records. De-noising is superior to filtering in the sense that filtering will remove or attenuate those frequencies which we want to retain. In

particular filtering low-frequency noise will also filter the low-frequency signal (i.e. the fling) so is to be avoided.

The application of a de-noising scheme initially applies a soft threshold [16, 35, 38, 39 and 40] to both the low-frequency and higher frequency sub-bands signals after applying the wavelet filters. However, it was subsequently found that for some earthquakes applying a threshold to the higher frequency sub-bands removed too much detail in the de-noising process (Haldorsson 2009, private communication). Therefore the soft threshold initially applied to the higher frequency sub-bands was removed from the algorithm. This retained the detail without affecting the overall displacement result and when overlaying the original time history on the corrected time history, didn't demonstrate any significant differences.

A soft threshold time-series \tilde{a}_i , where $i \in \{1, 2, \dots, N\}$, is given by equation(3), where τ is a threshold value. Hence, the low power components of x_i are de-noised (removed).

$$\tilde{a}_i = \begin{cases} (a_i - \tau) \text{sgn}(a_i) & |a_i| > \tau \\ 0 & |a_i| \leq \tau \end{cases} \quad (3)$$

Typically the threshold τ is estimated from the standard deviation of the data σ , multiplied by Donoho's "root two log N " [16, 38]

$$\tau = \sigma \sqrt{2 \log N}, \quad \sigma = \frac{MAD}{0.6745} \quad (4)$$

Though there are many other options for selection of a threshold value the critical component is the standard deviation σ of the noise in the data, which is unknown in a general case. Ideally we would have recordings from the accelerographs for in-situ cases where there is no earthquake to characterise the background noise levels and its statistics. However, this is not often available in practice. Furthermore, as we have indicated above, the presence of ground tilts introduces noise that is only present during the earthquake. Thus, we have an uncertain estimate of the statistics of the noise. In the case of accelerograms we use the highest frequency sub-band as an estimate of the noise for the purposes of computing the threshold. From this we compute the Median Absolute Deviation (MAD) that is a robust estimator and more

resilient to outliers in a data set than the sample standard deviation. In order to use MAD as consistent estimator for the standard deviation, it is divided by a scale factor that depends on the probability distribution of the noise (which is again unknown). For a normal distribution this scale factor is $\Phi^{-1}(3/4) = 0.6745$, where Φ^{-1} is the inverse of the cumulative distribution function for the standard normal distribution, and hence equation (4)

5.2 A note on the un-decimated wavelet transform

From an engineering and seismological perspective, the easiest way to envisage the wavelet transform is in terms of octave filters. These are quite common in digital audio. Octave filters form the basis of the wavelet transform, whether the transform is decimated or un-decimated. The wavelet transform comprises in this case well designed filter banks [33, 34, 35, 36, 37]. The decimated, discrete wavelet transform (DWT) is applied in an octave-band filter bank, implementing successive low-pass and high-pass filtering and down sampling by a factor of 2, so that every second sample is discarded. As an example, a 4-channel filter bank scheme is shown in Figure (11). The filters used in wavelet filter banks are digital finite impulse response filters (FIR), also called non-recursive filters because the outputs depend only on the inputs and not on previous outputs.

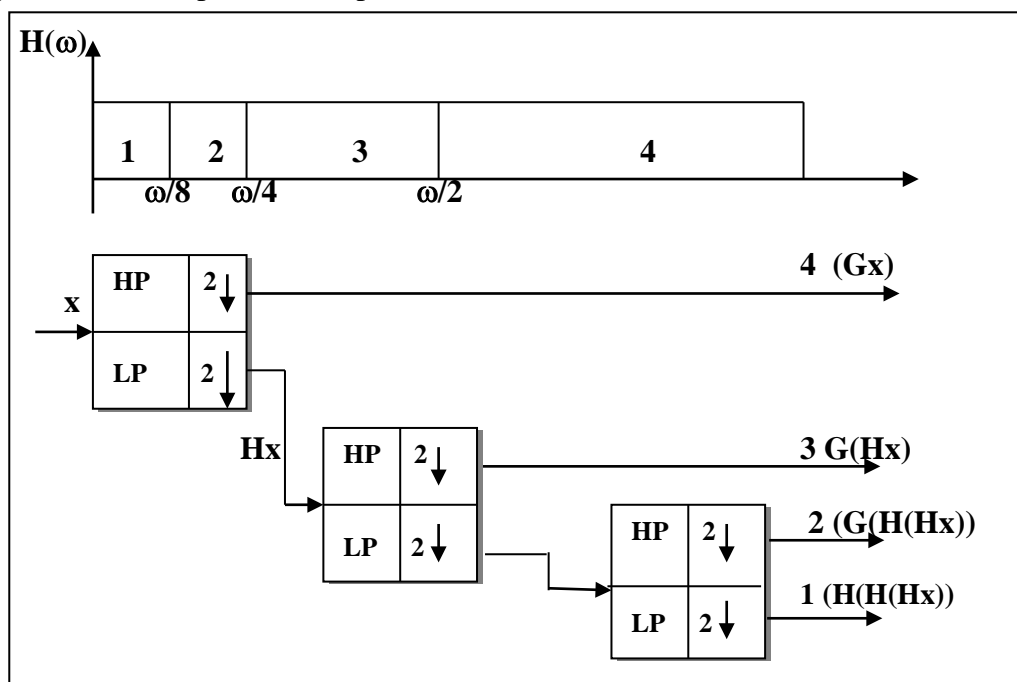


Figure 11: A 4- channel, analysis (decomposition) wavelet filter bank showing sub-band

However, there is a problem with the DWT in that due to down-sampling the DWT it is not shift-invariant. Aliasing can occur between the sub-bands, which is undesirable if the application needs de-noising as in this case. Therefore the easiest way to overcome this is not to down-sample so that the length of the signal remains constant and not as in the decimated DWT and so we use a generalization of the DWT, which is the un-decimated wavelet transform or stationary wavelet transform (SWT), which is shift-invariant. Since we don't decimate then instead we have to interpolate by pushing zeros into each level of the transform (i.e. between the filter coefficients) i.e. dyadically up-sampling, this is the *à trous* algorithm [37, 41] (*trous* = holes). It was also shown in [38 and 39] that the SWT de-noises with a lower root-mean-square error than that with the standard DWT and de-noising is a key requirement for this application. Furthermore, the inverse SWT (iSWT) averages the estimates at each level again minimizing the noise, so overall the SWT is a better transform to apply. Time domain filter banks in Figure (11) show the SWT, there are also the iSWT synthesis filter banks for reconstruction. In the analysis filter banks the easiest thing to do is to push zeros (*à trous*) in between the filter coefficients and keep filtering even and odd samples from every band. In the synthesis filter banks they are averaged at each level. The data of course is also de-noised between the analysis phase using the SWT and the synthesis phase using the iSWT. The appendix presents some pseudo code in order to illustrate how the undecimated wavelet transform with de-noising is constructed.

6 Results

6.1 Some results from Chi-Chi Event, Taiwan (1999), stations TCU052, TCU068 and TCU129

The TCU052NS station from the 1999 Chi-Chi event shows the low-frequency, fling profile time-history of Figure 12, which hides an acceleration tilt transient of 3.015cm/s/s peak, at 48.45s. The acceleration transient is recovered by subtracting the corrected and uncorrected 'fling' time history. The recovered tilt acceleration transient leads to a velocity offset and displacement trend after double-time

integration of the transient. These are precisely the error offsets observed in the velocity and displacement time histories after double-time integrating the (almost) sinusoidal acceleration time history of Figure 12. It is inferred that acceleration transient of 3.015cm/s/s is in fact a $g\theta$ tilt transient. The area of the acceleration tilt profile is 7.21cm/s, which is the velocity offset. Similarly the area under the velocity step is 294.7cm, the maximum displacement offset as shown in Figure 12. The corrected displacement is 641cm, which compares with those of other researchers, the GPS reading is 845cm. The point to note is that the area of the acceleration transient is exactly equal to the constant velocity offset after integrating the acceleration transient and observed in the velocity sub-band. Then after integrating the constant velocity offset, then the result matches exactly the linear trend in the displacement before correction. The TCU052EW low frequency, fling time-histories are shown in Figure 13. In this case the acceleration tilt transient occurs at 40.06s, approximately 8s earlier than the NS component. The displacement is -352cm (GPS -342cm) the instantaneous tilt acceleration $g\theta$, shown in Figure 14, is 12.96cm/s/s and θ the instantaneous tilt angle is 13.2mrad. The area of the acceleration tilt profile is 2.98cm/s, the velocity offset.

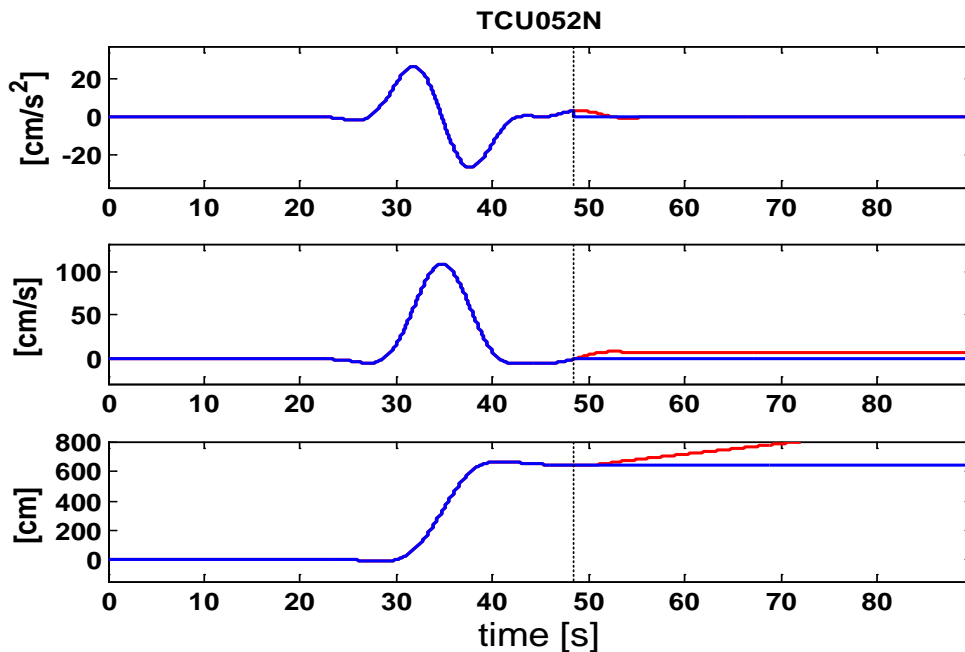


Figure 12: TCU052NS LFS, fling, which shows results before (red, green) and after (blue) baseline correction, wavelet used is the *bior1.3*

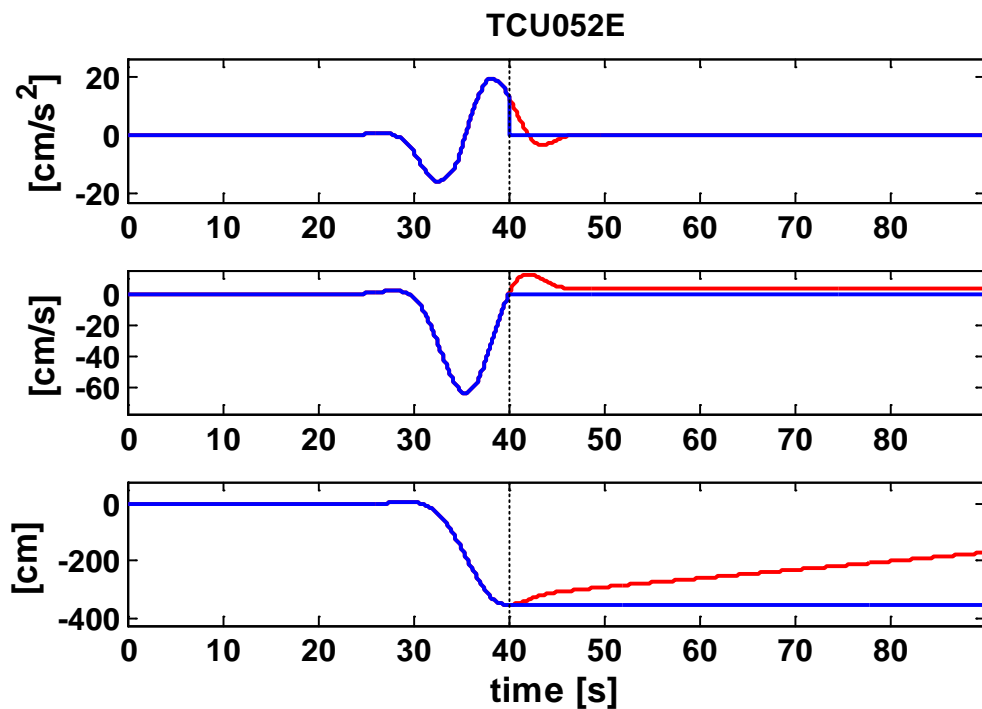


Figure 13: TCU052EW low-frequency sub-band, fling, which shows results before (red) and after baseline correction (blue). The wavelet used is the *bior1.3*

Similarly the area of the velocity step is 180.7cm, which is also the maximum displacement offset as shown in Figure 14 and Figure 15 shows the resulting, corrected time-histories. Moreover, as for the NS component, then on integrating the extracted acceleration transient, it yields the velocity dc shift and displacement offset of the velocity and displacement profile after integrating the acceleration time history as shown in Figure 15.

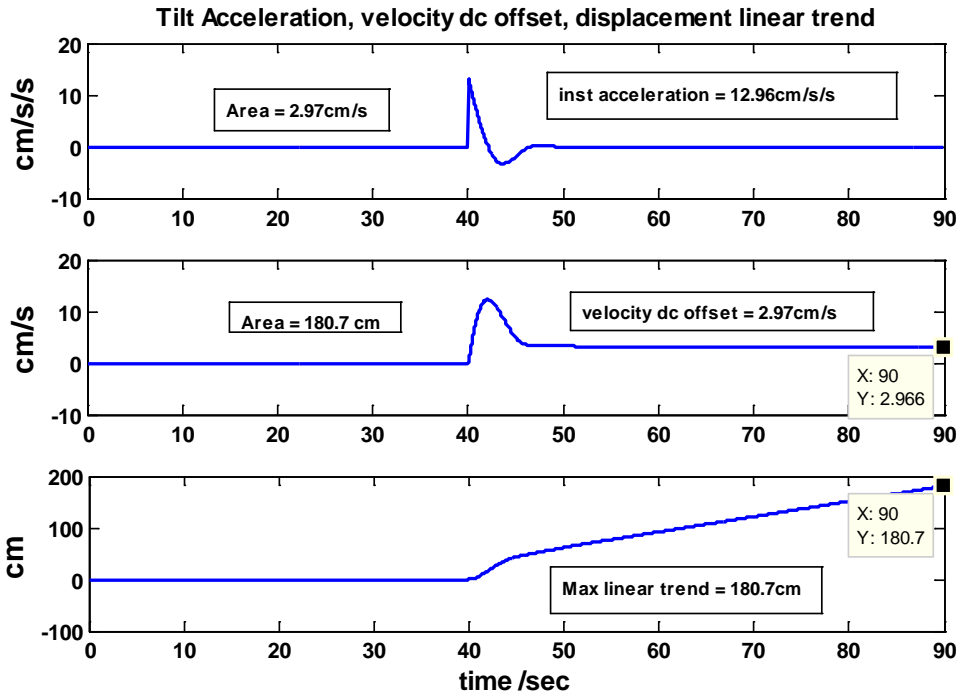


Figure 14 Recovered tilt $g\theta$ acceleration, velocity and displacement response of instrument A900 for the TCU052EW component

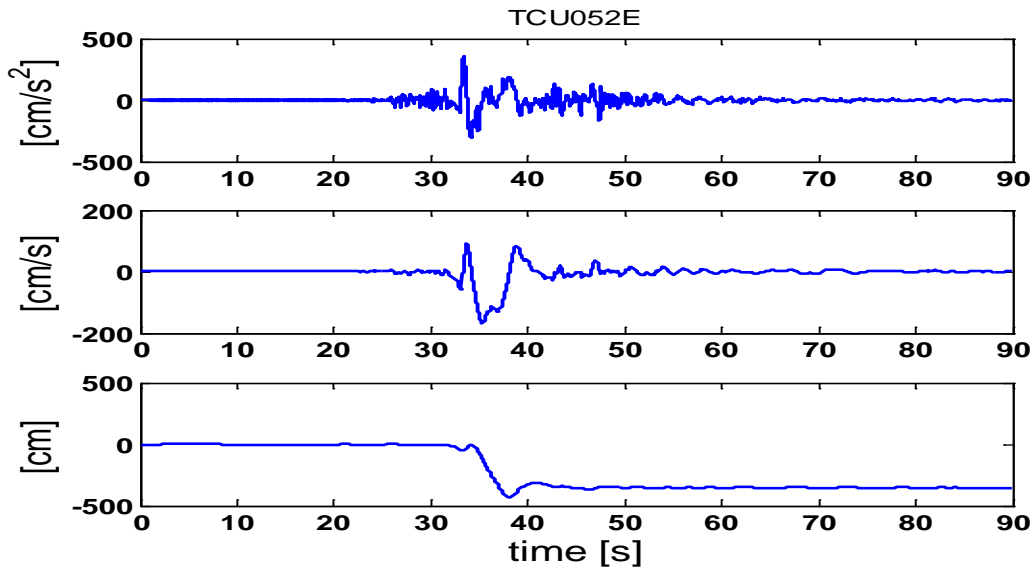


Figure 15 The resultant plots for TCU052EW after the corrected low frequency sub-band (LFS) are added to the high frequency sub-band (HFS)

Similar results are obtained for TCU068NS in Figure 16 and Figure 17, using the undecimated wavelet transform method, the peak instantaneous tilt angles calculated from the peak acceleration transient are calculated as -6.9mrad (-6.75cm/s^2) (EW) and 9.8mrad (9.57cm/s^2) (NS) and the resulting dynamic tilt amplitude obtained is

12.09mrad (11.86cm/s²). It is these peak acceleration transients, which are inferred as due to instantaneous tilt/rotation angles, that cause the dc shift in velocity in the latter portion of the time history and prevent stable double-time integration. These results are similar to those in [53] using a different method, with which to estimate the tilt angles. The estimates of displacement are shown in Table 5.

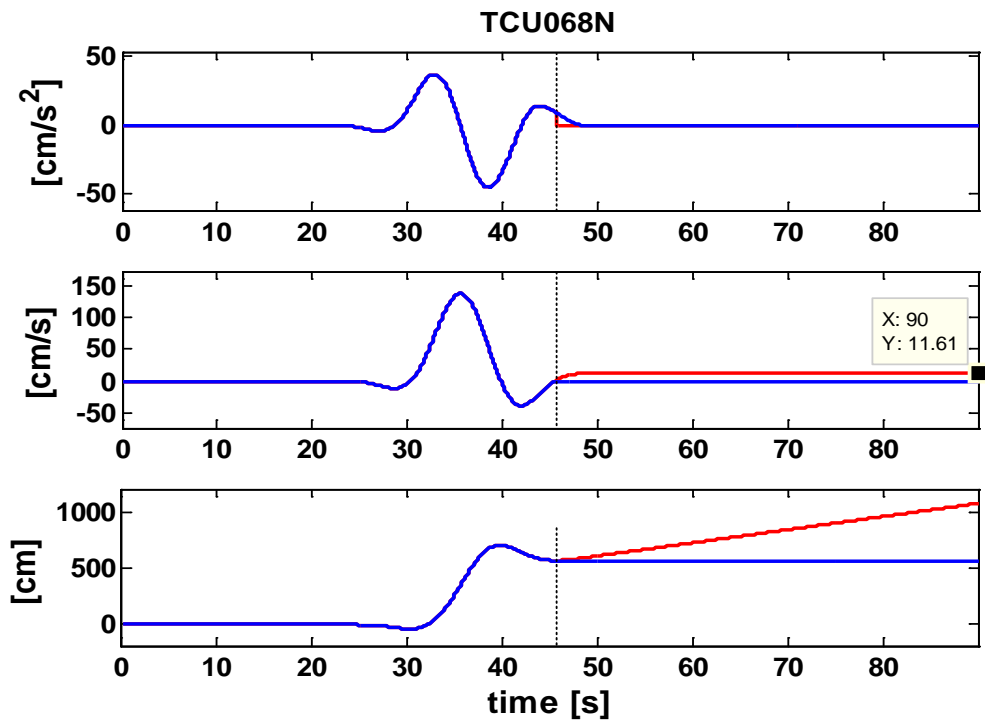


Figure 16 TCU068NS low-frequency sub-band, fling, which shows results before (light gray) and after (black) baseline correction. The triangular area in the acceleration is the results of an acceleration transient $g\theta$ at 45.65s. The resulting constant velocity dc shift of 11.61cm/s is shown in light gray as a post shaking, flat velocity time history

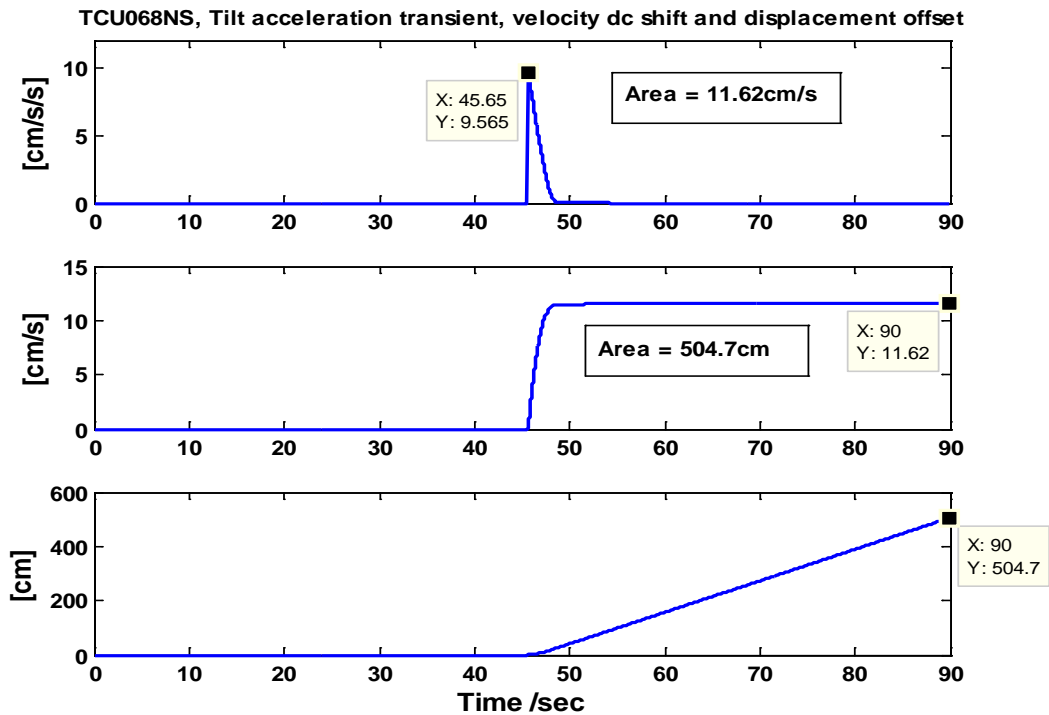


Figure 17 Acceleration Tilt transient for TCU068NS at 45.65s. The resulting constant velocity dc shift of 11.61cm/s is a clear example of a post shaking, flat velocity time history

6.2 Station TCU129 Chi-Chi Event (1999)

Figure 18 shows the low-frequency fling for record TCU129EW after the application of the undecimated wavelet transform, before and after baseline correction. There is clear post-fling distortion in the acceleration. At 30s Figure 19 there is a δ pulse-like jump in the acceleration of $g\theta = -4.8$ cm/s/s and so an instantaneous tilt angle $\theta = 4.9$ mrads, similar to that discussed for stations TCU052 and TCU068.

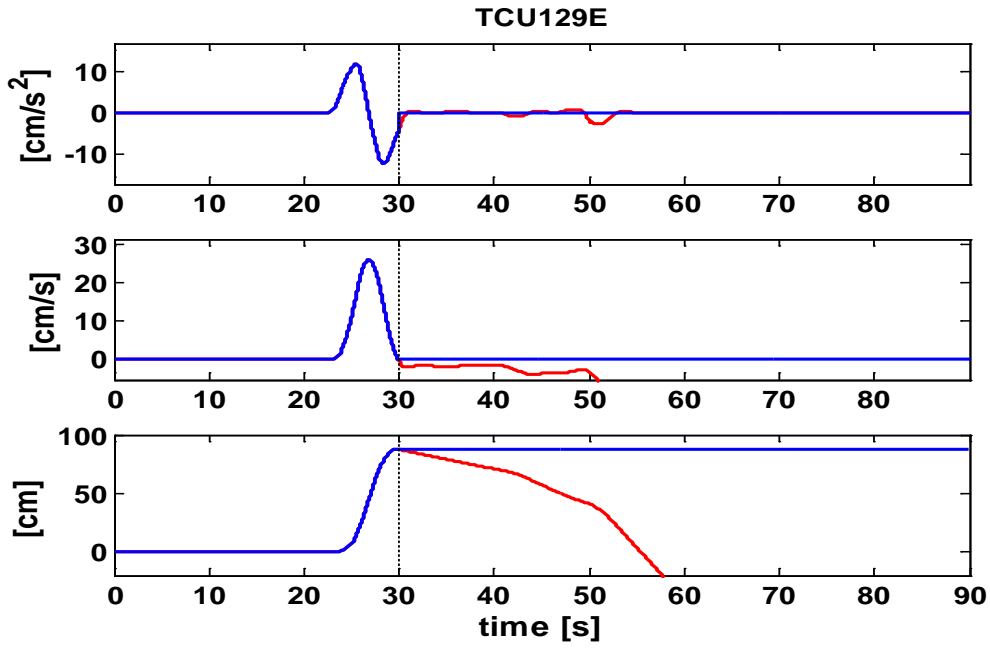


Figure 18 TCU129EW, low-frequency sub-band fling before (red) and after (blue) baseline correction showing tilt/rotation in acceleration and baseline dc shift in velocity

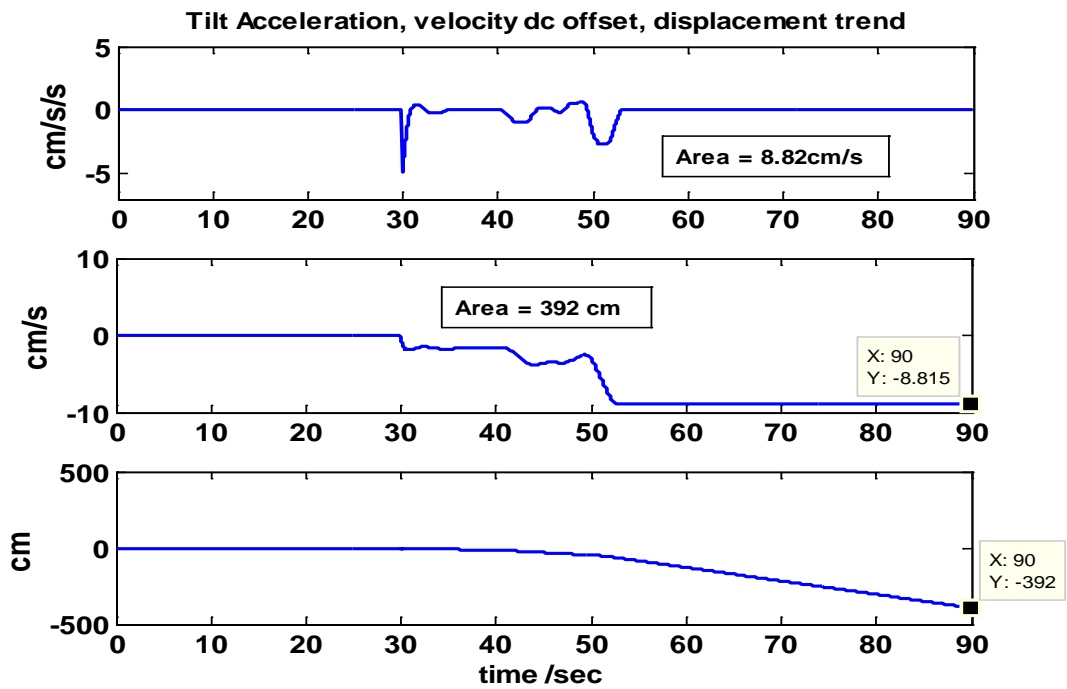


Figure 19 Recovered tilt $g\theta$ acceleration, velocity and displacement response of instrument (A900) for TCU129EW component

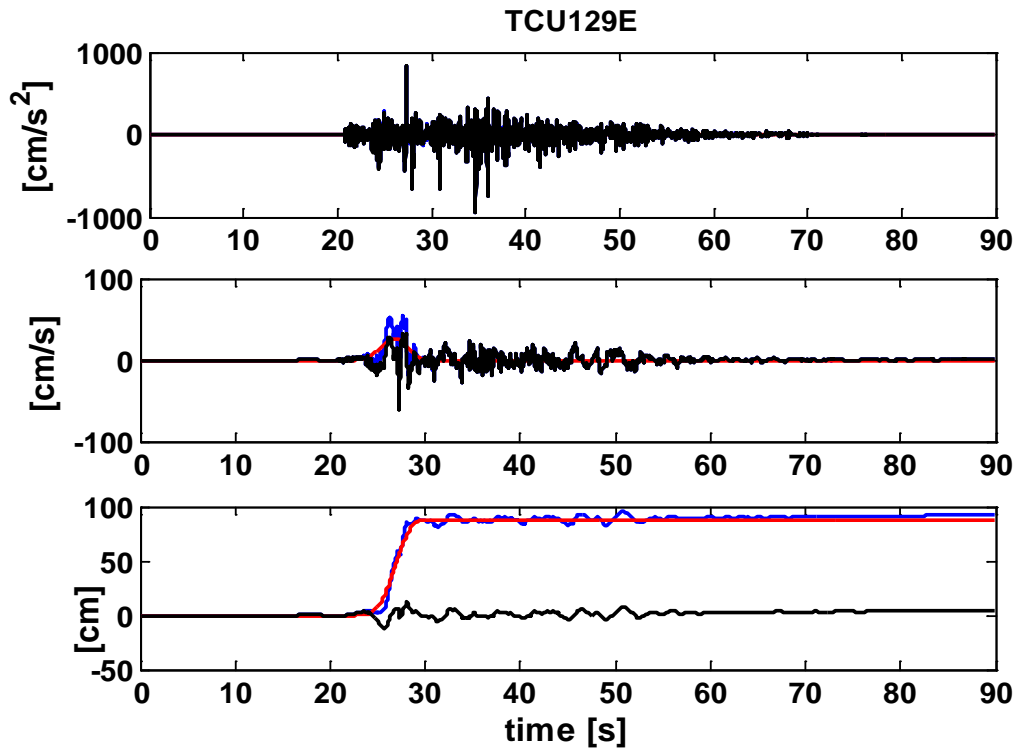


Figure 20 low frequency sub-bands (red), high frequency sub-bands (black), Corrected (blue) using *bior1.3* for TCU129EW component obtained at level 9

However, in addition there is another set of distortions at 40s to 55s. This has led to a series of downward steps in velocity giving rise to a velocity shift of -7.5cm/s/s from zero. The profile of these changes in the acceleration, in particular at $t > 40\text{s}$, with a spike at 30s shown in Figure 19 giving a step in velocity, followed by further velocity steps at $t > 40\text{s}$. Of course there isn't any certitude that these distortions are due to tilts/rotations, there are other effects that could have caused these. However, there is some justification for proposing that these distortions may be due to tilts/rotation. The net permanent displacement is shown in Figure 18 and Figure 20 as 78.48cm . The GPS station AF11 at 2.3km away measured a permanent displacement of approximately 100cm . The time history profiles for TCU129NS are shown in Figure 21 below and in this case the *bior2.6* wavelet was used at a level 9 of decomposition. At 28.1s the low-frequency fling showed an acceleration transient of magnitude $g\theta = 9.93\text{cm/s/s}$, giving a DC shift to the latter part of the velocity time history of 7.65cm/s . The velocity offset after integration then gave a linear trend with a DC offset of 435cm at 90s . These sorts of baseline errors make double-time integration impossible without removing the error. Therefore the undecimated wavelet algorithm

then zeroes-out the acceleration from 28.1s and re-integrates to give the corrected time histories shown below in Figure 21. The GPS displacement for the NS component was -32.1cm that obtained using the presented wavelet transform method is -26.8cm. The TCU129V component is interesting because it suggests either at least 9 more tilts, or just a very noisy instrument. However, in [15] there is a suggestion that the location of the instrument (A900) on a concrete pier may have been the cause of the oscillatory ringing. Certainly there are significant oscillatory effects as can be seen from the time history in Figure 22.

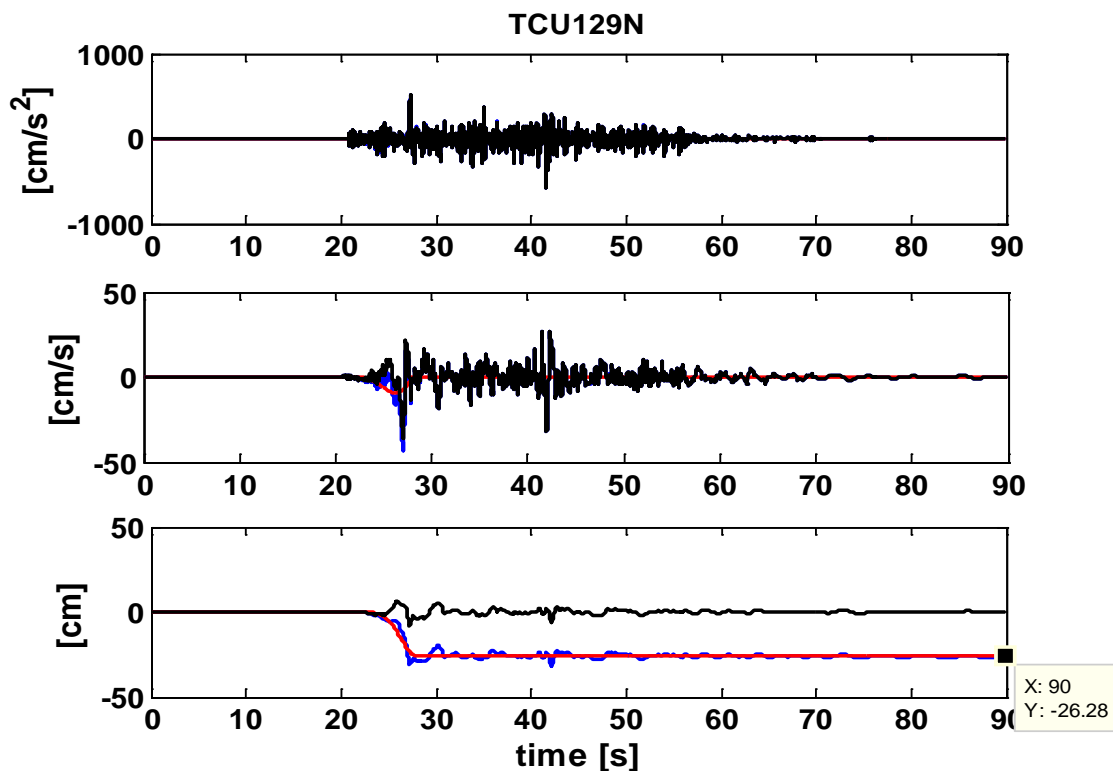


Figure 21 low frequency sub-bands (red), high frequency sub-bands (black), corrected (blue) using *bior 2.6* for TCU129NS component obtained at level 9

Nevertheless the fling pulse in TCU129V is clearly visible both in the acceleration and velocity time history and we take the zero velocity cross-over point at 33.97s immediately after the fling pulse in velocity, zero the acceleration from that point and re-integrate. The first acceleration transient occurs at 33.97s, with a magnitude of 2.12cm/s/s. The displacement is shown in the Figure 22 at -12.26cm that given by GPS is -17.7cm.

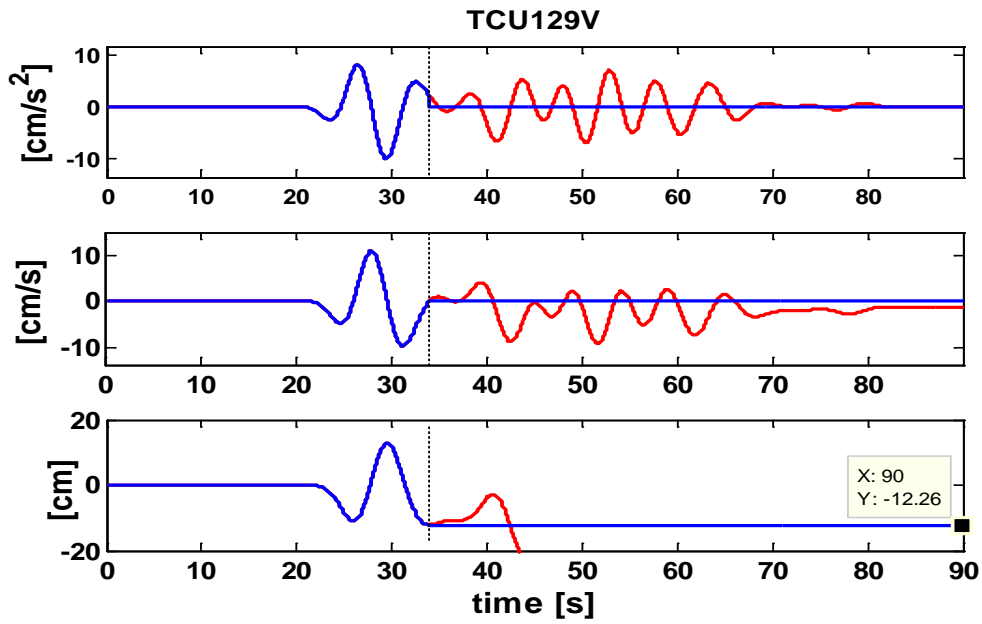


Figure 22: low frequency sub-band (red-before correction), LFS (blue-after correction) of the vertical component TCU129V

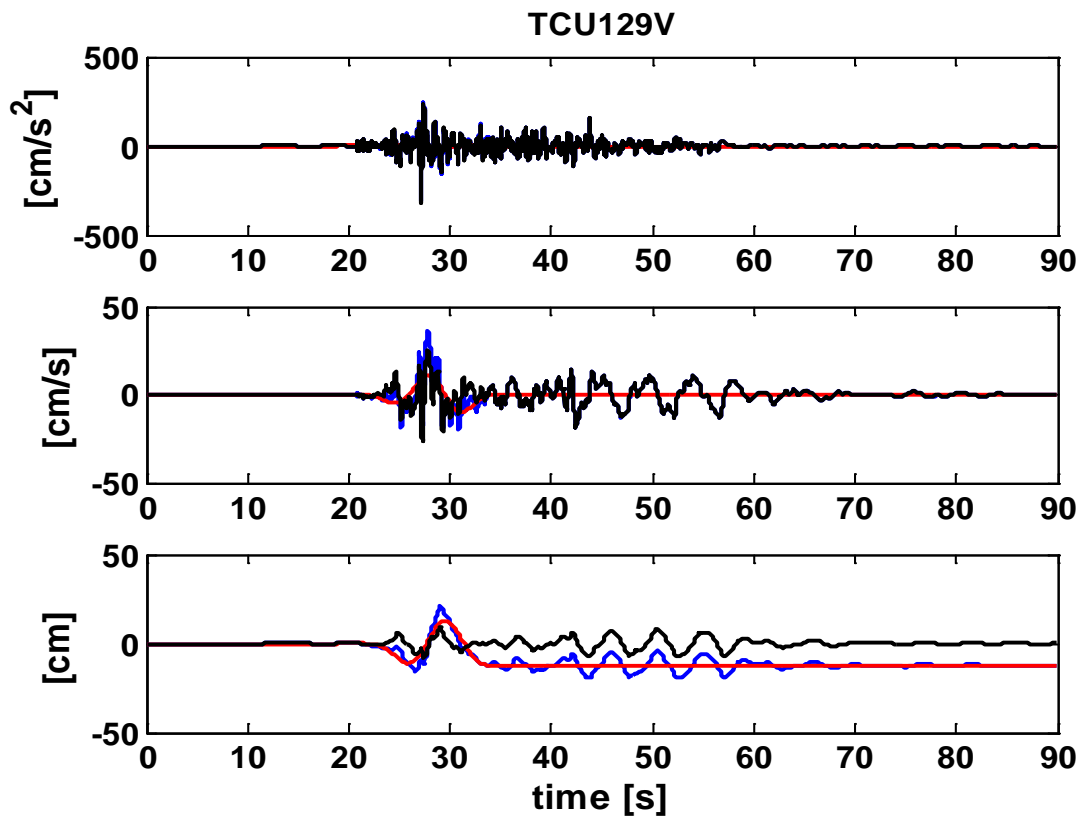


Figure 23: LFS (red), HFS (black), and Corrected (blue) for TCU129V

At the time point where the velocity fling pulse crosses the zero-axis the acceleration is zeroed to the end of the record and re-integrated, giving a displacement of -12.26cm, the GPS reading for that component is -17.7cm. The acceleration transient,

though not explicitly shown is small in magnitude (2.12cm/s/s) compared with that of other components, suggesting its origin may be from instrument noise.

6.3 Some Permanent Displacement and tilt estimate summaries

The results show some consistency in the occurrence of the acceleration transients in TCU129 and the other events displayed in Table 2. Generally the horizontal components ‘tilt’ acceleration transients are larger than that of the vertical component, in particular that for TCU129NS, TCU068NS and TCU102N are very much larger suggesting strong ground rotation.

Table 2: Summary of zero velocity points employed and estimated peak tilt acc

Chi-Chi Station	N-S Components		E-W Components		Vertical Components	
	Tilt Acc	Time	Tilt Acc	Time	Tilt Acc	Time
	cm/s/s	sec	cm/s/s	Sec	cm/s/s	sec
TCU129	9.93	28.1	-4.8	30	2.12	33.97
TCU052	3.015	48.45	12.96	40.06	3.15	44.23
TCU068	9.565	45.65	-6.75	45.83	n/a	n/a
TCU102	10.63	38.39	4.04	41.2	2.174	42.93

However it could also be argued that the component TCU129EW is too close in magnitude to that of the vertical and therefore could be attributed to noise. The results for TCU052 exhibit a large acceleration transient or ‘spike’ for the TCU052EW component (suggesting ground rotation), but demonstrate small acceleration transients for the TCU052NS and TCU052V, suggesting these are just noise. The disparity in the times of occurrence of the acceleration transients, for each component, also suggests instrument noise plays a part. The results in Table 2 for TCU068 and TCU102 are consistent with predicted behaviour, where the vertical components are either not responding to tilts or responding to small amounts of noise. Whilst the horizontal components are responding to ground rotations, given their large magnitudes. In all cases for the above events the estimates of residual displacements show good correlation with those from GPS.

Table 3: Comparison of residual displacement (wavelet method) vs GPS

Level	TCU052NS	TCU052EW	TCU052V
	[cm]	[cm]	[cm]
10	671	-352	369
GPS	845.1	-342.3	397

Table 4 Comparison of residual displacement (wavelet method) vs GPS

Level	TCU129EW	TCU129NS	TCU129V
	[cm]	[cm]	[cm]
9	78.46	-26.8	-12.26
GPS	88.2	-32.1	-17.7

Table 5 Displacements for station TCU068, Chi-Chi event 1999

Wavelet <i>bior1.3</i>		Baseline point	Residual disp.
	i	T_i	$x_i(t_{end})$
		[s]	[cm]
TCU068EW	1	45.7	-731
TCU068NS	2	45.67	555
TCU068V	3	56.84	300

he collated results in Table 3, Table 4 and Table 5, show that the wavelet transform method, [3, 4] produces a good estimate of residual ground displacements and estimates of the baseline error in the form of δ -like acceleration transients ('spikes') caused by ground rotations. There are many more results from events in New Zealand [64], Iceland and Taiwan in the literature published by the author and listed in the references.

7 Conclusions

In this thesis some of the techniques for mitigating noise/error in accelerogram time-series have been reviewed from the work performed by the author and already published in the literature. Older analogue accelerographs clearly present a greater challenge due to their design. Nevertheless these legacy recording are still an important source for structural and geotechnical earthquake engineering designer/analysts. Modern, digital accelerographs are a great improvement in many ways as they correct design problems of earlier instruments such as, higher dynamic range, higher sampling rate, automatic digitization and triggering, flat instrument response down to DC etc. However, the problem of ground rotation (tilt) noise corruption of low frequency components of accelerograms is still present. This is because all strong motion instruments are still only 3 (translational) axes instruments rather than full 6 axes instruments. This may be partially due to cost of designing and building a 6 axis instrument but it is also the case that rotation accelerometers (such as gyroscopic transducers) currently may have far low performance specifications than translational ones.

One solution may be to use multiple 3 axis instruments spaced on a rigid structure such that differences in translational accelerometers (in different instruments) can be used to obtain rotational acceleration estimates. This is often done on bridges for evaluating torsional (rotation) deck modes and could also be applied to ground motion. In this case the classical 3 axis instrument is not re-designed however it would have to be strategically positioned in-situ very close to other 3 axis instruments. Nevertheless modern, state-of-the-art signal processing techniques such as the undecimated wavelet transform with a de-noising algorithm demonstrate the usefulness of tri-axial data in order to facilitate meaningful double-time integration, to recover the fling-pulse, the displacement fling-step and to some extent the rotational (tilt) acceleration transients that are generated by ground rotations. This work go some way towards the recovery of credible ground motion velocity and displacement time-series and therefore better quality boundary conditions in the design of structural artefacts.

References

- [1] V. M. Graizer, "Effect of tilt on strong motion data processing," *Soil Dynamics and Earthquake Engineering*, vol. 25, pp. 197-204, 2005.
- [2] V. Graizer, "Strong motion recordings and residual displacements: What are we actually recording in strong motion seismology?," *Seismological Research Letters*, vol. 81, pp. 635-639, 2010.
- [3] A. Chanerley and N. A. Alexander, "Obtaining estimates of the low-frequency 'fling', instrument tilts and displacement timeseries using wavelet decomposition," *Bulletin of earthquake engineering*, vol. 8, pp. 231-255, 2010.
- [4] A. A. Chanerley, N. A. Alexander, J. Berrill, H. Avery, B. Halldorsson, and R. Sigbjornsson, "Concerning baseline errors in the form of acceleration transients when recovering displacements from strong motion records using the undecimated wavelet transform," *Bulletin of the Seismological Society of America*, vol. 103, pp. 283-295, February 1, 2013 February [doi: 10.1785/0120110352](https://doi.org/10.1785/0120110352).
- [5] M. D. Trifunac and M. I. Todorovska, "A note on the useable dynamic range of accelerographs recording translation," *Soil dynamics and earthquake engineering*, vol. 21, pp. 275-286, 2001.
- [6] M. D. Trifunac, "Zero baseline correction of strong-motion accelerograms," *Bulletin of the Seismological Society of America*, vol. 61, pp. 1201-11, 1971.
- [7] M. D. Trifunac, "A note on correction of strong-motion accelerograms for instrument response," *Bulletin of the Seismological Society of America*, vol. 62, pp. 401-409, 1972.
- [8] M. D. Trifunac and V. W. Lee, "Routine computer processing of strong motion accelerograms," *California Institute of Technology EERL 73(03)*, 1973.
- [9] S. S. Sunder and J. J. Connor, "A new procedure for processing strong-motion earthquake signals," *Bulletin of the Seismological Society of America*, vol. 72, pp. 643-661, 1982.
- [10] A. Converse, "Bap basic strong-motion accelerogram processing software version 1.0," *USGS Open-File Report: 92-296-B*, 1992.

- [11] D. M. Boore and J. J. Bommer, "Processing of strong-motion accelerograms: Needs, options and consequences," *Soil dynamics and earthquake engineering*, vol. 25, pp. 93-115, 2005.
- [12] A. A. Chanerley and N. A. Alexander, "Correcting data from an unknown accelerometer using recursive least squares and wavelet de-noising," *Computers and Structures*, vol. 85, pp. 1679-1692, 2007.
- [13] A. A. Chanerley and N. A. Alexander, "Using the total least squares method for seismic correction of recordings from unknown instruments," *Advances in Engineering Software*, vol. 39, pp. 849-860, 2008.
- [14] A. A. Chanerley and N. A. Alexander, "Deconvolution of seismic data using partial total least squares.," in *First European Conference on Earthquake Engineering and Seismology Geneva, Switzerland*, 2006.
- [15] D. M. Boore, "Effect of baseline corrections on displacements and response spectra for several recordings of the 1999 chi-chi, taiwan, earthquake," *Bulletin of the Seismological Society of America*, vol. 91, pp. 1199-211, 2001.
- [16] D. L. Donoho, "De-noising by soft-thresholding," *IEEE Transactions on Information Theory*, vol. 41, pp. 613-627, 1995.
- [17] R. W. Clough and J. Penzien, "Dynamics of structures", 2nd Ed ed.: McGrawHill Int., 1993.
- [18] N. A. Alexander, "Multi-support excitation of single span bridges, using real seismic ground motion recorded at the smart-1 array," *Computers & Structures*, vol. 86, pp. 88-103, 2008.
- [19] PEER. (2010, Last accessed: 14/Jan/2013). *Pacific earthquake engineering research center (peer) ground motion database*. Available: http://peer.berkeley.edu/peer_ground_motion_database/
- [20] A. A. Chanerley, N. A. Alexander, and B. Halldorsson, "On fling and baseline correction using quadrature mirror filters," *12th International Conference on Civil, Structural and Environmental Engineering Computing*, 2009.
- [21] N. H. Heck and F. Neumann, "Destructive earthquake motions measured for the first time, ," *Engineering News-Record*, vol. 110, pp. 804-807., 1933.
- [22] H. Halverson, "The strong motion accelerograph," in *Proceedings of the 3rd World Conference on Earthquake Engineering*, 1965, pp. 75-93.

- [23] J. G. Proakis, A. Dimitris, and G. Manolakis, "Digital signal processing (3rd ed.): Principles, algorithms, and applications". Prentice-Hall: Inc. Upper Saddle River, 1996.
- [24] M. D. Trifunac and M. I. Todorovska, "Evolution of accelerographs, data processing, strong motion arrays and amplitude and spatial resolution in recording strong earthquake motion," *Soil dynamics and earthquake engineering*, vol. 21, pp. 537-555, 2001.
- [25] *Seismic canterbury instruments*. Available: <http://csi.net.nz/>
- [26] *Ref tek, seismic and earthquake engineering systems* Available: <http://www.reftek.com/>
- [27] *Kinematics inc.* Available: <http://www.kinematics.com/p-163-Home.aspx>
- [28] B. Halldórsson, R. Sigbjörnsson, R. Rupakhety, A. A. Chanerley, and N. A. Alexander, "Permanent coseismic displacement across the icearray due to the 29 may 2008 m w 6.3 earthquake in south iceland."
- [29] O. Khemici and W. Chang, "Frequency domain corrections of earthquake accelerograms with experimental verification," in *Proc of the 8th World Conference on Earthquake Engineering*, San Francisco, USA, 1984, pp. pp 103-110.
- [30] J. F. A. Ormsby, "Design of numerical filters with applications in missile data processing," *Association for Computing Machinery Journal*, vol. 8, 1961.
- [31] L. Rabiner and B. Gold, "Theory and application of digital signal processing": Prentice-Hall, 1975.
- [32] A. V. Oppenheim and R. W. Schaffer, "Discrete-time signal processing": Prentice-Hall, 1989.
- [33] S. Mallat, "A theory for multiresolution signal decomposition: The wavelet representation," *IEEE Pattern Analysis and Machine Intelligence*, vol. 11, pp. pp674-693, 1989.
- [34] I. Daubechies, "Ten lectures on wavelets": Society for Industrial and Applied Mathematics, 1992.
- [35] Coifman R R and Wickerhauser, M. V, "Wavelets and adapted waveform analysis," in *Proc Symposia in Appl Mathematics*, American Mathematics Soc, Providence, Rhode Island., 1993, pp. pp 119-153.

- [36] M. Lang, H. Guo, J. E. Odegard, C. S. Burrus, and R. O. Wells, Jr., "Noise reduction using an undecimated discrete wavelet transform," *Signal Processing Letters, IEEE*, vol. 3, pp. 10-12, 1996.
- [37] M. Shensa, "The discrete wavelet transform: Wedding the a trous and mallat algorithms," *Signal Processing, IEEE Transactions on*, vol. 40, pp. 2464-2482, 1992.
- [38] R. Coifman and D. L. Donoho, "Translation invariant de-noising, wavelets and statistics, lecture notes in statistics" vol. 103, pp125-50: Springer-Verlag, 1995.
- [39] D. L. Donoho and J. M. Johnstone, "Ideal spatial adaptation by wavelet shrinkage," *Biometrika*, vol. 81, pp. 425-455, September 1, 1994 1994.
- [40] P. Abry, "Ondelettes et turbulence. Multirésolutions, algorithmes de décomposition, invariance d'échelles": Diderot Editeur, Paris, 1997.
- [41] Mallat S, (1989) 'A Theory for Multiresolution Signal Decomposition: The Wavelet Representation', *IEEE Pattern Analysis and Machine Intelligence*, 11:7 pp674-693
- [42] S. Haykin, "Adaptive filter theory, 3rd ed": Prentice-Hall, 1996.
- [43] A. Sayed and H. Kaileth, "A state-space approach to adaptive rls filtering," *IEEE signal Process. Mag*, vol. vol 11, pp. pp 18-60, 1994.
- [44] V. M. Graizer, "Determination of the true ground displacements by using strong motion records," *Izvestiya Phys Solid Earth*, vol. 15, pp. 875-885, 1979.
- [45] V. Graizer, (2006) "Tilts in strong ground motion," *Bulletin of the Seismological Society of America*, vol. 96, pp. 2090-2102, Dec
- [46] H.-C. Chiu, "Stable baseline correction of digital strong-motion data," *Bulletin of the Seismological Society of America*, vol. 87, pp. 932-944, August 1, 1997 1997.
- [47] W. D. Iwan, M. A. Moser, and C. Y. Peng, "Some observations on strong-motion earthquake measurement using a digital accelerograph," *Bulletin of the Seismological Society of America*, vol. 75, pp. 1225-46, 1985.
- [48] D. M. Boore, C. D. Stephens, and W. B. Joyner, "Comments on baseline correction of digital strong-motion data: Examples from the 1999 hector mine, california, earthquake," *Bulletin of the Seismological Society of America*, vol. 92, pp. 1543-1560, May 1, 2002 2002.

- [49] D. M. Boore, "Analog-to-digital conversion as a source of drifts in displacements derived from digital recordings of ground acceleration," *Bulletin of the Seismological Society of America*, vol. 93, pp. 2017-2024, October 1, 2003 2003.
- [50] S. Akkar and D. M. Boore, "On baseline corrections and uncertainty in response spectra for baseline variations commonly encountered in digital accelerograph records," *Bulletin of the Seismological Society of America*, vol. 99, pp. 1671-1690, June 1, 2009 2009.
- [51] Y.-M. Wu and C.-F. Wu, "Approximate recovery of coseismic deformation from taiwan strong-motion records," *Journal of Seismology*, vol. 11, pp. 159-70, 2007.
- [52] G.-Q. Wang, D. M. Boore, H. Igel, and X.-Y. Zhou, "Some observations on colocated and closely spaced strong ground-motion records of the 1999 chi-chi, taiwan, earthquake," *Bulletin of the Seismological Society of America*, vol. 93, pp. 674-693, April 1, 2003 2003.
- [53] R. Pillet and J. Virieux, "The effects of seismic rotations on inertial sensors," *Geophysical Journal International*, vol. 171, pp. 1314-1323, 2007.
- [54] S.-M. Chen and Loh C-H, "Estimates of permanent ground displacements from near-fault, strong-motion accelerograms," in *1st European Conference of Earthquake Engineering & Seismology*, Geneva, 2006.
- [55] Chanerley A. A., Alexander, N A, Halldorsson, B "On fling and baseline correction using quadrature mirror filters", 12th International Conference on Civil, Structural and Environmental Engineering Computing, paper 177, Madeira, Portugal, 1-4 September, 2009
- [56] Chanerley A. A., Alexander, N A. "Automated Baseline Correction, Fling and Displacement Estimates from the Chi-Chi Earthquake using the Wavelet Transform" 9th International Conference on Computational Structures Technology, Athens, Greece, 2-5th Sept., 2008
- [57] Chanerley, A. A., Alexander, N.A. "Novel Seismic Correction approaches without instrument data, using adaptive methods and de-noising", 13th World Conference on Earthquake Engineering, Vancouver, Canada, paper 2664, August 1st-6th, 2004
- [58] Chanerley, A. A., Alexander, N.A. "A New Approach to Seismic Correction using Recursive Least Squares and Wavelet de-noising", *Proc of the 9th*

International Conference on Civil and Structural Engineering Computing
ISBN 0-948749-88-1, paper 107, Egmond-aan-Zee, The Netherlands, 2-4
Sept, 2003.

- [59] Chanerley, A. A., Alexander, N.A., “An Approach to Seismic Correction which includes Wavelet De-noising”, Proc of The Sixth International Conference on Computational Structures Technology ISBN 0-948749-81-4, paper 44, Prague, The Czech Republic, , 4-6th September, 2002
- [60] S. S. Sunder, J. J. Connor, “Processing Strong Motion Earthquake Signals”, Bulletin of the Seismological Society of America, Vol. 72. No.2, pp. 643-661, 1982
- [61] A. Kumar, S. Basu, B. Chandra, “Blacs-A new Correction Scheme of Analog Accelerograms. Part-1: details of Scheme”, Bull. Indian Society of Earthquake Technology, Paper No 348, Vol. 32, No. 2 pp 33-50, 1999
- [62] Van Huffel S., Vanderwalle J., “The Total Least Squares Problem Computational Aspects and Analysis”, Siam, vol 9, Frontiers in Applied Mathematics, Philadelphia, 1999
- [63] Avery H R, et al ‘The Canterbury University Strong Motion Recording Project’ Proc 13th World Conf of Earthquake Eng, Vancouver, Canada Paper No. 1335, 2004
- [64] Berrill, J, et al “The Canterbury Accelerograph Network (CanNet) and some Results from the September 2010, M7.1 Darfield Earthquake”, Proc of the 9th Conf on Earthquake Eng., 14-16th April 2011, Auckland, New Zealand

APPENDIX I

The algorithm in pseudo-code is as follows:

Load data and enter subroutine:

function ()

1. Zero-pad data to next power of 2
2. At a high level, decompose data to low and high frequency acceleration subbands using un-decimated wavelet transform.
3. Find maximum decomposition level
4. *Fix high-frequency threshold: Thr1 % This is optional* (see 2010 and 2013 papers)*
5. Fix low-frequency threshold: Thr2 % This is mandatory
6. Threshold the low period sub-bands (*Thresholding the high-frequency sub-band is optional*)
11. Reconstruct low-frequency acceleration sub-band
12. Reconstruct high-frequency acceleration sub-band
13. Remove zero padding
14. Exit subroutine

Enter new subroutine:

15. Integrate low and high frequency acceleration sub-bands
15. Find time-point for 1st zero crossing in low-frequency, velocity sub-band, this should be at the fling
16. Zero-out acceleration at the located time-point
17. Re-integrate sub-bands down to displacement
18. Add the resulting sub-bands for corrected acceleration, velocity, displacement
19. Activate loop for another zero-crossing if necessary and re-run
20. Plot Results

*The point to note here is that to threshold the high frequency sub-band risks removal of the P-wave and other detail

APPENDIX II

Abstracts of the following Published Papers

- 1. Chanerley, A. A.,** Alexander, N. A. “Using a Total Least Squares approach for Seismic Correction of Accelerometer Data”, *Advances in Engineering Software*. Volume 39, Issue 10, pp 849-860, ISSN: 0965-9978, 2008
- 2. Chanerley, A. A.,** Alexander, N.A. “Correcting Data from an unknown Accelerometer using Recursive Least Squares and Wavelet De-noising”, *Computers and Structures*, Issue 21-22, 85 1679-1692, Nov 2007
- 3. Chanerley, A. A.,** Alexander, N. A. “Novel Seismic Correction approaches without instrument data, using adaptive methods and de-noising”, 13th World Conference on Earthquake Engineering, Vancouver, Canada, paper 2664, August 1st-6th, 2004.
- 4. Chanerley, A. A.,** Alexander, N.A. “An Approach to Seismic Correction which includes Wavelet de-noising”, Proc of the 6th International Conference on Computational Structures Technology ISBN 0-948749-81-4, , Prague, Czech Republic, paper 44, 4-6th Sept, 2002. [doi:10.4203/ccp.75.44](https://doi.org/10.4203/ccp.75.44)
- 5. Chanerley, A. A.,** Alexander, N.A., Berrill, J., Avery, H., Halldorsson, B., and Sigbjornsson, R. “Concerning baseline errors in the form of acceleration transients when recovering displacements from strong motion records using the undecimated wavelet transform”, *Bulletin of the Seismological Society of America*, vol. 103, pp. 283-295, February, 2013, [doi: 10.1785/0120110352](https://doi.org/10.1785/0120110352)
- 6. Chanerley, A. A.,** Alexander, N.A., ”Obtaining estimates of the low-frequency ‘fling’, instrument tilts and displacement time series using wavelet decomposition”, *Bulletin of European Earthquake Engineering*, vol. 8, pp231-255, 2010
<http://dx.doi.org/10.1007/s10518-009-9150-5>
- 7. Chanerley A. A.,** Alexander, N A, Halldorsson, B, 'On fling and baseline correction using quadrature mirror filters', *12th International Conference on Civil, Structural and Environmental Engineering Computing*, paper 177, Madeira, Portugal, 1-4 September, 2009 " [doi:10.4203/ccp.91.177](https://doi.org/10.4203/ccp.91.177)
- 8. Chanerley A. A.,** Alexander, N A., ‘Automated Baseline Correction, Fling and Displacement Estimates from the Chi-Chi Earthquake using the Wavelet Transform’*9th International Conference on Computational Structures Technology* Athens, Greece, 2-5th Sept., 2008 <http://dx.doi.org/10.4203/ccp.88.197>

Using the total least squares method for seismic correction of recordings from unknown instruments

A.A. Chanerley^a, N.A. Alexander^{b,*}

^a *School of Computing and Technology, University of East London, United Kingdom*

^b *Department of Civil Engineering, University of Bristol, Bristol, United Kingdom*

Available online 11 September 2007

Abstract

This paper describes the correction or recovery of the original ground motion acceleration time histories from accelerometer digital records. It deals specifically with the situation where the recording accelerometer instrument is unknown. This is the case with some older (legacy) records. The term instrument implies all processes that have modified the time history in some way, such as the accelerometer response transfer function, anti-alias filters used in A/D conversion, digital quantisation, etc. The total least squares (TLS) method is used to identify the unknown system (instrument) that must be used to de-convolute the recorded time histories. This approach is compared and contrasted with the recursive least squares method (QR-RLS) and a standard second order, single-degree-of-freedom, idealised instrument de-convolution. A range of seismic events from Iceland and Taiwan (SMART-1 array) are considered. These data sets include a number of different strong motion accelerometers, from Iceland: the SMA-1, DCA-333, A-700, SSA-1 instruments and the SA-3000 used in the SMART-1 array. Without any assumed information about the instrument the TLS is shown to provide a reasonable estimate of its characteristics from just the recorded time history data.

© 2007 Elsevier Ltd. and Civil-Comp Ltd. All rights reserved.

Keywords: Correction; Filter; Seismic; Wavelet; De-noising; Recursive; Least squares; Band-pass; Filtering; Filter; Inverse filter; Convolute; De-convolution; Butterworth

1. Introduction

In earthquake engineering the analysis of complex structural systems often requires a time history analysis based on the FE method. These types of analyses require in some cases real ground motion acceleration, velocity and displacement time histories. The databases of records held by various agencies [1,2], etc. contain a large quantity of data from historic events that are very important to the structural engineering analyst. However, these records often require processing and correction to recover the best estimate of the true ground motion.

Typical correction techniques [3] used are necessary to (i) digitise, i.e., equi- and up-sample the data; (ii) de-trend; (iii) de-noise using the wavelet transform or band-pass filter [4], using digital Butterworth, Chebyshev filters or digital

Finite Impulse Response (FIR) filters [5–8]; (iv) correct for instrument characteristics; (v) down-sample to an appropriate sampling rate. The sequence of the component (ii)–(v) and exact algorithms used in these correction techniques may vary significantly, as can the resulting recaptured original ground motion itself.

Recent methods, which describe the de-convolution of an instrument response from seismic data, apply a least squares based, inverse, system identification method [4,9,10] with which to de-convolute the instrument response from the ground motion. Previous methods assume a second order, single-degree-of-freedom (SDOF) [5,7] instrument function and apply an inverse filter in the time or frequency domain. This de-convolves the instrument response from the recorded time history. Whereas in other cases, corrected seismic data [1] are not explicitly de-convoluted, as a consequence of insufficient instrument parameter data in particular with older records.

* Corresponding author.

The advantage of the least squares based method is that it does not require any information regarding the instrument; it only requires the data, which the instrument has provided, from which to determine an estimate of the inverse of the instrument response. However, the least squares solution which minimises $\|\mathbf{A}\underline{x} - \underline{b}\|^2$ has been sought with the assumption that the data matrix \mathbf{A} is ‘correct’ and that any errors in the problem are in the vector \underline{b} . This paper applies the method of total least squares (TLS), [11–16] which allows for the fact that both \mathbf{A} and \underline{b} may be in error.

A range of instruments and their performance are compared using Icelandic and Taiwanese (SMART-1 array [2,17]) seismic data, digitally recorded and with some instrument parameters included. These parameters are the viscous damping ratio and the natural frequency, which are usually the transducer specification, therefore may not be ‘instrument’ in the global sense, since usually they do not include any pre- or post-filtering details. The instrument types compared include SMA-1, DCA-333, A-700, SSA-1 [1,18] and the SA-3000 for the SMART-1 array [2,17]. Each seismic record had some details of the instrument parameters, assumed here to be for the transducer only, but not all had details of filtering used in the instrument. The SA-3000 SMART-1 data however gave explicit details of the anti-alias filter used with a cut-off of 25 Hz, the transducer natural frequency as 140 Hz and damping of $0.7 \pm 2\%$.

Instrument performance was based on a comparison of time histories and frequency responses obtained by de-convoluting using the method of total least squares (TLS) and the QR-RLS [9,10,19,20]. Correlation was good up to and at the cut-off frequencies, thereafter the roll-off between the methods differed in gradient, with the TLS and QR-RLS showing steeper gradients than that for the second order, SDOF response. This is consistent with the fact that digital instruments would have an anti-alias filter whose impression would be embedded in the data.

A particular problem in seismic correction methods is that quite often the transfer function of the recording instruments is not known, in particular in some older (legacy) records. Where instrument parameters are provided, a second order SDOF transfer function is applied in either the time or frequency domain [5–8] in order to de-couple the instrument response. The time-domain expression is given by

$$a_g(t) = -\ddot{x}(t) - 2\gamma\omega\dot{x}(t) - \omega^2x(t) \quad (1)$$

where γ is the viscous damping ratio, ω is the transducer’s natural frequency and $a_g(t)$ is the ground acceleration.

The above expression (1) can be used to de-convolve the recorded motion from the ground acceleration in either the time or frequency domain. However, it should be noted that those instrument parameters given usually apply to the transducer only and not to the instrument as a whole. The transducer is certainly an important element, but included should be the responses due to any signal condi-

tioning such as amplification and filtering. In any seismograph there is a cascade of transfer functions due to different elements which make up the instrument.

However, where instrument parameters are not available, then unless some assumptions are made regarding instrument parameters, it is not possible to de-convolve (de-couple) the instrument response from the seismic data using a second order SDOF expression. Therefore, researchers either do not de-convolute the data or just apply a SDOF correction for the transducer only.

A least squares approach was proposed [10] embedded in an inverse system identification problem, with which to de-convolve the instrument response. This provides an estimate of the instruments inverse frequency response with which to de-convolve the data to obtain an estimate of the ground motion. The problem is formulated below:

$$\text{minimise } (\|\mathbf{A}\underline{x} - \underline{b}\|^2) \quad (2)$$

$$\underline{x} = (\mathbf{A}^T\mathbf{A})^{-1}\mathbf{A}^T\underline{b} = \mathbf{P}\mathbf{A}^T\underline{b} \quad (3)$$

The approach involves a least squares minimisation, Eq. (2), of the norm squared errors for a given choice of filter coefficients \underline{x} . This problem (2) has the well-known solution given by Eq. (3) where \mathbf{P} is the inverse correlation matrix and the coefficients.

Efficient methods used to find an estimate of the inverse filter coefficients are the recursive least squares algorithm (RLS) and its more stable variant, the square-root recursive least squares algorithm (QR-RLS) [19,20].

However, in all of these methods it is assumed that errors present are all in the observation matrix, in this case the matrix \underline{b} in (2). This assumption is not always realistic since errors are also present in the convolution matrix \mathbf{A} , given that it is derived from the recorded seismic data. Therefore, a better more general fitting method, the total least squares (TLS), is examined which compensates for errors both in the matrix \underline{b} and the matrix \mathbf{A} , and the problem is re-formulated.

2. The total least squares algorithm

The TLS solution is the minimum norm solution \hat{x} such that

$$\hat{\mathbf{A}}\hat{\mathbf{x}} = \hat{\mathbf{b}} \quad (4)$$

where $\hat{\mathbf{A}}$, $\hat{\mathbf{b}}$ is the best rank r approximation to \mathbf{A} , \mathbf{b} , $\hat{\mathbf{x}}$ is the TLS solution of (4), $\hat{\mathbf{A}} = \mathbf{A} + \Delta\mathbf{A}$, $\hat{\mathbf{b}} = \mathbf{b} + \Delta\mathbf{b}$ and \mathbf{A} and \mathbf{b} are the exact but unobservable data matrices and $\Delta\mathbf{A}$ and $\Delta\mathbf{b}$ are the perturbation errors

$$\text{so that } \|\Delta\hat{\mathbf{A}}|\Delta\hat{\mathbf{b}}\|_F = \|[\mathbf{A}|\mathbf{b}] - [\hat{\mathbf{A}}|\hat{\mathbf{b}}]\|_F \text{ is minimal} \quad (5)$$

$$\text{and } R(\hat{\mathbf{b}}) \subset R(\hat{\mathbf{A}}) \quad (6)$$

where $R(\mathbf{a})$ is the range (column space) of \mathbf{a} and $\mathbf{c}|\mathbf{d}$ means that \mathbf{c} and \mathbf{d} are arranged side-by-side (augmented). $\|\mathbf{a}\|_F$ signifies the Frobenius norm of matrix \mathbf{a} . To find a solution to the TLS problem we write (4) as follows:

$$[\mathbf{A} + \Delta\mathbf{A}]\hat{\mathbf{x}} = [\mathbf{b} + \Delta\mathbf{b}] \quad (7)$$

$$\text{or } [\mathbf{A}|\mathbf{b}] + [\Delta\mathbf{A}|\Delta\mathbf{b}][\hat{\mathbf{x}}^T, -1]^T = 0 \quad (8)$$

We can use the singular value decomposition (SVD) in order to find the TLS solution to (8). The augmented vector $[\hat{\mathbf{x}}^T, -1]^T$ must lie on the null-space of $([\mathbf{A}|\mathbf{b}] + [\Delta\mathbf{A}|\Delta\mathbf{b}])$ and the perturbation $[\Delta\mathbf{A}|\Delta\mathbf{b}]$ must be such that $([\mathbf{A}|\mathbf{b}] + [\Delta\mathbf{A}|\Delta\mathbf{b}])$ is rank deficient.

The generic solution of the TLS problem is developed in [11,12] and uses the SVD. Denote the SVD of $[\mathbf{A}|\mathbf{b}] \in \mathbb{R}^{m \times p}$ as (9); where $\mathbf{A} \in \mathbb{R}^{m \times n}$, $p = n + 1$

$$[\mathbf{A}|\mathbf{b}] = \mathbf{U}\mathbf{\Sigma}\mathbf{V}^T \quad (9)$$

$$\mathbf{U} = [\underline{u}_1 \underline{u}_2 \dots \underline{u}_m], \quad \mathbf{V} = [\underline{v}_1 \underline{v}_2 \dots \underline{v}_p],$$

$$\mathbf{\Sigma} = [\text{diag}(\sigma_1, \sigma_2, \dots, \sigma_r)] \quad (10)$$

where $\mathbf{U} \in \mathbb{R}^{m \times m}$ and $\mathbf{V} \in \mathbb{R}^{p \times p}$ are square orthogonal matrices, diagonal matrix $\mathbf{\Sigma} \in \mathbb{R}^{m \times p}$ with non-negative number on the diagonal; it is the same size as $[\mathbf{A}|\mathbf{b}]$. The number r is the rank of $[\mathbf{A}|\mathbf{b}]$. If $r = \min(m, p)$ then matrix $[\mathbf{A}|\mathbf{b}]$ full rank, i.e., all the columns (if $m \geq p$) or all the rows (if $m \leq p$) are linearly independent. The singular values are usually ordered such that $\sigma_1 \geq \sigma_2 \geq \sigma_3 \dots \geq \sigma_r \geq 0$.

However, this solution requires the reduced rank matrix closest to $[\mathbf{A}|\mathbf{b}]$, which in this case is $([\mathbf{A}|\mathbf{b}] + [\Delta\mathbf{A}|\Delta\mathbf{b}])$. Therefore, to obtain a minimum deviation $[\Delta\mathbf{A}|\Delta\mathbf{b}]$ such that (5) and (6) are satisfied we replace σ_{n+1} with zero. Therefore,

$$([\mathbf{A}|\mathbf{b}] + [\Delta\mathbf{A}|\Delta\mathbf{b}])[\hat{\mathbf{x}}^T, -1]^T = 0 \quad (11)$$

$$\text{with } ([\mathbf{A}|\mathbf{b}] + [\Delta\mathbf{A}|\Delta\mathbf{b}]) = \mathbf{U}\hat{\mathbf{\Sigma}}\mathbf{V}^T \quad \text{and} \quad \hat{\mathbf{\Sigma}} = \text{diag}(\sigma_1, \dots, \sigma_n, 0) \quad (12)$$

and so the desired TLS solution can be found from the last row in \mathbf{V}^T of the SVD of $[\mathbf{A}|\mathbf{b}]$ in (9) and is given by

$$\hat{\mathbf{x}} = -\underline{v}(1 : n)/v_{n+1, n+1} \quad (13)$$

Next the TLS solution is generalised by assuming that the smallest singular value is repeated:

$$\sigma_1 \geq \sigma_2 \geq \sigma_3 \geq \dots \sigma_k \geq \sigma_{k+1} = \sigma_{k+2} = \dots \sigma_{n+1}$$

An approach to obtain a solution is to find a Householder matrix \mathbf{Q} such that

$$\mathbf{V}\mathbf{Q} = \begin{bmatrix} \mathbf{W} & \underline{y} \\ \underline{0}^T & \alpha \end{bmatrix} \quad (14)$$

then the minimum norm solution is given by

$$\hat{\mathbf{x}} = -\underline{y}/\alpha \quad (15)$$

A procedure for computing the solution to the TLS problem is listed in the appendix.

3. Numerical results for seismic events in Iceland

The results confirm the usefulness of using this method of de-convoluting the instrument response. These are

shown for four types of instrument, the SMA-1, the A-700, the DCA-333 and the SSA-1, which were used in several Icelandic seismic events [1,18]. In all cases the data was de-noised using the stationary wavelet transform prior deconvolution, with the db8, Daubechies (8) wavelet [21–23] of order $N = 8$ as basis. In all cases for the Icelandic data the number of filter coefficients used is 51 for the TLS and 11 for the RLS. There is no any particular reason for this, except to demonstrate different filter features, because more coefficients with the RLS yield more ripples whereas a smaller number of coefficients give a smoother response and less ripples. However, there is a point to be made with the SMART-1 data from Taiwan, where instrument parameters are more detailed and the number of coefficients become a determining factor when comparing the TLS algorithm against the inverse of the fifth order, anti-alias Butterworth filter details provided.

3.1. SMA-1 instrument

Fig. 1 shows a comparison of inverse frequency responses using the theoretical second order SDOF at a frequency of 13 Hz and damping of 0.6 of an SMA-1 instrument which recorded the x -component of Icelandic seismic event 005267 in 1987. The correlation between the theoretical response, the response due to the QR-RLS and the TLS is high up to 13 Hz. However, thereafter the roll-off of both the QR-RLS and the TLS is much less steep that the theoretical response. It should be understood that the best-fit polynomial is drawn through the TLS solution, which comprises the finite impulse response (FIR) inverse filter side lobes (removed from Fig. 1). This is to give better visualisation of the trend as compared with the QR-RLS and the second order SDOF.

Fig. 2 compares the frequency responses in the y - and z -components of the same seismic event when de-convolved

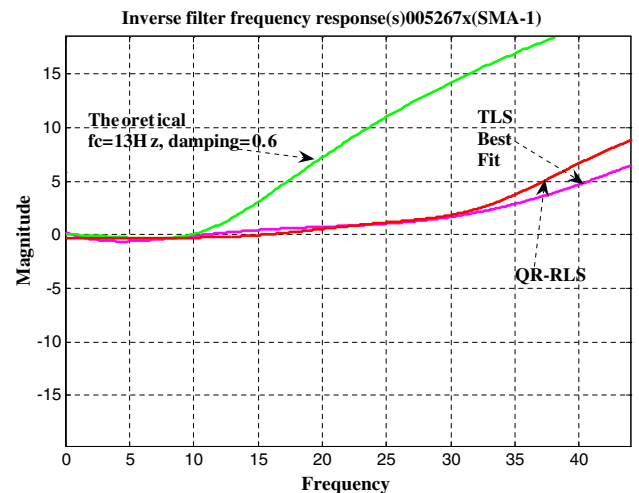


Fig. 1. Comparison of theoretical instrument response ($F_c = 13$ Hz, damping = 0.6) and that of the QR-RLS and the TLS best-fit seventh order polynomial.

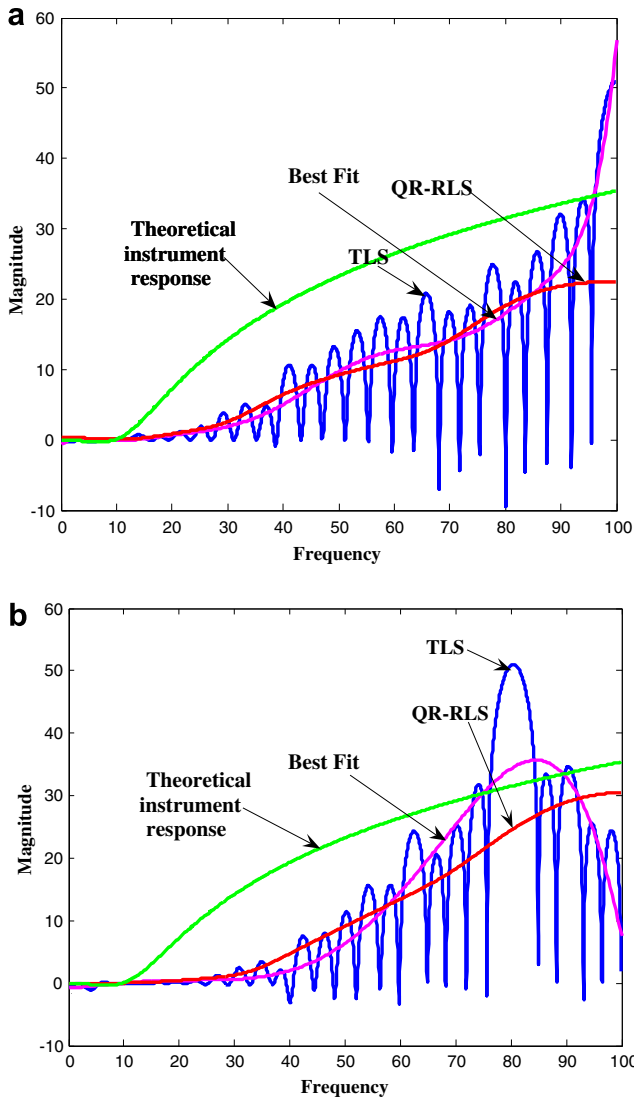


Fig. 2. Inverse frequency responses for the instrument SMA-1 using TLS and QR-RLS for accelerograms: (a) 005267y and (b) 005267z.

using the TLS (FIR) solution, the QR-RLS and the theoretical response. The TLS shows the finite impulse response (FIR) of the inverse filter generated by this method, with a best-fit, seventh order polynomial superimposed for better visual comparison with the QR-RLS and the theoretical instrument response. In all cases after 13 Hz, the theoretical curve has a much steeper roll-off than the TLS or QR-RLS. The two longitudinal components (005267x and 005267y) show very similar frequency response therefore only 005267y is shown, however the vertical component differs towards the higher frequency. Nevertheless, all components for the SMA-1 instrument demonstrate that the SMA-1 has a low-pass characteristic and certainly show a flat frequency response up to approximately 15 Hz. It should be noted that the response plots shown are for the inverse filter with which to de-convolute the seismic data obtained from the instrument. The instrument response is the reverse of the response shown, i.e., the instrument has

a low-pass response. The 005267 records unfortunately do not provide details of any anti-alias filter, but one assumption would be that such a filter would have a cut-off similar to the response of the instrument. The plots also illustrate the use of many coefficients in order to estimate the inverse filter. In this case 51 coefficients were used which generate the side-lobe ripple for illustration purposes only, in performing the de-convolution a smaller number of coefficients suffice 7, 9, 11 or 15 which give a smoother response as shown in Section 4 for the SMART-1 data.

3.2. A-700 instrument

The frequency response plots in Fig. 3 for Icelandic event 005268y and z using instrument A-700 show similar response trends to that of SMA-1. The instrument frequency is 45 Hz and the damping factor is 0.7, correlation up to about 50 Hz is good with the longitudinal compo-

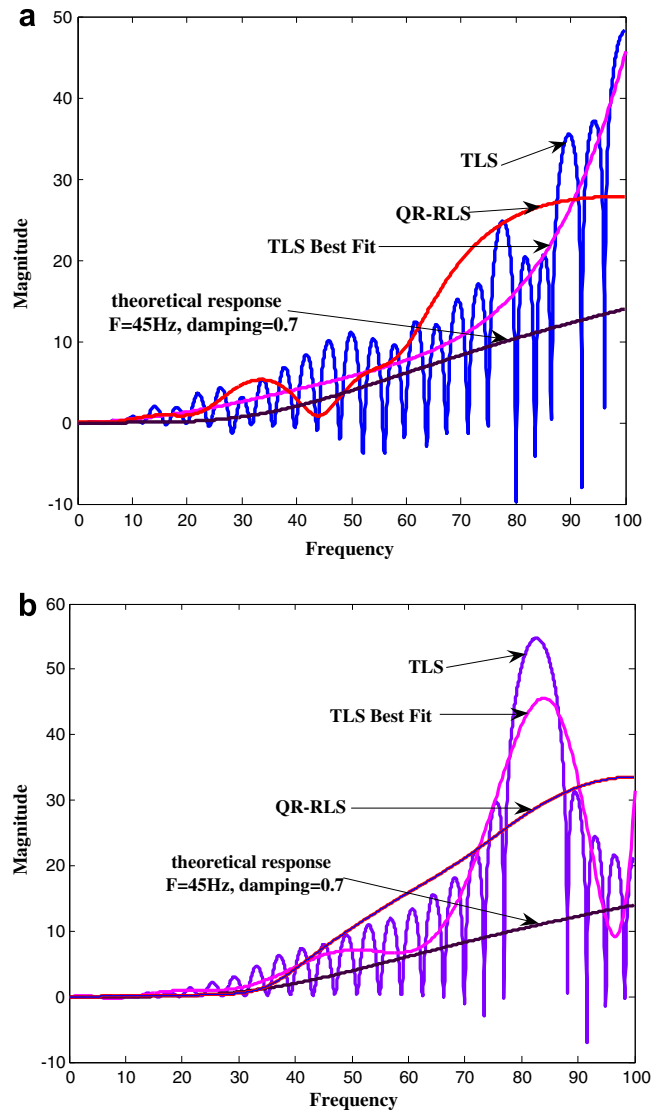


Fig. 3. Inverse frequency responses for the instrument A-700 using the TLS and QR-RLS for accelerograms: (a) 005268y and (b) 005268z.

nents showing similar response trends (only 005268y shown) and the z -component differing somewhat towards the higher frequency end. Nevertheless, as for the SMA-1 the response of the A-700 instrument(s) is decidedly low-pass. Again as for the SMA-1 data, anti-alias filter data was not available, but again one assumes such a filter is part of the instrument and would have a cut-off approximately 45 Hz. Both the x - and z -components do have considerable ripple in the pass-band up to and beyond 45 Hz and in taking the average through the TLS then the cut-off at 45 Hz occurs at 5 dB. The average roll-off does vary beyond 45 Hz, between theoretical and derived, but that is to be expected with both the QR-RLS and the TLS providing a more realistic assessment of the instrument response as they must also include the anti-alias filter whose specification is not included in the record. The TLS best fit is again a seventh order polynomial included for better visualisation and comparison.

3.3. DCA-333 instrument

Again as for the other instruments the frequency responses in Fig. 4 show the same general response trends, in this case the instrument frequency is 30 Hz and the damping parameter is 0.7. The correlation up to 30 Hz between the QR-RLS, the TLS and theoretical plot is not as good, with ripples in the pass-band, in this case the QR-RLS gives a more robust response. As for the other instruments details of the anti-alias filter are not available, but again it is reasonable to assume it would have a cut-off of about 30 Hz. In this case the x -component of the event shows an almost flat band using the TLS with the response rolling off after 30 Hz. However, the z -component shows a lot of ripple in the pass-band up to 30 Hz, which does of course smooth out, nevertheless the x -component does show a better response. The QR-RLS with a smaller number of coefficients however does show a better response in

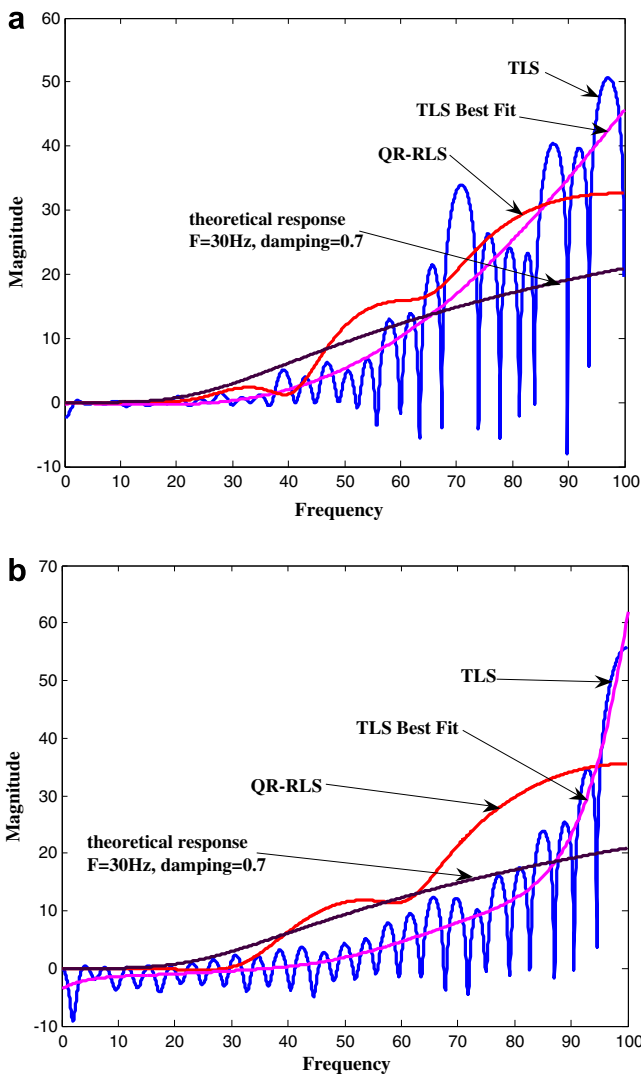


Fig. 4. Inverse frequency responses for the instrument DCA-333 using TLS and QR-RLS for accelerograms: (a) 005238x and (b) 005238z.

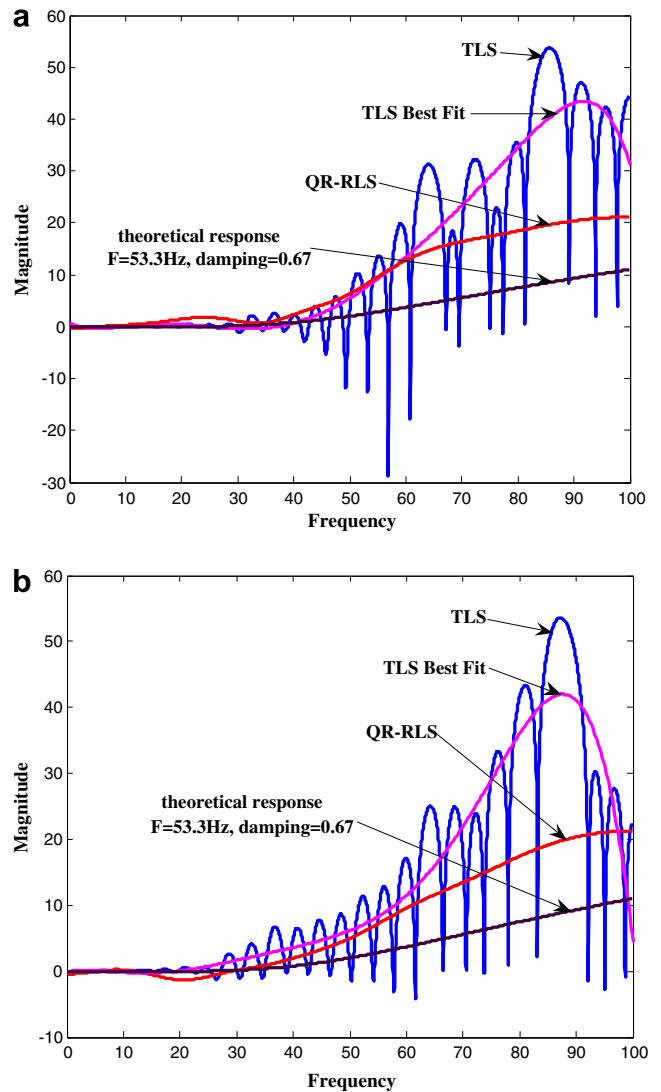


Fig. 5. Inverse frequency responses for the instrument SSA-1 using TLS and QR-RLS for accelerograms: (a) 005258y and (b) 005258z.

both the z - and x -components, but especially so in the case of the z -component beginning to roll-off at 30 Hz. In this case the theoretical inverse filter displays a reasonable response compared to both the TLS and the QR-RLS demonstrating that it is better to use the SDOF correction than not correcting at all.

3.4. SSA-1 instrument

The frequency response plots are shown in Fig. 5 for Icelandic event 005258 y and z . The instrument frequency is given as 53.3 Hz and the damping as 0.67. In this case the anti-alias filter is specified as 2-pole and with a cut-off at 50 Hz. The correlation to 50 Hz between the QR-RLS, the TLS and the theoretical response is good for the z -component, but not as good for the y -component. The best-fit roll-off of the TLS plotted through the inverse FIR filter response however, is approximately equivalent to a fourth order Butterworth, it can be argued that this is consistent with a cascade of the second order anti-alias filter and a second order SDOF instrument transfer function. Therefore, in this sense the TLS exhibits better performance than the QR-RLS or the second order SDOF. Nevertheless the y -component shows 5 dB of roll-off at 53 Hz and more ripples in the pass-band up to 53 Hz, in fact the y -component begins to roll-off much earlier than 53 Hz indeed at 30 Hz and so does not identify the anti-alias filter as well as the z -component. These are of course estimates in the least squares sense, nevertheless the point to make is that it is still better to de-convolute even with an estimate which may fall short of absolute values but gives a general acceptable trend in its estimated inverse response.

4. Numerical results for the Taiwan SMART-1 seismic array

This SMART-1 [2,17] array has the sensors laid out in concentric circles and is located in the Northeast corner of Taiwan near the city of Lotung. The original array comprises 37 force-balanced, tri-axial accelerometers (SA-3000) with a 25 Hz, high-cut anti-alias filter, configured in three concentric circles of radii 200 m, 1000 m and 2000 m. The three rings are labelled I (inner), M (middle) and O (outer), respectively. There are 12 equally spaced stations on each ring and a central station designated as C-00. Each accelerometer in the SMART-1 array is connected to a digital event recorder with 2 g full scale. The accelerometers trigger on all three components (nominally 0.02 g). The ground motions are digitised using a 12-bit Analogue to Digital converter sampling at 100 Hz. In addition, the instrument uses a 25 Hz, 5-pole, Butterworth, high-cut anti-alias filter [2] and the transducers have a natural frequency of 140 Hz. This means that the seismic data from each station should have a footprint of the anti-alias filter characteristics, therefore in this case the capability to de-convolute is relatively trivial.

However, the more detailed information provided affords a means by which it makes it possible to compare the inverse frequency response obtained using the TLS, with the fifth order Butterworth filter. The event used is 43 with $M_L = 6.5$, which was the largest earthquake located within 10 km of the array centre and was the first to be recorded by all 39 stations. The sections below outline procedures used on the Taiwan data with which to examine the usefulness of using the TLS as a tool for de-convolution, in particular where instrument parameters are not known as in a substantial amount of older seismic data records.

4.1. Reverse engineering the SMART-1 with the TLS

The procedure for comparison is straightforward and possible with the SMART-1 data sets because the details of the instrument processing are included. In particular, the transducer and anti-alias parameters are provided. Firstly and just as for the Icelandic events, the SMART-1 seismic data from the SA-3000 instrument is de-noised using a Debauchies (db8) wavelet as basis with decomposition to level 5.

The next step is to run the de-noised instrument data through the TLS algorithm in order to obtain the inverse FIR filter coefficients from the algorithm. The resulting coefficients are an estimate of the inverse filter and are then used to reverse engineer or de-convolute the time series in order to obtain an estimate of the ground motion. The original time series and that derived from the TLS, are then compared using their spectral density functions in order to obtain the coherency spectrum:

$$\gamma_{lm} = \frac{S_{lm}(f)}{\sqrt{S_l(f)S_m(f)}} \tag{16}$$

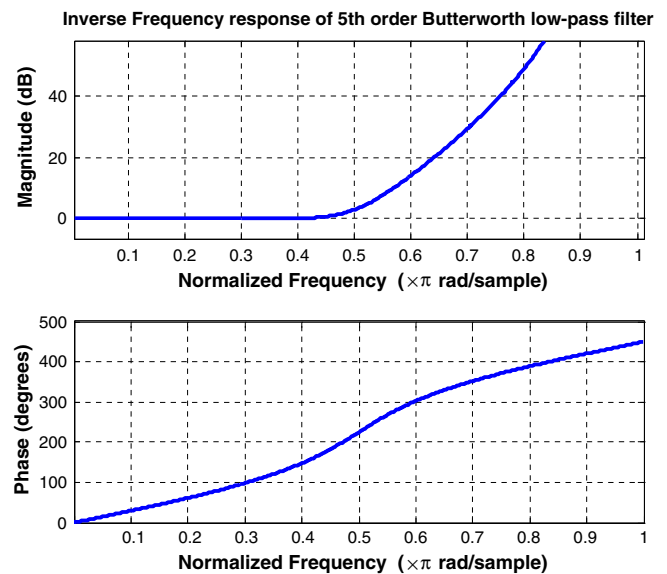
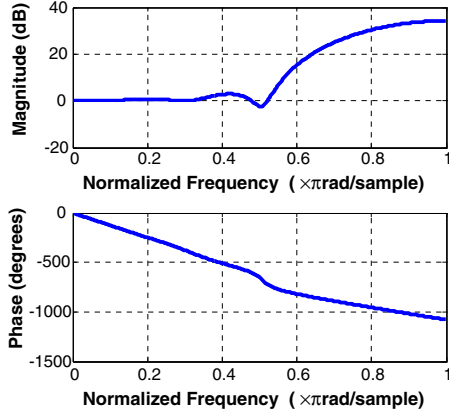
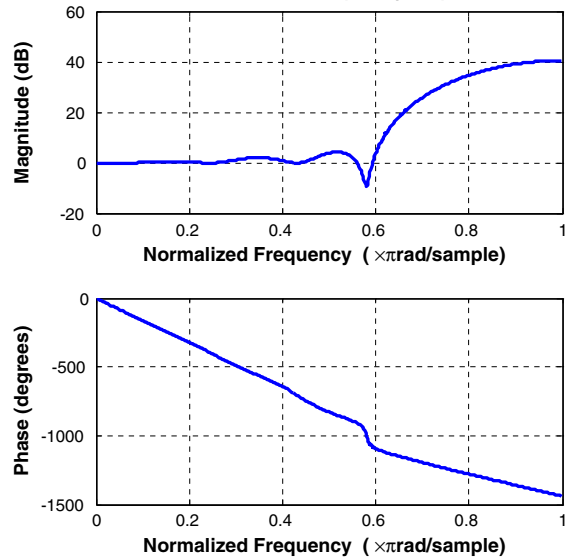


Fig. 6. Inverse frequency and phase response of theoretical Butterworth low-pass filter.

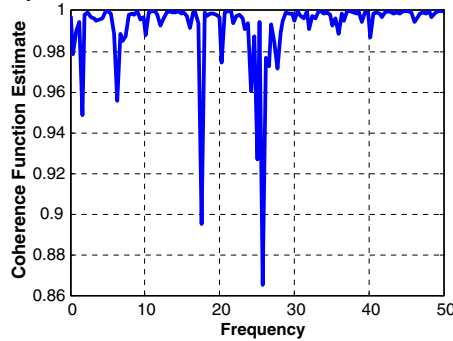
TLS instrument inverse filter frequency response:7-coeffs



TLS:instrument inverse filter frequency response:9-coeffs



Coherency for time histories form a 7-coeffs TLS and 5th order Butterworth



Coherency for 9-coeffs TLS v Butterworth

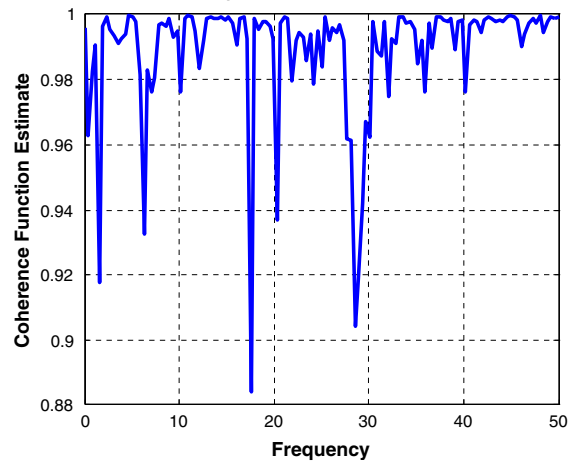


Fig. 7. Frequency and phase response plots (top) for a 7-coefficient TLS inverse filter. (Bottom) Coherency for time histories obtained using the TLS and Butterworth inverse filters, mean = 0.99. The event is TAI03.150N.

where S_{lm} = cross-spectral density function and S_l and S_m are the individual spectral densities of the two time series.

4.2. SMART-1 results in applying the TLS to de-convolute

The first example uses 7 TLS coefficients and shows the frequency response in Fig. 7. The response is in line with

Fig. 9. Frequency and phase response plots (top) for a 9-coefficient TLS inverse filter. (Bottom) Coherency for time histories obtained using the TLS and Butterworth inverse filters, mean = 0.9891. The event is TAI03.150N.

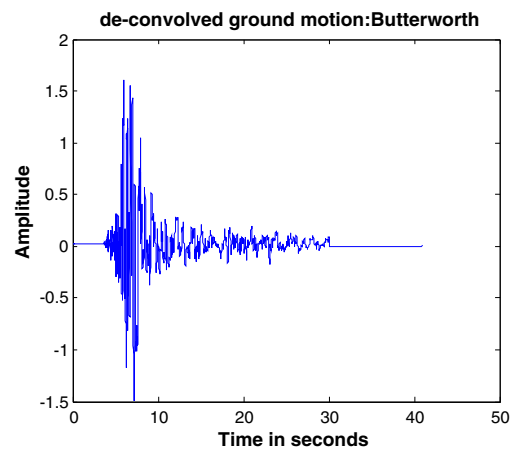
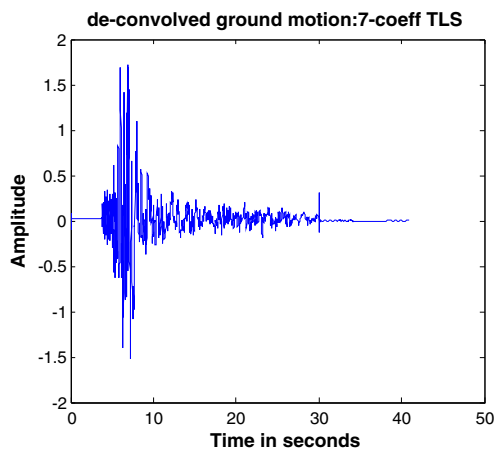


Fig. 8. (Left) Time series with 7-TLS coefficients compared to the (right) Butterworth derived time series. The event is TAI03.150N.

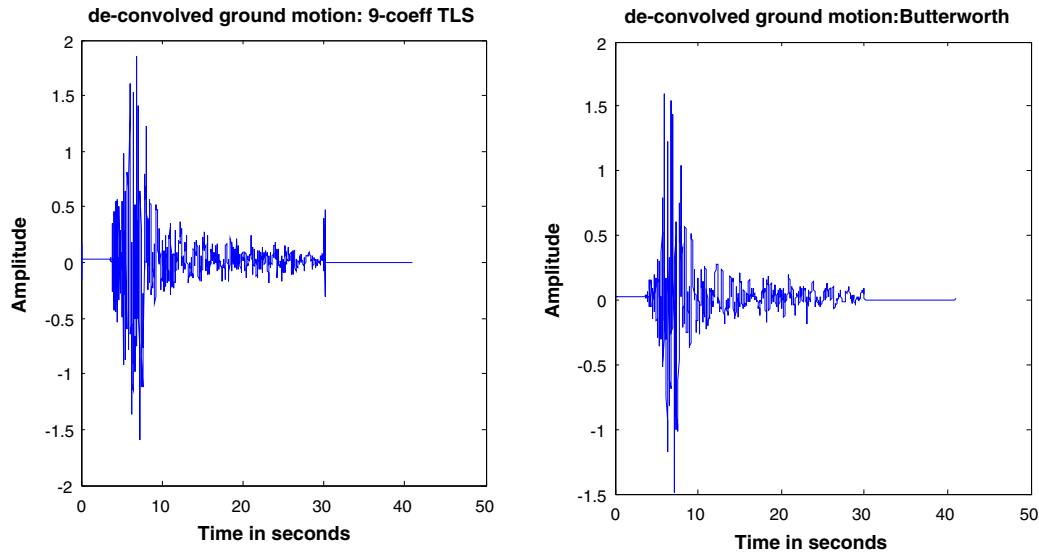


Fig. 10. (Left) Time series with 9-TLS coefficients compared to the (right) Butterworth derived time series. The event is TAI03.150N.

the inverse Butterworth filter response used, the response begins to roll-off at 25 Hz, but not as steeply as the theoretical fifth order shown in Fig. 6. In this case the number of coefficients used is now much smaller and therefore the frequency response is much smoother, it also accelerates computation. Fig. 7 shows the response against a normalised frequency axis where π is equivalent half the sampling frequency of 100 Hz. Therefore, 0.5π is at 25 Hz, which is where the inverse filter begins to roll-off. Given that the Butterworth filter cut-off is at 25 Hz, then this is indeed an excellent result, moreover it is the same result for all the SMART-1 data so far de-convoluted.

The phase response of the inverse filter is linear and indeed the phase response of the theoretical Butterworth filter is linearish, although it has to be pointed out that although the measured magnitude response is given [2] the measured phase response of the Butterworth fifth order filter used is not given. Butterworth filters in general have non-linear phase responses, but the fifth order demonstrates a good measure of approximate linearity. This is an important aspect of de-convolution, in general the ‘instrument’ should either preserve the phase of the ground motion or at most just impress a linear phase. This linear phase change is the same as shift in time for all data points in a time history. Whether the changes are positive or negative is immaterial as long as they are linear or approximately linear.

The two time series of Fig. 8 show one obtained from the TLS inverse filter and the other is the original. Although the two time series have a high coherency, the TLS does show a transient at the end of the time record. This transient can be smoothed out by using five coefficients, but then the inverse filter rolls off at much less than 25 Hz, which is not acceptable. A comparison is also shown using the analysis plots of Figs. 11 and 12 in particular the power spectral densities (PSDs) and the acceleration

response spectra, which in this case are similar for both the TLS and the SDOF de-convoluted. There are differences in the acceleration response spectrum and PSDs though the general trend of the power and acceleration response plots is similar. These differences in the acceleration response spectra are not insignificant and should be taken into account when using the time series or the spectra to excite models of structures. Moreover, it is clear that the time series in Fig. 11 decays more slowly than that corrected by using the standard SDOF in Fig. 12.

There is clearly good correlation between the time series derived from the 7-coefficient TLS inverse filter and the original time series. This is borne out in the coherency plot of Fig. 7 with a mean coherency of 0.99.

The next example in Fig. 9 uses 9 coefficients and again as for the 7-coefficient TLS filter the response is similar with a roll-off at about 25 Hz, the coherence between the time series obtained with the TLS and the original time series is also high with a mean coherence of 0.9891, clearly the correlation between the two time series is good. However, Fig. 10 shows that the transient at the end of the time record is even more pronounced than with 7-coefficients. Indeed as the number of coefficients increases to 11 coefficients then for this record the end transient remains with more emphasis, but with negligible power.

However, such good correlation does not always lead to identical or indeed similar response spectra and PSDs. The time series after TLS (7-coefficient) correction when analysed can yield different PSDs and acceleration response spectra. This is evident from Figs. 13 and 14 the analysis plots for event TAI03.161N (the middle circle). Fig. 13 the TLS corrected time series shows a high resonant peak at 43 Hz, which is not apparent in the analysis plot of Fig. 14 the SDOF de-convoluted time series. Moreover, the time series at the top-left of each of Figs. 13 and 14 show some marked differences. After 8 s the TLS corrected

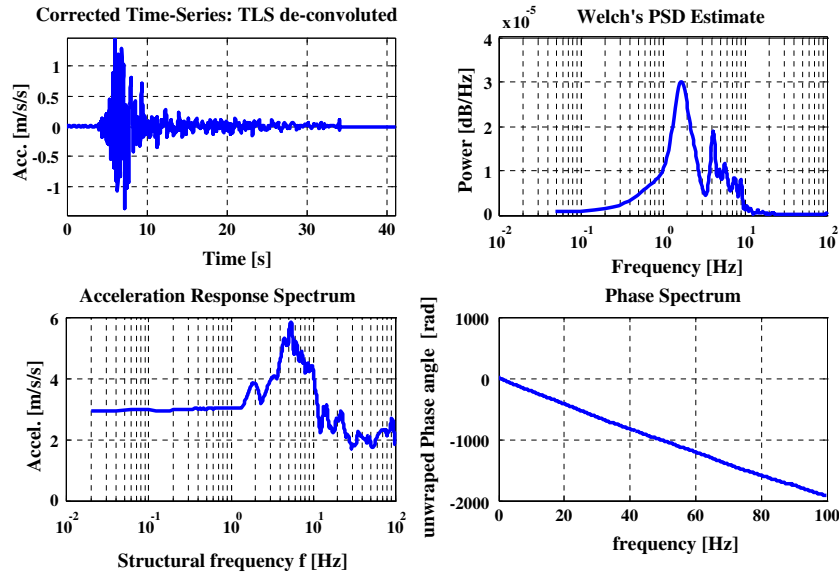


Fig. 11. TLS de-convoluted (7-coefficients) time series, PSD estimate, acceleration response spectrum and phase spectrum for event TAI03.149N.

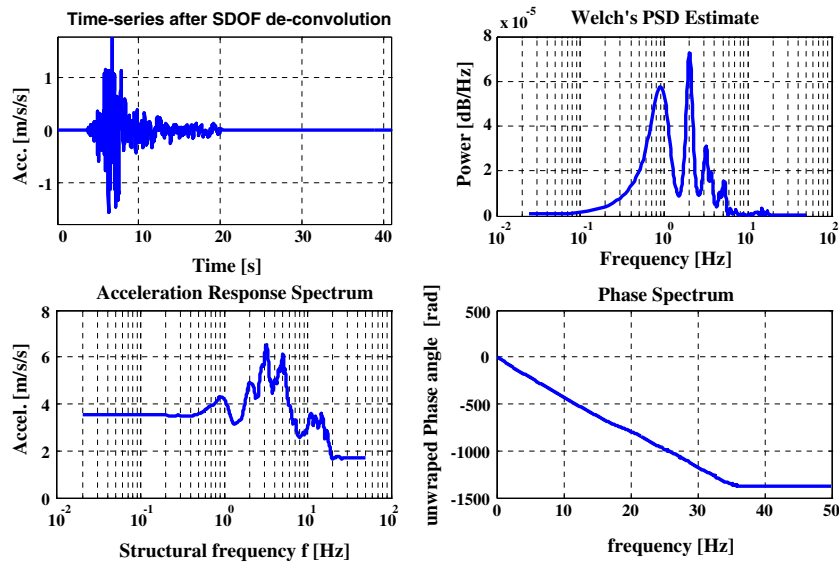


Fig. 12. SDOF de-convoluted time series, PSD estimate, acceleration response spectrum and phase spectrum for event TAI03.149N.

time series show a far slower rate of decay and stops abruptly at zero, whereas that corrected using the standard SDOF shows a gradual decay in the same amount of time. This is not unexpected since the TLS has effectively removed the influence of the 25 Hz, Butterworth anti-alias filtering applied to the data. This has brought out other features which illustrate the need to take care with sampled systems, the 43 Hz could be a higher frequency alias given that the resonant frequency of the transducer is 140 Hz, but it could also have some geophysical explanation or indeed the operation of the instrument itself.

4.3. Computational aspects

In general then the TLS algorithm demonstrates that it can be used effectively to de-convolve the instrument

response from the seismic data, in particular where the instrument parameters are either not known or not available. However, computationally the TLS algorithm requires a large amount of memory when working with large data sets and in double precision. The SVD generates an $m \times m$ matrix when processing, therefore for a data set of 8000 points and double precision this is approximately $8000 \times 8000 \times 8 = 0.512$ Gbytes of RAM. Allowing for the operating system, then clearly memory limits on a standard PC are easily exceeded. Single precision at 4 bytes alleviates the problem but of course there is a trade-off. Nevertheless, off-line the TLS provides a reasonable tool for de-convoluting the instrument response providing an inverse filter as good as if not better to that of the QR-RLS and the second order SDOF, providing a means of de-coupling the instrument to obtain an estimate of the ground motion.

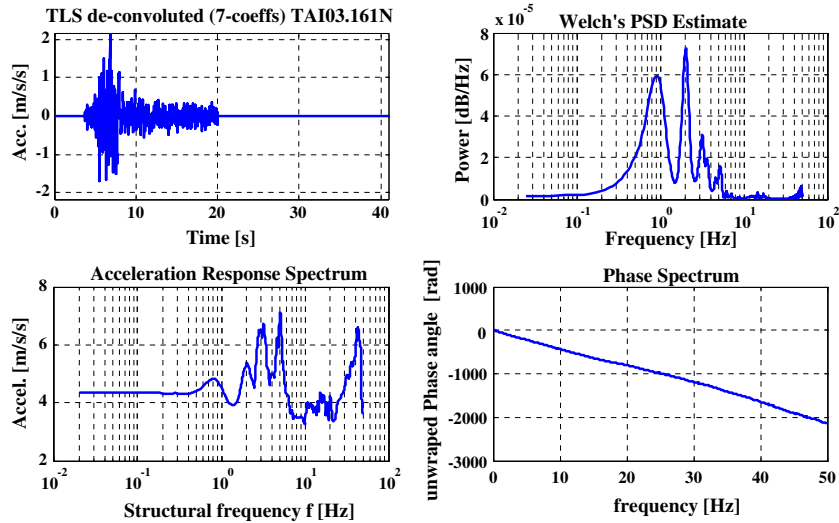


Fig. 13. TLS de-convoluted time series, PSD estimate, acceleration response spectrum and phase spectrum for event TAI03.161N. Acceleration spectrum shows a high resonant peak at 43 Hz, attenuated in the original record by the anti-alias, 25 Hz Butterworth filter.

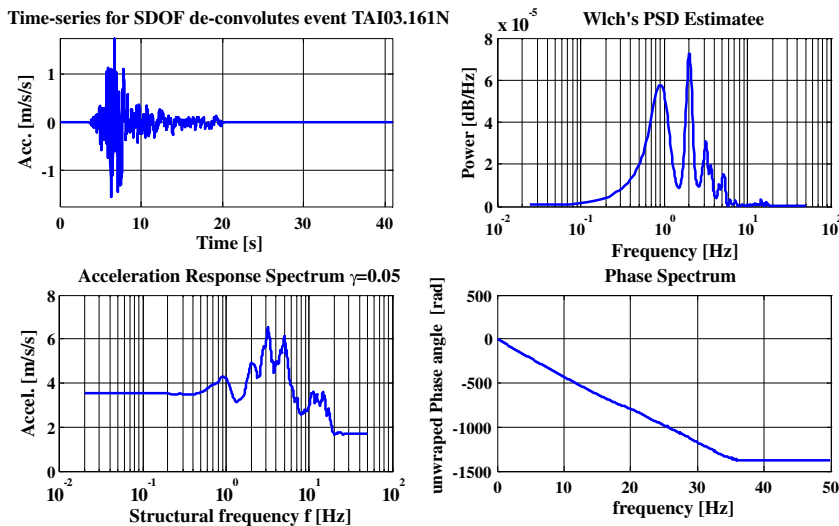


Fig. 14. SDOF de-convoluted time series, PSD estimate, acceleration response spectrum and phase spectrum for event TAI03.161N. Acceleration spectrum does not show a high resonant peak around 40 Hz.

5. Summary and conclusion

The results demonstrate that the TLS algorithm is a very useful tool for correcting seismic data when instrument parameters are not known. The SMART-1 data in particular has produced some excellent results in securing an estimate of the inverse filter with a cut-off at 25 Hz, which mirrors the cut-off of the actual anti-alias filter used. Although only some results are shown, the inverse filter characteristics are similar for all the *x*-, *y*- and *z*-components analysed from the inner, middle and outer rings of the SMART-1 array namely the seismic events from the TAI03.149_{xyz}, TAI03.150_{xyz}, TAI03.161_{xyz} and the TAI03.170_{xyz} records. The inverse filter response plots of Figs. 7 and 9 show good agreement with the Butterworth

theoretical response of Fig. 6. The Icelandic responses also demonstrate estimates of responses in good agreement with the instrument data where these are available as in Fig. 5, with a cut-off at 53.3 Hz. Where only transducer data is available then it is assumed that an anti-alias filter used in the digital recording system would have a cut-off at least at the natural frequency of the transducer. This seems to have been borne out in the records from which the frequency responses of Figs. 1–4 are derived with the TLS and QR-RLS. Transducer details only are available for those records and the cut-off frequencies derived by the TLS and QR-RLS are in line with the transducer natural frequencies. This suggests that the anti-alias filter had a cut-off at similar frequencies, just as for Fig. 5 record 005258_y- and _z-components where the anti-alias filter has

a cut-off at approximately the same point as the transducer natural frequency.

The phase response for both the TLS and the QR-RLS are both linear and one assumes that the phase response of the actual Butterworth filter used for the SMART-1 data is similar to that predicted in theory as shown in Fig. 6. This is approximately linear which then impresses a time shift on the record as a whole with minimal distortion. The inverse filters will also impress their own linear time shift, but both can be easily corrected by shifting the record by the same amounts.

The time series of Fig. 10 demonstrate similarity between the TLS derived time series and that obtained from the SMART-1 record using the Butterworth filter. Nevertheless there are transients visible in the record and these become more pronounced as the number of coefficients increase. These transients do not have much power, but nevertheless may well be a function of instrument performance or ground motion. Figs. 11 and 12 also bring out some more interesting features in that the TLS corrected time series show a much slower decay down to zero indeed extending for approximately 35 s as compared to the 20 s of the SDOF corrected time series.

Finally, Figs. 13 and 14 again demonstrate more gradual decay of the SDOF corrected time series compared to that corrected using the TLS. The Butterworth filter would have attenuated any higher frequencies which might be modulated by the lower frequencies present in the recovered data, but on the application of the TLS inverse filter these higher frequencies would be amplified and approximately reconstructed. The higher frequency peak at 43 Hz in the acceleration response spectrum of Fig. 13 could be a frequency alias or have some geophysical explanation. Clearly, data recorded digitally and de-convoluted to diminish the effects of any anti-alias filters may have to contend with alias frequencies. Of course with some of the old analogue data records digitised manually, this may not be such a problem.

In conclusion, both the Icelandic and the SMART-1 data have given an opportunity to test the TLS algorithm against the information provided regarding the transducer and the anti-alias filter. The algorithm has been found to be robust and works very well with a small number of coefficients, which reduces the computational requirements. Its utility has been clearly and well demonstrated in de-coupling the instrument response from the recorded seismic data. This is of particular significance where quite often the older data records simply do not have any instrument parameters included.

Appendix. Summary of TLS procedure

The algorithm is as follows:

1. Compute the SVD of $[A|b] = U\Sigma V^T$.
2. Compute the index p , $\sigma_p \geq \sigma_{n+1} + \varepsilon \geq \sigma_{p+1} \geq \dots \geq \sigma_{n+1}$. This approach regards all computed singular

values in the interval $[\sigma_{n+1}, \sigma_{n+1} + \varepsilon]$ as identical; where $\varepsilon > 0$ is a machine dependent parameter.

3. Let $V = [v_1 v_2 \dots v_n]$ be a column partition of V ; compute a Householder matrix Q using Eq. (12).
4. If $\alpha = 0$, then in the algorithm used here, the TLS solution does not have a solution. Otherwise the solution is given by Eq. (13). There are more generalised algorithms [24] (non-generic TLS solutions) which allow for α being singular.

References

- [1] Ambraseys N, Smit P, Berardi R, Rinaldis D, Cotton F, Berge-Thierry C. Dissemination of European strong-motion data. CD-ROM Collection, European Council, Environment and Climate Research Programme <<http://www.ISESD.hi.is>>; 2000.
- [2] Data Management Centre. Academia Sinica, Taiwan: Institute of earth science. <<http://www.earth.sinica.edu.tw/~smdmc/smart1/smart1.htm>>.
- [3] Alexander NA, Chanerley AA, Goorvadoo N. A review of procedures used for the correction of seismic data. In: Topping BHV (Ed.), Proceedings of the eighth international conference on civil and structural engineering, paper 39. Stirling, UK: Civil-Comp Press; 2001.
- [4] Chanerley AA, Alexander NA. An approach to seismic correction which includes wavelet denoising. In: Topping BHV (Ed.), Proceedings of the sixth international conference on computational structures technology, paper 44. Stirling, UK: Civil-Comp Press; 2002.
- [5] Sunder SS, Connor JJ. Processing strong motion earthquake signals. Bull Seismol Soc Am 1982;72(2):643–61.
- [6] Khemici O, Chang W. Frequency domain corrections of earthquake accelerograms with experimental verification. In: Proceedings of the eighth world conference on earthquake engineering, San Francisco, USA, vol. 2. 1984. p. 103–10.
- [7] Ormsby JFA. Design of numerical filters with applications in missile data processing. Assoc Comput Mach J 1961;8:440–66.
- [8] Converse AM. BAP: Basic strong-motion accelerograms processing software. Version 1.0. USGS, Denver, CO. Open-file report 92(296A); 1992.
- [9] Chanerley AA, Alexander NA. A new approach to seismic correction using recursive least squares and wavelet de-noising. In: Topping BHV (Ed.), Proceedings of the ninth international conference on civil and structural engineering computing, paper 107. Stirling, UK: Civil-Comp Press; 2003.
- [10] Chanerley AA, Alexander NA. Novel seismic correction approaches without instrument data, using adaptive methods and de-noising. In: Proceedings of 13th world conference on earthquake engineering, paper 2664, Vancouver, Canada; August 1–6, 2004.
- [11] Golub G, Van Loan CF. An analysis of the total least squares problem. SIAM J Numer Anal 1980;17(6):883–93.
- [12] van Huffel S, Vandewalle J. The use of total linear least squares for identification and parameter estimation. In: Proceedings of IFAC/IFORS symposium on identification and parameter estimation. July 1985. p. 1167–72.
- [13] Golub G, Reinsch C. Singular value decomposition and least squares solutions. Numer Math 1970;14:403–20.
- [14] Van Huffel S, Vanderwalle J. The total least squares problem computational aspects and analysis. Frontiers in applied mathematics, vol. 9. Philadelphia (PA): SIAM; 1991.
- [15] Moon T, Stirling W. Mathematical methods and algorithms for signal processing. New Jersey: Prentice-Hall; 2000.
- [16] Golub GH, Van Loan CF. Matrix computations. 3rd ed. Baltimore (MD): John Hopkins; 1996.
- [17] Abrahamson NA, Bolt BA, Darragh RB, Penzien J. The SMART-1 accelerograph array (1980–1987) a review. Earthq Spect 1987;3(2): 263–84.

- [18] Sigbjornsson R, Olafsson S, Thorarinsson O. Strong-motion recordings in Iceland. In: Proceedings of the 13th world conference on earthquake engineering, paper 2370. Vancouver; 2004.
- [19] Haykin S. Adaptive filter theory. 3rd ed. New Jersey: Prentice-Hall; 1996, p. 562–628.
- [20] Sayed A, Kailath H. A state-space approach to adaptive RLS filtering. *IEEE Signal Process Mag* 1994;11:18–60.
- [21] Donoho DL. De-noising by soft thresholding. *IEEE Trans Inform Theory* 1995;41(3):613–27.
- [22] Coifman R, Donoho DL. Translation invariant de-noising. Wavelets and statistics. In: Lecture notes in statistics 103. New York: Springer-Verlag; 1995. p. 125–50.
- [23] Daubechies I. Ten lectures on wavelets. Philadelphia (PA): SIAM; 1992.
- [24] Van Huffel S, Vanderwalle J. Analysis and solution of the nongeneric total least squares problem. *Siam J Matrix Anal Appl* 1988;9(3): 360–72.

Correcting data from an unknown accelerometer using recursive least squares and wavelet de-noising

A.A. Chanerley^a, N.A. Alexander^{b,*}

^a School of Computing and Technology, University of East London, Docklands Campus, 4-6 University Way, London E16 2RD, United Kingdom

^b Department of Civil Engineering, University of Bristol, Queen's Building, University Walk, Bristol BS81TR, United Kingdom

Received 5 September 2006; accepted 5 February 2007

Available online 12 April 2007

Abstract

Non-linear finite element analyses of structures that are subject to seismic actions require high quality accelerogram data. Raw accelerogram data needs to be adjusted to remove the influence of the transfer function of the instrument itself. This process is known as correction. Unfortunately, information about the recording instrument is often unknown or unreliable. This is most often the case for older analogue recordings. This paper uses a recursive least squares (RLS) algorithm to identify the instrument characteristics even when completely unknown. The results presented in the paper implement a modern approach to de-noising the accelerogram by employing the wavelet transform. This technique removes only those components of the signal whose amplitudes are below a certain threshold and is not therefore frequency selective. It supersedes to some extent conventional band pass filtering which requires a careful selection of cut-off frequencies, now unnecessary.

© 2007 Elsevier Ltd. All rights reserved.

Keywords: Correction; Accelerograms; Wavelet de-noising; Recursive least squares; Adaptive filtering

1. Introduction

This paper is an extended and updated version of conference paper [1]. Advances in finite element programs and the increase in computational power are resulting in an evolution of approach to the analysis of complex structural systems. This is particularly true in the case of the design of structural systems that are subject to seismic actions. The engineering analyst's approach is changing from a predominantly modal (eigenvalue) analysis that uses a design spectrum to a non-linear timehistory analysis that uses accelerogram timeseries, see [2].

Displacement based design and performance based design approaches are becoming more fashionable and feasible. The main components of these design philosophies are damage limit states that are often taken to be functions

of structural displacement. This interest in damage and displacement requires a full non-linear timehistory analysis of the structural system. The importance of credible ground motion timeseries cannot be underestimated here. These approaches require reliable and extensive sets of ground motion timeseries recorded from actual earthquakes. Many agencies around the world are cataloguing and collecting databases of recorded time series that are becoming increasingly available to design engineers. However, the instruments that record the ground acceleration are not perfect, and usually record a timeseries that needs to be corrected to recover the "original ground motion" itself. These databases contain, by definition, information about various historic seismic events recorded on a variety of accelerometers, some analogue, and some digital. Most of these records, in the databases, were recorded on older analogue instruments of unknown or questionable characteristics. In fact, even today, many analogue instruments are maintained because of their robustness and low cost.

* Corresponding author. Tel.: +44 117 928 8687.

E-mail address: nick.alexander@bristol.ac.uk (N.A. Alexander).

Nomenclature

\underline{a}	accelerogram timeseries (known, uncorrected), vector	ε_k	local error estimate, target of least square minimisation, scalar
\underline{a}_g	accelerogram timeseries (unknown, corrected), vector	\mathbf{P}_k	k th estimate of inverse correlation matrix
\underline{d}	desired timeseries (unknown, estimated \underline{a}_g), vector	λ	forgetting factor, scalar
\underline{g}	instrument system filter (unknown), vector	\underline{h}_k	k th estimate of instrument filter
\underline{h}	instrument system inverse filter (unknown), vector	\mathbf{Q}	unitary matrix (QR-RLS algorithm)
\mathbf{A}	convolution of \underline{a} , matrix	\mathbf{R}	upper triangular matrix (QR-RLS algorithm)
\mathbf{P}	inverse correlation matrix	\mathbf{Q}_k	k th estimate of unitary matrix
\underline{u}_k^T	k th row vector of \mathbf{A} , vector	\underline{k}_k	k th estimate of gain vector
d_k	k th element of \underline{d} , scalar	γ_k	householder numerically assigned, scalar
		\mathbf{A}_k	k th householder modification of \mathbf{A} , matrix
		\underline{v}_k	first column of \mathbf{A}_k , vector
		H_1, H_2	quadrature mirror filters, functions.

Thus, corrected accelerograms are required in order to undertake a non-linear timehistory analysis of structures, which are subject to seismic actions. A correction technique needs to (i) digitise, that is equisample the data, (ii) correct for instrument characteristics (iii) de-trend, (iv) de-noise with wavelets, or band-pass filter (v) resample to an appropriate sampling rate. A review of various proposed schemes is presented in [3,4]. The sequence of the component (ii) to (v) and exact algorithms used in these correction techniques vary significantly, as can the resulting recaptured “original ground motion” itself.

In this paper the role of removal and/or recovery of the instrument characteristic are assessed. In particular, the question is posed, whether instrument correction of seismic data is possible where the frequency-response characteristics of the instrument are unknown. Almost all correction schemes, like [5], assume a second order, single-degree-of-freedom (SDOF) instrument function with which to de-convolve the instrument response from the ground motion. For some databases [6] however, the whole issue of correcting for an unknown instrument is too problematic hence instrument de-convolution is not performed. The authors did not want to present time series ground motion that have imposed and incorrect processing, but they present data without instrument correction which is not necessarily useful. This paper builds on the work [1,4] to discuss an implementation of the recursive least squares (RLS) algorithm in the context of a system identification problem. The RLS algorithm is used to determine, *a posteriori*, the filter characteristic or fingerprint, if you like, that the instrument leaves imposed on the time series. The resulting inverse filter is then applied to the data in order to de-convolve the instrument response.

2. Inverse filtering using adaptive algorithms

The Least Mean Square (LMS) algorithm [7] is the simplest and easiest adaptive algorithm to implement. How-

ever, its performance, in terms of computational cost and fidelity, is not as good as the Recursive Least Square (RLS) and Square Root RLS algorithms. The RLS algorithm [4,8–10] was chosen for inverse system identification in preference to the LMS adaptive algorithm. Another reason is that the RLS algorithm is dependent on the incoming data samples rather than the statistics of the ensemble average as in the case of the LMS algorithm. Therefore, the coefficients will be optimal for the given data without making any assumptions regarding the statistics of the process.

Telephone communication systems commonly use inverse filtering with which to identify the inverse system response to compensate for signal distortion as it propagates through the transmission medium. Speech data transmitted across telephone lines is distorted through the wires that behave as a filter, whose frequency response is unknown, but which rolls-off at higher frequencies. An adaptive filter, executing in real-time, will produce a response that is the inverse to that of the transmission medium. This increases the available frequency range and data rate for the telephone system. In this telecoms application the original signal and the system that modifies the signal are both unknown. In this paper, the actual ground acceleration \underline{a}_g and the accelerometer system \underline{g} are unknown, see Fig. 1.

In the time domain, the actual ground acceleration \underline{a}_g is convolved “*” with the filter function of the accelerometer \underline{g} to give the recorded signal \underline{a} .

$$\underline{a} = \underline{a}_g * \underline{g} \quad (1)$$

In this paper, the implementation of the adaptive algorithm attempts to find a solution to the inverse problem, Eq. (2) where ideally the inverse filter \underline{h} is such that $\underline{h} = \underline{g}^{-1}$ and then the desired signal \underline{d} equals the actual ground motion \underline{a}_g .

$$\underline{a} * \underline{h} = \underline{d} \quad (2)$$

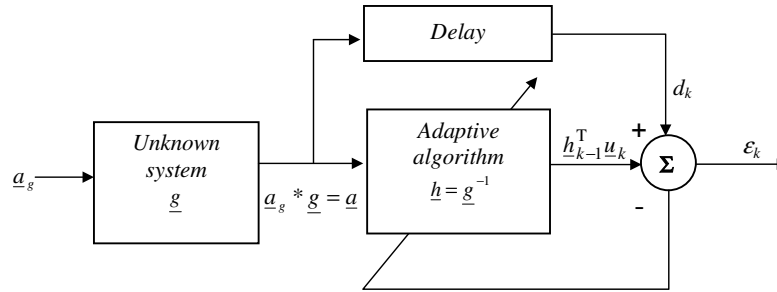


Fig. 1. Adaptive RLS diagram.

Solution of this problem, in general, is not possible; however under certain limited condition it is possible to produce an estimate of \underline{h} from the recorded signal \underline{a} that is shown in this paper to be reasonable. The conditions for the application of the recursive least squares method is that \underline{a} and \underline{a}_g are very similar and the amplitude of noise is low, i.e. the signal to noise ratio is high. The telecoms example, described previously, is an example of the implementation of this approach.

3. Using RLS algorithm on artificial accelerograms

The frequency response characteristics of accelerometer instruments are typically a low pass filter designed to have a nearly flat response up to approximately 10 Hz. The exact frequency response characteristic of an accelerometer may not be known for two reasons: (i) omissions in documentation (ii) due to the time the instrument has spent *in situ* without calibration or testing.

Instruments can be modelled as a single degree of freedom system (SDOF) which describes the mechanical dynamics of some accelerometers well. However, it does

fail to capture the convoluted anti-alias filter that almost certainly precedes the Analogue to Digital conversion. Thus, there may be more uncertainty about the “instrument” system than is ideal.

3.1. Example, using white noise artificial accelerogram

Consider a test case of a random (white noise) signal \underline{a}_g that is passed through a low-pass, finite impulse response, FIR, filter \underline{g} to give a filtered signal \underline{a} . This low pass filter is an idealisation of the accelerometer. The system identification of this FIR filter is performed by using the square root RLS algorithm, described in Section 5. Two approaches are employed (i) the system ID with \underline{d} and \underline{a} known; this is the classical system ID problem (ii) the case where \underline{a} is known but \underline{d} is estimated (unknown); this is the application of interest in this paper. The estimate of the desired signal \underline{d} is obtained by delaying \underline{a} by the length of the estimated adaptive filter. The role of this delay is discussed in Section 4.

Fig. 2 show the original 21-tap FIR low pass filter with cut-off frequency at 0.55 of the Nyquist. Approach (i) is

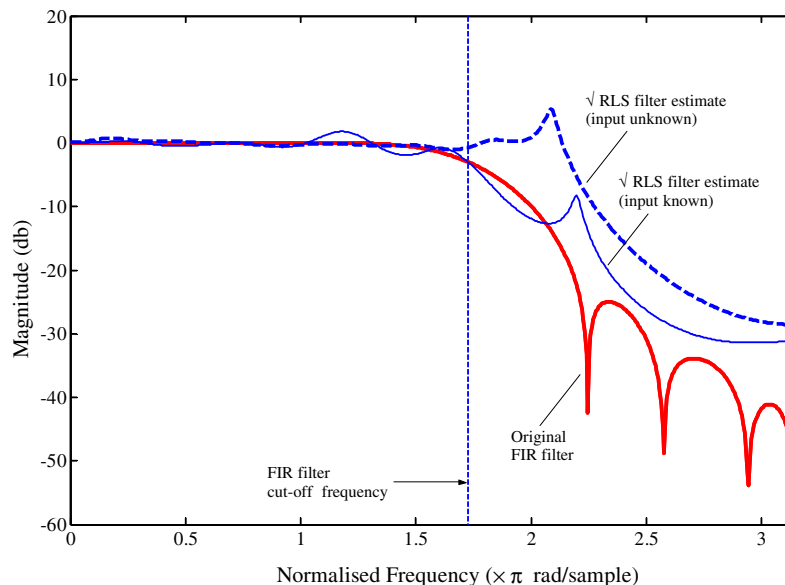


Fig. 2. Comparison of RLS recovered filters and original “unknown” FIR test filter (white noise).

more accurate than (ii) as is expected. However, approach (ii) produces an approximation to the “unknown” system filter from \underline{a} only.

3.2. Example using Kanai–Tajimi artificial accelerogram

Kanai–Tajimi proposed a smoothed power spectrum estimate for accelerograms; this is described in [11]. It was based on 367 recorded accelerograms. In this paper, this model is used to generate an artificial accelerogram. The Kanai–Tajimi power spectrum supplies the amplitude information while the phase information is assumed random. The time domain description of the artificial accelerogram is generated using an inverse FFT. Note that a Hanning windowing function is used to reduce the amplitude of the accelerogram at the beginning and end of the trace. This makes the envelope of the artificial accelerogram more like a real accelerogram. Fig. 3 displays the Kanai–Tajimi target power spectrum, the actual spectrum used and the time domain artificial accelerogram. The Kanai–Tajimi parameters chosen were for horizontal motion and rock near surface geology; ground intensity parameter $G_0 = 0.07$, ground frequency $\omega_g = 27$ rad/s and ground damping parameter $\xi_g = 0.34$.

This artificial accelerogram is filtered by the FIR filter used in Section 3.1. Fig. 4 displays the two approaches used in Section 3.1. Again having information about both \underline{d} and \underline{a} provides the best system ID estimate. However in the case where only \underline{a} is known, i.e. the output of the accelerometer, the square root QR-RLS algorithm is able to provide a reasonable estimate of this unknown instrument. Compar-

ison of Figs. 2 and 4 suggests that the square-root QR-RLS algorithm may work better for a real accelerogram than for a purely white noise signal.

4. The recursive least squares algorithm

The notation used in this paper is bold, non-italicised, capital letter to designate matrices; italicised, lower-case, underscored letter for a column vector and italicised, lower-case letter for a scalar. The RLS algorithm can be considered in terms of a least squares solution [8] of the system of linear equation (2). \mathbf{A} is a convolution data matrix, size $(m \times p)$, of the accelerogram data; where $m = n + p - 1$ and n is the length of the accelerogram time-series, \underline{h} is a vector $(p \times 1)$ of the inverse system filter coefficients and \underline{d} is a $(m \times 1)$ vector which represents the signal convolved by the instrument, often termed the *desired* signal

$$\mathbf{A}\underline{h} = \underline{d}, \quad \begin{bmatrix} a_1 & 0 & 0 \\ a_2 & a_1 & 0 \\ a_3 & a_2 & a_1 \\ a_4 & a_3 & a_2 \\ 0 & a_4 & a_3 \\ 0 & 0 & a_4 \end{bmatrix} \begin{bmatrix} h_1 \\ h_2 \\ h_3 \end{bmatrix} = \begin{bmatrix} d_1 \\ d_2 \\ d_3 \\ d_4 \\ d_5 \\ d_6 \end{bmatrix} \quad (3)$$

In order to clarify, an example is also displayed in (3) for an accelerogram time-series $\underline{a} = [a_1 \ a_2 \ a_3 \ a_4]^T$ and a system filter $\underline{h} = [h_1 \ h_2 \ h_3]^T$. A classical inverse system identification problem is to find the vector \underline{h} of filter coefficients. Given that there are more equations than unknowns, there is no precise solution to (3) in general.

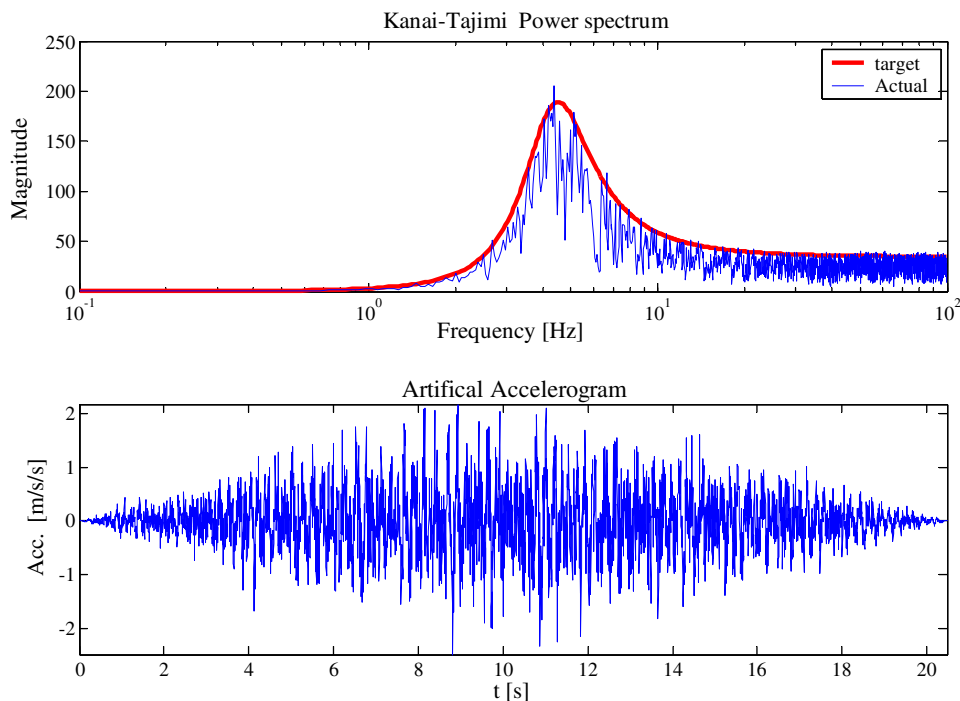


Fig. 3. Artificial accelerogram based on Kanai–Tajimi spectrum.

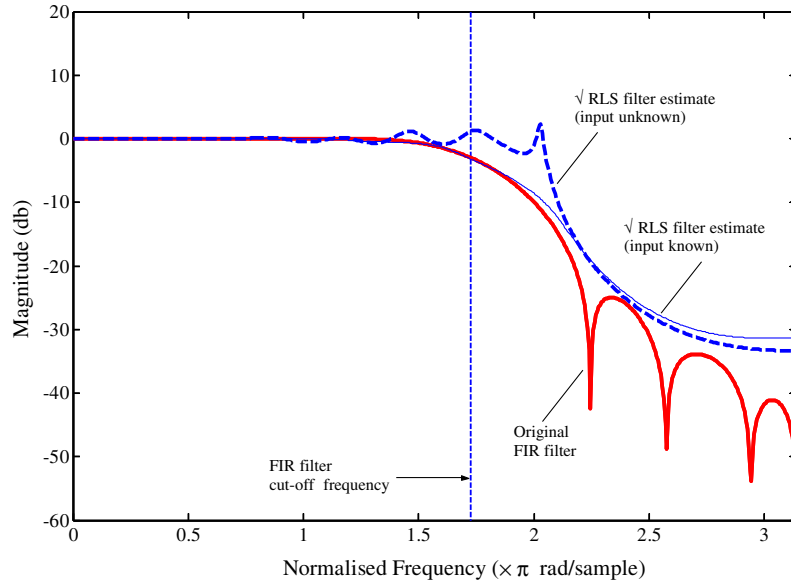


Fig. 4. Comparison of RLS recovered filters and original “unknown” FIR test filter (Kanai–Tajimi accelerogram).

However, one approach involves a least-square minimization, Eq. (4), of the norm-squared errors in satisfying (3) for a given choice of filter coefficients \underline{h} , i.e. which \underline{h} is nearest to satisfying (3). This problem (4) has the well-known solution [4,8,12] given by Eq. (5) where \mathbf{P} is the inverse correlation matrix

$$\text{minimise } (\|\mathbf{A}\underline{h} - \underline{d}\|^2) \quad (4)$$

$$\underline{h} = (\mathbf{A}^T \mathbf{A})^{-1} \mathbf{A}^T \underline{d} = \mathbf{P} \mathbf{A}^T \underline{d} \quad (5)$$

However, in order to obviate the need of evaluating explicitly the inverse autocorrelation matrix \mathbf{P} , the RLS algorithm provides an efficient method of updating the least squares estimate of the inverse filter coefficients as new data arrive. This is shown in the expression (6) where \underline{h}_k is the current estimated vector of filter coefficients; \underline{h}_{k-1} is the previous estimated vector filter coefficients; \mathbf{P}_k is the current ($p \times p$) inverse correlation matrix; d_k is the k th element in \underline{d} ; \underline{u}_k^T is a row vector of data taken from the convolution data matrix \mathbf{A}

$$\underline{h}_k = \underline{h}_{k-1} + \mathbf{P}_k \underline{u}_k (d_k - \underline{h}_{k-1}^T \underline{u}_k) \quad (6)$$

The updated value of the filter coefficient \underline{h}_k is obtained by adding to the previous value, the second term on the right of Eq. (6), which can be considered as a “correction term”. The term in brackets is the *a priori* estimation local error defined by (7)

$$\varepsilon_k = d_k - \underline{h}_{k-1}^T \underline{u}_k \quad (7)$$

The second term on the right of Eq. (7) represents an estimate of the desired signal, based on the previous least squares estimate of the filter coefficient.

The inverse auto-correlation matrix \mathbf{P}_k is initially estimated, its initial value does not have to be explicitly evaluated. However further updates can be evaluated using Woodbury’s identity, which provides an efficient method

of updating the matrix, once initialised with an arbitrary value. The update is given in (8) where the forgetting factor is λ ; this is the *Riccati equation* for the RLS algorithm. It can be shown that (9) is valid hence (6) becomes (10).

$$\mathbf{P}_k = \lambda^{-1} \mathbf{P}_{k-1} - \lambda^{-1} \underline{k}_k \underline{u}_k^T \mathbf{P}_{k-1}, \quad \underline{k}_k = \frac{\lambda^{-1} \mathbf{P}_{k-1} \underline{u}_k}{1 + \lambda^{-1} \underline{u}_k^T \mathbf{P}_{k-1} \underline{u}_k} \quad (8)$$

$$\mathbf{P}_k \underline{u}_k = \underline{k}_k \quad (9)$$

$$\underline{h}_k = \underline{h}_{k-1} + \underline{k}_k (d_k - \underline{h}_{k-1}^T \underline{u}_k) \quad (10)$$

Eqs. (6)–(10) form the basis of the RLS algorithm used in order to obtain the inverse filter coefficients with which to de-convolve the instrument response.

The algorithm requires \underline{d} , an estimate of this is derived from actual seismic data \underline{a} , as described in Section 2, with reference to Fig. 1. The approach used is to delay the accelerogram data \underline{a} by the estimated filter order and use this new vector as the desired training data, \underline{d} , in the algorithm, see Appendix 1.

Ultimately, only the forgetting factor needs to be adjusted. Typically this is between 0.9 and 0.99 and in this case was assigned a value of 0.9, this attenuates an error from 10 samples in the past for example by $(0.9)^{10}$. The beauty of the algorithm lies in the fact that the initial inverse correlation matrix is estimated and not evaluated, as shown in Appendix 1. Prior knowledge of the $\mathbf{P}_k (p \times p)$ matrix is not required, i.e. the algorithm is independent of the statistics of the ensemble and depends only on the data. This algorithm was initially designed for the case of real-time data processing where it is not possible to determine \mathbf{P}_k as future data is not known. In this case, all the accelerogram data is known however explicitly evaluating \mathbf{P}_k is inefficient and not recommended.

In essence, the delay in the data allows the Riccati equation (8) to provide an estimate of \mathbf{P}_k before the non-zero

desired data arrives in the algorithm. This prevents the adaptive filter from trying to adapt to a signal that it has not yet seen or, in this case, prevents the adaptive filter from trying to adapt to a signal for which it has no information. Without this delay, the whole algorithm fails to converge to any useful result.

5. The square root, inverse QR-RLS algorithm

The RLS algorithm can become numerically unstable in this application. Therefore, a variant of the RLS algorithm is used here reduces the dynamic range and guarantees stable solutions. This is the QR decomposition-based RLS algorithm derived from the square-root Kalman filter counterpart [5,6]. The ‘square-root’ is in fact a Cholesky factorisation of the inverse correlation matrix. The derivation of this algorithm depends on the use of an orthogonal triangulation process known as QR decomposition

$$\mathbf{Q} \cdot \mathbf{A} = \mathbf{R} = \begin{bmatrix} r & r & r & r \\ 0 & r & r & r \\ 0 & 0 & r & r \\ 0 & 0 & 0 & r \end{bmatrix} \tag{11}$$

where \mathbf{R} is an upper triangular matrix and \mathbf{Q} is a unitary matrix and \mathbf{A} is a data matrix. The QR decomposition of a matrix requires that certain elements of a vector be reduced to zero. The unitary matrices usually used are those due to Givens or Householder [10,13,14]. The Givens matrix is a rotation, which zeros out the matrix elements one-by-one and leaves an upper triangular matrix. The Householder matrix on the other hand zeros out the elements on a column-by-column basis. The matrix used in the algorithm in this implementation is the Householder transformation that zero’s out the necessary elements of the input data matrix elements and updates the (square root) inverse correlation matrix. The QR-RLS is as follows in Eq. (12); where γ_k is a scalar.

$$\mathbf{Q}_k \begin{bmatrix} 1 & \lambda^{-1/2} \underline{\mathbf{u}}^T \mathbf{P}_{k-1}^{1/2} \\ 0 & \lambda^{-1/2} \mathbf{P}_{k-1}^{1/2} \end{bmatrix} = \begin{bmatrix} \gamma_k^{-1/2} & \underline{\mathbf{0}}^T \\ \underline{\mathbf{k}}_k \gamma_k^{-1/2} & \mathbf{P}_k^{1/2} \end{bmatrix} = \begin{bmatrix} r_{11} & \underline{\mathbf{L}}_{12}^T \\ r_{21} & \mathbf{R}_{22} \end{bmatrix} \tag{12}$$

The gain vector $\underline{\mathbf{k}}_k$ is determined from the first column of the post-array. \mathbf{Q}_k in the above expression is a unitary (Householder) transformation which operates on the elements of $\lambda^{-1/2} \underline{\mathbf{u}}^T \mathbf{P}_{k-1}^{1/2}$ and the rows of $\lambda^{-1/2} \mathbf{P}_{k-1}^{1/2}$ in the pre-array zeroing out each one to give a zero-block entry in the post-array. The least-squares weight vector $\underline{\mathbf{h}}_k$ is updated in Eq. (13), but through Eq. (15) the gain vector, from the post-array Eq. (13), and Eq. (14) the a priori estimation error

$$\underline{\mathbf{k}}_k = r_{21} r_{11}^{-1} \tag{13}$$

$$\varepsilon_k = d_k - \underline{\mathbf{h}}_{k-1}^T \underline{\mathbf{u}}_k \tag{14}$$

$$\underline{\mathbf{h}}_k = \underline{\mathbf{h}}_{k-1} + \underline{\mathbf{k}}_k \varepsilon_k \tag{15}$$

These inverse-filter weights are then convolved with the original seismic data in order to obtain an estimate of the true ground motion. As in the standard RLS, the inverse correlation matrix is estimated, prior knowledge is not required, i.e. the algorithm is independent of the statistics of the ensemble. More detail regarding the algorithm used and matrix dimensions is shown in Appendix 2.

QR decomposition is a well-known procedure for matrix triangulation, [10–12] which works as follows. The Householder matrix is defined in Eq. (16)

$$\mathbf{Q}_k = \mathbf{I} - \frac{2 \underline{\mathbf{v}}_k \underline{\mathbf{v}}_k^T}{\|\underline{\mathbf{v}}_k\|^2} \tag{16}$$

where the vector $\underline{\mathbf{v}}_k$ is formed from the first column of a matrix \mathbf{A} , in this case the matrix pre-array in Eq. (12). The matrix \mathbf{Q}_1 then operates on the matrix \mathbf{A} and zeros out all elements of the first column, but the first. The matrix \mathbf{A} is shown below as a 4×3 matrix in (17),

$$\mathbf{Q}_1 \mathbf{A} = \begin{bmatrix} \beta_1 & n & n \\ 0 & n & n \\ 0 & n & n \\ 0 & n & n \end{bmatrix} = \mathbf{A}_1 \tag{17}$$

it can be seen that but for the first element, the first column elements have been annihilated. The procedure then repeats for \mathbf{A}_1 with a Householder matrix \mathbf{Q}_2 being formed from the elements of the next column. The new matrix is now as shown below,

$$\mathbf{Q}_2 \begin{bmatrix} \beta_1 & n & n \\ 0 & n & n \\ 0 & n & n \\ 0 & n & n \end{bmatrix} = \mathbf{Q}_2 \mathbf{Q}_1 \mathbf{A} = \begin{bmatrix} \beta_1 & n & n \\ 0 & \beta_2 & n \\ 0 & 0 & n \\ 0 & 0 & n \end{bmatrix} = \mathbf{A}_2 \tag{18}$$

The procedure repeats with a new Householder matrix formed from the last column of \mathbf{A}_2 , were the new \mathbf{Q}_3 matrix operates on \mathbf{A}_2 , giving the final triangular matrix below in Eq. (19)

$$\mathbf{Q} \mathbf{A} = \mathbf{Q}_3 \mathbf{Q}_2 \mathbf{Q}_1 \mathbf{A} = \begin{bmatrix} \beta_1 & n & n \\ 0 & \beta_2 & n \\ 0 & 0 & \beta_3 \\ 0 & 0 & 0 \end{bmatrix} = \mathbf{A}_3 = \mathbf{R} \tag{19}$$

Since the Householder matrices are unitary then so are the \mathbf{Q}_k matrices and so the matrix \mathbf{A} reduces to the product of an upper-triangular matrix and a unitary matrix, that is,

$$\mathbf{A} = \mathbf{Q}^T \mathbf{R} = (\mathbf{Q}_1 \mathbf{Q}_2 \mathbf{Q}_3)^T \mathbf{R} \tag{20}$$

This scheme can annihilate on a row-wise basis or as in this implementation by just transposing to secure the triangular matrix format in Eq. (19) for further computation. There are several computational schemes [10,12] available which pay due regard to computational efficiency, round off errors and other numerical issues [11], but once the fully

annihilated matrix is obtained then the relevant parameters can be extracted from the post-array and applied to Eqs. (13)–(15).

6. Wavelet de-noising seismic data

The point to make here is that de-noising is a better alternative to noise reduction than using the standard commonly used low-pass filtering methods [3,15–20]. Wavelet de-noising [21–26] is based on taking the discrete wavelet transform (DWT) [20,23,27] of a signal, passing the transform through a threshold which removes the resulting coefficients below a certain value and then taking the inverse DWT in order to reconstruct a de-noised time signal. The DWT is able to concentrate most of the energy of the signal into a small number of wavelet coefficients, after low-pass filtering with the appropriate filter weights depending on the selection of a wavelet basis.

The forward wavelet transform of a set of data comprises low and high-pass filtering of the data then down-sampling by a factor of 2. The filters used for this purpose are FIR filters of order N , called quadrature mirror filters (QMF). These have mirror image symmetry in both magnitude and phase about the frequency $\pi/2$. The transfer functions relating such filters are given by

$$H_1(z) = H_2(-z) \tag{21}$$

For example, $H_1(z) = 1 + z^{-1}$ and $H_2(z) = 1 - z^{-1}$ form a QMF pair, with coefficients [1, 1] and [1, -1]. The Daubechies filters of order $N = 2$ will filter in the forward direction and then down sample by 2. The forward FIR, decomposition, QMF filter-pair coefficients, are given by

$$\text{Low-pass} = [-0.1294 \quad 0.2241 \quad 0.8365 \quad 0.4830] \tag{22}$$

and the high-pass

$$\text{High-pass} = [-0.4830 \quad 0.8365 \quad -0.2241 \quad -0.1294] \tag{23}$$

Similarly, for the reverse direction when after thresholding the transform reconstructs the remaining waveform, by up-sampling by 2 and applying an inverse QMF filter-pair, the reconstruction filters, whose coefficients are given by

$$\text{Low-pass} = [0.4830 \quad 0.8365 \quad 0.2241 \quad -0.1294] \tag{24}$$

$$\text{High-pass} = [-0.1294 \quad -0.2241 \quad 0.8365 \quad -0.4830] \tag{25}$$

These filter coefficients are derived from the Daubechies (2) scaling filter

$$\text{db2} = [0.3415 \quad 0.5915 \quad 0.1585 \quad -0.0915] \tag{26}$$

these coefficients have a norm of 0.7071 used to obtain the above decomposition and reconstruction filters. These can be described as

$$\text{Recon-Low} = [c_0 \quad c_1 \quad c_2 \quad c_3] \tag{27}$$

$$\text{Recon-High} = [c_3 \quad -c_2 \quad c_1 \quad -c_0] \tag{28}$$

$$\text{Dec-Low} = [c_3 \quad c_2 \quad c_1 \quad c_0] \tag{29}$$

$$\text{Dec-High} = [-c_0 \quad c_1 \quad -c_2 \quad c_3] \tag{30}$$

This can be generalised to any length of decomposition and reconstruction filter. In this implementation the Daubechies (8) wavelet [28] of order $N = 8$ was used (see Fig. 5), with decomposition and reconstruction to five levels of down and up sampling.

Up sampling and convolving the Daubechies (8) low-pass and high-pass filter coefficients produces the wavelet

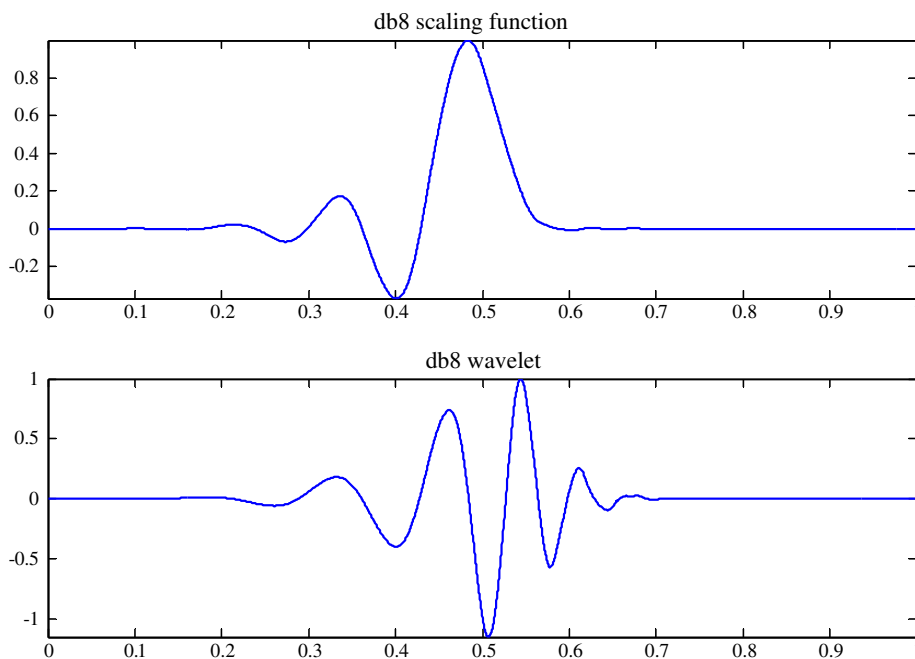


Fig. 5. db8 Wavelet and scaling function.

and scaling functions shown above. These functions are not explicitly used in this application, but their associated QMF filters form the basis of the de-noising scheme. It should be emphasised that although the scheme uses low and high-pass filters, these are not used to eliminate prescribed frequency bands, as is the normal case when using filters. The QMF filters and down samplers are applied in order to separate (decompose) the low and high frequency content of a signal and then to apply a thresholding scheme in order to eliminate unwanted amplitudes across the frequency spectrum contained in the signal. Finally up sampling and applying the reconstruction QMF filters rebuilds the signal from the wavelet transform, but without the unwanted noise. The QMF filter banks are in fact a set of *perfect reconstruction filters* used in a de-noising scheme, as shown in the block diagram of Fig. 6 for one level of decomposition.

However the DWT is not translation invariant and so this implementation uses the stationary or translation invariant wavelet transform [29]. This essentially applies a range of signal shifts to allow for misalignment of the signal and wavelet features, it then averages out the shifts in order to obtain the de-noised signal.

The block diagram, Fig. 6, essentially shows one level of decomposition with a low and high-pass filter and down sampling by a factor of 2 (taking every second sample of the original signal). Once the low pass and high-pass channels have been subject to a threshold, the resulting signal is then up-sampled by the same factor and low and high-pass filtered, then reconstructed to give the resulting de-noised signal. The de-noising scheme is not as frequency selective as in a scheme using standard digital filters, so it does not remove as much energy before or after certain frequencies. Rather it removes those coefficients below a certain value that represent low-energy noise, the coefficients in this case being just the filtered and down-sampled data at the low and high frequency end of the original signal. The inverse transform then re-constructs the signal from the data but

without the amplitudes below the threshold values [2,23,24].

7. Frequency responses for the El-centro and the garvey reservoir seismic events

The plots of Fig. 7, show frequency and phase profiles of two inverse filters derived from the data from the El-Centro 18/5/1940 N and E component seismic events. The frequency responses were obtained after the data was wavelet de-noised. The x -axis is a log-plot to reveal details at the low frequencies of interest and to emphasise the fact that de-convolution filters perform in a manner consistent with the single degree of freedom accelerometer model. Fig. 7 also shows the results of modelling the accelerometer by a perfect single degree of freedom system with natural frequency 10 Hz and ratio of critical damping 0.552. These parameter value were recorded with the accelerogram data in the header information [30]. The plots show that at low frequencies to approximately 40 Hz for the El-Centro Eastern component the RLS inverse filter show an approximately flat response (0 dB) in the region of interest. The El-Centro Northern component is approximately flat to about 75 Hz and the phase plots are approximately linear. However, there is an element of uncertainty in both of the de-convolution methods. It is not known whether at the time the instrument behaved as a perfect second order SDOF system or that given its years in situ its calibration parameters were still correct; nor indeed whether the RLS characterises the instrument response to a better degree. The characteristic of the anti-alias filter is also unknown. However, both give similar response characteristics and the RLS provides a means of estimating the instrument response without any assumptions about the instrument. The RLS approach does perform quite well in the pass band region in Fig. 2, which is, for the engineering, the region of interest. The differences in magnitude between the two approaches are small in this region. In

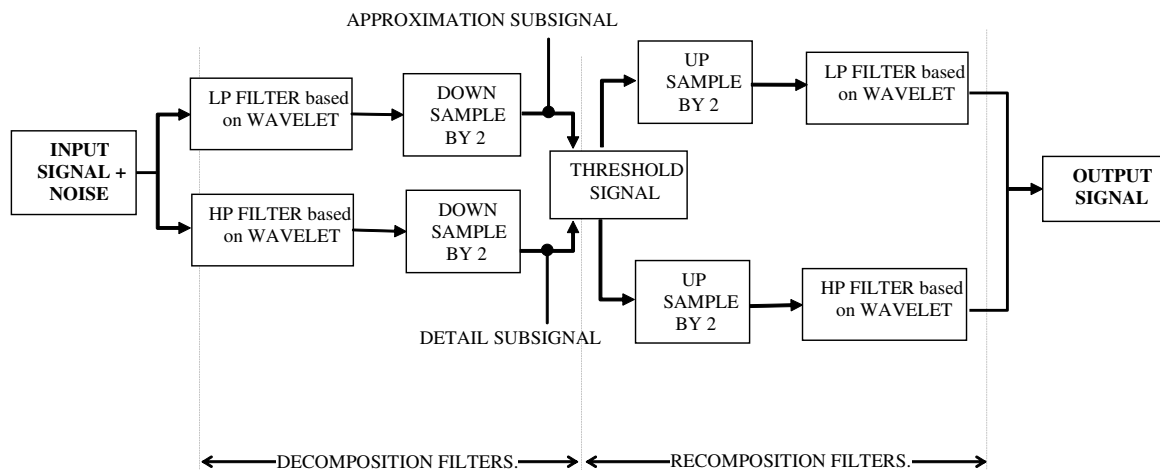


Fig. 6. Block diagram of a 1-stage, 2-band wavelet de-noising scheme.

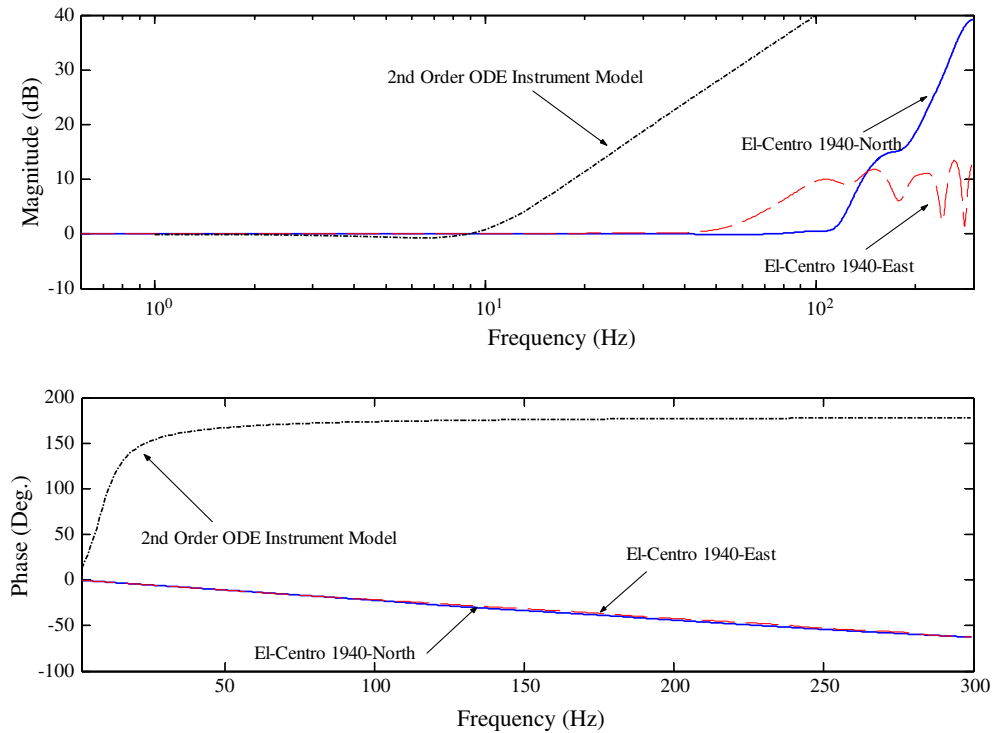


Fig. 7. Comparison of extracted instrument characteristic from El-Centro (1940) event using (i) RLS adaptive filter and wavelet pre-denoising (ii) SDOF instrument response ($f=10$ Hz, $\zeta = 0.552$).

addition, the RLS results suggest that the “actual unknown instrument” performs better than is expected by SDOF model, i.e. it may have a broader operational bandwidth. The RLS therefore provides a reasonable indication of instrument performance. These results demonstrate the usefulness of using the QR-RLS in order to de-convolve the instrument response without any prior knowledge of the instrument parameters.

When considering the phase response of the two approaches, differences are observed. The SDOF imposes a non-linear phase character while the RLS induces a linear phase character. It is worth pointing out that the adaptive model of the inverse filter is FIR, which has a linear phase property, i.e. it will always impress a linear phase. This linear phase is the same as a time shift in the time domain e.g. shifting all the data points in the timeseries by a constant amount in time. Since the beginning of the timeseries is arbitrary, it can be argued that in most cases this will have no effect on the dynamics of a structure subject to this record. Thus, the RLS algorithm is fairly neutral with respect to phase, this is it effectively makes no adjustment to the phase content. This compares with the non-linear SDOF phase response, which can be thought to shift different frequency components by dissimilar amounts of phase.

One is then confronted with the issue as to whether there is any advantage accrued in phase recovery by using the RLS. In the situation of an unknown instrument, it is better to use the RLS approach since it estimates the magnitude behaviour of the instrument well and does not corrupt the phase further. In the case where the instrument

characteristics, in term of SDOF parameters, are known; the engineer must decide which approach to employ. The SDOF may induce an incorrect non-linear phase but the RLS may do nothing to correct the phase.

In using the RLS for instrument de-convolution it is necessary to review the order in the implementation of noise removal and the application of the inverse filter. In using Butterworth or Elliptic band-pass filters or wavelet de-noising in conjunction with the standard second order differential equation, it doesn't make any difference to the output as to whether the filtering/de-noising is pre-or post-the instrument de-convolution. This is because the solution to the differential equation is the same in both situations, it is not an estimate based on corrupted or de-corrupted input data, and therefore necessarily the inverse filter response is always the same. This is changed with the application of the RLS algorithm. The estimate of the inverse filter is dependent on the input data. Noise errors should, as far as is possible, be removed before an RLS instrument correction is applied. This is because the instrument response matrix may be ill-conditioned or non-invertible over a band of frequencies. Therefore, the inverse de-convolution matrix may amplify the noise inherent in a seismic data set and distort the frequency response, in particular towards the end of the seismic event when the signal is comparable with the noise. To illustrate the point, below in Figs. 8 and 9 are two sets of plots for the 1940 El Centro N and E components, where the RLS de-convolutions were performed without prior wavelet de-noising of the signal. The inverse filter responses in magnitude are quite different,

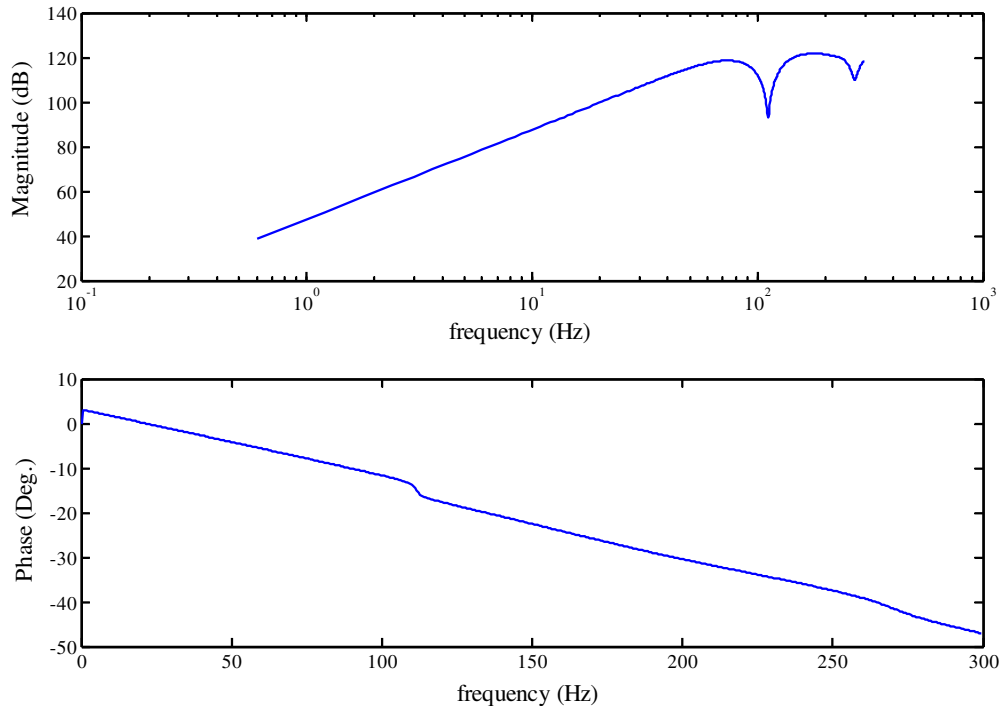


Fig. 8. Inverse filter for El-Centro N without de-noising.

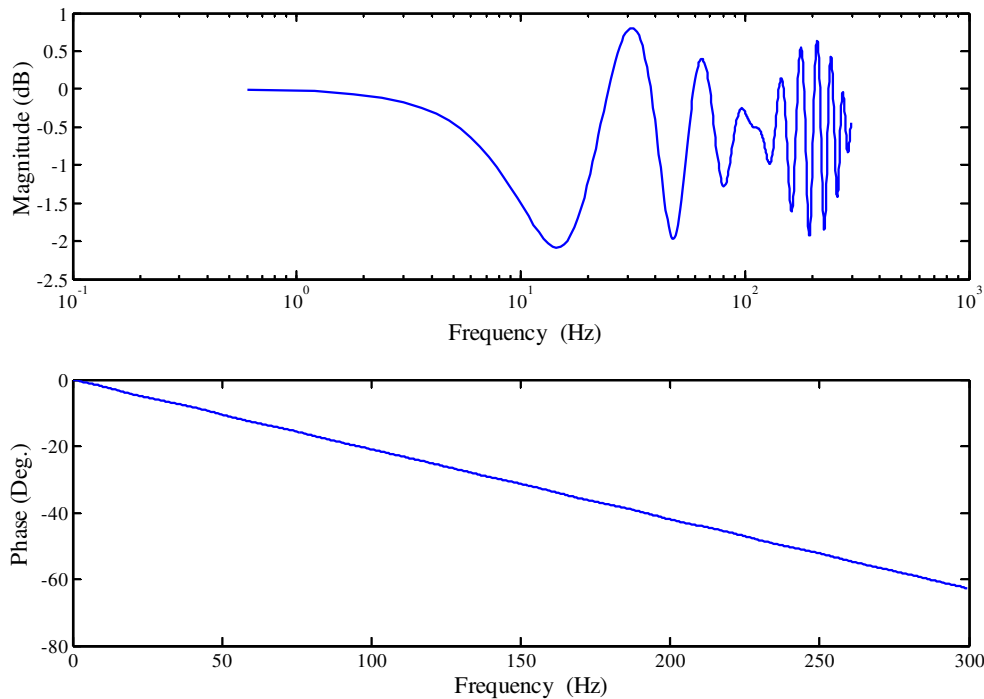


Fig. 9. Inverse filter for El-Centro E without de-noising.

correlation between them would be expected given that the recordings must have used similar instruments.

Fig. 8 shows the northern component of the seismic event, the phase response is linear. On the other hand, Fig. 9 shows a completely different magnitude response, which does not bear any relation to that of Fig. 8 and with instabilities at the higher frequencies. However, it does

exhibit a flat frequency response as in Fig. 7, but at much lower frequencies. The discrepancy between the two sets of inverse filter response plots is considerable, the frequency responses should be similar, and having some resemblance to theoretical predictions. However, the flat magnitude response for the 1940-E component indicates that use of this inverse filter would, in the low-frequency range, produce the

similar amplitude results as a theoretical inverse filter, though with different phases. The El-Centro 1940-N component results produce a linear-phase response but quite different amplitude output to that obtainable by using theoretical methods and that for the Eastern component.

Further magnitude and phase plots are shown in Figs. 10 and 11 for the Garvey Reservoir event 01/10/87. In this case, Fig. 10 shows good correlation between the two components in the magnitude plots obtained using QR-RLS de-convolution after wavelet de-noising. In particular, up

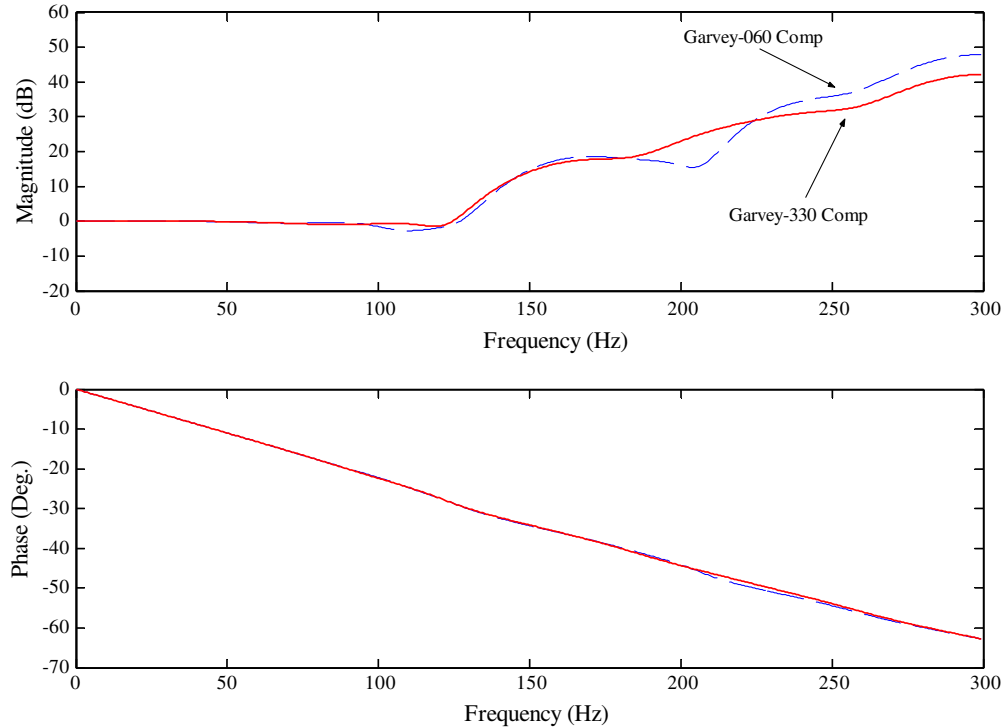


Fig. 10. Inverse filter response plots for the Garvey Reservoir where RLS de-convolution is preceded by wavelet de-noising.

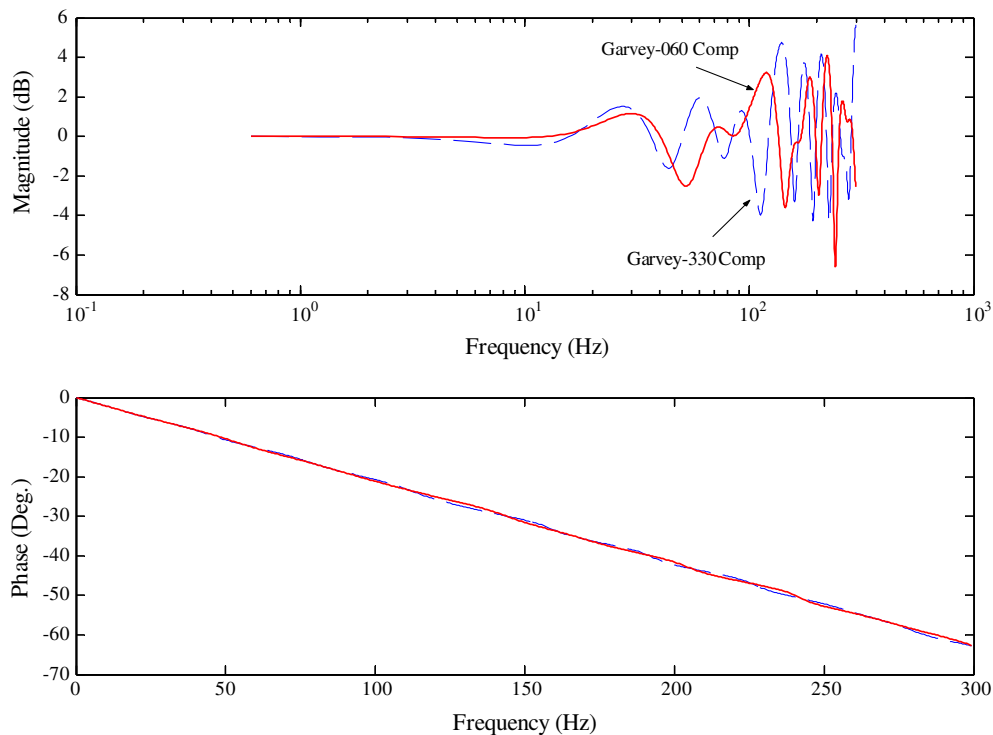


Fig. 11. Inverse filter response plots for the Garvey Reservoir where RLS de-convolution is not preceded by wavelet de-noising.

to approximately 30–35 Hz the magnitude response is almost flat and the phase responses are linear. The plots of Fig. 10 are in fact a good indicator of instrument performance during the seismic event. On the other hand, Fig. 11 applies instrument de-convolution to the Garvey components before any de-noising, showing a frequency response that is markedly different, but consistent with instabilities resulting from small signal to noise ratios at higher frequencies. It should be noted that a flat response is only in the low frequency range between 5 and 15 Hz for the two components and a linear phase response consistent with the behaviour of FIR filters.

The plots of Fig. 11 would seem to be a good result, since they are almost consistent with a requirement that the instrument response in this range is equal to the true ground motion up to 15 Hz. However, the general shape of the frequency response militates against this. This demonstrates that with some seismic data, performing a de-convolution first and de-noising after may still yield good results in the range of interest, but the implementation is inherently applied incorrectly.

Fig. 12 shows plots of elastic response spectra, power spectra, phase spectra and timehistories for the El-Centro event. It compares the standard method of correcting seismic data with that of wavelet de-noising and instrument correction through recursive least squares. The standard method uses a Butterworth filter to filter the noise and

follows this with a SDOF instrument correction in the frequency domain using the fast Fourier transform [1,31]. The differences are especially apparent in the response spectra. The frequencies at which the differences are most noticeable are essentially those that govern the response of low-rise multi-storey buildings.

8. Summary

The paper demonstrates that inverse filtering using the RLS adaptive algorithm can recover an unknown system. In the case of an unknown accelerometer filtering the ground motion to produce the response time-series, it is possible to recover a good estimate of the original unknown ground motion; this is without any knowledge of the instrument and anti-alias filter response characteristics.

Ordering of events is important; the data should be de-noised prior to the RLS instrument correction. Thus, the signal to noise ratio is maximised before utilising the adaptive algorithm. This is to prevent any amplification of noise during the de-convolution process. It is clear from Figs. 8 and 9 that the instability in the RLS algorithm when passing un-denoised data through it occurs at the higher frequencies where the noise energy is comparable to the seismic signal, i.e. at the frequencies where the seismic signal produces little power. The results do show that over

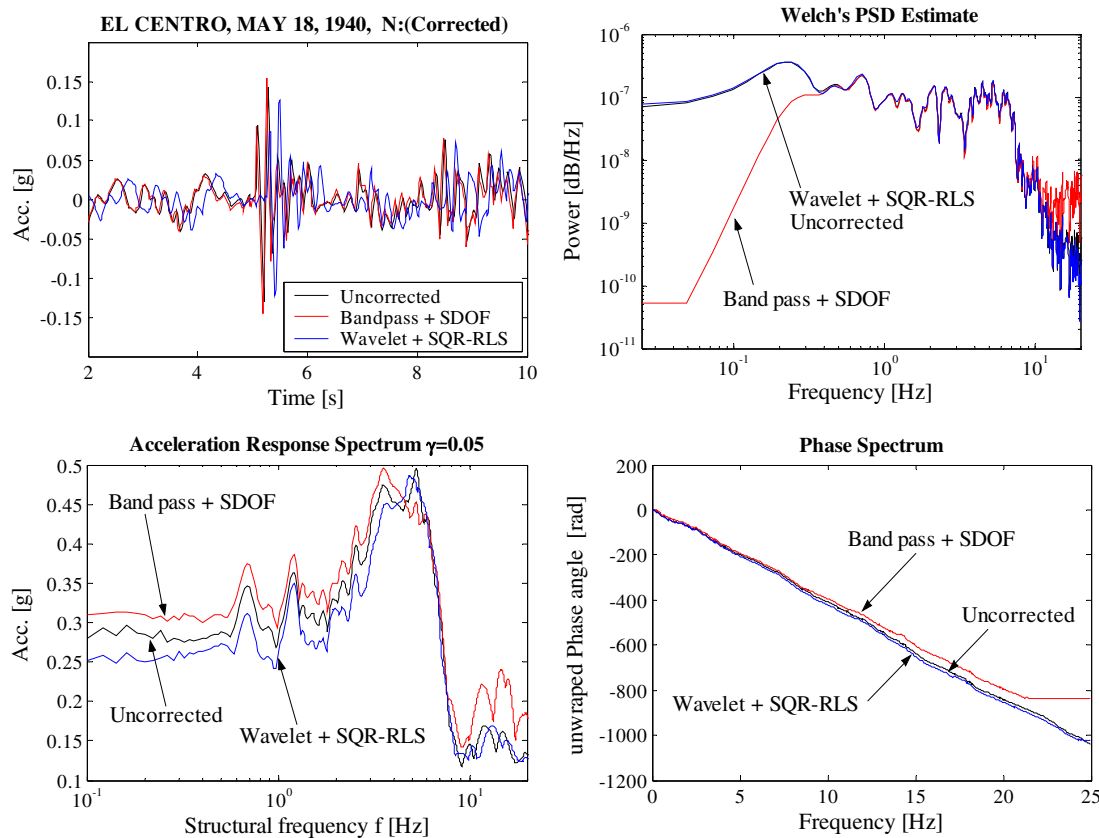


Fig. 12. Comparison of the El-Centro 1940 seismic event between using wavelet de-noising and the QR-RLS inverse filter with band-pass filtering and standard instrument de-convolution from the second order expression.

limited frequencies of interest it may be possible to obtain approximately zero magnitude and linear phase response when de-convolving prior to de-noising or filtering, however it is also clear that at higher frequencies distortion became a lot more apparent. Therefore, de-noising should precede the instrument de-convolution.

Comparisons of the effectiveness of the RLS approach were made with a conventional second order ordinary differential equation model, SDOF. It was observed that the RLS adaptive algorithm produced magnitude responses that were compatible with the SDOF results. In fact, as the original unknown ground motion is always indeterminate, it is difficult to say which approach is more accurate. What is interesting is that for the time-series, processed in this paper, the RLS algorithm concludes that the actual accelerometers used were perhaps better, this is they had a broader no gain frequency range, than expected by the SDOF model. Thus, when considering magnitudes of the time-series, the RLS seem to be more attractive than the SDOF as it does not make any assumptions about the instrument.

The influence of the RLS de-convolution method on the phase content is not destructive, but the algorithm does not explicitly recover the original phase, The RLS always produces a linear phase response because the adaptive model is of the FIR type, while the SDOF model has its own non-linear phase response. A linear phase response is equivalent to a time shift of the time-series. Thus, for the case of most dynamic structural analyses, the RLS algorithm can be thought to be neutral with respect to phase. The SDOF model phase response is almost linear for low frequencies and thus can be thought to be fairly neutral for these frequencies. If the SDOF model is used it may introduce more uncertainty by adjusting phase content of the mid to high frequency range in a non-linear manner. This could be due to the instrument not actual being an SDOF and errors in its parameters.

In the case where instrument information is unknown and even when it is known, the RLS algorithm is a reasonable approach; it recovers magnitude information well and does not introduce greater uncertainty into the data because it modifies phase content in a linear manner.

Appendix 1. The RLS algorithm

$\underline{a} = [a_1 \ a_2 \ \dots \ a_n]^T$	Seismic data ($n \times 1$)
$\underline{h}_0 = 0$	Initialise vector of estimated ($p \times 1$) filter coefficients
$\underline{d} = [\text{zeros}(p); \underline{a}]$	Estimate of desired data; i.e. shifted seismic data
$\mathbf{P}_0 = \delta \mathbf{I}$	First estimate of the ($p \times p$) inverse auto-correlation matrix, \mathbf{I} is the identity matrix, δ is small constant.
$\mathbf{A}(n + p - 1, p) = \text{convmtx}(\underline{a})$	Convolution data matrix accelerogram \underline{a} (see Eq. (1))
for $k = 1$ to $n+p-1$	Main loop
$\underline{u}_k^T = \mathbf{A}(k, :)$	take row k of convolution matrix
$\underline{k}_k = \frac{\lambda^{-1} \mathbf{P}_{k-1} \underline{u}_k}{1 + \lambda^{-1} \underline{u}_k^T \mathbf{P}_{k-1} \underline{u}_k}$	update gain
$\varepsilon_k = \underline{d}_k - \underline{h}_{k-1}^T \underline{u}_k$	determine local error
$\underline{h}_k = \underline{h}_{k-1} + \underline{k}_k^T \varepsilon_k$	update filter coefficients
$\mathbf{P}_k = \lambda^{-1} \mathbf{P}_{k-1} - \lambda^{-1} \underline{k}_k \underline{u}_k^T \mathbf{P}_{k-1}$	Use Riccati equation to update auto-correlation matrix.
end	end main loop
$\underline{a}_g = \text{conv}(\underline{h}, \underline{a});$	Inverse filter the data using best estimate of filter coefficients to model instrument response.

Appendix 2. Square-root QR-RLS algorithm

$\underline{a} = [a_1 \ a_2 \ \dots \ a_m]^T$	Seismic data
$\underline{h}_0 = 0$	Initialise vector of estimated ($p \times 1$) filter coefficients
$\underline{d}_0 = [\text{zeros}(p), \underline{a}]$	First estimate of desired data; i.e. shifted seismic data, where p is the length of the inverse filter coefficient vector
$\mathbf{P}_0 = \delta \mathbf{I}$	Initial estimate of ($p \times p$) inverse auto-correlation matrix, \mathbf{I} is the identity matrix, δ is small constant.
$\mathbf{A}(n + p - 1, p) = \text{convmtx}(\underline{a})$	Convolution data matrix accelerogram \underline{a}
$\mathbf{P}^{1/2} = \text{cholesky_sqr}(\mathbf{P}_0)$	Square-root of the initial, ($p \times p$) inverse auto-correlation matrix
for $k=1$ to $n+p-1$	begin loop
$\underline{u}_k^T = \mathbf{A}(k, :)$	take row k of convolution matrix

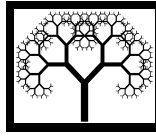
(continued on next page)

Appendix 2 (continued)

$\mathbf{B} = \begin{bmatrix} 1 & \lambda^{-1/2} \underline{\mathbf{u}}^T \mathbf{P}_{n-1}^{1/2} \\ \underline{\mathbf{0}} & \lambda^{-1/2} \mathbf{P}_{n-1}^{1/2} \end{bmatrix}$	Set up pre-array as in [5]
$\mathbf{R} = \text{householder}(\mathbf{B}, p) = \begin{bmatrix} r_{11} & \underline{\mathbf{L}}_{12}^T \\ \underline{\mathbf{L}}_{21} & \mathbf{R}_{22} \end{bmatrix}$	Annihilate pre-array forming post-array by calling a householder-matrix subroutine. The post-array, \mathbf{R} , formed by successive householder matrix operations on the columns (or rows) of the pre-array.
$\underline{\mathbf{k}}_k = \underline{\mathbf{L}}_{21} r_{11}^{-1}$	The gain vector $\underline{\mathbf{k}}_k$ is extracted from the post-array as is the updated,
$\mathbf{P}_n^{1/2} = \mathbf{R}_{22}$	Square root of the inverse correlation matrix.
$\varepsilon_k = d_k - \underline{\mathbf{h}}_{k-1}^T \underline{\mathbf{u}}_k$	Update the local error with previous estimates of filter coefficients
$\underline{\mathbf{h}}_k = \underline{\mathbf{h}}_{k-1} + \underline{\mathbf{k}}_k \varepsilon_k$	now update filter coefficients from extract gain term to form coefficient vector update $\underline{\mathbf{h}}_k$
end	end loop
$\underline{\mathbf{a}}_g = \text{conv}(\underline{\mathbf{h}}, \underline{\mathbf{a}});$	inverse filter the data using optimal estimate of filter coefficients to model instrument response.

References

- [1] Chanerley AA, Alexander NA. A new approach to seismic correction using recursive least squares and wavelet de-noising. In: Topping BHV, editor. Proceedings of the ninth international conference on civil and structural engineering computing, paper 107. Stirling, United Kingdom: Civil-Comp Press; 2003.
- [2] Priestley MJN, Myths and fallacies in earthquake engineering, revisited. The 9th Mallet Milne Lecture, IUSS press, 2003.
- [3] Alexander NA, Chanerley AA, Goorvadoo N. A review of procedures used for the correction of seismic data. In: Topping BHV, editor. Proceedings of the eighth international conference on civil & structural engineering, paper 39. Stirling, United Kingdom: Civil-Comp Press; 2001.
- [4] Chanerley AA, Alexander NA. An approach to seismic correction which includes wavelet denoising. In: Topping BHV, editor. Proc of the sixth international conference on computational structures technology, paper 44. Stirling, United Kingdom: Civil-Comp Press; 2002.
- [5] Converse AM, BAP: Basic strong-motion accelerograms processing software; Version 1.0, USGS, Denver, Colorado. Open-file report 92 (296A), 1992.
- [6] Ambraseys N, Smit P, Berardi R, Rinaldis D, Cotton F, Berge-Thierry C. Dissemination of european strong-motion data. CD-ROM Collection. European Council, Environment and Climate Research Programme, 2000.
- [7] Haykin S. Adaptive filter theory. 3rd ed. Prentice-Hall; 1996. p. 562–628.
- [8] Sayed A, Kailath H. A state-space approach to adaptive RLS filtering. IEEE signal Process Mag 1994;11:18–60.
- [9] Stearns SD, Vortman LJ. Seismic event detection using adaptive predictors. IEEE Proc ICASSP ICASSP, 1981.
- [10] Chong E, Zak S. An introduction to optimisation. Wiley; 2001. p. 187–212.
- [11] Kramer SL. Geotechnical earthquake engineering. Prentice-Hall, Inc.; 1996.
- [12] Lindfield G, Penny J. Numerical methods using Matlab. Ellis Horwood; 1995.
- [13] Golub GH, Van Loan CF. Matrix computations. John Hopkins University Press; 1996.
- [14] Fausett LV. Applied numerical analysis using Matlab. Prentice Hall; 1999.
- [15] Trifunac MD, Lee VW. Routine computer processing of strong motion accelerograms, Earthq Eng. Research Lab. Report. California Institute of Technology, Pasadena, California. CalTechEERL 1973;73(03).
- [16] Kumar A, Basu S, Chandra B. Blacs-A new correction scheme of analog accelerograms Part-1: details of Scheme. Bull. Indian Society of Earthquake Technology, Paper no. 348, 1995;32(2):33–50.
- [17] Kumar A, Basu S, Chandra B. The effects of band limited interpolation of non-uniform samples on records of analog accelerograms. Bull. Indian Society of Earthquake Technology, Paper No 327, 1992;29(4):53–67.
- [18] Sunder SS, Connor JJ. Processing strong motion earthquake signals. Bulletin of the seismological society of America 1982;72(2): 643–61.
- [19] Orsmy JFA. Design of numerical filters with applications in missile data processing, Association for Computing Machinery, Journal 8, 1961.
- [20] Khemici O, Chang W. Frequency domain corrections of earthquake accelerograms with experimental verification, San Francisco, USA, In: Proc of the 8th world conference on earthquake engineering, 1984;2:103–110.
- [21] Donoho DL. De-noising by soft thresholding. IEEE Trans Inform Theory 1995;41(3):613–27.
- [22] Burrus C, Gopinath RA, Guo H. Introduction to wavelets and wavelet transforms. Prentice-Hall; 1998.
- [23] Donoho DL, Johnstone IM. Ideal spatial adaptation via wavelet shrinkage. Biometrika 1994;81:425–55.
- [24] Lang M, Guo H, Odegard J, Burrus C, Wells R. Noise reduction using an un-decimated discrete wavelet transform. IEEE Signal Process Lett 1996;3(1):10–2.
- [25] Mix D, Olejniczak K. Elements of wavelets for engineers and scientists. Wiley; 2003.
- [26] Fliege N. Multirate digital signal processing. Wiley; 1994.
- [27] Walker JS. A primer on wavelets and their scientific applications. Chapman and hall: CRC; 1999.
- [28] Daubechies I. Ten lectures on wavelets. Philadelphia, PA: SIAM; 1992.
- [29] Coifman R, Donoho DL. Translation invariant de-noising. Wavelets and Statistics, Lecture Notes in Statistics 103, Springer-Verlag, 1995, p. 125–50.
- [30] Earthquake Strong Motion CD, National Geophysical Data Center, Boulder, Colorado, USA, NOAA, 1996.
- [31] Khemici O, Chang W. Frequency domain corrections of Earthquake Accelerograms with experimental verification, San Francisco, USA, In: Proc of the 8th world conference on earthquake engineering, 1984;2:103–10.



An Approach to Seismic Correction which includes Wavelet De-noising

A.A. Chanerley and N.A. Alexander
School of Engineering
University of East London, Dagenham, United Kingdom

Abstract

This paper begins with a brief introduction to some methods used to correct seismic data [1,2,3]. It describes standard methods of de-convolving instrument and structural responses from seismic accelerograms. These are the convolution of ground motion with the transfer function of the recording instrument and structure on which the instrument is mounted. The instrument response can be deconvolved in the time or frequency domain to recover an estimate of the ground motion of the seismic event. This is usually followed by a band-pass filtering of the data, however this removes any ground motion outside the band and hence the accelerograms may not adequately represent an estimate of true ground motion. It is proposed therefore to use wavelet [12] de-noising [11] as an alternative to band-pass filtering. The de-noising removes low and high frequency corrupting signals but retains relevant data giving a better estimate of true ground motion. Some sample seismic signals are threshold de-noised using the stationary wavelet transform (SWT) and compared with the more standard band-pass filtering techniques. The paper compares power spectral plots and the total acceleration response spectra of earthquakes using the band-pass filtering and wavelet de-noising methods.

Keywords: Correction, filter, seismic, wavelet, de-noising, recursive.

1 Introduction

A good summary of seismic correction methods is found in [1] commencing with Trifunac (1973) [2], BAP (Converse, 1982) [3] and UEL (A) and (B) (2001) [1]. Trifunac interpolates to 100Hz, then uses an FIR filter (Ormsby filter) and decimates to 50Hz and finally applies a baseline correction. It is not clear whether Trifunac uses the Ormsby filter as a zero-phase filter. Converse (BAP) [3] interpolates to 600Hz, then applies a baseline correction, segments and zero-pads the data and

applies a cosine taper window. Band-pass filtering and decimation to 200Hz then follows. The filters used were in most cases zero-phase so as not to corrupt seismic phase data.

UEL (A) is similar to BAP except that zero-phase filtering is used in all cases; the data is processed throughout as one segment without having to use a cosine taper window. UEL (B) uses an optimal recursive algorithm by minimizing a weighted least squares error, the justification for its use being that the filter coefficients will be optimal for a given set of seismic data. This method doesn't filter out-of-band relevant seismic data in the same sense as standard filtering techniques for stationary processes and therefore should provide a better estimate of the true ground motion, however the computational overhead can be substantial for long data sets.

2 De-convolution of instrument response

In many of the corrected data records available, instrument correction is not applied because the header of the original data does not provide any information on useful instrument parameters or indeed the type of instrument used. In a lot of cases the seismic data analysed did not, after processing without instrument de-convolution, produce marked differences in outputs when processed with instrument de-convolution. However, with some data analysed the differences in outputs, in particular for the acceleration response spectra were clear and not insignificant. In most of the older records the accelerograms recorded the characteristics of strong-motion earthquakes with single-degree-of-freedom, stiff and highly damped transducers whose relative displacement $x(t)$ is approximately proportional to the ground acceleration $a_g(t)$. To obtain estimates of the ground acceleration from the recorded relative displacement response, an instrument correction can be applied as follows:

$$a_g(t) = -\ddot{x}(t) - 2\gamma\omega\dot{x}(t) - \omega^2x(t) \quad (1)$$

where γ is the viscous damping ratio, ω is the transducer's natural frequency and $a_g(t)$ is the ground acceleration. The above expression (1) can be used to de-convolve the recorded motion from the ground acceleration in either the time [6] or frequency domain [4, 7].

2.1 Time domain de-convolution of instrument response, using differential mapping

Applying the central difference [6] to equation (1) and using the approximation [4], that the values of the acceleration of the uncorrected accelerograms are $-\omega_n^2x(t)$ gives a 3-tap FIR convolver for $-(\omega^2T^2)a_g(t)$, where T is the sampling rate of the digitised accelerograms, as:

$$y = -4\omega^2 T^2 a_g = (1 + 4\gamma\omega T + 4\omega^2 T^2)a_i - (2 + 4\gamma\omega T)a_{i-2} + a_{i-4} \quad (2)$$

where now $a_{i-n} = -\omega^2 x_{i-n}$ are the discrete values of the instrument acceleration output of the uncorrected accelerograms. For values of $\gamma = 0.6$, $f = 25\text{Hz}$ and $T = 1/600$ the expression becomes:

$$y = -0.10432a_g = 0.72386a_i - a_{i-2} + 0.38046a_{i-4} \quad (3)$$

The backward difference approximation gives a similar expression:

$$y = -\omega^2 T^2 a_g = (1 + 2\gamma\omega T + \omega^2 T^2)a_i - 2(1 + \gamma\omega T)a_{i-1} + a_{i-2} \quad (4)$$

For values of $\gamma = 0.6$, $f = 25\text{Hz}$ and $T = 1/600$ the expression becomes:

$$y = -0.2962a_g = 0.5975a_i - a_{i-1} + 0.43211a_{i-2} \quad (5)$$

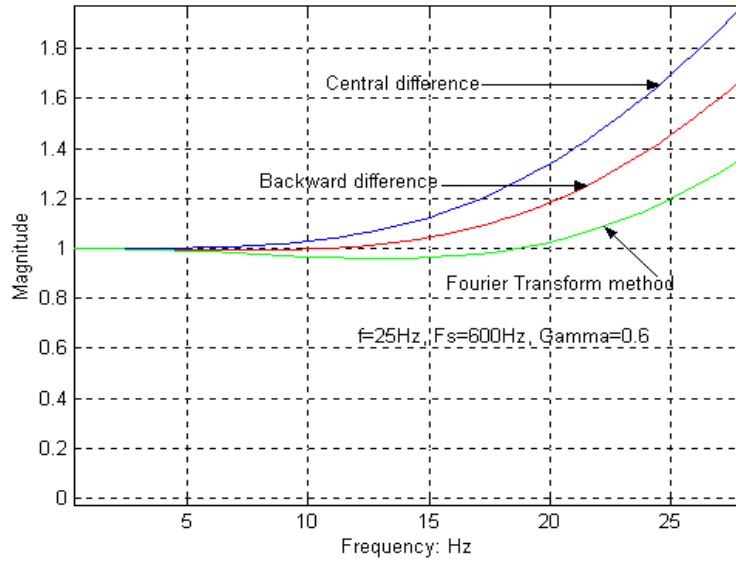


Figure 1: Frequency response curves for Instrument correction methods

The frequency response using central and backward difference is shown in Figure 1. It vindicates the conclusions in [6] in respect of the central difference correction, at sampling rates greater than 4 times the instrument response frequency. The frequency response at a lower sampling rate in this case at $T = 0.02\text{sec}$, using central difference doesn't however exhibit suppression at higher frequencies, nor does it exhibit the same degree of linearity up to 6Hz as reported in [6]. The frequency responses at $T = 1/600$ in Figure 1 also indicate that the backward difference is approximately linear up to 12Hz, compared to 6Hz for the central difference. The strong-motion, unevenly spaced data has an average sampling rate of

approximately 600Hz, which is then interpolated to give an evenly spaced data at 600Hz or a Nyquist rate of 300Hz.

2.2 Frequency domain de-convolution of instrument response

Equation (1) can also be transformed into the frequency domain [1,4,7] by applying the Fourier transformation

$$\ddot{X}g = -H(f)A(f) \quad \text{where} \quad H(f) = \left\{ \left(1 - \frac{f}{f_i} \right) + i \left(2\gamma \frac{f}{f_i} \right) \right\} \quad (6)$$

where the approximate acceleration output of the instrument is $A(f) = \omega^2 X(f)$. The ground acceleration in time can therefore be recovered from the inverse Fourier transform of the ground acceleration $\ddot{X}_g(f)$, obtained from the Fourier transform of the relative displacement $X(f)$. Figure 1 compares these most popular three methods used in correcting for the instrument response. It shows that over a limited range the responses are almost the same with the backward difference demonstrating a flat response up to approximately 12Hz, therefore over this range it can be inferred that the acceleration is approximately equal to the ground acceleration. At higher frequencies further corrections must be applied. However Figure 1 also demonstrates that using frequency domain de-convolution the response is approximately flat up to 20Hz; therefore results presented in this paper have been processed using this method.

3 De-noising using a band-pass filtering method

Some of the earlier correction procedures as reported in [6] implemented a digital band-pass filter in order to remove the low and high frequency noise. A widely used digital filter was the Ormsby filter [8], whose order is given by:

$$N = \frac{2(0.012)}{\varepsilon \Delta FT} + 1 \quad \text{where} \quad \varepsilon = |H(\Omega) - H_d(\Omega)| \quad (7)$$

ε is the error bound and $H_d(\Omega)$ is the desired frequency response function. This is a finite impulse response (FIR) filter whose output is a weighted sum of previous inputs given by:

$$y(n) = \sum_{k=0}^p a_k x(n-k) \quad (8)$$

To minimise the filter order, the filter is applied to a decimated version of the signal. For example, with $T=0.2\text{sec}$ and $\Delta F=0.02\text{Hz}$ at the low-frequency end, an error bound of $\varepsilon = 0.012$ the required order $N = 501$. It is not clear whether low-pass

filtering to prevent aliasing preceded the decimation, but it is reported [6] that this procedure produced aliasing and other distortional effects which in turn caused marked distortions in the processed accelerograms. In general equation (7) was found to be inaccurate for values of $N > 201$, the error was in fact considerably larger than that predicted by the equation. The Ormsby filter required large values of N in order to meet the required band-pass design specifications, and at the time utilised a considerable computational effort.

Infinite impulse response (IIR) digital filters are now normally employed in order to meet the required stringent band-pass specification and reduce computation time. The filter output is the weighted sum of previous inputs and the weighted sum of previous outputs and is given by:

$$y(n) = \sum_{k=0}^m a_k x(n-k) + \sum_{k=1}^p b_k y(n-k) \quad (9)$$

These designs are based on classical analogue filter methods such as Butterworth, Chebyshev and elliptic filter types which use a suitable transformation, typically the bilinear z-transformation (BZT) in order to map the s-plane poles and zeros to the z-plane circle. These filters however have a non-linear phase response whereas a zero-phase response is essential. A zero-phase characteristic is achieved through a magnitude-square response implementation procedure [9] given by the following:

$$|H(z)|^2 = |H(z)H(z^{-1})| \quad (10)$$

where $H(z) = |H(z)e^{j\beta(z)}|$ and $H(z^{-1}) = |H(z)e^{-j\beta(z)}|$ (11)

There is a loss of computational optimality though it is still superior to the computational effort required for the FIR filter. However, a zero phase response is also secured by processing the data in both the forward and reverse direction [10]. The data is first filtered in the forward direction, then the filtered data is reversed and run back through the filter. This latter method is computationally more efficient. This paper uses the latter method in order to process the data for comparison with wavelet de-noising.

4 De-noising using wavelets

This method is based on taking the discrete wavelet transform (DWT) [12] of a signal, passing the transform through a threshold [11, 15] which removes the coefficients below a certain value and then taking the inverse DWT in order to reconstruct a de-noised time signal. The DWT is able to concentrate most of the energy of the signal into a small number of wavelet coefficients, after low-pass filtering with the appropriate filter weights depending on the selection of a wavelet basis. The dimensions of the wavelet coefficients will be large compared to those of

the noise coefficients obtained after high pass filtering. Therefore thresholding or shrinking the wavelet transform will remove the low-amplitude noise in the wavelet domain and the inverse DWT will retrieve the desired signal with little loss of detail. A block diagram of a 1-stage, 2-band the operation is shown below:

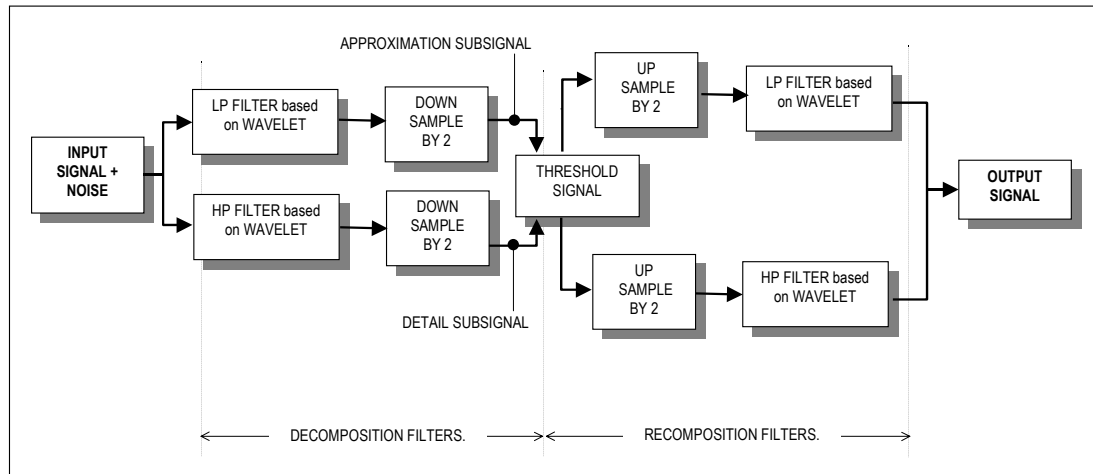


Figure 2: 1-stage, 2-band Wavelet de-noising block diagram

The rules behind thresholding are due to D L Donoho and I M Johnstone [11,13,14] and are based on decision theory. These rules are briefly described below.

Let y_i be a finite signal with additive noise given by

$$y_i = x_i + \varepsilon n_i \quad \text{where } i=1, \dots, N \quad (12)$$

where the signal x_i is corrupted by zero mean, white Gaussian noise n_i with standard deviation ε . The objective is to recover the signal x_i from the noisy data. Let W be a wavelet transformation matrix of the DWT, therefore in the transformation domain eqn(12) becomes:

$$Y = X + N \quad (13)$$

Here the upper case symbols denote the same variables but in the transformation space, such that

$$Y = W y \quad (14)$$

The inverse transform matrix must also exist therefore we have that:

$$W^{-1} W = I \quad (15)$$

If \hat{X} is the estimate of X based on the observation Y ,

then Donoho's scheme for de-noising can be summarised as follows:

- (a) determine the DWT ie $Y = Wy$
- (b) apply one of the following non-linear thresholding schemes:
- (i) 'hard' thresholding $\hat{X} = T_{hard}(Y, t) = \begin{cases} Y, & |Y| \geq t \\ 0, & |Y| < t \end{cases}$ (16)
- (ii) 'soft' thresholding $\hat{X} = T_{soft}(Y, t) = \begin{cases} \text{sgn}(Y)(|Y| - t), & |Y| \geq t \\ 0, & |Y| < t \end{cases}$ (17)
- where the threshold is given by $t \approx (2 \log n)^{1/2}$, where n is the data length.
- (c) transform back using the inverse DWT $\hat{x} = W^{-1} \hat{X}$

In general hard thresholding exhibits spurious oscillation and doesn't have the same smoothness properties of the soft thresholding scheme. However, there is a trade-off between suppression of noise and over-smoothing the data, as is the case with traditional low-or high pass filtering, but to a lesser extent.

4.1 The stationary wavelet transform (SWT) (translation invariant DWT)

There is however a problem with the wavelet transforms; the DWT is not translation invariant [15,16,17]. The coefficients of the DWT do not shift with a signal, this means that the signal is no longer orthogonal to most of the basis functions. Many more coefficients would be necessary to describe the signal and the coefficient dimensions would also be much smaller reducing the effectiveness of any de-noising scheme.

The problems with shift-invariance are connected with the alignment between features in the signal and features of the wavelet basis. In particular at discontinuities where Gibbs like phenomena can occur with unwanted oscillations. An approach to surmount this problem is described in [16] where it is suggested to forcibly shift the signal, so that it's features change positions in relation to the wavelet basis. Then to un-shift and retrieve the de-noised signal hopefully without any unwanted noise or spurious oscillation.

Following the arguments of Coifman and Donoho [16] we introduce a circulant shift operator such that

$$(S_h x)_t = x_{(t+h) \bmod n} \quad (18)$$

where the operator S_h denotes the circulant shift by h . The operator has an inverse $(S_h)^{-1}$, therefore whole process is described as follows:

For an analysis technique A , calculate the time-shifted version of A , \tilde{A} therefore,

$$\tilde{A}(x : S_h) = (S_h)^{-1}(A(S_h(x))) \quad (19)$$

However a problem does occur if a signal contains many discontinuities, because in this case a best shift for one discontinuity may not be that for another. Therefore Coifmann and Donoho propose to apply a range of shifts H and then to average over several such shifts obtained.

Therefore equation (19) is modified to the following

$$\tilde{A}(x : (S_h)_{h \in H}) = \text{Average}_{h \in H}(S_h^{-1}(A(S_h(x)))) \quad (20)$$

or

$$\text{Average [Shift } \rightarrow \text{ Denoise } \rightarrow \text{ UnShift]} \quad (21)$$

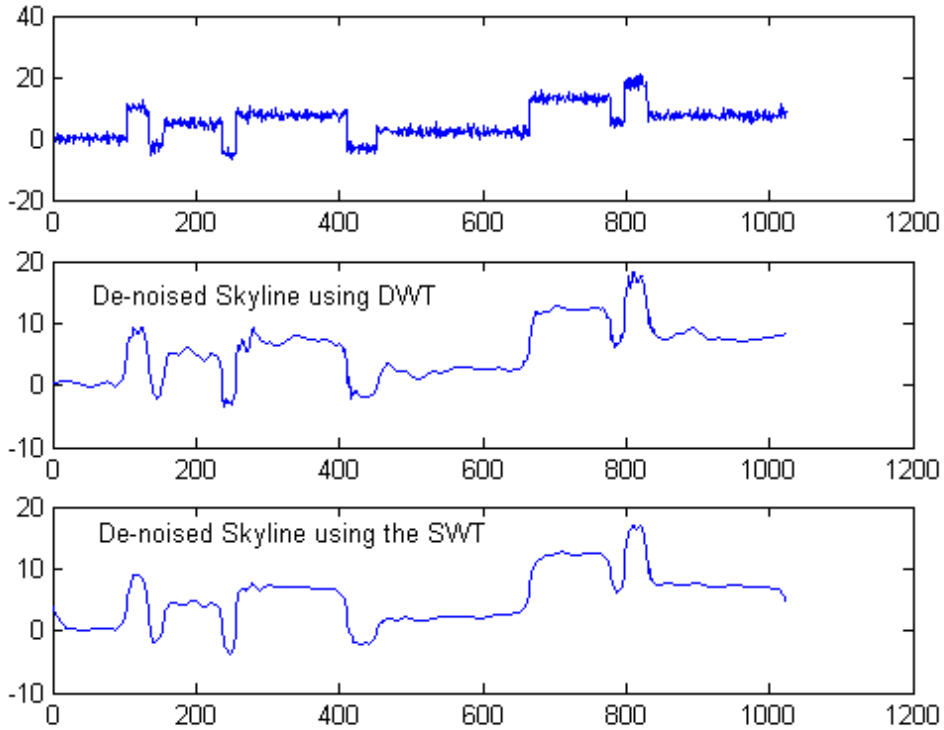


Figure 3: Example of de-noising a skyline signal

This is the approach used in the results published in this paper. However it must be said that for most results obtained, the differences between the using a DWT and SWT for de-noising are marginal; output plots such as power spectral densities and the acceleration response spectra are virtually the same. Nevertheless discontinuities in seismic records do occur therefore the SWT seems a more effective choice with which to de-noise. Figure 3 displays results similar to that of Donoho and Johnstone. This is to demonstrate the difference between using the DWT and the SWT for de-noising purposes.

Figure 3 shows the de-noised skyline using the Daubechies wavelet db8 [12] wavelet, using 8 levels of decomposition, for both the DWT and the SWT.

5 Discussion of results

The plots in Figure 4 show the SWT corrected plots and those corrected using a 4th order Butterworth band-pass filter, cut-off frequencies 0.08Hz and 20Hz.

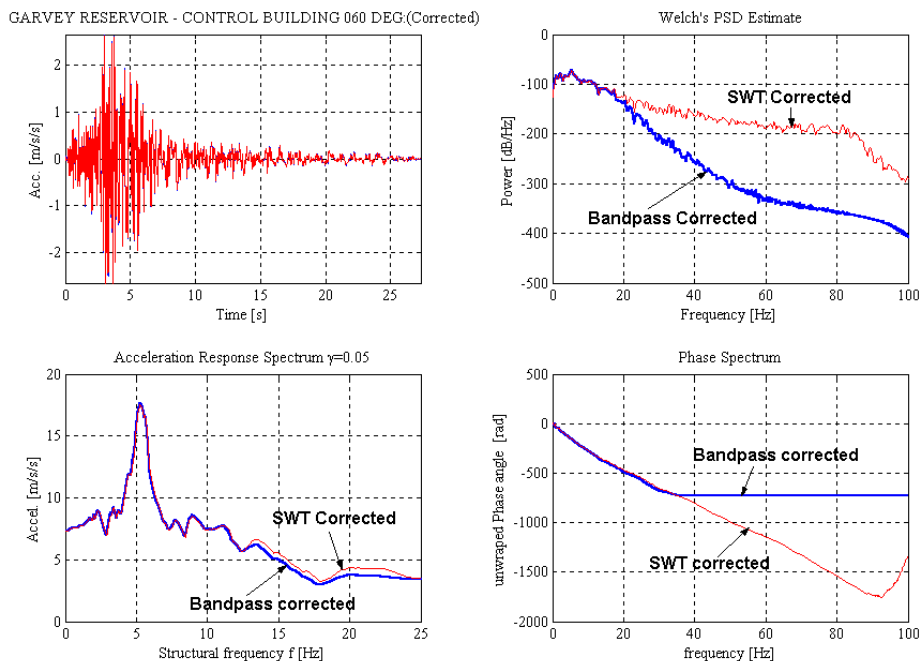


Figure 4: Garvey Reservoir seismic event (USA)

The SWT correction is essentially non-linear, whereas that band-pass filtering is a linear process. Furthermore in this case the spectral density plot shows a high degree of correlation with the acceleration response spectrum in the frequencies of interest.

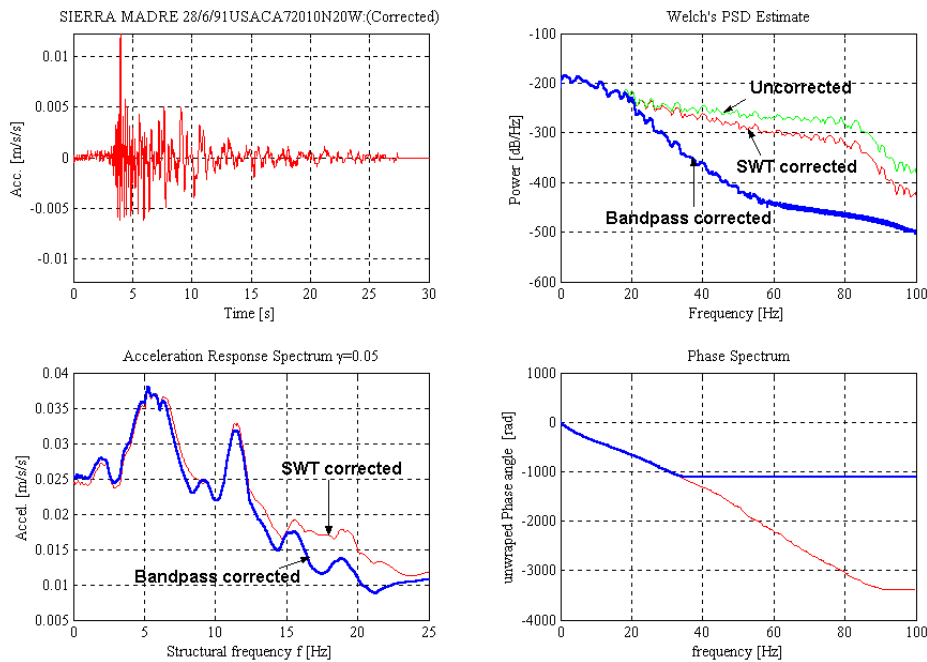


Figure 5: Sierra Madre event (USA)

In Figure 4 the power spectra demonstrate that the out-of-band energy of the signal ($>20\text{Hz}$) for the band-pass corrected Power Spectral Density (PSD) estimate has been reduced far more than the PSD estimate of the SWT corrected estimate. The acceleration response spectra for both of the correction methods are shown that up to approximately 10Hz the corrections produce almost identical structural frequencies. There is however some difference beyond 10Hz .

The Sierra Madre seismic event shown in Figure 5 shows three PSD plots for the uncorrected, band-pass filter corrected and SWT corrected record. Clearly the band-pass filter has filtered out a lot of the out of band energy, whereas the SWT denoising has not. The acceleration response spectrum does show some significant differences beyond 10Hz between the two methods. The plots of Figure 6 on the other hand show the low frequency detail on a log scale and clearly some differences between the two correction methods are again apparent. As an aside the PSD demonstrates that the large approximately 1Hz ground peak has had an insignificant impact on the structural frequency, whereas the smaller 5Hz ground peak of the PSD has had a considerable impact on the structural frequency.

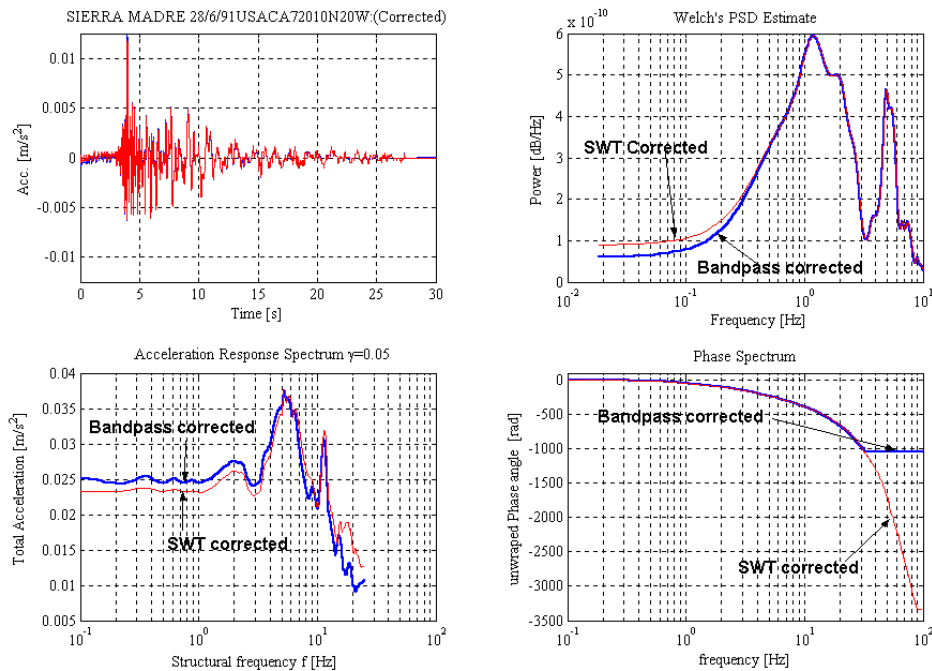


Figure 6: Sierra Madre Event (USA)

6 Summary

The paper has demonstrated that the implementation of the translation invariant wavelet transform (SWT), in the correction of seismic data has yielded some significant results. The de-noising of seismic data using the SWT removes only those signals whose amplitudes are below a certain threshold and is not therefore frequency selective. This is the fundamental difference between using a band-pass filter and wavelet thresholding. The band-pass filtering does not consider the energy content of the signal and noise. Hence the removed "noise" may or may not have a high-energy content. In the examples show the removed "noise" does have significant energy. The SWT only removes "noise" that has a low energy content and is independent of frequency. SWT de-noising obviates the need to adjust filter cut-off's to fit particular seismic events and is computationally efficient. It is evident that selection of filter cut-off frequencies varies for different groups of researchers around the world. The differences between band pass filtering and SWT methods exist, rather unsurprisingly, at the low and high frequency range of the spectrum. The low frequency or long period end is of importance in the design of large dams or tall building structures. These high cost structures may well require the use of detailed and accurately corrected acceleration timehistories.

References

- [1] N. A. Alexander, A. A. Chanerley, N. Goorvadoo, “ *A Review of Procedures used for the Correction of Seismic Data*”, Sept 19th-21st, 2001, Eisenstadt-Vienna, Austria, Proc of the 8th International Conference on Civil & Structural Engineering ISBN 0-948749-75-X
- [2] M.D. Trifunac and V.W.Lee, “*Routine computer processing of strong motion accelerograms*”, Earthq. Eng. Research Lab. Report. California Institute of Technology, Pasadena, California. EERL 73(03), 1973
- [3] A.M. Converse, “*BAP: Basic Strong-Motion Accelerograms Processing Software; Version 1.0*”, USGS, Denver, Colorado. Open-file report 92(296A), 1992
- [4] A. Kumar, S. Basu, B. Chandra, “*Blacs-A new Correction Scheme of Analog Accelerograms. Part-1: details of Scheme*” Bull. Indian Society of Earthquake Technology, Paper No 348, Vol. 32, No.2 June 1995, pp 33-50
- [5] A. Kumar, S. Basu, B. Chandra, “*The effects of Band Limited interpolation of non-uniform samples on records of Analog Accelerograms*” Bull. Indian Society of Earthquake Technology, Paper No 327, Vol. 29, No.4 Dec 1992, pp 53-67
- [6] S. S. Sunder, J.J. Connor, “ *Processing Strong Motion Earthquake Signals*”, Bulletin of the Seismological Society of America, Vol. 72. No.2, pp. 643-661, April 1982
- [7] O. Khemici, W. Chang, “*Frequency domain corrections of Earthquake Accelerograms with experimental verification*”, San Francisco, USA, Proc of the 8th World Conference on Earthquake Engineering, 1984, Vol 2, pp 103-110
- [8] J F A Ormsby, “*Design of numerical filters with applications in missile data processing*”, Association for Computing Machinery, Journal 8, 1961
- [9] L Rabiner, B Gold, “*Theory and Application of Digital Signal Processing*”, Prentice-Hall, 1975, pp 209-210
- [10] A V Oppenheim, R W Schaffer, “*Discrete-Time Signal Processing*”, Prentice-Hall, 1989, pp 311-312.
- [11] D L Donoho, “*De-noising by soft thresholding*”, IEEE Transactions on Information Theory, 41(3):613-627, May 1995.
- [12] Ingrid Daubechies, “*Ten Lectures on Wavelets*”, SIAM, Philadelphia, PA, 1992
- [13] D. L. Donoho, I. M. Johnstone, “*Ideal Spatial adaptation via wavelet shrinkage*”, Biometrika, 81:425-455, 1994
- [14] D L Donoho, I M Johnstone, “*Adapting to unknown smoothness via wavelet shrinkage*”, Stanford Statistics report TR-425, 1993
- [15] C Burrus, R A Gopinath, H Guo, “*Introduction to wavelets and wavelet transforms*”, Prentice-Hall, 1998
- [16] R Coifman, D L Donoho, “*Translation Invariant de-noising*”, Wavelets and Statistics, Lecture Notes in Statistics 103: Springer-Verlag, p125-150, 1995

- [17] M Lang, H Guo, J Odegard, C Burrus, R Wells, "*Noise reduction using an undecimated discrete wavelet transform*", IEEE Signal Processing Letters, 3(1):10-12, January 1996
- [18] "*The Wavelet Toolbox*" The Mathworks, Inc, Natick, MA, USA
- [19] J. S.Walker, "*A primer on wavelets and their scientific applications*" Chapman and hall/CRC, 1999

Concerning Baseline Errors in the Form of Acceleration Transients When Recovering Displacements from Strong Motion Records Using the Undecimated Wavelet Transform

by A. A. Chanerley, N. A. Alexander, J. Berrill, H. Avery, B. Halldorsson, and R. Sigbjornsson

Abstract This paper discusses the progression of a novel algorithm that uses a wavelet-transform approach. The transform is a generalization of the decimated, discrete wavelet transform (DWT) that is the undecimated DWT or stationary wavelet transform (SWT) also known as the undecimated *à trous* algorithm. It forms the basis for recovering displacements from acceleration time histories. The approach recovers a low-frequency fling that is usually an almost sinusoidal or cosinusoidal pulse responsible for the big ground motions in strong motion events. The algorithm implements a well known and non-linear, denoising scheme and is applied to the low-frequency sub-band and, in particular, succeeds in recovering the acceleration-fling pulse. The progression is that in order to obtain estimates of displacements, the algorithmic baseline-correction scheme can now locate an acceleration transient (i.e., a spike), which creates the DC shift in velocity and the linear trend in displacement, and is therefore the baseline error. Once this acceleration transient is corrected for or eliminated, double-time reintegration recovers the velocity-fling pulse and residual displacement. The paper infers that these acceleration transients may be due to ground rotation, embedded in the translational data. The scheme provides for easier integration once the low- and higher-frequency accelerations are extracted.

Online Material: Additional results for the Chi-Chi TCU068 (1999) station, the New Zealand Darfield Station (2010), and the Ölfus Earthquake (2008) in Iceland.

Introduction

This paper contains the results from Chi-Chi record TCU102 (see [Data and Resources](#)) that are presented as exemplars. The remainder of the results, on which some of the discussions and conclusions are based, are presented in the  electronic supplement to this paper. This supplement includes results from (1) the Chi-Chi (1999) event, station TCU068 using the A900 instrument, (2) the ICEARRAY station data designed by Iceland's Earthquake Engineering Research Center (EERC) (University of Iceland) with data from the 29 May 2008 Ölfus earthquake using the CUSP instrument and (3) data from the 4 September 2010 earthquake in Christchurch, New Zealand, recorded by the GeoNet Network (New Zealand Earthquake Commission) also using the CUSP instrument.

This paper introduces a novel wavelet-transform method, which is progressed further in this paper and examines the removal of baseline-error and its location in time. Interestingly, the form of the baseline error is simply a sudden spike in the acceleration that occurs just after the low-frequency fling. The wavelet method differs from those

of previous methods cited in the review below, because it locates the baseline error without having to make any assumptions with regard to its existence in time or its form in the acceleration time history. The algorithm discussed in this paper simply finds the baseline error embedded in the fling sinusoid, or almost sinusoid, and removes it, thereby enabling double-time integration of the acceleration time history to recover the residual displacement.

When trying to obtain displacements, baseline shifts and baseline correction are part of a more common problem encountered in double integrating the acceleration time history. These have been discussed with various solutions ([Trifunac, 1971](#); [Trifunac and Lee, 1973](#); [Bogdanov and Graizer, 1976](#); [Wong and Trifunac, 1977](#); [Graizer, 1979](#); [Iwan et al., 1985](#); [Chiu, 1997](#); [Todorovska, 1998](#); [Trifunac et al., 1999](#); [Boore, 2001](#); [Trifunac and Todorovska, 2001](#); [Boore et al., 2002](#); [Boore, 2003](#); [Wang et al., 2003](#); [Boore and Bommer, 2005](#); [Graizer, 2005, 2006](#); [Boroschek and Legrand, 2006](#); [Kalkan and Graizer, 2007](#); [Pillet and Virieux, 2007](#); [Wu and Wu, 2007](#); [Kinoshita, 2008](#); [Akkar and Boore, 2009](#); [Chanerley](#)

and Alexander, 2010; Graizer, 2010). The integration gives DC shifts in velocity and linear or quadratic trends in displacement in the latter portion of the record, which is a consequence of variations in the signal baseline of the acceleration. These are brought about by instrument noise, tilts/ground rotations, or cross-coupling, giving abrupt jumps in acceleration.

Sophisticated methods exist for correcting baseline errors and obtaining stable double-time integration. Graizer (1979) was the first to advocate a baseline correction procedure by obtaining and fitting a straight line to a segment of the velocity. Chiu (1997) high-pass filtered before integration, Iwan *et al.* (1985) removed pulses and steps by locating the time points that exceeded a predefined acceleration, later generalized by Boore (2001), Akkar and Boore (2009) by adding further time points and making the time points t_1 and t_2 free of any acceleration thresholds, the accumulated effects of these baseline changes represented by average offsets in the baseline. Wu and Wu (2007) also used a modified method due to Iwan *et al.* (1985) on the Chi-Chi event and defined t_1 at the beginning of the ground motion, and defined t_2 on the basis of a flatness coefficient and defined a further parameter t_3 , the time at which the displacement had reached a final value. Wang *et al.* (2003) removed pulses and steps fitted with amplitudes that gave the same areas as the slope of the displacement to achieve stable double integration. Pillet and Vireaux (2007) on the other hand, using data from station TCU068 from the 1999 Chi-Chi earthquake, recovered a baseline error as an average acceleration from a linear trend in the velocity and removed it at the time points at which the velocity crossed the zero axes.

Chen and Loh (2007) also used a wavelet-transform method that was mainly procedural, and which applied the discrete wavelet transform (DWT) with decimation, using a finite-impulse-response (FIR) filter approximation to the Meyer wavelet. Their method, however, does not use a denoising scheme, nor do they recover the fling time history. The wavelet method described in this paper is entirely algorithmic, rather than procedural, and uses the undecimated wavelet transform with a denoising scheme. Although the two wavelet methods are quite dissimilar in approach and implementation, the displacements obtained for the Chi-Chi event in both cases are comparable with Global Positioning System (GPS).

Rotations (Tilts) as Baseline Error

Rotations (tilts) are an often cited reason for baseline errors, contributing to the baseline offsets and causing unstable double integration. These have been a major area of investigation for a number of years. A number of researchers have investigated and continue to investigate ground rotations (tilts), including Wong and Trifunac (1977), Bouchon and Aki (1982), Trifunac (1982), Graizer (1989, 1991, 2005, 2006), Nigbor (1994), Spudich *et al.* (1995), Todorovska (1998), Boore (2001), Trifunac and Todorovska (2001),

Boore *et al.* (2002), Zahradnik and Plesinger (2005), Boroschek and Legrand (2006), Kalkan and Graizer (2007), Graizer and Kalkan (2008), Lin *et al.* (2010).

In particular, Trifunac and Todorovska (2001), Wong and Trifunac (1977), and Graizer (2005) found that, in the main, accelerometer data comprised translational and tilt data, as well as contributions from cross-axis sensitivity and sensor-misalignment data. The latter effects, though, were small compared with the former for modern digital accelerometers. Graizer (2005) numerically imposed a tilt-angle time history on a corrected Hector Mine record and demonstrated that an upward linear trend occurs after the displacement ramp and when the residual displacement begins to appear. Graizer (2006) proposed a method for identifying the existence of tilts by comparing the sensitivity of the vertical (z) and horizontal (*north-south* and *east-west*) components to rotational ground motion using Fourier spectra, given that the vertical component is insensitive to tilts.

Pillet and Vireaux (2007) have estimated and subtracted a jump in the acceleration, though there is no data on the time of occurrence of this jump. Pillet and Vireaux (2007) point out that these acceleration jumps may be due to tilt angles for which the magnitudes are two or three orders greater than generally predicted, and in their paper are given as -0.049 cm/s^2 for the vertical, 4.077 cm/s^2 for the *north-south* and -3.446 cm/s^2 for the *east-west* component.

Kinoshita (2008) used broadband velocity seismograms on data from the Noto-Hanto earthquake (M_w 6.9) 29/03/2007, in order to estimate tilt accelerations. Kinoshita (2008) concludes that several tilts arising from multiple ground motions occurred during the Tokachi-Oki event. This type of multiple ground-tilt motion may also be inferred from some of the results presented in this paper.

Baseline Correction and the Acceleration Spike

When inspecting an acceleration-fling time history recovered by the wavelet transform and denoising scheme, it is not immediately obvious from the time history whether any acceleration offsets, short-duration or otherwise, actually occurred, which gave rise to DC shifts in velocity. The acceleration-fling time histories presented in the results show this. However, once the corrected and uncorrected acceleration-fling time histories are subtracted, the subtraction yields an acceleration transient, that is, a spike. On double-time integrating the spike, it gives the exact post-shaking, flat-velocity DC shift and the displacement linear trend found when integrating the uncorrected, low-frequency, acceleration-fling pulse commencing at the time of the occurrence of the spike. Boore *et al.*, 2002 discuss this type of post-shaking, flat-velocity time history in some detail, relating it to errors due to rotation and torsion-induced distortion causing a finite duration offset in the acceleration. Boore *et al.*, 2002, p. 1550 states:

“we note that the rotation- and torsion-induced distortions should be very small after the strong shaking has ceased; for this reason, the accumulated effect would be a finite duration offset in the acceleration, which would integrate to a post-shaking flat velocity trace.”

This is precisely what is found when using the algorithm presented and described in this paper.

The net result, and indeed a novel result, is that the transform locates and recovers the baseline error embedded within the low-frequency fling, which turns out to be an acceleration transient or, as initially referred to in Wang *et al.* (2003), just a short duration spike, shown in the Results. The removal of the offending spike from the low-frequency, acceleration-fling pulse, then enables double-time integration of the low-frequency fling to a stable, residual displacement. This is a significant progression on the wavelet-transform method proposed originally in Chanerley and Alexander (2010) and modified and discussed in more detail in this paper. The method has automated baseline correction and the algorithm itself locates the time and form of the baseline error, which hitherto has been unobtainable, and which in the first place causes the instability in the double-time integration. Once located, the algorithm then removes the error, thereby permitting stable double-time integration.

The form of these baseline errors in digital records has already been suggested in Boore *et al.* (2002), as a finite-duration offset, in Wang *et al.* (2003), as a spike, or in Akkar and Boore (2009) as near instantaneous. Essentially the fitting and removal of 1.0 s acceleration transients in Wang *et al.* (2003) is in a sense similar to the recovery of the acceleration transient using the presented wavelet-transform method, except that the wavelet-transform algorithm automatically recovers and defines the acceleration transient that is embedded within the seismic data. Clinton (2004, pp. 61–64) also shows in his thesis that passing a δ -function through a mathematical model of the FBA-23 produces similar outcomes as obtained in the Results.

The isolation and recovery of an optimal fling, which appears as almost a sinusoid or cosinusoid, from the recorded acceleration time history is the constraint used in order to achieve stable double-time integration and to retrieve the acceleration spike. This spike is then either removed at its time point T_i of occurrence or equivalently the acceleration is zeroed from $t \geq T_i$ and reintegrated. The time point T_i is the point at which the low-frequency, velocity sub-band crosses the zero axes and at which point the sharp acceleration transient occurs and prevents stable double-integration. The point at which the velocity crosses the zero axes is also the point at which the DC shift in the velocity fling space begins and which then gives a first-order trend in the displacement. It is also noted that some earthquakes have multiple, zero-crossing points any one of which provides stable, double-time integration. This is discussed in detail in the Results.

After applying the algorithm the profile of the baseline-error is isolated as an acceleration transient operating at a

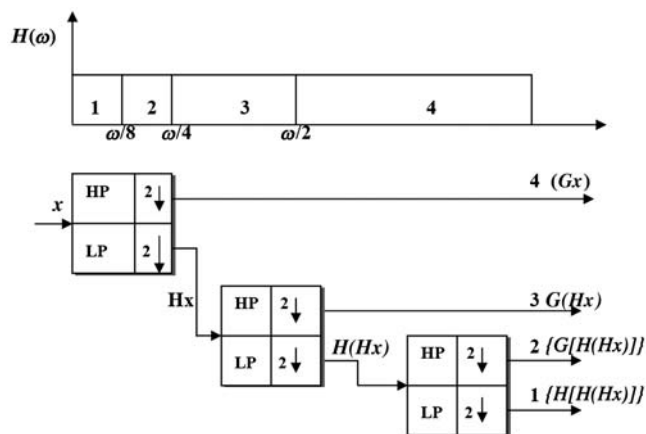


Figure 1. Four-channel, analysis (decomposition) wavelet filter bank showing sub-bands.

clearly visible and defined time point T_i in the velocity-fling that the algorithm itself locates. The outcome of applying the algorithm to recorded events is discussed in the Results. On the other hand (and so far), the higher-frequency, sub-band velocity space does not exhibit such catastrophic baseline drift and integrates to a stable, though oscillatory, time series that is then added to the baseline corrected low-frequency fling to give the final, corrected time history as shown in the Results.

Generalization of the DWT

From an engineering and seismological perspective, the easiest way to envisage the wavelet transform is in terms of octave filters. These are quite common in digital audio. Octave filters form the basis of the wavelet transform, whether the transform is decimated or undecimated. The wavelet transform comprises in this case well-designed filter banks (Mallat, 1989; Daubechies, 1992; Coifman and Wick-erhauser, 1993). The decimated, DWT is applied in an octave-band filter bank, implementing successive low-pass and high-pass filtering and down-sampling by a factor of 2, so that every second sample is discarded. As an example, a four-channel filter-bank scheme is shown in Figure 1. The filters used in wavelet filter banks are digital finite-impulse-response filters, also called non-recursive filters because the outputs depend only on the inputs and not on previous outputs. The discrete convolution expression for a FIR filter is given by

$$y(n) = \sum_{k=0}^{N-1} h(k)x(n-k), \quad (1)$$

for which $h(k)$ are the filter coefficients and $x(n-k)$ are the time-shifted samples of data. Equation (1) lends itself to the multiply-accumulate-data-shift architecture (MACD) of most modern processing engines.

Therefore, we proceed in octave sub-bands as per Figure 1, for which the filters H and G operate on the data vector, x , as follows:

first octave low-frequency sub-band = Hx
 second octave low-frequency sub-band = $H(Hx)$
 third octave low-frequency sub-band = $H[H(Hx)]$
 first octave higher-frequency sub-band = Gx
 second octave higher-frequency sub-band = $G(Hx)$
 third octave higher-frequency sub-band = $G[H(Hx)]$.

The behavior of the filters is to operate on a column vector of data by convolving the data with the filter coefficients and to down-sample by 2, that is, discard half the values. The inverse operation requires up-sampling by a factor of 2, followed by synthesis filter banks, and is shown in Figure 2.

However, there is a problem with the DWT in that due to down-sampling the DWT is not shift invariant. Aliasing can occur between the sub-bands if not all of the coefficients are used during reconstruction, which is undesirable if the application needs denoising, as in this case. Therefore, the easiest way to surmount this is not to down-sample, so that the length of the signal remains at N rather than $N/2$ as in the decimated DWT, but rather to use a generalization of the DWT that is the undecimated wavelet transform or stationary wavelet transform (SWT) that is shift invariant (Lang *et al.*, 1996). Because we do not decimate them, instead we have to interpolate by pushing zeros into each level of the transform (i.e., between the filter coefficients), that is, dyadically up-sampling; this is the *à trous* algorithm (trous = holes) (Shensa, 1992; Mallat, 1999). It was also shown in Coifman and Donoho (1995) and Donoho and Johnstone (1994, 1995) that the SWT denoises with a lower root-mean-square error than that with the standard DWT, and denoising is a key requirement for this application. Furthermore, the inverse SWT (ISWT) averages the estimates at each level resulting from all shifts, again minimizing the noise, so overall the SWT is a better transform to apply. Time-domain filter banks in Figure 3 show the SWT and the ISWT. In the analysis filter

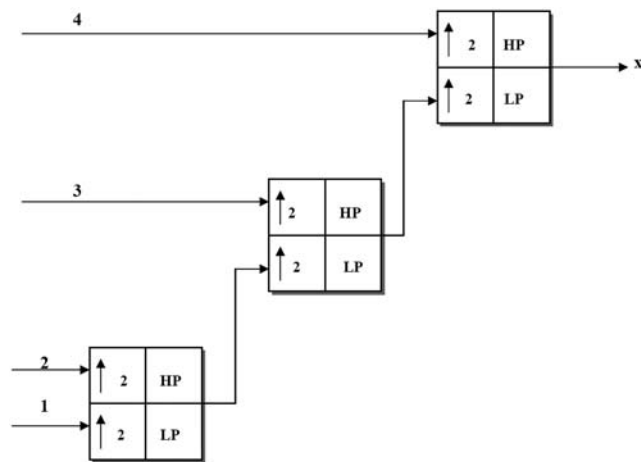


Figure 2. Wavelet-synthesis transposition of filter bank for sub-band reconstruction.

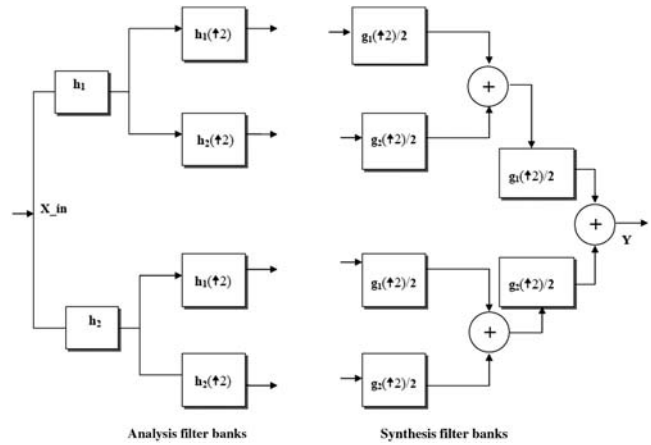


Figure 3. Undecimated or stationary wavelet-transform (SWT) filter banks, showing the dyadic up-sampling of the filter coefficients, that is, the pushing of zeros in between the coefficients.

banks, the easiest thing to do is to push zeros (*à trous*) in between the filter coefficients and keep filtering the even and odd samples from every band. In the synthesis filter banks, they are averaged at each level as shown. The data, of course, is also denoised between the analysis phase using the SWT and the synthesis phase using the ISWT.

Denoising Scheme

Denoising is a non-linear method of removing unwanted signals. It is advantageous because spectra (of signal and noise) can overlap, whereas when filtering they should not. It is the amplitude which is clipped or to which a threshold is applied. It has been applied together with the wavelet transform by Chanerley and Alexander (2007, 2008, 2010), and Chanerley *et al.* (2009a,b, 2010) to seismic events when deconvolving records. Denoising is superior to filtering in the sense that filtering will remove or attenuate those frequencies that we want to retain. In particular, filtering low-frequency noise will also filter the low-frequency signal (i.e., the fling), so is to be avoided.

The application of a denoising scheme initially applies a soft threshold (Donoho and Johnstone, 1994, 1995; Coifman and Donoho, 1995; Donoho, 1995), to both the low-frequency and higher-frequency sub-bands signals after applying the wavelet filters. However, it was subsequently found that for some earthquakes applying a threshold to the higher-frequency sub-bands removed too much detail in the denoising process (B. Halldorsson, personal comm., 2009). Therefore, the threshold initially applied to the higher-frequency sub-bands was removed from the algorithm. This retained the detail without affecting the overall displacement result, and overlaying the original time history on the corrected time history did not demonstrate any significant differences.

In the low-frequency fling space the threshold is retained, but there is some flexibility, if desired, in the number

of threshold iterations applied. At high decomposition levels, such as at level 10 and above, there is usually very little post-fling detail or perturbation in the time history. However, at lower levels of decomposition, between 7 and 9, for example, and if a light threshold is applied, that is, one or two threshold iterations, detail in the post-fling time history is preserved. Extra detail can be retained if so desired, but the algorithm is constructed to apply the rule stated in Graizer (2005) that everything past the fling is distortion and so should be removed if displacement is the objective. The correction algorithm zeroes the acceleration after the end of the fling pulse to remove any such distortion. However, if the objective is to locate any possible acceleration spikes, then more detail may be appropriate.

The Results, and also the additional material in the   electronic supplement, demonstrates and discusses this, and shows in the tables of results multiple acceleration transients in the post-fling history, which could, of course, be dismissed as distortion.

It should again be emphasized that most of the discussion that follows refers to the low-frequency sub-bands, the higher frequencies double-integrated to an oscillation around zero in velocity and displacement, and did not require the same correction.

Applying the Wavelet Transform

When applying the wavelet transform, a high octave level (e.g., level 10) with respect to the sampling rate, is initially applied. This is to limit the low-frequency, sub-band bandwidth to the lowest frequency band feasible for a particular set of seismic time series, in order to isolate the low-frequency, acceleration fling. For example, for a sampling rate of 200 Hz, level 10 decimates down to a low-frequency band in the range $f \leq 0.1$ Hz, basically $100 \text{ Hz}/2^{10}$. However, should the fling profile be too far removed from the sinusoidal or cosinusoidal profiles, then the next level down is used. Thus far, we have only used bior1.3 and bior2.6, from the bi-orthogonal wavelet set that gives linear phase filters. The bior2.6 wavelet filters provided a zero-velocity crossing for which this was not possible with bior1.3. This is because at times with bior1.3, the velocity behaved asymptotically and never actually crossed the zero axis; therefore it made sense to either change level or change the wavelet to the bior2.6.

Moreover, we have applied wavelet filters from level 10 down to level 7, the latter for earthquakes that were less than

M_w 7, such as for the M_w 6.3 in Iceland in 2008. The displacements recovered for the Iceland event from the ICEARRAY were small, suggesting a fling pulse of shorter duration than, for example, the Chi-Chi TCU068, the latter giving displacement in meters rather than in centimeters as recorded by the ICEARRAY and GPS. A shorter duration fling suggests a lower decomposition level, therefore, higher frequencies (though still less than 1 Hz). Level 7 for the ICEARRAY is the 0.78 Hz band, whereas level 10 for TCU068 is the 0.097 Hz band. Therefore, applying level 10 to some of the ICEARRAY data did not yield anything sensible, because some of the really low frequencies apparent in Chi-Chi TCU068, for example, were simply not present in the ICEARRAY event, therefore, a lower decomposition level was necessary.

Ideally, the same octave level would be expected to be used for all three components of a seismic event, though that may not always be possible due to the velocity not crossing the zero axis, as explained previously, which sometimes requires a change in level or a change in wavelet. The time point itself is also an aspect to consider in the sense that the transform may obtain more than one zero-crossing on the velocity axis, though the point to note is that the time points are all located by the transform. At the time point nearest the fling pulse, the spike is removed through zeroing. However, the two horizontal time points should normally be close to one another as the results indeed show. Suffice to say, therefore, that the low-frequency, zero-velocity, crossover time points T_i should occur at about the same time for the longitudinal components, with only a small margin of difference as demonstrated in the Results.

Results

This section discusses the results for the Chi-Chi (1999) event station TCU102. Additional results in Tables S1–S5 and Figures S1–S12 are presented in the   electronic supplement from (1) Chi-Chi (1999) event station TCU068, (2) the New Zealand (2010) Darfield event, and the (3) ICEARRAY results from the Iceland (2008)  lfus event.

Acceleration Transient for Chi-Chi TCU102

The data for this event comes from Lee *et al.* (2001) in the BSSA CD ROM, an excellent source of data from the Chi-Chi (1999) event. The acceleration transients and their times of occurrence are shown in Table 1, together with those

Table 1
Estimates of Acceleration Transients for two Chi-Chi Stations, for Each Component, and their Time of Occurrence

Chi-Chi Station	North–South Components		East–West Components		Vertical Components	
	Tilt Acceleration (cm/s/s)	Time (s)	Tilt Acceleration (cm/s/s)	Time (s)	Tilt Acceleration (cm/s/s)	Time (s)
TCU068	9.565	45.65	–6.75	45.83	No Tilt	n/a
TCU102	10.63	38.39	4.04	41.2	2.174	42.93

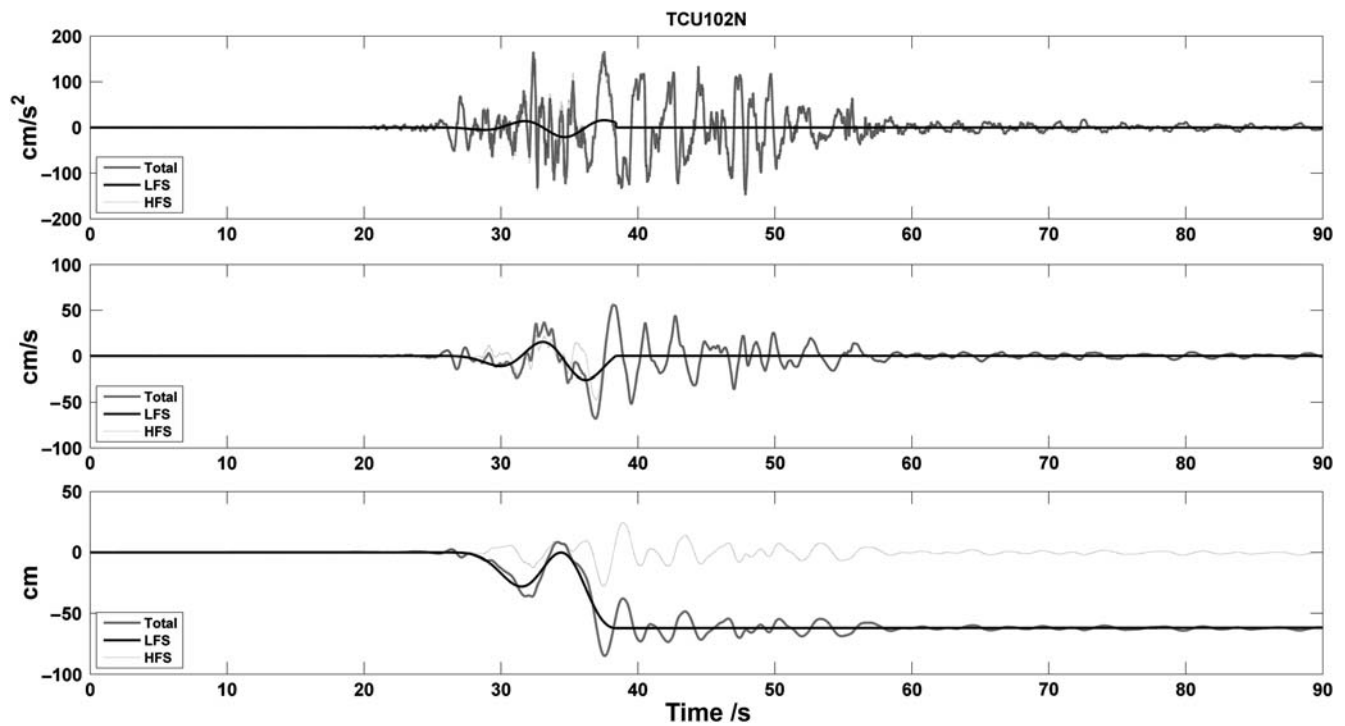


Figure 4. Comparison of the low-frequency sub-band fling, and higher-frequency sub-band, and the resulting total using bior2.6 for TCU102NS component obtained at level 9, with a displacement of -61.82 cm, with zero-velocity crossover taken at 38.39 s.

of station TCU068. The instrument for this station was the A900. The accelerogram and GPS stations are on the footwall side of the fault (Wu and Wu, 2007). The wavelet transform used was bior2.6, rather than the bior1.3, as discussed above in [Applying the Wavelet Transform](#).

The *north-south* component gave an almost sinusoidal fling profile at level 9, whereas the *east-west* and vertical components gave an almost sinusoidal fling profile at level 10 after wavelet filtering. Figures 4, 5, and 6 show the acceleration, velocity, and displacement sub-bands, respectively,

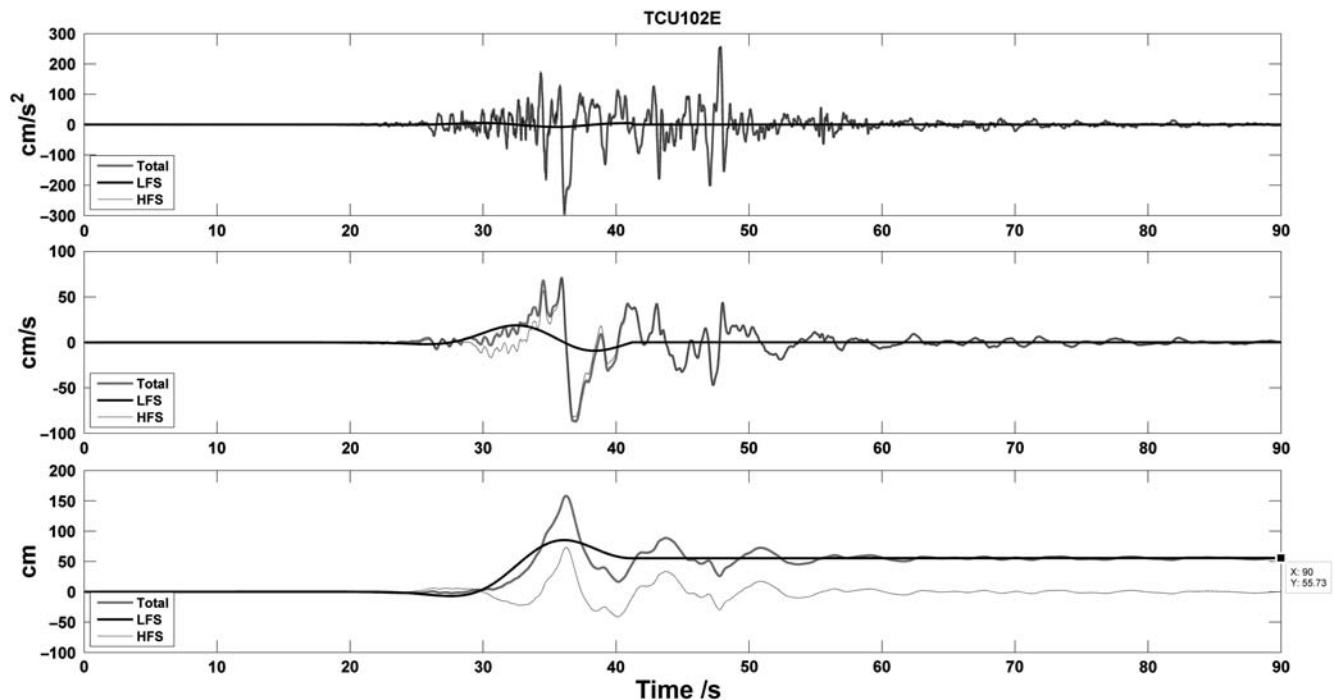


Figure 5. Comparison of the low-frequency (LFS) sub-band fling and higher-frequency sub-band (HFS) and the resulting total using bior2.6 for TCU102EW component obtained at level 10, with a displacement of 55.73 cm, with zero-velocity crossover taken at 41.2 s.

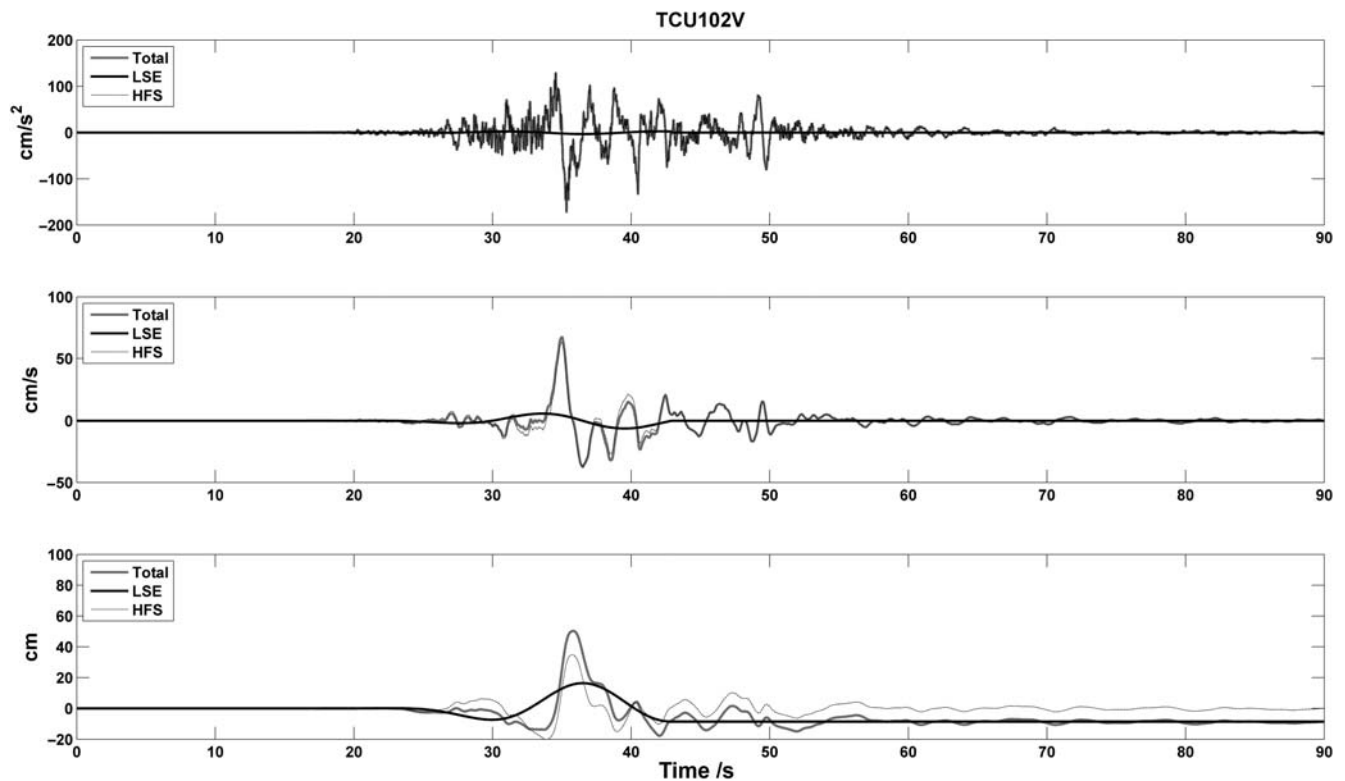


Figure 6. Comparison of the low-frequency (LFS) sub-band fling and higher-frequency sub-band (LFS) and the resulting total using bior2.6 for TCU102V component obtained at level 10, with a displacement of -8.536 cm, with zero-velocity crossover taken at 42.93 s.

as well as their resultants after adding the low-frequency time series to the higher-frequency time series. The displacement estimates are summarized in Table 2 and show good correlation with GPS station G103, 1.7 km away (Boore, 2001; Wu and Wu, 2007).

The zero-velocity crossover point at which final baseline correction is applied for each component is in the first and second columns, and is indicated in Table 3, and shown in the low-frequency fling for the horizontal components in each of the Figures 7 and 8. Figure 9 shows the double-integrated acceleration transient for the TCU102EW component. The shown time points are the times of occurrence of the acceleration transients at which baseline correction was applied, and which are given in Table 1.

Returning first to Figure 7, it shows at decomposition level 9 the TCU102NS, low-frequency, fling profile with post-fling perturbations, and after applying two threshold iterations. An optimal acceleration-fling profile is similar

to a theoretical benchmark, that is, similar to a sine or cosine and the first zero-velocity, crossover point occurs at $T_i = 38.39$ s just at the end of the fling sinusoid and the estimated tilt acceleration transient at that point is 10.63 cm/s^2 . In addition there are two further post-fling, zero-velocity crossover points, as listed in Table 3. These are too large in magnitude to be attributed to just noise. With reference to the comments in Denoising Scheme, this is a level-9 decomposition profile, with a lot more post-fling detail than the *east-west* components at level 10. If we infer that these transients are due to tilt, then more than one zero crossing suggests that the instrument may have experienced more than one tilt acceleration transient during the course of the earthquake in the low-frequency fling space.

Figure 8 shows, at decomposition level 10 and after applying only one threshold iteration, the TCU102EW low-frequency fling profile.

It has two zero-velocity crossover points in the wavelet-transformed velocity time series. Table 3 lists the acceleration transient values, 4.4 cm/s^2 for TCU102EW at a time point of 41.2 s. There is another transient at 46.2 s, but this is small and could be attributable to noise. Figure 9 shows the TCU102EW velocity and displacement response after double integrating the tilt acceleration transient, extracted from the fling. The responses for the acceleration transients of the other two components are not shown, but are similar.

The low-frequency TCU102V fling time series (not shown) at decomposition level 10 shows some post-fling

Table 2
Chi-Chi TCU102 Displacement Estimates
at Levels 9 and 10

Level	TCU102NS (cm)	TCU102EW (cm)	TCU102V (cm)
9	-61.82	n/a	n/a
10	n/a	55.73	-8.54
GPS	-59.2	66.3	-10

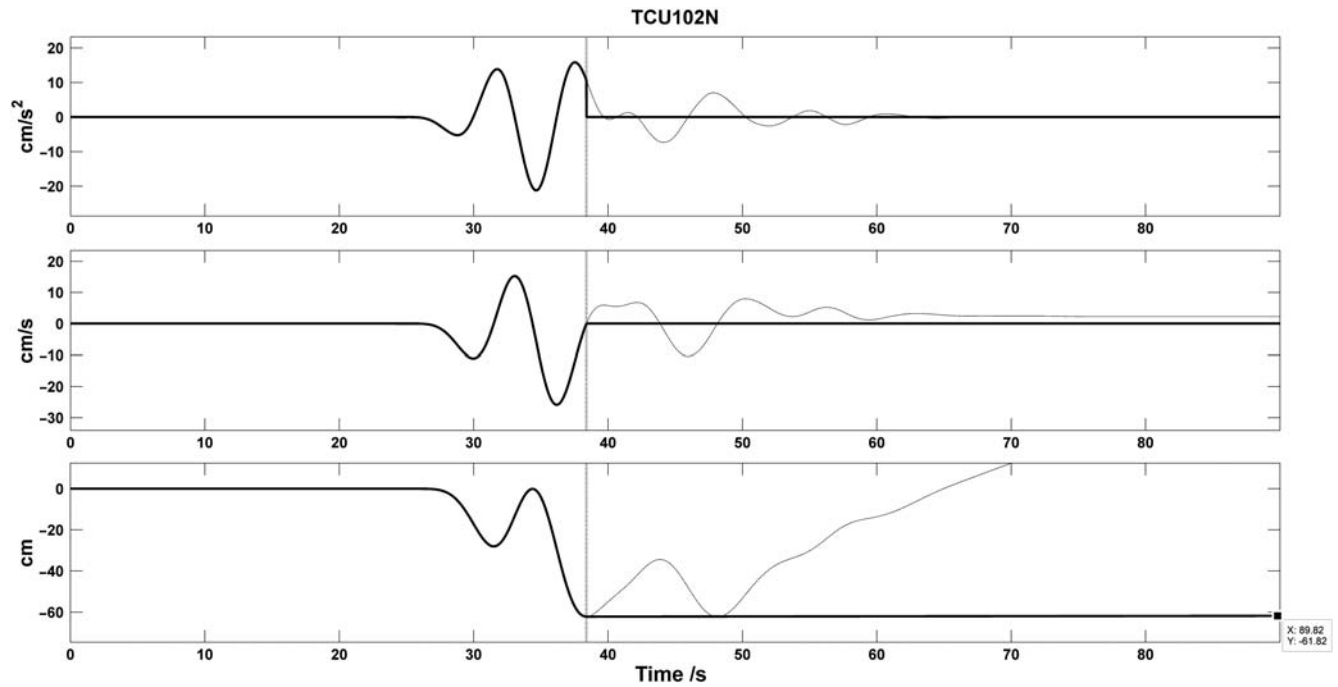


Figure 7. Station TCU102N, showing results before and after baseline correction. The triangular area in the acceleration is the result of a $g\varphi$ acceleration tilt transient taken at 38.39 s. The resulting constant velocity DC shift (2.26 cm/s) is shown in light gray, as is the linear displacement offset. The velocity time series shows three zero-velocity crossover points, suggesting three tilt acceleration transients in the low-frequency fling space.

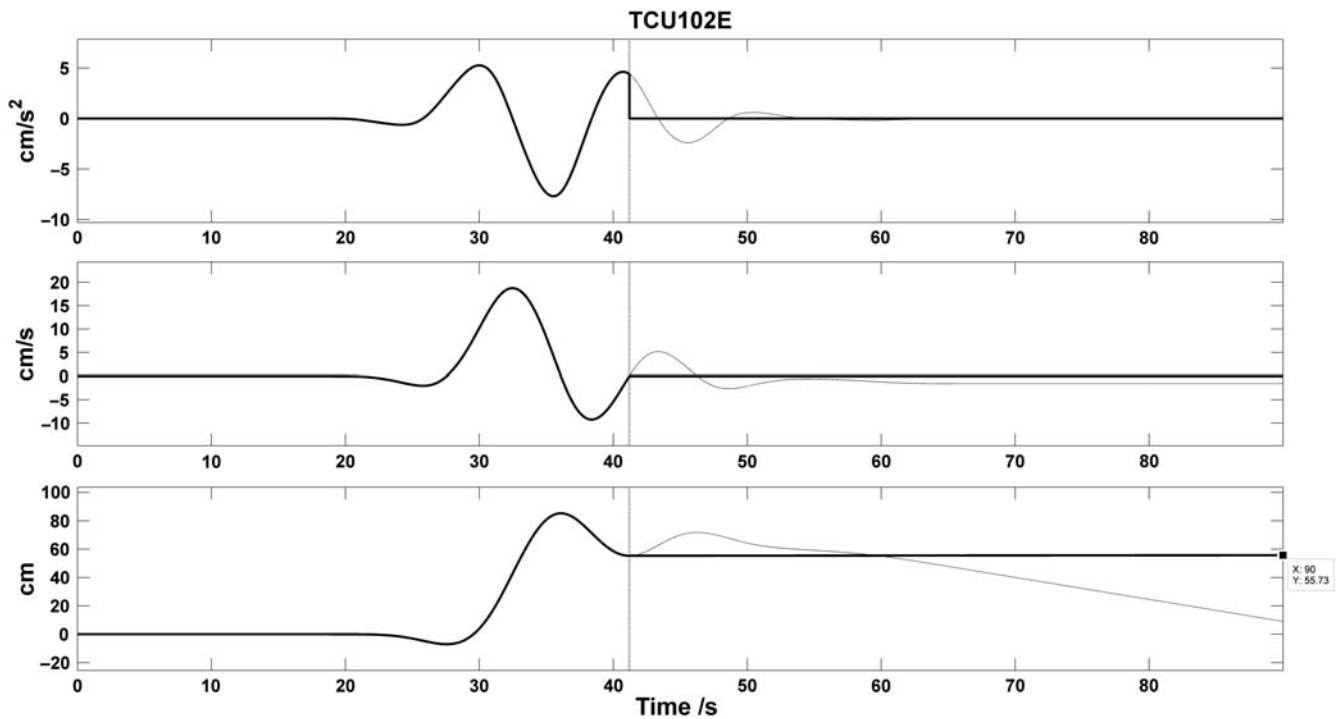


Figure 8. Station TCU102E, low-frequency sub-band (LFS): showing results before and after baseline correction. The triangular area in the acceleration is the results of a $g\varphi$ acceleration tilt transient taken at 41.2 s. The resulting constant velocity DC shift (-1.55 cm/s) is shown in light gray, as is the linear displacement offset. The velocity time series shows two zero-velocity, crossover points, suggesting two tilt acceleration transients in the low-frequency fling space.

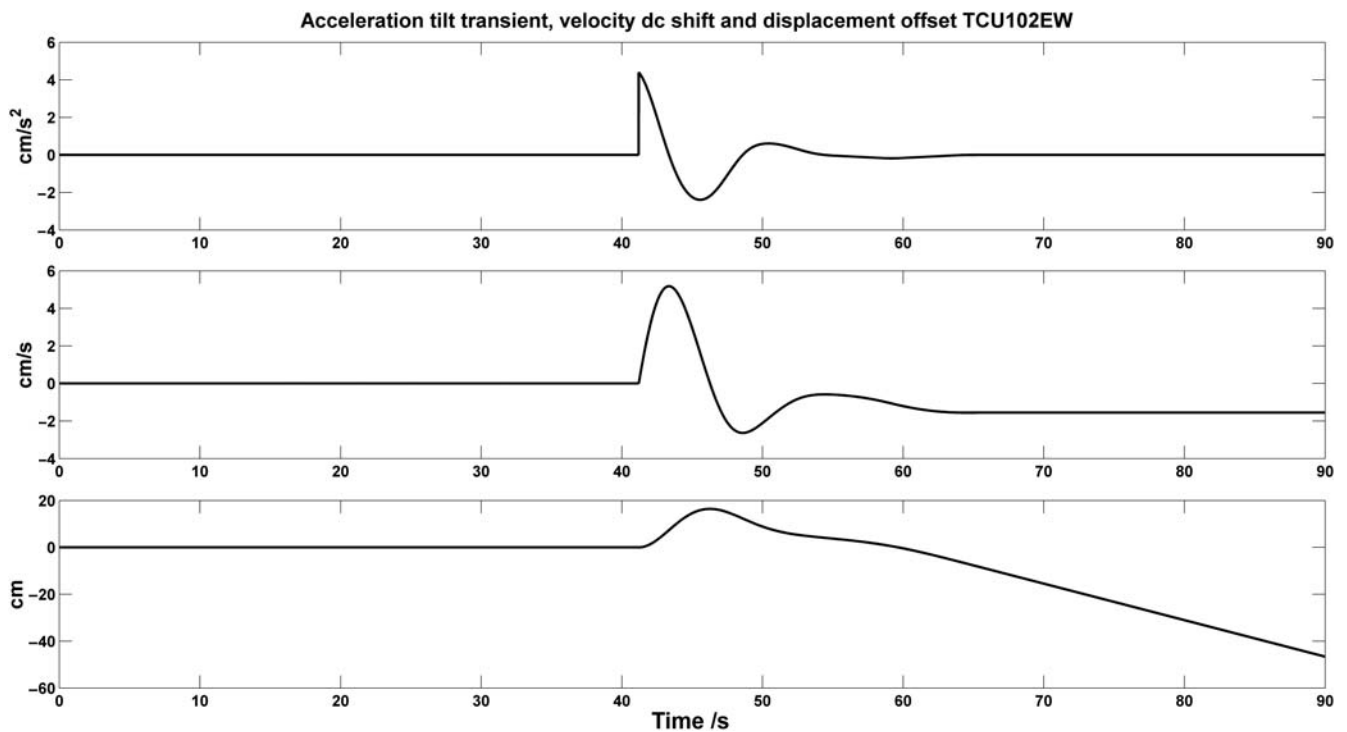


Figure 9. Acceleration tilt transient at 41.2 s and 4.40 cm/s/s, velocity and displacement response after integration of acceleration transient at 41.2 s, for the TCU102EW component using instrument (A900).

detail with four zero-velocity crossover points and associated acceleration transients listed in Table 3. However, these are small in magnitude compared to those of the *north–south* and *east–west*, and we attribute these to noise.

Is the Spike a Facet of Instrument Noise or an Artifact of the Algorithm?

These have been two often-asked questions with respect to the results, which we now discuss. With regard to noise the papers from [Trifunac and Todorovska \(2001\)](#), [Wang et al. \(2003\)](#), and [Graizer \(2005\)](#) give good guides. First, [Graizer \(2005\)](#) in his equations shows that the *z*-component is insensitive to ground rotations/tilts, therefore we may reasonably expect that the *z*-component would not have any spikes. The equations show that the two horizontal components, on the other hand, are susceptible to distortions due to rotations/tilts.

It is found, for example, that after the wavelet transform, the fling pulse of the *z*-component of TCU068 integrated without correction, and did not produce any spikes,

suggesting that the instrument noise was too small for that particular instrument and did not appear in the time history. In Chi-Chi station TCU102, the Greendale (NZ) station, and the ICEARRAY, the vertical components have spikes, but these are small compared with those of the horizontal components as shown in Tables 1, 3, ⑤ S2, and S5 (see supplement). It is suggested that any *z*-component spikes in general gives a measure of instrument noise and that any larger spikes in acceleration for the horizontal components must be due to sources other than the instrument. In this context, the work of [Boore et al. \(2002\)](#) as quoted in the [Baseline Correction and the Acceleration Spike](#), suggests these short-duration offsets, that is, spikes, are due to ground rotation and torsion, and therefore it can be inferred that the obtained spikes in the horizontal accelerations are just such short duration offsets.

This brings us to [Trifunac and Todorovska \(2001\)](#) and [Wang et al. \(2003\)](#). The latter paper refers to the Hualien seismic station where two collocated, A-900As were installed (HWA019 and HWA2) and one A-800 (HWA),

Table 3

Estimates of Acceleration Transients at the Various Zero-Velocity Crossover Points and their Time of Occurrence for TCU102

Station	First Tilt Acceleration (cm/s/s)	Time (T_i) (s)	Second Tilt Acceleration (cm/s/s)	Time (s)	Third Tilt Acceleration (cm/s/s)	Time (s)	Fourth Tilt Acceleration (cm/s/s)	Time (s)
TCU102NS	10.63	38.39	-7.29	44.09	6.84	48.15	—	—
TCU102EW	4.4	41.2	-2.18	46.2	—	—	—	—
TCU102V	2.174	42.93	-1.44	47.61	1.13	52.81	-0.55	59.36

separated by approximately 1 km from each other. Wang *et al.* (2003) p. 679 states:

“The difference in the trends of the displacement for the same component of motion on the three collocated instruments indicate that the baseline offsets are not the same for all instruments, as would be the case whether the offsets are caused by ground rotation or ground tilt, either transient or permanent (Trifunac and Todorovska, 2001), which suggests that the source of the baseline offsets must be internal to each instrument.”

The conclusion they reached was that the differences in the trends produced by the baseline offsets for the three Hualien station instruments suggest that the principal source of the offsets was some transient disturbance within the instruments A-900A and A-800.

However, in the results presented in this paper the principal source of the offsets did not come from instrument noise, certainly not for all the components and in particular not for the z -component. We cite the additional results provided in ⑤ Tables S1–S3 (see supplement) from Chi-Chi (1999) and Christchurch (2010) and ⑤ Tables S4 and S5 (see supplement) from the ICEARRAY stations (Halldorsson and Sigbjornsson, 2009; Halldorsson *et al.*, 2009; Decriem *et al.*, 2010; Halldorsson *et al.*, 2010; Rupakhety *et al.*, 2010) for which we present results from 11 of the 14 stations, at 50 m between each station, spanning an aperture of 1.9 km, that were installed in the SISZ. The results in ⑤ Table S5 (see supplement) for the ICEARRAY show consistency for each set of components over the 11-ICEARRAY stations. In particular for the 11-EW components, for which the acceleration spikes are much greater than for either one of the other two components and with similar magnitudes and in the same direction (all positive) in the *east–west* components, that is, without any difference in the initial spike, implying the same initial displacement trends for all 11-CUSP instrument stations. In the light of the above and from Wang *et al.* (2003), then it is strongly suggested that certainly for the *east–west* component the acceleration spikes are a measure of ground rotations. The z -component and the *north–south* component shown in ⑤ Table S5 (see supplement) both display smaller acceleration spikes compared to the *east–west* component and suggest that these may be due to instrument or other noise. Instrument noise may certainly be a factor and a possible source of the recovered small acceleration transients for the z - and maybe the *north–south* component as well. The z -component transient, however, shows a bit more dispersion than the *north–south* component in its acceleration magnitudes, suggesting that for the z -component the transients are due to noise. However, for the horizontal *east–west* components, the magnitudes of the transients are large even after subtracting out the noise estimates. It is inferred, therefore, from the above that these transients are ground-rotation induced.

The second question as to whether the acceleration spike is an artifact of the method used had in fact been tested by using the TCU068-NS component. The test involved removing the low-frequency, acceleration-fling pulse from the time history and replacing it by a synthetic sinusoidal pulse of approximately the same duration, frequency, and amplitude. The algorithm was then applied and the wavelet transform recovered the sinusoid without any spikes and, therefore, without the need for any baseline correction. This was deemed as sufficient evidence that the spike obtained from the real earthquake of TCU068-NS was not an algorithmic artifact, otherwise the synthetic sinusoid would not have been retrieved without correction.

Discussion

The wavelet-transform method provides the basis for an automated baseline-correction procedure, but in particular for locating and isolating the form and time of occurrence of baseline error that for all the events studied thus far is a Dirac-like acceleration transient, after which the objective remains simply to remove the transient and proceed to stable integration.

The new result for TCU068 shown in ⑤ Figures S1–S3 (see supplement) is that the acceleration transients obtained using the wavelet-transform method compare reasonably with those published in Pillet and Virieux (2007) using a non-wavelet-transform method, and are shown in ⑤ Table S1 (see supplement) for the same station.

Station TCU102 (Table 2) and Figures 4–9 are new results for the presented method and examples of records giving several zero-crossing points (Table 3) in the low-frequency, velocity-fling sub-band. The zero crossings give four consecutive acceleration transients given in Table 3. However, the baseline error, which is from the first zero-velocity crossing point, occurs at almost the same time for both horizontal components. Where there are several zero-crossing points in velocity, the rule is to use the zero-crossing point that is nearest the clear-cut fling, on the assumption that any time history after $t \geq T_i$ may be due to distortions (Graizer, 2005). The displacement results show good agreement with GPS.

The Darfield earthquake (see ⑤ Fig. S4 in the supplement) in Christchurch, New Zealand, at the Greendale station was processed by the wavelet transform and found to give reasonable displacement estimates in ⑤ Table S2 (see supplement) compared with GPS (Berrill *et al.*, 2011). Other results and discussion are given in Berrill *et al.* (2011) mainly for the N55°W component. New results in this paper are the low-frequency fling-pulse plots for N55°W in ⑤ Figure S5 (see supplement) and its acceleration transient in ⑤ Figure S6 (see supplement) and their double-time integrations and the S35°W plots in ⑤ Figure S7 (see supplement). New results in ⑤ Table S2 and Table S3 (see supplement) show the acceleration transients. The vertical component in ⑤ Table S2 is 0.49 cm/s^2 , suggesting instrument noise as the cause of the

baseline error. On the other hand, the acceleration spikes for the two horizontal components, though small, are five and seven times bigger than that for the vertical component, suggesting therefore that these are due to ground rotations.

For the S35°W component it is demonstrated that at a lower level of decomposition, in this case, level 9 in ⑤ Figures S8 and S9 (see supplement), several threshold iterations can remove post-fling perturbations, without affecting the magnitude of the displacement or the acceleration transient. It is argued, however, that in general a light-touch threshold of only one to two iterations is applied with the baseline-error transient removed at the fling pulse. Again, and as for TCU102, the time points at the clear-cut fling were used showing good agreement with GPS.

The Ölfus event, ⑤ Figures S10–S12, (see supplement) is interesting, however, from the perspective that the results from the 11-ICEARRAY stations show behavior as expected from ground rotations described by others in their research work as discussed in [Is the Spike a Facet of Instrument Noise or an Artifact of the Algorithm?](#) The displacement results of the Ölfus earthquake in Iceland are shown in ⑤ Table S4 (see supplement) and are hitherto unpublished as a full set for the SWT method and correlate well with those obtained by others and GPS after the acceleration transients are removed. Estimates of the acceleration transients of the Ölfus earthquake in Iceland May 2008 are significant because of the proximity of the accelerographs within the array. ⑤ Table S5 (see supplement) shows that there is a good correlation in the magnitude of the acceleration transients and good correlation for the T_i time points, at which the baseline correction is applied for each instrument and component. To some extent it may be argued that these results are self-validating, because it is difficult to envisage eleven 3-DOF CUSP instruments malfunctioning almost simultaneously. The acceleration transients in ⑤ Table S5 (see supplement) for this data set also show that the *east–west* component in the accelerographs has the highest initial acceleration transients, averaging 16 cm/s² at the time points at which the baseline error was obtained and removed and residual displacements measured. The results from this array are important for the wavelet-transform method because they support some of the conclusions in [Trifunac and Todorovska \(2001\)](#), [Boore et al. \(2002\)](#), [Wang et al. \(2003\)](#), and [Graizer \(2005\)](#) as discussed in this paper, and from their work we can infer that these transients may be due to ground rotations.

Conclusion

It is demonstrated that the wavelet transform reveals a finer structure to the acceleration jumps (transients) in the baseline, which make recovery of stable residual displacements problematic. On integrating the acceleration transients from the events used in this paper and the ⑤ electronic supplement, then their double integrations match the velocity DC shift and displacement error in the low-frequency, velocity, and displacement time series.

It can also be concluded that certainly some of these transients, occurring in the low-frequency, fling pulse are not always due to noise or some malfunction, though the lower values of the acceleration transients occurring in the z -component may be attributed to noise. Further, there is no need to alter the shape of the transient by keeping the area constant, and the time at which the pulses occur is not a free parameter. Indeed, the baseline error in the form of the acceleration transient occurs as a clearly defined time, located by the wavelet transform and that occurs toward the end of the low-frequency velocity-fling pulse. Moreover, it has been shown for TCU102, the Greendale Station, and the Ölfus earthquake that there can be more than one clearly defined velocity zero-crossing point at different times, however, and as often emphasized the algorithm uses the time point at the velocity fling, the rest can be eliminated if recovering displacement alone is the objective, which it usually is.

When using the wavelet transform, low-cut filtering is not recommended, because the long-period fling is then removed, and the whole purpose of applying the transform is then rendered void. Fortunately, through good design neither the A900 nor the CUSP ([Avery et al., 2004](#); [Avery, 2005](#)) instruments have built-in low-cut filters.

Finally, the wavelet-transform method as presented in this paper locates the baseline error in the form of an acceleration transient and removes it. Thereafter, recovery of displacement is possible. The wavelet-transform method is therefore a reasonable alternative with which to obtain displacements by double integration. Furthermore and based on the results obtained for the acceleration transients, and if we use the assumption as in [Trifunac and Todorovska \(2001\)](#), [Boore et al., 2002](#), [Wang et al. \(2003\)](#), and [Graizer \(2005\)](#), then it may be concluded that some of these acceleration transients causing the baseline error may be due to ground-induced tilt/rotation.

Data and Resources

The New Zealand records for the Darfield Event, 4 September 2010 can be obtained from the following database sites: ftp://ftp.geonet.org.nz/strong/processed/Proc/2010/09_Prelim/2010-09-03_163541/Vol1/data/ (last accessed July 2012). The image in ⑤ Figure S13 (in the electronic supplement to this paper) is from <http://db.nzsee.org.nz/PUBS> (last accessed January 2011). The records for the Chi-Chi Event is obtained from [Lee et al. \(2001\)](#) (last accessed October 2011). The ICEARRAY records are as yet not in the public domain, but can be obtained by contacting Benedikt Halldorsson at skykkur@hi.is (last contacted May 2012).

Acknowledgments

Many thanks to Ragnar Sigbjornsson, Benedikt Halldorsson, and all of the EERC team at the University of Iceland, who made possible the ICEARRAY, from which emerged such a useful stream of results. Thanks to the CUSP Company and team, headed by John Berrill, who produced the

successful CUSP instrument, and in particular to Hamish Avery, the designer and principal research officer, for the technical discussions and assistance. Thanks also to John Berrill, CUSP CEO and instrument originator, and the helpful discussions. Many thanks also to John Zhao and Caroline Holden, GNS Science, New Zealand, for the helpful email exchanges. Finally, we are grateful to the two anonymous reviewers, whose constructive comments improved the paper. *Deo gratias*.

References

- Akkar, S., and D. M. Boore (2009). On baseline correction and uncertainty in response spectra for baseline variations commonly encountered in digital accelerographs, *Bull. Seismol. Soc. Am.* **99**, no. 9, 1671–1690.
- Avery, H. R. (2005). The development of a low-cost strong-motion seismic data logger, *Ph.D. Thesis*, University of Canterbury, Christchurch, New Zealand.
- Avery, H. R., J. B. Berrill, P. F. Coursey, B. L. Deam, M. B. Dewe, C. C. François, J. R. Pettinga, and M. D. Yetton (2004). The Canterbury University strong motion recording project, in *Proc. 13th World Conf Earthq. Eng.*, Vancouver, Canada, Paper No. 1335.
- Berrill, J., H. Avery, M. B. Dewe, A. Chanerley, N. Alexander, C. Dyer, and C. Holden (2011). The Canterbury Accelerograph Network (CanNet) and some results from the September 2010, *M* 7.1 Darfield earthquake, in *Proc. 9th Conf. Earthq. Eng.*, Auckland, New Zealand, 14–16 April 2011.
- Bogdanov, V., and V. Graizer (1976). The determination of the residual displacement of ground motion from the seismogram, Reports of the Academy of Sciences USSR, Vol. 229, 59–62.
- Boore, D. M. (2001). Effect of baseline corrections on displacements and response spectra for several recordings of the 1999 Chi-Chi, Taiwan, earthquake, *Bull. Seismol. Soc. Am.* **91**, 1199–1211.
- Boore, D. M. (2003). Analog-to-digital conversion as a source of drifts in displacements derived from digital recordings of ground acceleration, *Bull. Seismol. Soc. Am.* **93**, 2017–2024.
- Boore, D. M., and J. J. Bommer (2005). Processing of strong motion accelerograms: Needs, options and consequences, *Soil Dynam. Earthq. Eng.* **25**, 93–115.
- Boore, D. M., C. D. Stephens, and W. B. Joyner (2002). Comments on baseline correction of digital-strong motion data: Examples from the 1999 Hector Mine, California, earthquake, *Bull. Seismol. Soc. Am.* **92**, 1543–1560.
- Boroschek, R. L., and D. Legrand (2006). Tilt motion effects on the double-time integration of linear accelerometers: An experimental approach, *Bull. Seismol. Soc. Am.* **96**, 932–944.
- Bouchon, R., and K. Aki (1982). Strain, Tilt and rotation associated with strong ground motion in the vicinity of earthquake faults, *Bull. Seismol. Soc. Am.* **72**, 1717–1738.
- Chanerley, A. A., and N. A. Alexander (2007). Correcting data from an unknown accelerometer using recursive least squares and wavelet de-noising, *Comput. Struct.* **85**, no. 21–22, 1679–1692.
- Chanerley, A. A., and N. A. Alexander (2008). Using the total least squares method for seismic correction of recordings from unknown instrument, *Adv. Eng. Software* **39**, 849–860.
- Chanerley, A. A., and N. A. Alexander (2010). Obtaining estimates of the low-frequency ‘fling’, instrument tilts and displacement time series using wavelet decomposition, *Bull. Earthq. Eng.* **8**, no. 2, 231–255, doi: [10.1007/s10518-009-9150-5](https://doi.org/10.1007/s10518-009-9150-5).
- Chanerley, A. A., N. A. Alexander, and B. Halldorsson (2009a). Recovering ground displacement and velocity time series using wavelet decomposition, in *1st International Symposium on Strong Motion Earthquake Effects, (ISSEE)*, Reykjavik, Iceland, May 2009.
- Chanerley, A. A., N. A. Alexander, and B. Halldorsson (2009b). On fling and baseline correction using quadrature mirror filters, in *Proc. of the Twelfth International Conference on Civil, Structural and Environmental Engineering Computing, paper 177*, Madeira, Portugal, 1–4 September, doi: [10.4203/ccp.91.177](https://doi.org/10.4203/ccp.91.177).
- Chanerley, A. A., N. A. Alexander, B. Halldorsson, R. Sigbjornsson, and R. Perryman (2010). Baseline correction made easy using an automated method based on the wavelet transform, in *Proc. of the 9th U.S. National and 10th Canadian Conference on Earthquake Engineering, paper 358*, 25–29 July, Toronto, Canada.
- Chen, S.-M., and C.-H. Loh (2007). Estimating permanent ground displacement from near-fault strong-motion accelerograms, *Bull. Seismol. Soc. Am.* **97**, no. 1B, 63–75, doi: [10.1785/0120060060](https://doi.org/10.1785/0120060060).
- Chiu, H.-C. (1997). Stable baseline correction of digital strong motion data, *Bull. Seismol. Soc. Am.* **87**, 932–944.
- Clinton, J. F. (2004). Modern digital seismology-instrumentation and small amplitude studies in the engineering world, *Ph.D. thesis*, California Institute of Technology, Pasadena, California.
- Coifman, R., and D. L. Donoho (1995). Translation invariant de-noising, wavelets and statistics, in *Lecture notes in statistics-proceedings*, Vol 103, Springer, New York, 125–150.
- Coifman, R. R., and M. V. Wickerhauser (1993). Wavelets and adapted waveform analysis, in *Proc. Symposia in Appl. Mathematics*, Vol. 47, American Mathematics Soc., Providence, Rhode Island, 119–153.
- Daubechies, I. (1992). *Ten Lectures on Wavelets*, SIAM, Philadelphia.
- Decriem, J., T. Árnadóttir, A. Hooper, H. Geirsson, F. Sigmundsson, M. Keiding, B. G. Ófeigsson, S. Hreinsdóttir, P. Einarsson, P. LaFemina, and R. A. Bennett (2010). The 2008 May 29 earthquake doublet in SW Iceland, *Geophys. J. Int.* **181**, 1128–1146.
- Donoho, D. L. (1995). De-noising by soft-thresholding, *IEEE Trans. Inform. Theor.* **41**, 613–627.
- Donoho, D. L., and I. M. Johnstone (1994). Ideal spatial adaptation by wavelet shrink-age, *Biometrika* **81**, no. 3, 425–455.
- Donoho, D. L., and I. M. Johnstone (1995). Adapting to unknown smoothness via wavelet shrinkage, *J. Am. Stat. Assoc.* **90**, no. 432, 1200–1224.
- Graizer, V. (1979). Determination of the true ground displacements by using strong motion records, *Izvestiya Phys. Solid Earth* **15**, 875–885.
- Graizer, V. (1989). Bearing on the problem of inertial seismometry, *Izvestiya Acad. Sci., USSR, Phys. Solid Earth* **25**, no. 1, 26–29.
- Graizer, V. (1991). Inertial seismometry methods, *Izvestiya Phys. Solid Earth* **27**, no. 1, 51–61.
- Graizer, V. (2005). Effects of tilt on strong motion data processing, *Soil Dynam. Earthq. Eng.* **25**, 197–204.
- Graizer, V. (2006). Tilts in strong motion, *Bull. Seismol. Soc. Am.* **96**, 2090–2102.
- Graizer, V. (2010). Strong motion recordings and residual displacements: What are we actually recording in strong motion seismology, *Seismol. Res. Lett.* **81**, no. 4.
- Graizer, V., and E. Kalkan (2008). Response of pendulums to complex input ground motion, *Soil Dynam. Earthq. Eng.* **28**, 621–631.
- Halldorsson, B., and R. Sigbjornsson (2009). The *M*_w 6.3 Olfus earthquake at 15:45 UTC on 29 May 2008 in South Iceland: ICEARRAY strong-motion recordings, *Soil Dynam. Earthq. Eng.* **29**, 1073–1083.
- Halldorsson, B., R. Sigbjornsson, A. Chanerley, and N. A. Alexander (2010). Near-fault strong-motion array recordings of the *M*_w 6.3 Olfus earthquake on 29 May 2008 in Iceland, in *Proc. of the 9th U.S. National and 10th Canadian Conference on Earthquake Engineering, paper 1157*, Toronto, Canada, 25–29 July.
- Halldorsson, B., R. Sigbjornsson, and J. Schweitzer (2009). ICEARRAY: The first small aperture, strong-motion array in Iceland, *J. Seismol.* **13**, no. 1, 173–178.
- Iwan, W. D., M. A. Moser, and C. Y. Peng (1985). Some observations on strong-motion earthquake measurements using a digital accelerograph, *Bull. Seismol. Soc. Am.* **99**, 1225–1246.
- Kalkan, E., and V. Graizer (2007). Coupled tilt and translational ground motion response spectra, *J. Struct. Eng.* **133**, no. 5, 609–619.
- Kinoshita, S. (2008). Tilt measurement using broadband velocity seismograms, *Bull. Seismol. Soc. Am.* **98**, no. 4, 1887–1897.
- Lang, M., H. Guo, J. E. Odegard, C. S. Burrus, and R. O. Wells Jr. (1996). Noise reduction using an undecimated discrete wavelet transform, *IEEE Signal Process. Lett.* **3**, no. 1, 10–12.

- Lee, W. H. K., T. C. Shin, K. C. Kuo, and C. F. Wu (2001). CWB free strong-motion data from the 21st Sept Chi-Chi, Taiwan, earthquake, *Bull. Seismol. Soc. Am.* **91**, 1370–1376, CD ROM.
- Lin, C.-H., H.-P. Huang, C.-C. Liu, and H.-C. Liu (2010). Application of rotational sensors to correcting rotation-induced effects on accelerometers, *Bull. Seismol. Soc. Am.* **100**, no. 2, 585–597.
- Mallat, S. (1989). A theory for multiresolution signal decomposition: The wavelet representation, *IEEE Trans. Pattern Anal. Mach. Intell.* **11**, no. 7, 674–693.
- Mallat, S. G. (2009). *A Wavelet Tour of Signal Processing*, Third Ed., Academic Press, Burlington, Massachusetts.
- Nigbor, R. L. (1994). Six-degree-of-freedom ground motion measurement, *Bull. Seismol. Soc. Am.* **84**, no. 2, 1665–1669.
- Pillet, R., and J. Virieux (2007). The effects of seismic rotations on inertial sensors, *Geophys. J., Int.* **171**, 1314–1323.
- Rupakhety, R., B. Halldorsson, and R. Sigbjornsson (2010). Estimating co-seismic deformation from near source strong motion records: Methods and case studies, *Bull. Earthq. Eng.* **8**, 787–811.
- Shensa, M. J. (1992). The discrete wavelet transform: wedding the a trous and Mallat algorithms, *IEEE Trans. Inform. Theor.* **40**, 2464–2482.
- Spudich, P., L. K. Steck, M. Hellweg, J. B. Fletcher, and L. M. Baker (1995). Transient stresses at Parkfield, California, produced by the *M* 7.4 Landers earthquake of June 28, 1992: Observations from the UPSAR dense seismograph array, *J. Geophys. Res.* **100**, 675–690.
- Todorovska, M. I. (1998). Cross-axis sensitivity of accelerographs with pendulum-like transducers, mathematical model and the inverse problem, *Earthq. Eng. Struct. Dynam.* **27**, 1031–1051.
- Trifunac, M. (1982). A note on rotational components of earthquake motions on ground surface for incident body waves, *Soil Dyn. Earthq. Eng.* **1**, no. 1, 11–19.
- Trifunac, M., and V. Lee (1973). Routine computer processing of strong motion accelerograms, *Earthq. Eng. Res. Lab.*, Report EERL 73-03, California Institute of Technology, Pasadena, California.
- Trifunac, M., and M. Todorovska (2001). A note on the usable dynamic range of accelerographs recording translation, *Soil Dynam. Earthq. Eng.* **21**, 275–286.
- Trifunac, M., V. Lee, and M. Todorovska (1999). Common problems in automatic digitisation of strong motion accelerograms, *Soil Dynam. Earthq. Eng.* **18**, 519–530.
- Trifunac, M. D. (1971). Zero baseline correction of strong motion accelerograms, *Bull. Seismol. Soc. Am.* **61**, no. 5, 1201–1211.
- Wang, G.-Q., D. M. Boore, H. Igel, and X.-Y. Zhou (2003). Some observations on collocated and closely spaced strong ground-motion records of the 1999, Chi-Chi, Taiwan, earthquake, *Bull. Seismol. Soc. Am.* **93**, no. 2, 674–693.
- Wong, H. L., and M. D. Trifunac (1977). Effect of cross-axis sensitivity and misalignment on response of mechanical-optical accelerographs, *Bull. Seismol. Soc. Am.* **67**, 929–956.
- Wu, Y.-M., and C.-F. Wu (2007). Approximate recovery of co-seismic deformation from Taiwan strong-motion records, *J. Seismol.* **11**, 159–170.
- Zahradnik, J., and A. Plesinger (2005). Long-period pulses in broadband records of near earthquakes, *Bull. Seismol. Soc. Am.* **95**, no. 5, 1929–1936.

University of East London
School of Architecture, Computing & Engineering
Dockland Campus, London E16 2RD
England
andrew2@uel.ac.uk
(A.A.C.)

Department of Civil Engineering
University of Bristol
Queens Building
Bristol BS8 1TR
England
(N.A.A.)

Canterbury Seismic Instruments Ltd.
University of Canterbury
149 Rutherford Building
Christchurch 8140
New Zealand
(J.B., H.A.)

Earthquake Engineering Research Centre
University of Iceland
IS-800 Selfoss
Iceland
(B.H., R.S.)

Manuscript received 8 September 2011

Electronic Supplement to

Concerning Baseline Errors in the Form of Acceleration Transients When Recovering Displacements from Strong Motion Records Using the Undecimated Wavelet Transform

by A. A. Chanerley, N. A. Alexander, J. Berrill, H. Avery, B. Halldorsson, and R. Sigbjornsson

This BSSA supplement presents additional results to those in the main paper. These additional results are for the Chi-Chi TCU068 (1999) station, the New Zealand Darfield Station (2010) and the ICEARRAY results from the Ölfus Earthquake (2008) in Iceland.

Acceleration transients for Chi-Chi TCU068

The 1999 Chi-Chi event from station TCU068 is considered first, the data for this is from the BSSA CD-ROM Lee, et al (2001), a very good and useful data set from the Chi-Chi 1999 event. A point to note is that the instrument used was the A900, which does not have an in-built low-cut filter, therefore retains the low frequency signals. The following discussion on the wavelet transform method however focuses only on the low-frequency, fling profile from which the acceleration transient is extracted.

Focusing on the wavelet transform method, then on applying wavelet *bior1.3* at decomposition level 10, we obtain as in **Figure S1** the TCU068NS low-frequency, fling superimposed before and after correction. It reveals a new and small, sharp triangular structure at time-point T_i , hidden in the latter portion of the low-frequency, strong-motion acceleration fling and whose numerical area is equal to a flat dc shift in velocity as per Boore *et al* (2002), in the latter portion of the velocity plot after the strong motion. This structure is more clearly shown in **Figure S2** for TCU068NS after the triangular area is subtracted-out from the corrected and uncorrected, low-frequency acceleration time history at $T_i (= 45.65\text{s})$. It shows quite clearly a sharp 9.57cm/s^2 , peak acceleration transient, or 'spike', which may be attributed to a tilt/ground rotation/torsion at time T_i , which as discussed in the 'Baseline correction and the acceleration spike' section and which on removal from the low-frequency, sub-band acceleration allows stable, double-time integration.

Figure S3 shows the (inverted) extracted peak acceleration transient of -6.75cm/s^2 at $T_i = 45.83\text{s}$ from the TCU068EW fling component and the dc velocity shift and displacement offset after double integrating the acceleration transient. The area of the acceleration transient is 5.65cm/s , which matches the constant velocity dc shift after the fling pulse of TCU068EW. The area under the dc shifted velocity curve is 255.65cm , which is the displacement error from the residual permanent displacement.

The vertical components of TCU068 doesn't show any need for baseline correction it showed only a small transient towards the end of the time history. Effectively this component integrates to displacement after filtering with the wavelet transform. Table 1 shows the estimates of the acceleration transients and their times of occurrence for TCU068 and TCU102 Chi-Chi event. The times T_i at which these transients occur are the time-points at which the baseline correction is applied and is therefore an important parameter.

Using the wavelet transform method, the peak instantaneous tilt angles calculated from the peak transient acceleration in **Table S1** are calculated as -6.9mrad (-6.75cm/s^2) (EW) and 9.8mrad (9.57cm/s^2) (NS) and the resulting dynamic tilt amplitude obtained is 12.09mrad (11.86cm/s^2). It is these peak acceleration transients, which are inferred as due to instantaneous tilt/rotation angles, that cause the dc shift in velocity in the latter portion of the time history and prevent stable double-time integration.

For comparison, Pillet and Vireaux (2007) obtained estimates of the average acceleration for TCU068,

from the velocity slopes of the last 30% from the velocity time histories of all components and removed these 'small jumps in the baseline of the acceleration' from the acceleration time history, as described in their paper. They then integrated the acceleration time history to obtain estimates of the displacements. The magnitude of these 'small jumps', were -0.049cm/s^2 for the vertical, 4.077 cm/s^2 for the NS and -3.446 cm/s^2 for the EW component and Pillet and Vireaux (2007) attributed these to tilt. The average accelerations using the wavelet transform method, estimated from the initial slope of the largely constant velocity dc shift in **Figure S2** and **Figure S3** for the NS and EW components is approximately 3.76cm/s and -3.21 cm/s^2 respectively. These are similar to those obtained by Pillet and Vireaux (2007). A comparison of estimates of the acceleration transients using the wavelet transform method with the method used by Pillet and Vireaux (2007) is given in **Table S1**. The values show a similar order of magnitude. Moreover, both methods show that the NS acceleration transient and the Pillet and Vireaux (2007) 'small jump' is greater than EW and the vertical component, the latter being the least significant in both cases.

Both methods give reasonable estimates of the displacements though the wavelet transform method gives estimates which are more comparable with GPS readings. Given that the methods are quite different and were applied to initially obtain the displacements, the degree of correlation between the offending acceleration transients and jumps is reasonable. The wavelet transform method however reveals a clear structure to the offending baseline error acceleration transient shown in **Table S1** and in **Figure S2** and **Figure S3** and gives stable double integration if the dynamic transient is removed from the acceleration time history or when the acceleration is zeroed from $t = T_i$.

Another point to make is that there may well be a tilt-time series, Graizer (1991, 2005), Trifunac (1971), Trifunac et al, (1999), Nigbor (1994, 2009), but when applying the wavelet transform, it is only in the low-frequency fling in the range $f = 0.1\text{Hz}$, towards the end of the strong motion, that the acceleration transient, the velocity dc shift and the displacement errors become apparent. Moreover, the acceleration transient is embedded in the low-frequency fling time history and not immediately obvious and has to be subtracted out from the low-frequency, acceleration time series. It is also likely that the higher frequencies present in the acceleration time series and separated out by the wavelet transform, may have also recorded some acceleration transients. However, it is concluded that any acceleration transients, trends and other outliers in the higher frequencies have been removed. This is because at the higher frequencies the final integration proceeds to an average, zero-velocity dc shift and an average, zero permanent displacement.

New Zealand Mw 7.1, Darfield Event, 4th Sept 2010

The Canterbury region on the South Island of New Zealand experienced a magnitude M_w 7.1 earthquake on the 4th Sept 2010. The epicentre was located about 10 km SE of the town of Darfield and about 40 km west of the city of Christchurch. The seismic event produced a right-lateral, strike-slip surface rupture = 28 km long, approximately west-east, **Figure S4**. Much damage occurred to residential buildings as well as a lot of liquefaction and lateral spreading. The situation however deteriorated further after a 2nd earthquake of M_w 6.3 hit, damaging the Christchurch city centre and with considerable loss of life. One hopes and prays that the residents of Christchurch people will overcome these tragic events.

New fling pulse examples are presented for N55W and the S35W components and the acceleration transient and displacement results from the Darfield earthquake as recorded on a 14-bit, CUSP-3B at the Greendale station, using the wavelet transform method. More displacement results obtained using the wavelet transform method is in Berrill *et al* (2011). **Table S2** gives a summary for all components of the Greendale Station. The horizontal displacements give a resultant of 183.6cm, which compares well with GPS at 189.79cm Berrill *et al* (2011), 1.6 km away. **Table S2** also gives estimates of the tilt acceleration transients taken at the fling zero-velocity time point, at which the correction is applied.

Figure S5 shows the low-frequency, sub-band for the N55W component, at level 10 decomposition and **Figure S6** shows the velocity and displacement responses after double integrating the extracted transient acceleration. **Table S2** also demonstrates that the vertical acceleration transient is small compared to the two horizontal components, as would be expected Graizer (2005) and may be a measure of the noise floor. It should be noted that as for the Chi-Chi station TCU068, level 10

decomposition has removed any post-fling perturbations in the fling acceleration and produced an almost sinusoidal time history. The zero-velocity, cross-over time-point is taken at time $T_i = 26.55\text{s}$ at the end of the fling, at which the correction is applied. The acceleration transient at that zero-velocity, cross-over point is 2.33cm/s^2 .

For the S35W component, the low-frequency time history showed a much distorted acceleration fling and was abandoned at level 10 decomposition. At level 9 decomposition on the other hand and as shown in **Figure S7** and after two threshold iterations, a reasonable strong motion fling is observed and post-fling perturbations with 3 zero-velocity cross-over points suggesting that more acceleration transients occurred (**Table S3**) further down the time series, but as before we use T_i at the end of the double-fling.

However in **Figure S8**, the low-frequency S35W component is shown after seven threshold iterations at level 9 decomposition and it is clear that most of the post-fling perturbations in the acceleration time history have been removed. This is in a sense equivalent to level 10 of decomposition, which unfortunately gave too much distortion. This time though only one acceleration transient is evident at 3.341cm/s^2 at time-point of 27.65s, which are almost the same values as in **Table S2** and **Table S3** for the two threshold iterations at level 9 decomposition, the final displacement too is almost unaffected. However, the velocity dc shift is considerably more at 7.23cm/s, indicating that the sum of the post-fling oscillations at two threshold iterations lowered the velocity dc shift.

It is argued here that there isn't any advantage to implementing so many threshold iterations. Indeed it may be disadvantageous because post-fling detail may yield additional information, such as the number of times the instrument tilted and in which direction of rotation. However, because the algorithm is almost automated and executes rapidly therefore it's worthwhile to sometimes experiment with different iteration thresholds. Finally, **Figure S9** shows the power plots for the S35W component, which demonstrate that at frequencies as low as 0.012Hz there is significant power in the low-frequency spectrum, with a peak at 0.21Hz.

Acceleration Transients for the ICEARRAY after the M_w 6.3 Ölfus Earthquake (29th May 2008), in the South Iceland Seismic Zone (SISZ)

The Icelandic Strong-motion Array (ICEARRAY), the first of its kind in Iceland, was installed in 2007 (Halldorsson et al., 2009) and has already produced a globally unique dataset of near-fault earthquake strong ground motion (Halldorsson & Sigbjörnsson 2009) during the magnitude 6.3 Ölfus earthquake in the SISZ at 15:45 on 29 May 2008. (see **Figure S10**). The array was designed as consisting of 14 stations with an aperture of approximately 1.9 km and minimum inter-element distance of 50 m. The recording system at each ICEARRAY station is a CUSP-3Clp strong-motion accelerograph unit manufactured by Canterbury University Seismic Project in New Zealand, for the Canterbury Network in New Zealand. The units are equipped with 24-bit, tri-axial, low-noise ($\sim 70 \mu\text{g rms}$) Micro-Electro-Mechanical (MEM) accelerometers with a high maximum range ($\pm 2.5 \text{ g}$) and a wide-frequency pass-band (0-80Hz at 200 Hz sampling frequency) (Halldorsson *et al.* 2009; Halldorsson and Avery 2009).

During the Ölfus earthquake on 29 May 2008 the ICEARRAY produced 33 components of near-fault earthquake ground accelerations (Halldorsson and Sigbjörnsson 2009). Estimates of coseismic ground displacements during this earthquake were first recovered in May 2009 using the wavelet transform method of Chanerley and Alexander (2010). The results show considerable permanent displacements at all stations along both NS and EW components (Chanerley *et al.*, 2009; Chanerley and Alexander 2010; Halldorsson et al. 2010; Rupakhety et al., 2010;). Here we present the full time-series of processed earthquake ground motion demonstrating the wavelet transform method for obtaining displacement estimates as well as the inferred tilt acceleration transients. Also included are the horizontal displacements obtained using the wavelet transform method in **Table S4**, which lists the NS and EW, permanent displacements obtained for the 11 ICEARRAY stations. A comparison of the displacement given in **Table S4** for station IS609, showing a resultant of 16.81 cm NW using the wavelet transform method, which is in reasonable agreement with estimates from continuous GPS station located 1.6 km away (Decriem et al. 2010: 19.90 cm NW). Using a quite different method based

on the work of Iwan, et al (1985) and Wu and Wu (2007) the results in Rupakhety et al., (2010) compare favorably with those obtained using the wavelet transform method and all listed in this paper for the 1st time.

Figure S11 shows the corrected acceleration, velocity and displacement for station IS604 EW as an example. The decomposition level is 7 with only one threshold iteration and in this case using *bior1.3*. This is a somewhat lower decomposition level than previous, probably due to a lower magnitude earthquake compared for example to that of the Chi-Chi event, as discussed in the 'Applying the Wavelet Transform' section. When using levels 8, 9 and 10 it was difficult to isolate a zero-crossing point as well as an optimal fling profile. Level 7 on the other hand, produced a clear fling from which the zero-velocity, cross-over time-point, $T_i = 20.21\text{s}$, is used to zero the acceleration at $t = T_i$ and re-integrate the fling, sub-band acceleration to give a sub-band velocity without a dc shift and a displacement without any linear/quadratic errors as shown in **Figure S12**. The acceleration transient is taken at the fling at $T_i = 20.21\text{s}$ and has a value of 18.6 cm/s^2 . As for the Chi-Chi records above, the higher frequency sub-bands didn't require baseline correction and double-time integrated normally. Level 7 includes a band of frequencies up to 0.78Hz , higher than for Chi-Chi TCU068.

Other stations for the EW component give similar results and all at level 7 decomposition and all time points, T_i , were measured at the optimal fling and all acceleration transients were removed at that point. This gave some consistency in analysis. The focus here is on the acceleration transient at the low-frequency fling, since it is from there that the correction for baseline shift is applied and the permanent displacement obtained. **Table S5** gives the complete list of acceleration transients obtained from each of the ICEARRAY stations. **Table S5** shows that the EW components have the largest initial acceleration transients, though most stations had several velocity zero-crossings. Station IS604 has for example an initial tilt of approximately 1 degree just after the velocity-fling. This is high compared to the NS component; moreover these components have several zero-crossing and therefore several possible acceleration transients. In a similar manner to Chi-Chi station TCU102, station IS604 shows, six zero-velocity, cross-over time points and each time point has an acceleration transient in the low-frequency acceleration, which contribute to the dc shift in velocity, their values and time-points are given in **Table S6** as an example. Their magnitudes diminish as shown in **Table S6** for station IS604, with a 1 cm change in displacement between the value on removing baseline error from the 1st transient and that on removing from the 6th transient and re-integrating to displacement.

The EW component of most stations had several zero-crossing points at level 7 with smaller acceleration transients further along the time history in much the same way as station IS604. Therefore any one of those could have been used by the algorithm and which also gave sensible displacement values. However, following Graizer (2005) a clear-cut fling profile of the velocity-pulse is used by the algorithm at which time-point the acceleration transient removed. The results also shows that the acceleration transients and their T_i times correlate well for each component for each stations, but that the NS transients are much lower in magnitude and similar to those of the vertical component and so can be attributed to noise. As discussed the much larger acceleration transients for the EW component may be indicative of tilts/rotations.

The results are consistent with the fact that the aperture of the ICEARRAY is as mentioned, small at 1.9 km, therefore perhaps it is right to expect some degree of correlation from such a close-knit array of sensors. This consistency in results does lend some weight to the fact that certainly in the EW component these transient accelerations may be due to tilts/rotations rather than to instrument malfunctions or noise. The results form a significant contribution to the discussions and conclusions from Boore, Stephens and Joyner (2002) and Trifunac and Todorovska (2001), Wang, et al (2003) and Graizer (2005) as discussed in section on 'Baseline correction and the acceleration spike' and in the 'Discussion' section.

Tables

▼ **Table S1.** Comparison of the estimated acceleration transients obtained by Pillet and Vireaux (2007) with that obtained using the wavelet transform method for Chi-Chi station TCU068.

Methodology due to:	TCU068NS	TCU068EW	TCU068V
Pillet and Vireaux (2007) (cm/s/s)	4.077	-3.446	-0.049
Chanerley and Alexander (2010) (cm/s/s)	9.57	-6.75	ignore

▼ **Table S2.** Estimates of the component accelerations transients and displacements and the time at which the transients and occurred at which baseline corrections were applied (Greendale station).

Component	Tilt Acc., (cm/s/s)	Time, (s)	Displacement, (cm)
N55W	2.33	26.55	-177.8 (Level 10)
S35W	3.44	28.56	-47.85 (Level 9)
UP	0.49	27.2	-66.5 (level 10)

▼ **Table S3.** Estimates of the acceleration transients and time of occurrence for the Greendale station, S35W. The velocity dc shift is 2.14 cm/s (Greendale station S35W).

Order of Tilt Acc	Tilt Acc., (cm/s/s)	Time, (s)
1st Tilt Acc.	3.44	28.56
2nd Tilt Acc.	-3.44	38.34
3rd Tilt Acc.	3.92	41.06

▼ **Table S4.** Estimates of permanent (horizontal) ground displacements at each ICEARRAY station that recorded the Ölfus earthquake in South Iceland on 29 May 2008.

Station	NS, (cm)	EW, (cm)	Resultant, (cm)	W(degrees)N
IS601	12.88	-9.98	16.3	53
IS602	14.93	-17.37	20.71	41
IS603	15.38	-13.62	20.55	49
IS604	15.58	-9.448	18.23	59
IS605	14.48	-11.61	18.56	52
IS607	15.36	-10.67	18.71	56
IS608	19.48	-9.73	21.78	64
IS688	17.36	-11.41	20.78	57
IS609	10.93	-12.76	16.81	41
IS610	9.173	-8.68	12.63	47
IS611	16.57	-14.77	22.2	49
Mean	14.74	-11.82	19.04	-

▼ **Table S5.** Estimates of three-component acceleration transients and their time of occurrence at each ICEARRAY station that recorded the Ölfus earthquake in South Iceland on 29 May 2008.

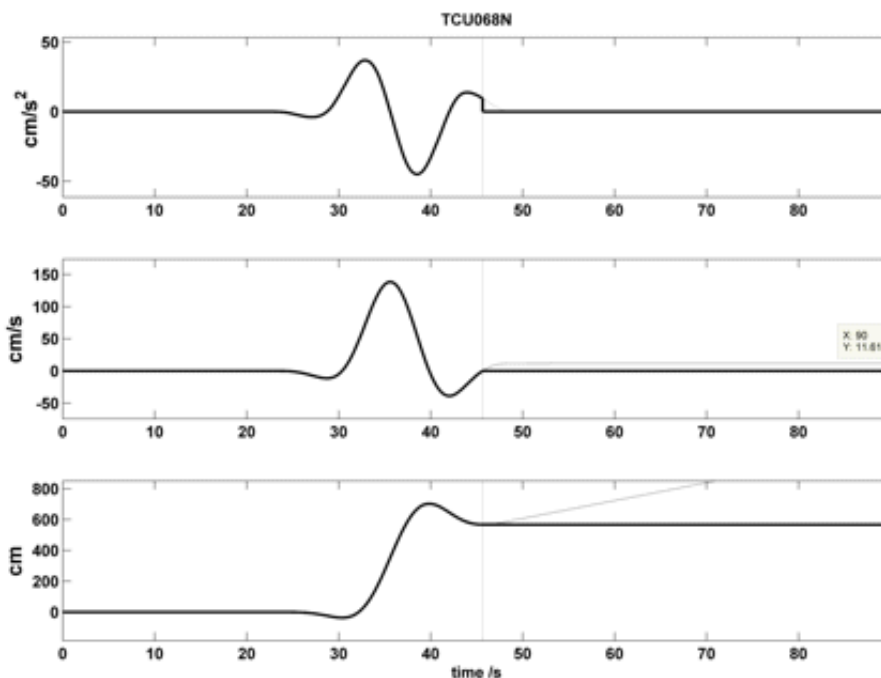
Station	N-S Tilt Acc, cm/s/s	N-S Time, s	E-W Tilt Acc, cm/s/s	E-W Time, s	V Tilt Acc, cm/s/s	V Time, s
IS601	-0.8894	19.54	14.71	20.26	0.8263	20.87
IS602	-3.194	18.95	26.14	20.29	-0.66	22.67
IS603	-3.014	19.14	20.6	20.29	-2.22	20.16
IS604	-3.503	19.04	18.6	20.21	-2.064	20.13
IS605	-2.861	19.21	15.52	20.29	-5.559	19.8
IS607	-2.804	19.27	23.24	20.28	-8.99	19.56

IS608	-2.758	19.45	16.42	20.30	-2.317	19.94
IS688	-2.936	19.34	15.72	20.30	-1.761	20
IS609	-2.052	19.00	9.18	20.23	-1.328	20.53
IS610	-1.119	19.15	2.8	22.27	-1.76	20.36
IS611	-2.456	19.38	12.9	20.32	-2.001	20.36
Mean	-2.51	19.23	15.99	20.46	-2.54	20.4
Std. Dev.	0.84	-	6.74	-	2.63	-

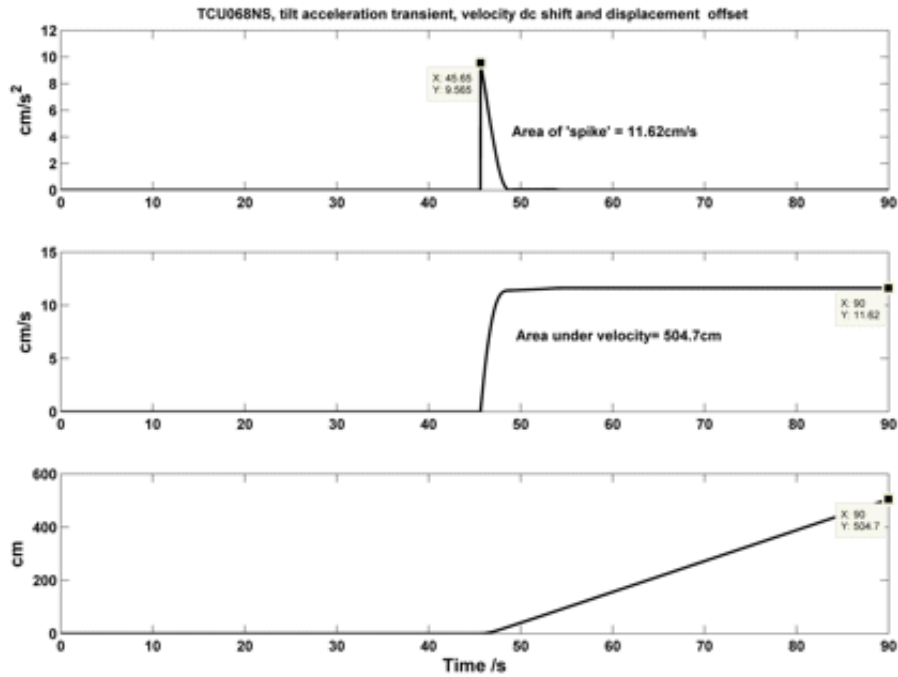
▼ **Table S6.** Estimates of the 6 tilt-acceleration transients and their time of occurrence for the EW component of station IS604. (Station IS604 EW).

Order of Tilt Acc.	Acc., cm/s/s	Transient, s
1st Tilt Acc.	18.6	20.21
2nd Tilt Acc.	-13.23	21.41
3rd Tilt Acc.	5.9	22.29
4th Tilt Acc.	-7	23.11
5th Tilt Acc.	2.45	24.19
6th Tilt Acc.	-1.98	24.64

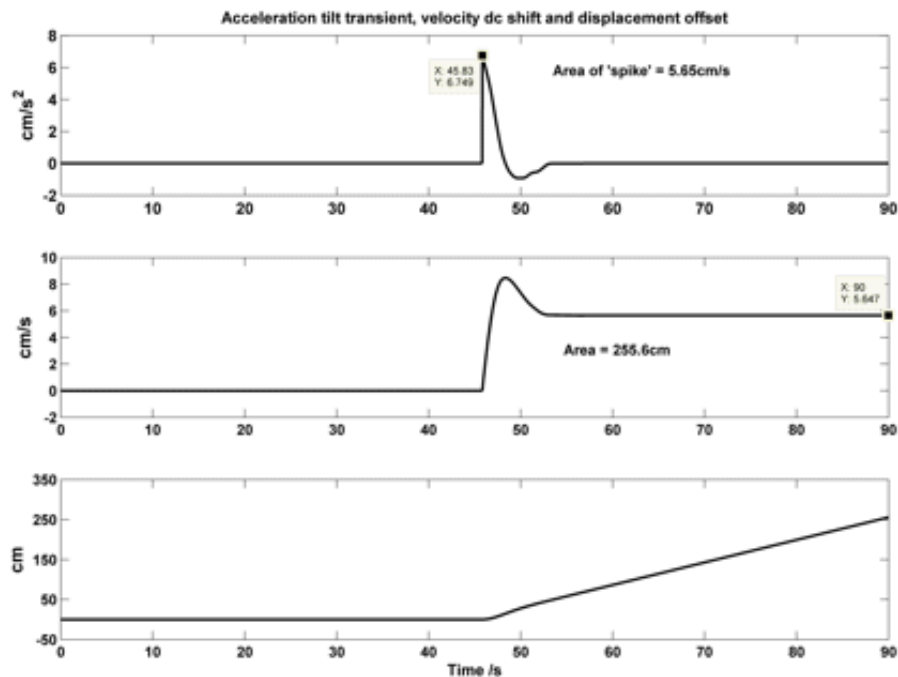
Figures



▲ **Figure S1.** TCU068NS low-frequency sub-band, fling, which shows results before (light gray) and after (black) baseline correction. The triangular area in the acceleration is the results of an acceleration transient g_f at 45.65s. The resulting constant velocity dc shift of 11.61 cm/s is shown in light gray as a post shaking, flat velocity time history



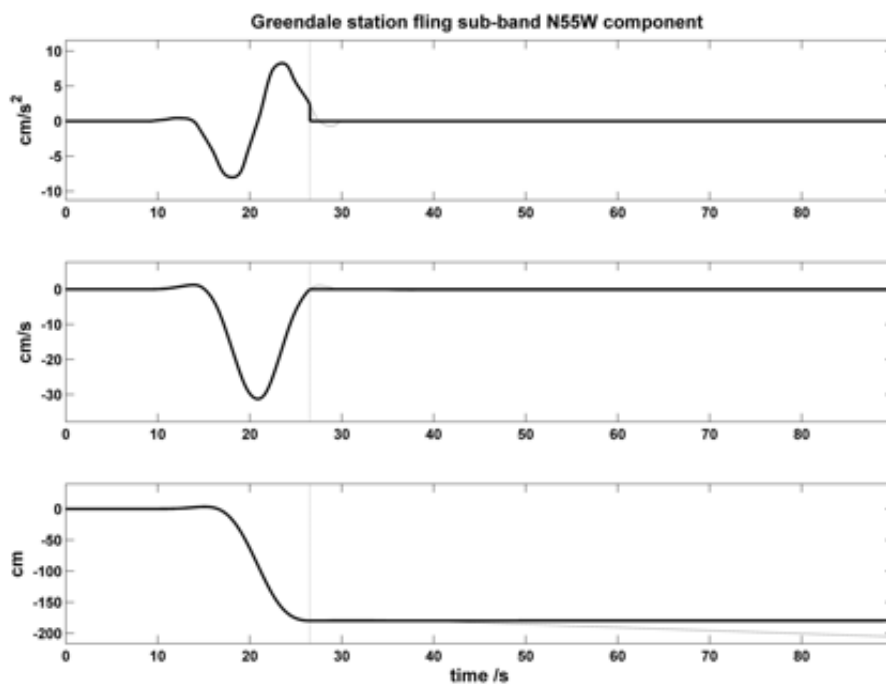
▲ **Figure S2.** Acceleration Tilt transient for TCU068NS at 45.65s. The resulting constant velocity dc shift of 11.61cm/s is a clear example of a post shaking, flat velocity time history (Boore *et al* (2002))



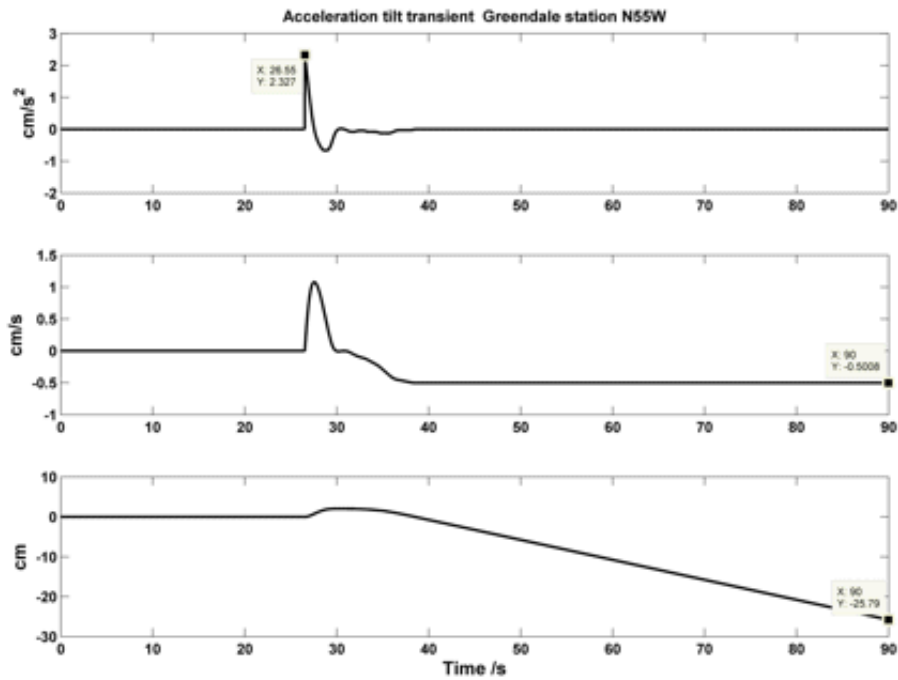
▲ **Figure S3.** Acceleration tilt transient (inverted) at 45.83s and 6.749cm/s/s, velocity and displacement response after integration of acceleration transient, for the TCU068EW component using instrument (A900)



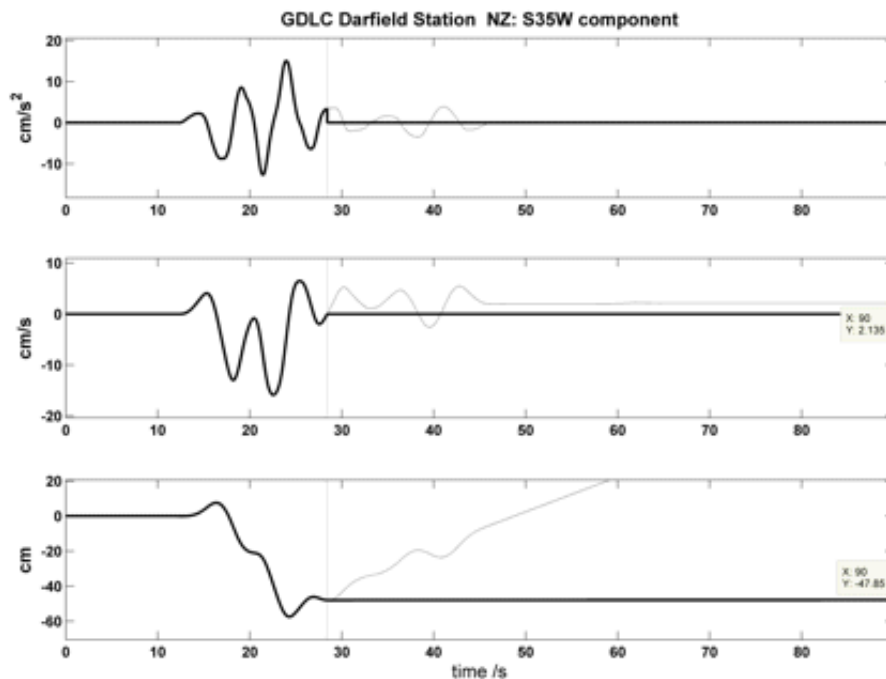
▲ **Figure S4.** Aerial shot of the Christchurch area showing the surface fault rupture and the epicentre of the Darfield EQ the image is about 117 km across.



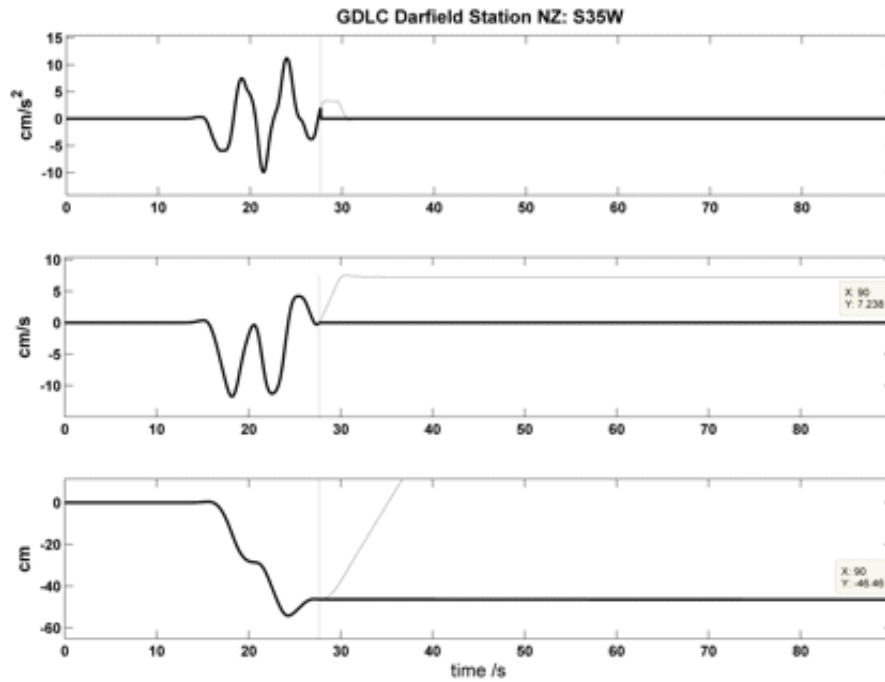
▲ **Figure S5.** N55W component time-series, bior1.3 wavelet, at decomposition level 10, showing low-frequency fling with a (tilt) acceleration transient of 2.33 cm/s/s at 26.55 s giving a velocity dc shift of -0.5 cm/s and a displacement offset of 25.8 cm . Instrument is CUSP 3B



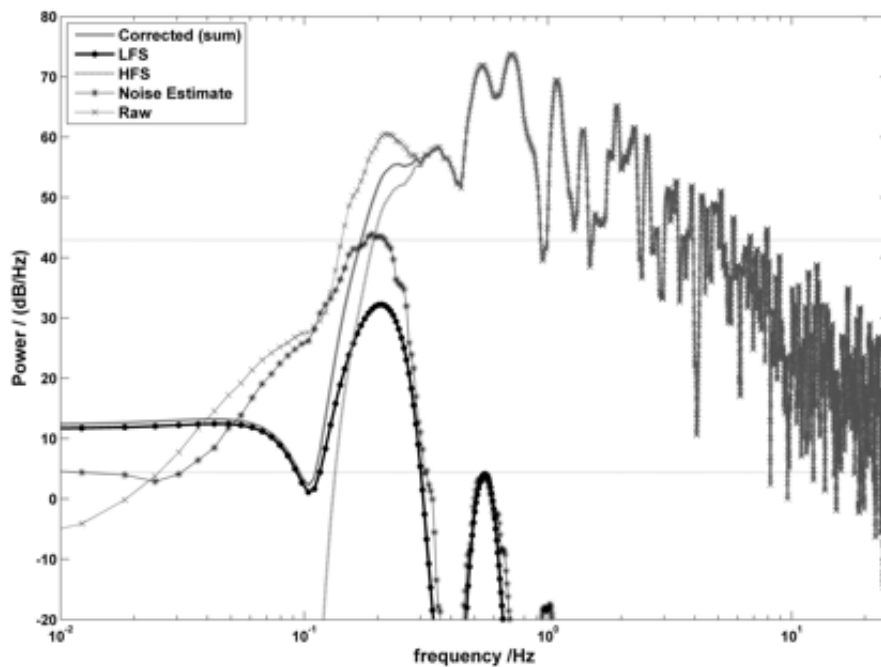
▲ **Figure S6.** Acceleration tilt transient at 26.55s and 2.33cm/s/s, a velocity dc shift of -0.5cm/s and displacement response after integration of acceleration transient for the N55W Greendale component using a CUSP instrument



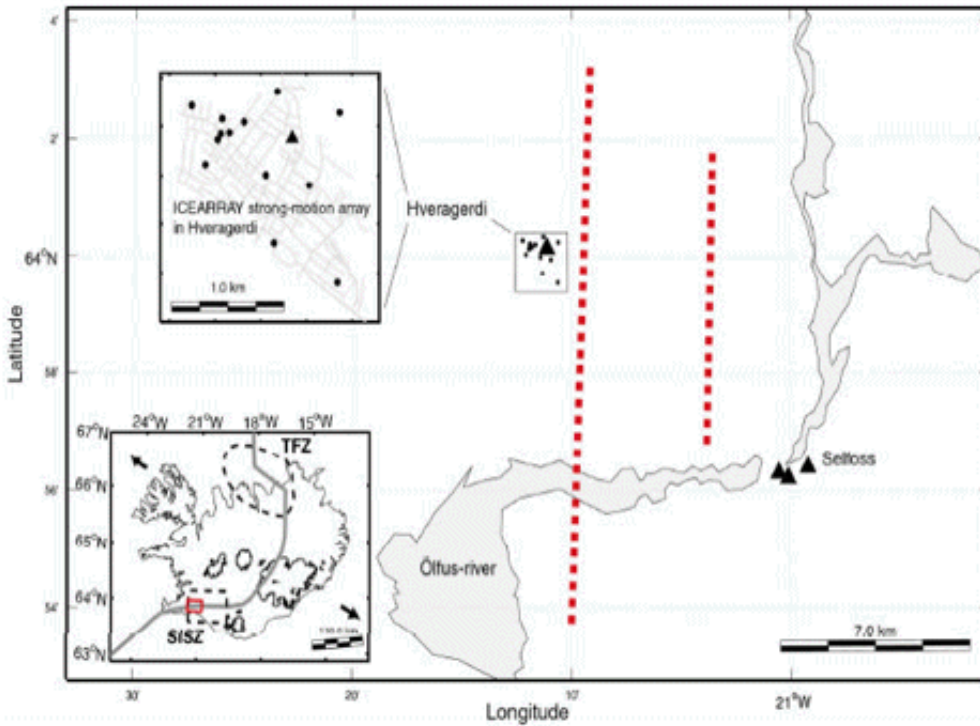
▲ **Figure S7.** S35W component time-series, at decomposition level 9, after 2 x threshold iterations, showing low-frequency fling and post-fling perturbation, with the first (tilt) acceleration transient of 3.54cm/s/s at 28.56s. The resulting velocity dc shift is 2.135cm/s. Two other possible acceleration transients at 2 x more velocity zero-crossing points are shown and listed in **Table S3**. Instrument is the CUSP 3B and the displacement is -47.85cm.



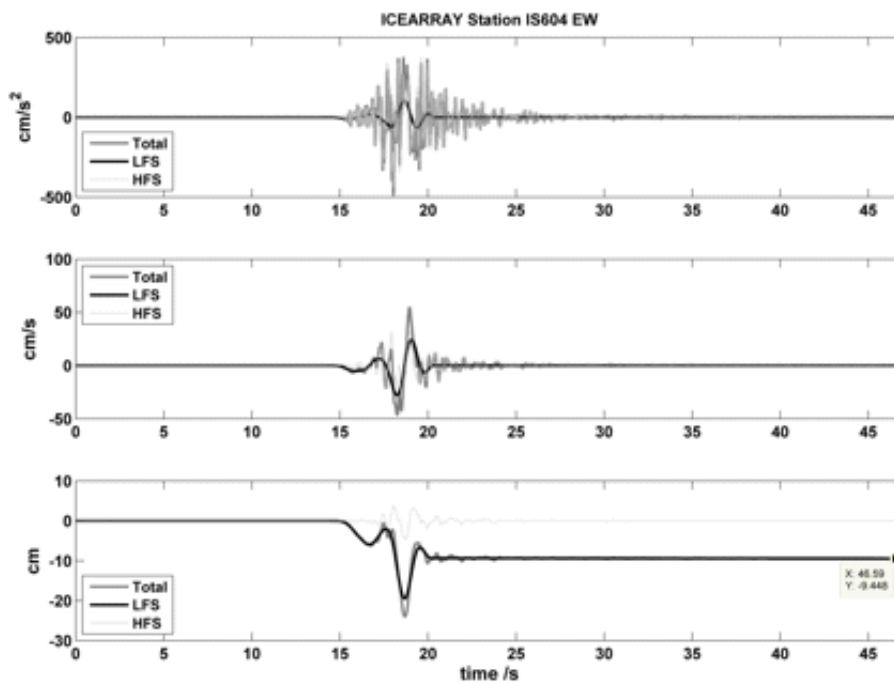
▲ **Figure S8.** S35W component time-series, at decomposition level 9, after 7 x threshold iterations, with almost all post-fling perturbations removed. The plots show a low-frequency fling with only one (tilt) acceleration transient of 3.341 cm/s/s at 27.65 s . The resulting velocity dc shift is 7.24 cm/s . The permanent displacement is -46.46 cm .



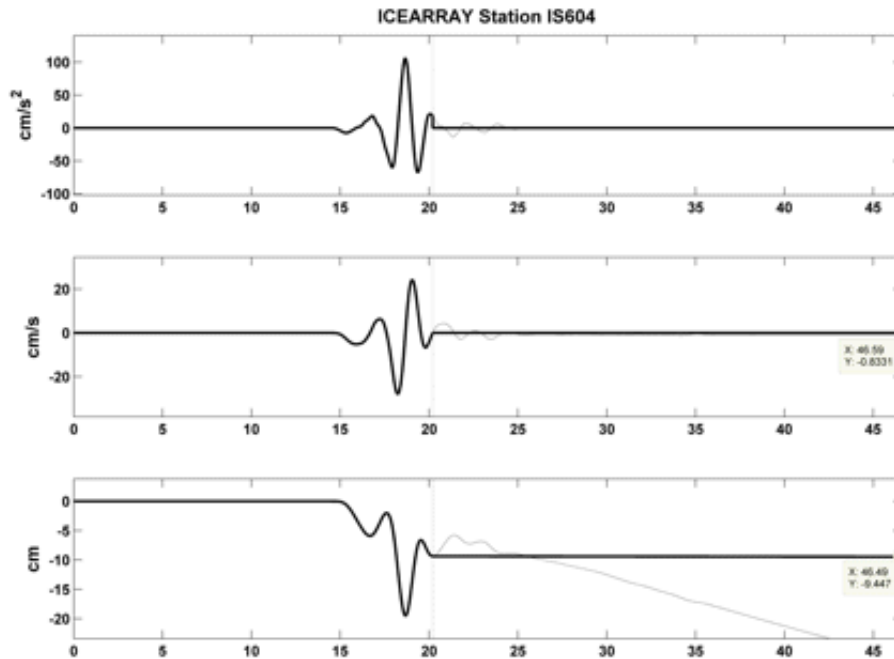
▲ **Figure S9.** S35W component power plots showing significant low-frequency power, down to 0.012 Hz and a low-frequency power peak at 0.21 Hz .



▲ **Figure S10.** The Ölfus earthquake of 29 May 2008 in South Iceland. The map indicates the macro-seismic area of the Ölfus earthquake which occurred on two separate but parallel north-south trending faults (red dashed lines) as outlined by the extent of aftershock activity. Of the two towns Selfoss and Hveragerdi closest to the earthquake faults, the town of Hveragerdi suffered the largest earthquake ground motion during the earthquake. The ICEARRAY stations in Hveragerdi are shown by black dots and a triangle (triangles denote stations of the Icelandic Strong-motion network). The small map inset at top left shows a close-up of Hveragerdi with the street-layout of the town shown as gray lines. For reference, the small map inset at bottom left shows Iceland in reference to the present-day Mid-Atlantic Ridge extensional plate boundary (gray line) between the North American and Eurasian tectonic plates, respectively. Major transform zones are indicated with black dashed lines. The earthquake occurred in the Ölfus district, marked with the solid red rectangle within the SISZ.



▲ **Figure S11.** Corrected low-frequency sub-band (LFS) fling and higher frequency sub-bands (HFS) and the resulting total using *bior1.3* for ICEARRAY station IS604, EW component obtained at level 7, with a displacement of -9.448cm, with a time point at 20.21s.



▲ **Figure S12.** ICEARRAY Station IS604 EW, low frequency sub-band (LFS): showing results before and after baseline correction. The triangular area in the acceleration is the results of g_f acceleration tilt transient taken at 20.21s. The resulting constant velocity dc shift (-0.833cm/s) is shown and the linear displacement offset. The velocity time series shows 6 zero-velocities, cross-over points, suggesting 6 tilt acceleration transients in the low-frequency, fling space; these are given in **Table S6**.

[**Back**]

Obtaining estimates of the low-frequency ‘fling’, instrument tilts and displacement timeseries using wavelet decomposition

A. A. Chanerley · N. A. Alexander

Received: 11 December 2008 / Accepted: 30 July 2009
© Springer Science+Business Media B.V. 2009

Abstract This paper proposes a novel, wavelet-based algorithm, which by extracting the low-frequency fling makes it possible to automatically correct for baseline shift and re-integrate down to displacement. The algorithm applies a stationary-wavelet transform at a suitable level of decomposition to extract the low frequency fling model in the acceleration time histories. The low frequency, acceleration fling should be as close as possible to the theoretical type A model, which after correction leads to a pulse-type velocity and ramp-like displacement after first and second integration. The wavelet transform essentially decomposes the seismic record using maximally flat filters and these together with a de-noising scheme form the core of this approach, which is to extract the lower and higher frequency sub-band acceleration, velocity and displacement profiles and correct for baseline shift. The correction automatically selects one time point from the low-frequency sub-band and then zeros the acceleration baseline after the fling. This implies pure, translation without any instrument tilts. Estimates of instrument tilt angles are also obtainable from the wavelet transformed time history as well as estimates of signal-to-noise ratios. The acceleration data used in this study is from station TCU068 in the near-fault region of the Chi-Chi, Taiwan, earthquake of 20th September 1999.

Keywords Correction · Seismic · Wavelet transform · Integration · Acceleration · Velocity · Displacement · Chi-Chi · Fling · Decomposition · Reconstruction

1 Introduction

Strong ground motions at near-fault sites may contain low frequency, pulse type waves which induce substantial permanent ground deformation. Standard filtering methods

A. A. Chanerley (✉)
School of Computing & Technology, University of East London, London, UK
e-mail: andrew2@uel.ac.uk

N. A. Alexander
Department of Civil Engineering, University of Bristol, Bristol, UK
e-mail: Nick.Alexander@bristol.ac.uk

(Trifunac et al. 1999; Trifunac 1971) cannot extract such permanent displacements of the ground from acceleration time-histories. This is partly because the low frequency acceleration may be buried in noise of similar magnitude, making it hitherto difficult to extract the long period information using standard filtering methods. It is proposed and shown that the wavelet transform overcomes some of the problems associated with obtaining low frequency, pulse type waves. The wavelet transform (Debauchies 1992) has been used (Chanerley and Alexander 2008, 2007) for de-noising the seismic record prior to de-convoluting the instrument response. The wavelet transform has also been used (Chen and Loh 2006) in order to implement baseline correction scheme and consequent estimates of permanent displacement of some Chi–Chi seismic recordings. A three-phase procedural approach is used in Iwan et al. (1985), but the approach is still involved requiring selection processes at the various phases, their results compare favourably with GPS readings.

Other recent work in Wu and Wu (2007) compares estimates of displacement obtained through first and second integration's from the Chi–Chi events with those of GPS readings taken near the sites of the strong-motion recordings. In order to obtain reasonable estimates of displacements a baseline correction procedure has been required. Thus approximate methods have been used in order to correct for baseline shift and then integrate for velocity and integrate again for displacement. Most of the approximate baseline correction schemes have been based on a two-point scheme proposed in Iwan et al. (1985) with modifications proposed by Boore (2001) and Boore and Bommer (2005). A good corrected displacement history is similar to a ramp function (Wu and Wu 2007) between two points suitably chosen. However, the limitation of all of the above methods is that they cannot extract the low-frequency fling and the choice of different time points can lead to considerably different estimates of final different displacements. The difficulty is that a standard and automated procedure for the correction of baseline-shift has not hitherto existed. This paper aims to show an approach, which corrects automatically for the baseline-shift occurring in seismic records and extracts the fling.

The paper proposes a novel wavelet-based algorithm for the routine processing of seismic data, in particular near-fault, strong-motion data. The method provides a scheme for straightforward and automated baseline correction of the acceleration and its integration to stable and unbiased estimates of velocity and displacement. The method also demonstrates that the wavelet transform extracts completely naturally the low-frequency fling that appears in near-fault velocity time histories, a phenomenon caused by the earthquake. In order to demonstrate the utility of the method, the seismic record TCU068 from the 1999 Chi–Chi event, shown in Fig. 1, has been used.

The paper shows that the application of wavelet transform filters extracts the low-frequency, sub-band fling by applying filter banks for decomposition and reconstruction. The wavelets also give depth of decomposition such that an optimal estimate of fling and thus consequent displacement is obtained. Moreover the method need not be transform specific, though the choice of transform is guided by linear phase requirements. In some cases the wavelet transform can automatically correct for baseline shifts and extract the fling, in other cases a straightforward correction can be applied which relies only on improving the extracted long-period fling and pulse-like velocity and therefore removes some of the decisions in the published methods of Chanerley and Alexander (2008, 2007), Chen and Loh (2006), Wu and Wu (2007), Iwan et al. (1985), Boore (2001), Alexander et al. (2001) and Chanerley and Alexander (2002). It is a simplified procedure for baseline correction, which makes it easier to integrate to displacement. The displacements are compared with GPS readings and the initial results are encouraging.

Figure 2 shows a comparison of existing and the proposed approaches. The raw acceleration is twice integrated to produce a displacement timeseries that is grossly in error. As a

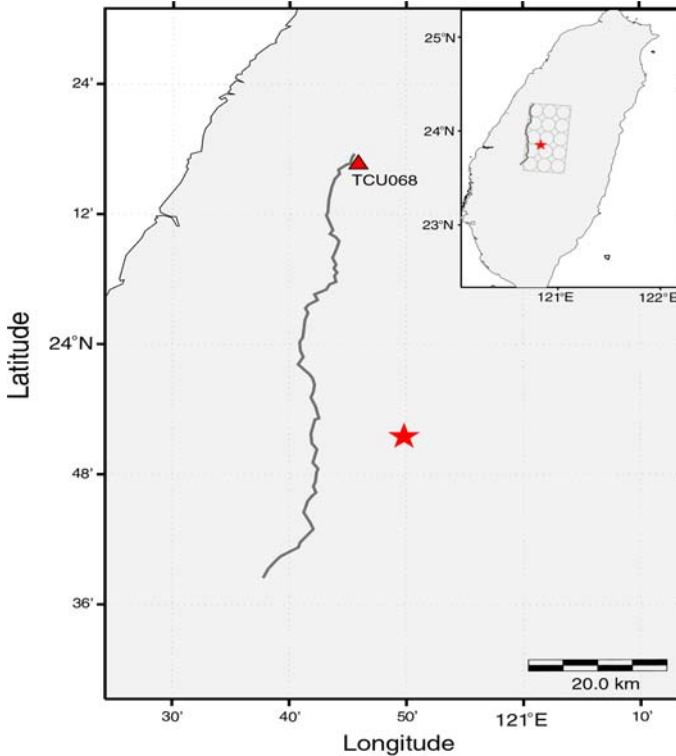


Fig. 1 A zoom of the epicenter (*star*) of the magnitude 7.6 Chi-Chi, Taiwan, earthquake of 20 September 1999 and the associated fault trace of surface rupture (“*irregular*” line). The *triangle* at the northern end of the fault indicates the extreme near-fault location of the recording station TCU068, the data of which is the topic of this study. The *inset* map at top right shows a wider view of Taiwan where the *gray rectangle and circles* show the extent of the fault plane of the Chi-Chi earthquake as assumed by Halldorsson et al. (2009) and the respective sub-events of the specific barrier model of the earthquake

comparison a standard low-cut filters of 0.02, 0.05, and 0.1 Hz are passed over the acceleration timeseries before double integration. The results are better; however, the filters unfortunately remove the fling component that is a low-frequency phenomenon. A piecewise linear detrend is applied to the acceleration and velocity timeseries by defining two breakpoints. This procedure is similar to Iwan et al. (1985) and Boore (2001). Note that without nuancing these breakpoints, as in Iwan et al. (1985) and Boore (2001), the results can be no better than employing filters. The proposed scheme recovers the fling phenomenon and estimates the permanent displacement at the end of the record.

2 Components of accelerogram records

2.1 The fling model

In the 1970s Bolt (1971, 1975) identified coherent ground velocity pulses radiating from a rapidly slipping fault gives rise to a wave pattern called fling. Bertero et al. (1976, 1978), showed that the near source destructive ground motions were due to the low frequency

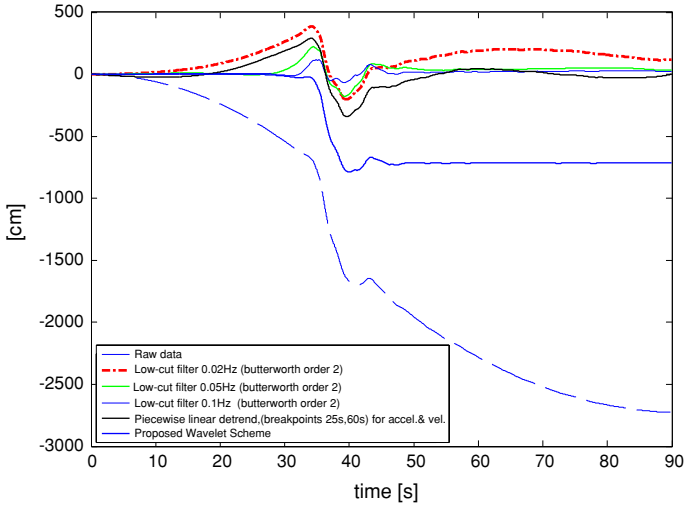


Fig. 2 Comparison of existing correction techniques with proposed wavelet scheme for TCU068EW component

acceleration ground pulses. The model fling pulse parameters are related by the following (Veletsos et al. 1965; Makris 1997; Makris and Black 2003) Eq. (1)

$$\ddot{s}(t) = A \sin\left(\frac{2\pi(t - t_1)}{T}\right), \quad T = t_2 - t_1, \quad t_1 \leq t \leq t_2 \quad (1)$$

for the sine, type A fling model, where, $s(t)$ is the ground displacement time-series, t_1 and t_2 are the start and stop times and T is the duration of the acceleration sine.

For the cosine type B type fling model the expression is similar

$$\ddot{s}(t) = A \cos\left(\frac{2\pi(t - t_1)}{T}\right), \quad T = t_2 - t_1, \quad t_1 \leq t \leq t_2. \quad (2)$$

Integration of the above equations gives the type A and type B profiles for velocity and displacement. The sine type A and cosine type B are shown in Figs. 3 and 4.

The profile is type A where the acceleration is shown as a sine pulse, leading to a one-sided velocity pulse and ramp-like displacement. This means that the displacement retains its permanency and doesn't recover. The type B cosine profile leads to a two-sided velocity profile where the displacement recovers. In the profiles analyzed in this paper from the Chi-Chi 1999 event, the wavelet transform extracts mainly type A profiles in the lower frequency sub-band and type B profiles in the higher frequency sub-band. The latter are summed with the former and give rise to an estimate of the local ground motion.

2.2 Influence of instrument tilts

It is reported and discussed in Boore (2001) and Graizer (2005) that instrument and/or sensor tilting causes baseline shifts in acceleration and velocity, in particular in the long period which leads to offsets in the final displacement. Moreover Graizer (2005) has demonstrated displacement offsets using numerical simulations, by contaminating the Hector Mine seismic data with artificial instrument tilts of 0.1° (1.75 mrad). The simulation [in Fig. 4 of Graizer

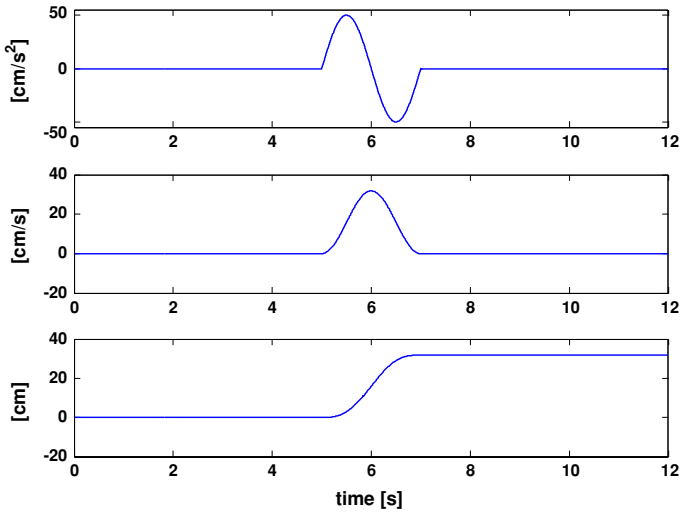


Fig. 3 Sine model of type A fling profiles. Type A fling leaves a permanent displacement

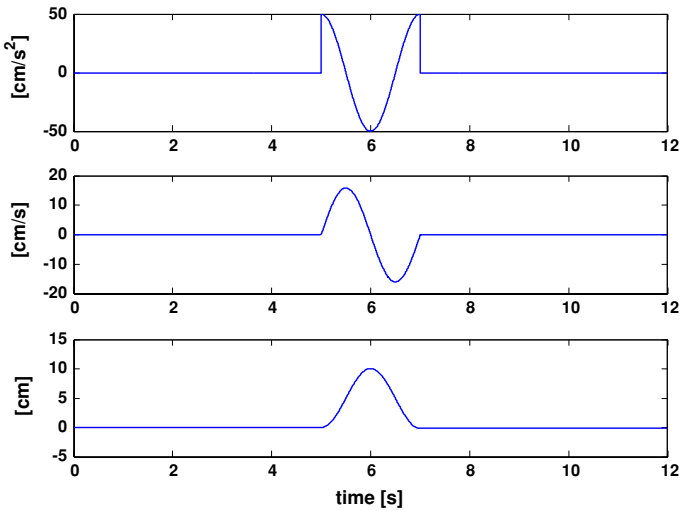


Fig. 4 cosine models of type B fling profiles. Type B fling leads to a recovery in displacement

2005] showed that the contaminated Hector Mine data had a similar profile in the displacement, to that of an actual displacement from the Chi–Chi TCU068 data discussed in the results of Sect. 5. We show therefore that after processing the seismic data using the wavelet transform, the angle of tilt can be estimated.

The approximate equations (Graizer 2005) which describe small tilt angles are as follows,

$$\ddot{a}_1 + 2\mu_1\omega_1\dot{a}_1 + \omega_1^2 a_1 = -\ddot{x}_1 + g\psi_2 + \varepsilon \tag{3}$$

$$\ddot{a}_2 + 2\mu_2\omega_2\dot{a}_2 + \omega_2^2 a_2 = -\ddot{x}_2 + g\psi_1 + \varepsilon \tag{4}$$

$$\ddot{a}_3 + 2\mu_3\omega_3\dot{a}_3 + \omega_3^2 a_3 = -\ddot{x}_3 + \varepsilon \tag{5}$$

where (a_1, a_2, a_3) are the recorded responses of the accelerometer, $(\omega_1, \omega_2, \omega_3)$ are its natural frequencies, (μ_1, μ_2, μ_3) are its ratios of critical damping, g is the acceleration due to gravity, (ψ_1, ψ_2) are the rotation of the ground surface about horizontal basis (i.e., roll and pitch), $(\ddot{x}_1, \ddot{x}_2, \ddot{x}_3)$ are the actual translational ground accelerations, in the Easterly, Northerly and Vertical directions respectively, and ε is the instrument noise timeseries.

The conclusions from the above equations are that the two horizontal sensors are responding to horizontal acceleration and tilts (pitch and roll) and that the vertical sensor is responding to vertical acceleration only. The yaw rotation has only a second order effect on the accelerograms, as do axes cross-coupling terms (Graizer 2005). Using the results presented, it is demonstrated that the tilt angle can be estimated from the lower frequency sub-band displacement offsets after the wavelet operation, but before correction for baseline shift is applied. The wavelet transform does not remove the tilt, but it makes it easier to adjust for the final imposed residual tilt. Estimating this final imposed residual tilt angle allows the baseline shift to be corrected more precisely.

According to Graizer (2005) the following conditions (repeated below) are necessary in order to extract the true displacement from real accelerograms:

- (i) The input ground motion must be purely translational, without any tilting or any other natural distortion.
- (ii) The record must contain clear beginning and ending parts with relatively small amplitudes to allow baseline correction.
- (iii) The signal to noise ratio (SNR) must be high enough at least 40 dB.

From the Chi–Chi (1999) records condition (i) is difficult to obtain without correction. When applying the proposed wavelet scheme (without baseline tilt correction) a large displacement offset can be observed at the end of the record, as discussed in the result Sect. 5. This is consistent with simulations shown in Graizer (2005) and is due to residual instrument tilt. Therefore, in this case condition (ii) is implicit in that small amplitudes exist in both the acceleration and velocity time histories and require baseline correction in order to approximate pure translation. Condition (iii) requiring a SNR of 40 dB is optimistic, the SNR found were much less than that required in Graizer (2005). It is shown in this paper that, using only the lower frequency sub-band (timeseries) extracted by the wavelet transform, it is possible to approximate the pure translational ground motion.

3 Employing the wavelet transform

3.1 Optimal filter banks

The wavelet transform may be considered as a set of complementary low-pass and band-pass filters, which can convolute and down sample by a factor of 2, a noisy signal by successively applying the filters. Effectively the process decomposes, i.e., halves the frequency band each time (hence the name dyadic sampling) creating sub-bands. Each time it applies a low-pass filter bank it decomposes the transition band by a factor of 2 moving to lower sub-band frequencies at each level of decomposition. A similar argument applies to the band-pass filter banks for the shorter period parts of a signal.

Moreover the method takes the discrete wavelet transform (DWT) (Debauchies 1992) of a signal, and passes the transform through a threshold (Coifman and Donoho 1995; Donoho 1995), which de-noises the signal. Reconstruction is the inverse process of decomposition, which up samples by a factor of 2 and applies low-pass and high pass filter banks. For the

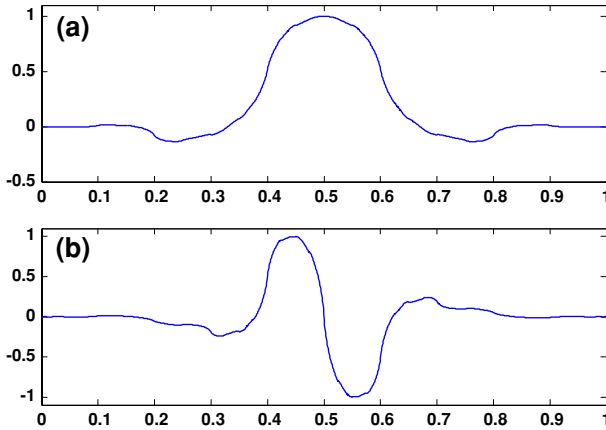


Fig. 5 **a** The *bior1.3* scaling function and **b** *bior1.3* Wavelet

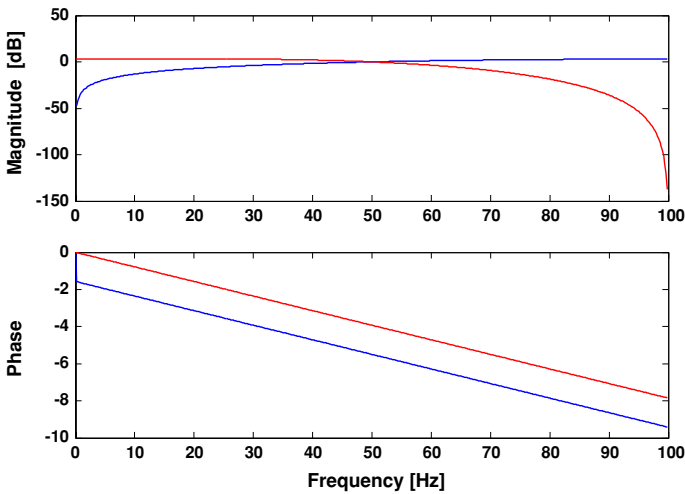


Fig. 6 Wavelet *bior1.3* associated low pass and high pass filters and their phase. Note that these QMFs are maximally flat

events used in this paper wavelets *db2* (Daubechies wavelet order 2), and *bior1.3* (Bi-orthogonal wavelet, order 1 associated filter length 3) were tried, though similar results were obtained for some of the other wavelets. However, *bior1.3* is the wavelet of choice since one of its properties is linear phase. The dimensions of the wavelet coefficients after low-pass filtering will be large compared to those of the noise coefficients obtained after high pass filtering. Therefore after thresholding the noise in the wavelet domain, the inverse DWT will retrieve the desired signal with little loss of important detail. Figure 5 show the scaling and wavelet functions for *bior1.3*. Figure 6 display the quadrature mirror filters (QMF) associated with *bior1.3*; these are maximally flat low pass and high pass filters and have linear phase.

The forward wavelet transform of a set of data comprises successive down sampling by a factor of 2, then filtering the data with low and high-pass filter coefficients. The filters used for this purpose are FIR (Finite Impulse Response) filters of order N , called quadrature

mirror filters (QMF). These have mirror image symmetry in both magnitude and phase about the frequency $\pi/2$. The transfer functions relating such filters are given by

$$H_1(z) = H_2(-z). \quad (6)$$

For example, $H_1 = 1 + z^{-1}$ and $H_2 = 1 - z^{-1}$ form a QMF pair, with coefficients $[1, 1]$ and $[1, -1]$. The Daubechies filters of order $N = 2$ will filter in the forward direction and then down sample by 2. The forward FIR, decomposition, QMF filter-pair coefficients, are given by:

$$\text{Decomposition low-pass coefficients} \quad [c_3 \ c_2 \ c_1 \ c_0] \quad (7)$$

$$\text{Decomposition high-pass coefficients} \quad [-c_0 \ c_1 \ -c_2 \ c_3] \quad (8)$$

and the reconstruction filter coefficients are given by:

$$\text{Reconstruction low-pass coefficients} \quad [c_0 \ c_1 \ c_2 \ c_3] \quad (9)$$

$$\text{Reconstruction high-pass coefficients} \quad [c_3 \ -c_2 \ c_1 \ -c_0] \quad (10)$$

where the c_i are the filter coefficients of the QMF pairs. The reconstruction filters are used after up sampling by a factor of 2 in order to reconstruct the signal after it has been de-noised. Though this scheme was used to ascertain a measure of the noise performance, it was not initially required to explicitly reconstruct the de-noised acceleration time histories. Rather the decomposed lower and higher frequency sub-band acceleration time histories were used separately for the first and second integration and for correcting low frequency baseline shifts. The QMF filters are maximally flat in the pass-band and it is these filters together with thresholding, which gives this method its measure of success.

3.2 The stationary wavelet transform (SWT)

Unfortunately the DWT is not translation invariant. This implementation, for denoising, uses the stationary or translation invariant wavelet transform (SWT) (Coifman and Donoho 1995). This essentially applies a range of signal shifts to allow for misalignment of the signal and wavelet features, it then averages out the shifts in order to obtain the de-noised signal.

The problems with shift-invariance are connected with the alignment between features in the signal and features of the wavelet basis. In particular at discontinuities where Gibbs-like phenomena can occur with unwanted oscillations. An approach to surmount this problem is described in Coifman and Donoho (1995) where it is suggested to forcibly shift the signal, so that its features change positions in relation to the wavelet basis. Then to un-shift and retrieve the de-noised signal hopefully without any unwanted noise or spurious oscillation. Following the arguments of Coifman and Donoho (1995) the procedure is an average of (1) shifting, (2) denoising, and (3) un-shifting.

Figures 7 and 8 show a wavelet decomposition tree. At each level of decomposition lower and higher frequency components are separated. The resulting low frequency component is further decomposed showing the lower frequency pulse type signal with greater clarity as we move to lower levels of the decomposition tree.

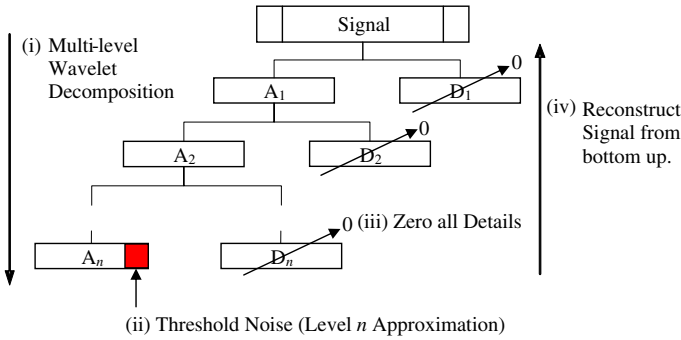


Fig. 7 Identifying lower frequencies sub-band (LFS) using multi-level wavelet decomposition

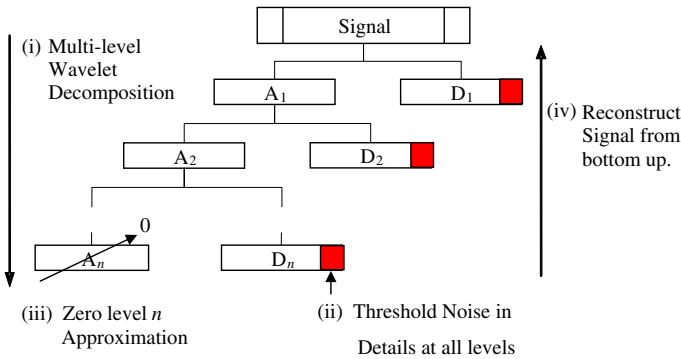


Fig. 8 Identifying higher frequencies sub-band (HFS) using multi-level wavelet decomposition

4 The proposed algorithm

4.1 Wavelet selection

Intuitively a choice of scaling function, associated with low-pass decomposition filters, which has the closest resemblance to the low frequency, fling of Fig. 3, should give good low frequency acceleration. In fact most of the scaling functions of the Daubechies wavelets bear some resemblance to the acceleration fling model.

However, it should be clear that ultimately the reasonable results are due to the maximally flat decomposition low-pass and high-pass filters, the non-linear scaling and the thresholding. These are the properties, which determine the usefulness of this method and give a better insight into the profile of the earthquake, as well as making the task of correcting for baseline shifts somewhat easier, in particular at long periods.

4.2 Wavelet decomposition of signal

The classical multi-level wavelet de-noising scheme involves (1) decomposition down to level n as shown in Fig. 7, (2) soft-thresholding of the decomposed components of the signal, and (3) re-composition of the signal.

Hence initially, the signal is decomposed into Approximation A_1 and Detail D_1 . The QMF that separate the low and high frequency components of the signal at level 1 achieve this.

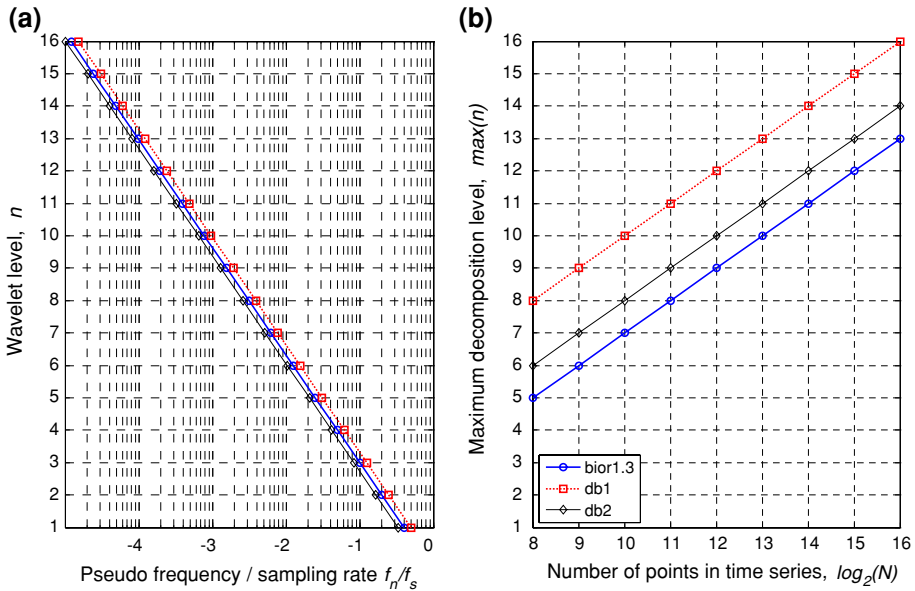


Fig. 9 a The wavelet level’s pseudo frequency versus wavelet level. b Maximum wavelet level of decomposition permitted versus number of point in timeseries

Subsequently, the approximation A_1 is further decomposed into A_2 and D_2 . This process of decomposition is repeated until the signal is decomposed into a set of frequency sub-bands, Eq. (11). The level n approximation A_n contains the lowest frequency content of the signal. The Details D_n to D_1 contain progressively higher frequency sub-bands of the signal s .

$$s = A_n + \sum_{k=1}^n D_k. \tag{11}$$

In this paper, the approximation, A_n , is termed the lower frequencies sub-band (LFS) and the sum of the details, $\sum D_k$, is termed the higher frequencies sub-band (HFS).

Down to what level n decomposition should one go? Clearly this will depend on the low-frequency fling feature one is trying to characterize. Wavelet scale (or level) and frequency have an approximate relationship (Abyr 1997), Eq. (12),

$$f_n = \frac{f_s f_w}{2^n} \tag{12}$$

where f_n is the pseudo-frequency [Hz] of a level n decomposition, f_w is the central frequency [Hz] of a mother wavelet and f_s is the sampling rate [Hz] of the timeseries. Note that wavelet scale 2^n must have units [Hz]. This equation provides an estimate of n . In addition the maximum level of wavelet decomposition must not be exceeded. This is dependant on the mother wavelet and number of points in the timeseries. Generally, the larger the number of points N , in the timeseries, the greater the level of decomposition available n . Figure 9a depicts Eq. (12) for the mother wavelets suggested here and Fig. 9b shows the maximal level of decomposition permitted.

In this paper the records processed have $N = 2^{14}$ points and are sampled at $f_s = 200$ Hz. This corresponds to a maximum level of decomposition for the $bio1.3$ wavelet of 11. The fling

feature we are trying to identify is within the frequency sub-band <0.2 Hz thus $f_n/f_s < 10^{-3}$. From Fig. 9a we obtain range of levels of decomposition from 9 to 11 (the maximum permitted here). Thus, some expert opinion still remains as to which level to choose. In this paper we choose the level that produces a LFS most topologically similar to simple fling type A response.

Knowledge of the lower frequency limit is not a pre-requisite, because we know that to reach the lower frequencies, down sampling by several levels is necessary. A general guideline or rule of thumb, which might be useful, is just to follow the operation of the wavelet transform. This down-samples by a factor of 2 each time as the level increases, therefore to isolate for example frequencies <0.2 Hz, then starting at half the sampling frequency (in this case 100 Hz) we divide by 2 each time. Therefore we reach 0.19 Hz at level 9, 0.09 Hz at level 10 etc. A 100 Hz sampling rate for example brings us to level 8 for frequencies <0.2 Hz etc. As pointed out above, we choose the most topologically similar sine type A response.

4.3 Defining thresholds for denoising

A soft thresholded timeseries \check{x}_i , where $i \in \{1, 2, \dots, N\}$, is given by Eq. (13), where τ is a threshold value. Hence, the low power components of x_i are de-noised (removed).

$$\check{x}_i = \begin{cases} (x_i - \tau) \operatorname{sgn}(x_i) & |x_i| > \tau \\ 0 & |x_i| \leq \tau \end{cases} \tag{13}$$

Different threshold values are employed for LFS and HFS of the simplified signal. The LHS threshold τ_L is estimated from the standard deviation of the data σ , multiplied by Donoho’s “root two log N ” (Coifman and Donoho 1995; Donoho 1995)

$$\tau_L = \sigma \sqrt{2 \log N}. \tag{14}$$

The HFS threshold τ_H uses a consistent estimator of the standard deviation, $\hat{\sigma}$ (median absolute deviation MAD, Coifman and Donoho 1995; Donoho 1995), used in image processing. The scaling factor 0.6745 is obtained by assuming a normal distribution of the noise

$$\tau_H = \hat{\sigma} \sqrt{2 \log N}, \quad \hat{\sigma} = \frac{\text{MAD}}{0.6745}. \tag{15}$$

It was found that repeated application of the thresholds enables an improved identification of fling in the acceleration. This repetition is more aggressive in terms of removing noise in the signal.

4.4 Re-composition of signal

The signal is recomposed by inverse stationary wavelet transforming (ISWT) of thresholded LFS and HFS. The lowest level n detail and approximations recomposed to produce the level $n - 1$ Approximation and so on until the signal is recomposed.

It is also possible to re-compose just the LFS and HFS separately. Computationally this is achieved by, for example zeroing D_n and using thresholded A_n or zeroing A_n and using thresholded D_n and applying ISWT.

4.5 Integration of errors and tilts

Typically, an accelerometer records timeseries a_i or \ddot{a}_i from which estimate \hat{x}_i , Eq. (16), can be obtained through deconvolution, see Eq. (3). Note that all equations in this section only apply to the horizontal components of the accelerometer.

$$\hat{x}_i = \ddot{x}_i - g\psi_{3-i} - \varepsilon, \quad i \in \{1, 2\} \tag{16}$$

However, it is clear that recorded and obtained estimate of \hat{x}_i is not precisely the translational ground acceleration \ddot{x}_i , i.e., it is corrupted by the tilt timeseries ψ_{3-i} and the instrument noise timeseries ε , both of which are unknown. In order to obtain the velocity and displacement timeseries we must integrate \hat{x}_i and recognize it is not precisely \ddot{x}_i .

The estimate \hat{x}_i contains three terms. The first term is the actual translational ground acceleration. From mechanics we note that the dynamic motion of the ground starts from rest and ends at rest; hence $\dot{x}_i(0) = \dot{x}_i(T_i) = 0$. In addition, $\dot{x}_i(t > T_i) = 0$, where T_i is an estimate of the duration of the LFS of the seismic timeseries.

The second term of \hat{x}_i is the unknown tilt timeseries. There is no way of removing this unknown error during the earthquake. At present we have very limited information about the statistics of ψ_{3-i} . Note that the ground tilts are likely to be very small. Evidence for this is given later in this paper. The mean of the tilt timeseries $\bar{\psi}_{3-i}$ is not necessarily zero as there is no argument from mechanics to suggest it should be zero.

$$\int_0^{T_i} \psi_{3-i} dt = T_i \bar{\psi}_{3-i} \neq 0 \tag{17}$$

At the end of the earthquake vibration a residual tilt angle of ψ_{3-i}^* is attained, i.e., if the accelerometer is no longer horizontal. Integrating this constant residual tilt angle ψ_{3-i}^* results in the following, Eq. (18)

$$\int_{T_i}^t \psi_{3-i}^* dt = \psi_{3-i}^* (t - T_i). \tag{18}$$

Hence, the effect of residual tilt angles on velocity timeseries after the end of the earthquake is a linear function with time.

The third term of \hat{x}_i is due to instrument noise ε . Integrating noise is very problematic. Fundamentally, it is analogous to summing a set of N random variables. For arguments sake, let us assume that these random variables have a zero mean and variance σ^2 . The expected value of this sum is zero, which is good. However, the variance of this sum of random variables is, unfortunately, $N\sigma^2$, i.e., it increases with N , see Freund (2003). This is clearly very bad. Consequently, given a particular sample of N random variables, its cumulative sum will be very unpredictable and it is likely to have increasing amplitude oscillation with increasing N .

Note that the above argument suggests that down-sampling a timeseries has a positive effect on noise mitigation in summation processes. Down sampling is a component of the multi-level wavelet decomposition. Thus, it seem likely that efficacy of wavelet decomposition, in the process of integrating timeseries, is good for this very reason.

It is worth noting that summing and integration are not completely analogous. Summing is a very poor integrator; in particular it does not have the correct frequency domain characteristics. Integration is the same as dividing by Fourier frequency ω_f in the frequency domain.

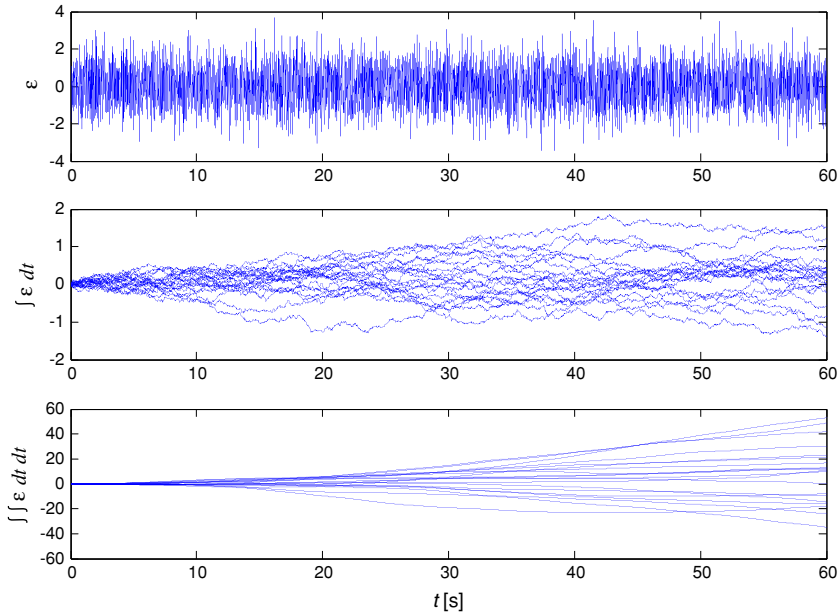


Fig. 10 Example Integration (Simpson’s Rule) of 20 timeseries of Gaussian noise $N(0,1)$. Sampled at 100 Hz, with 6,001 data points

As a result, it is a low-pass filter, i.e., it attenuates higher frequency components. Integrating noise does the same, high frequencies are attenuated but lower frequencies are amplified.

Nevertheless, the argument for summation of random variables still applies. Integration of a noise timeseries is very unpredictable. Yet, we do know that the resulting timeseries is likely to be of a lower frequency character. Figure 10 shows that on integrating Gaussian noise twice (i.e., low pass filtering twice), the offsets produced are similar to those observed when integrating noisy seismic data to displacement, even after standard filtering, contributing therefore to the source of errors in displacement.

For the horizontal components, the estimate of velocity timeseries is given by Eq. (19)

$$\hat{x}_i = \begin{cases} \dot{x}_i + g \int_0^t \psi_{3-i} dt + \int_0^t \varepsilon dt & t \leq T_i \\ g (\bar{\psi}_{3-i} - \psi_{3-i}^*) T_i + g \psi_{3-i}^* t + \int_0^t \varepsilon dt & t > T_i \end{cases} \quad (19)$$

By integrating again an estimated displacement timeseries Eq. (20) is obtained

$$\hat{x}_i = \begin{cases} x_i + g \int_0^t \int_0^t \psi_{3-i} dt dt + \int_0^t \int_0^t \varepsilon dt dt & t \leq T_i \\ x_i(T_i) + g (\bar{\psi}_{3-i} - \psi_{3-i}^*) T_i t + \frac{1}{2} g \psi_{3-i}^* t^2 + \int_0^t \int_0^t \varepsilon dt dt & t > T_i \end{cases} \quad (20)$$

In general, the tilt angles impose a linear error in velocity and quadratic error in displacement after the end of the timeseries. While the instrument noise may produces oscillations of low frequency content that may also be linear/quadratic like after the end of the timeseries.

Thus, it is essential that an effective noise reduction strategy is employed to increase the signal to noise ratio.

In this paper wavelet denoising is employed to reduce the magnitude of instrument noise. This allows a clearer distinction between errors due to tilts and errors due to noise in derived displacement timeseries. A wavelet based de-noising strategy is far superior to band pass filtering, as it make no assumption as to the frequency content of the noise.

4.6 Baseline correction and estimation of tilt angles

Now, to remove this quadratic from the displacement timeseries for $t > T_i$ we could detrend both velocity and displacement timeseries for $t > T_i$. Or more simply we could zero the LFS acceleration timeseries for $t > T_i$. Note that it is not necessary in this case to zero the HFS acceleration for $t > T_i$. The time T_i is the time at which the LFS velocity timeseries returns to zero. In this paper this approach is perfectly adequate for defining T_i . Locating T_i is an approach, which does bear some resemblance to the tried and tested methods, and indeed there isn't any reason why this shouldn't be the case. However, the process de-noises well; it is made easier by the fact the wavelet transform can isolate the low-frequency fling making it possible to automatically apply baseline correction.

In this way the quadratic term for the LFS for $t > T_i$ is removed. This is what we term correcting the baseline for tilt angles in this paper. The profile of Fig. 15 for example without baseline correction, is similar to that in the simulation of Graizer (2005) obtained after adding an artificial tilt of 0.1° to the corrected Hector Mine data discussed in Sect. 2.2. The automated baseline correction scheme then locates T_i , then zeros the acceleration from that point and re-integrates down to displacement producing the corrected profile in the component of Fig. 15.

A least squares fit of form (21) is obtained from the displacement timeseries for $t > T_i$. From this optimal quadratic and Eq. (20) the following estimates of tilt angles, Eq. (22), are achieved

$$x = c_2 t^2 + c_1 t + c_0 \quad (21)$$

$$\psi_{3-i}^* = \frac{2c_2}{g}, \quad \bar{\psi}_{3-i} = \frac{c_1}{gT_i} - \psi_{3-i}^*. \quad (22)$$

4.7 General comments

Some general comments on the transforms used: both wavelets *db1* and *db2* can give a greater depth of decomposition, useful for some of the records, on the other hand their filters don't have guaranteed linear phase properties and in general using linear phase filters is recommended. Though *db2* has an almost linear phase response and gives reasonable results. The bi-orthogonal wavelets have symmetric filters and guaranteed linear phase which are useful properties when correcting seismic records, *bior1.3* wavelet was used for most of the analyses. These bases and their associated low-pass and high-pass filters are well suited to the task and give reasonable results for the seismic records under investigation. The scaling and wavelet functions or more precisely their associated filters are successively applied with thresholds to de-noise the acceleration time history. The object being to automatically obtain as good a fling output as is possible in the LFS acceleration, followed by a pulse-like velocity time-history after the first integration, and a ramp-like displacement after the second integration. Both the acceleration sine-type fling and velocity pulse is obtained, but not without some distortion as the results show. Other wavelet transforms also give good results, because

as mentioned, it is the properties of the associated filters in conjunction with thresholding, which makes the method useful.

5 Results

The results obtained using the wavelet transform (filter banks) have been easily and quickly obtained using the automated procedure and give results comparable with Wu and Wu (2007) and Boore (2001) and GPS. The point being that by running the wavelet filters an almost idealized fling is obtained in the LFS acceleration, then after applying a baseline correction, the velocity fling follows almost naturally after integration as does the subsequent displacement. The results below commence with an in-depth study of a seismic event from the Chi–Chi event, Taiwan, 1999/09/20.

5.1 Processing vertical component, TCU068V

The fling in the vertical components, in the events used is the easiest to analyze. The type A sine, fling profiles are obtained almost immediately after application of the wavelet transform and first and second integration. This is because as pointed out in Eq. (3) from Graizer (2005) the vertical component is the least sensitive to tilts and is almost purely translational. Figure 11 shows the LFS acceleration, velocity and displacement using wavelet *bior1.3* at level 10 decomposition. Similar results are obtained using wavelet *db2*, or *db1* at level 10. The LFS acceleration shows a type A fling profile, which after integration yields a veloc-

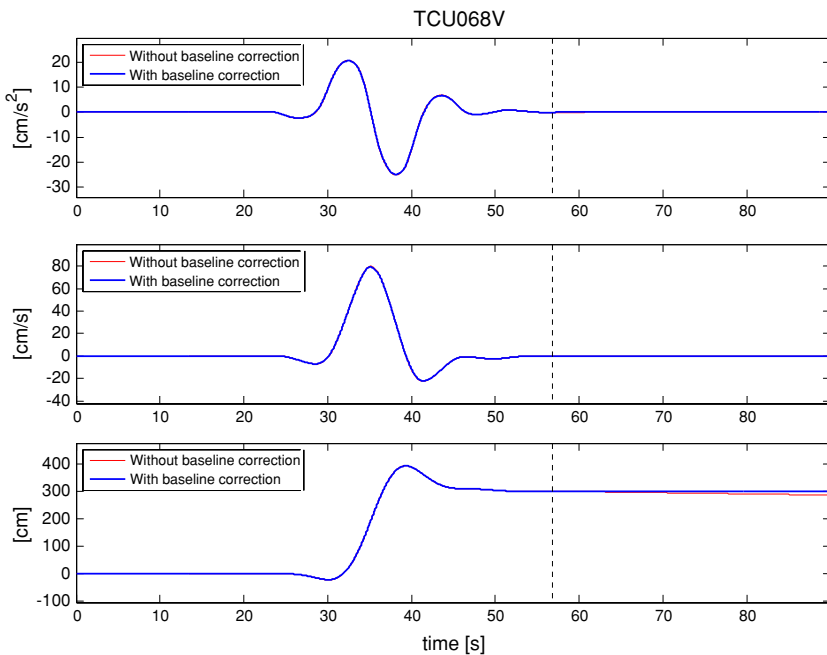


Fig. 11 Baseline correction lower frequency sub-band (LFS) for TCU068V component obtained at level 10 with *bior1.3*

Table 1 Estimated data obtained from corrected Chi-Chi event

Wavelet <i>bior1.3</i>	<i>i</i>	Baseline point	Residual disp.	Fit coeff.	Fit coeff.	Mean tilt	Residual tilt
		T_i (s)	$x_i(t_{\text{end}})$ (cm)	c_2 (cm/s ²)	c_1 (cm/s)	$\tilde{\psi}_{3-i}$ (Deg.)	ψ_{3-i}^* (Deg.)
TCU068EW	1	45.7	-731	1.43E-2	-7.7	-0.0082	0.0017
TCU068NS	2	45.67	555	3.67E-3	11.18	0.015	4.3E-4
TCU068V	3	56.84	300	-9.17E-4	-0.298	-	-

ity pulse and a displacement ramp after second integration. The HFS velocity profile is an asymmetric type B, such that the HFS displacement produces local ground movement and eventual displacement recovery. The LFS fling profile is almost like the model type A shown in Figure except that it is extracted from a real event. The acceleration peaks are at +20 and -25 [cm/s²]. This is not very large when compared to the HFS.

The TCU068V LFS displacement shows an almost horizontal trace for $t > T_i$. The coefficients of a quadratic fit to displacement data in range $t > T_i$ results in coefficients in Table 1. Both of these coefficients are small suggesting that there is no tilt error. And this is as it should be; given the vertical component should be insensitive to tilt angles, Eq. (5). This very shallow optimal quadratic is a result of noise integration. This gives us an estimate of the magnitude of noise integration error after wavelet denoising.

To correct for the very small baseline shift (due to noise) in the vertical component it is necessary to zero the baseline after the lower frequency acceleration fling. In this case the process is almost trivial since after applying the wavelet transform and integrating, a type A sine acceleration fling, velocity pulse and ramp displacement occur almost naturally since the motion is almost purely translational. The baseline adjustment requires one time-point selection at 56.84 [s] that is obtained automatically from the zero of the LFS velocity timeseries. This is a reasonable and straightforward correction to apply because it removes the small artifacts in the later portion of the acceleration record. The object being, to achieve an almost perfect type A sine, fling model as shown in Fig. 3. Thus satisfying condition (i) and (ii) in Sect. 2.2 as described in Graizer (2005) and this implies pure translation.

Moreover, the correction only affects the LFS. Then first and second re-integration of the corrected LFS acceleration automatically adjusts the velocity baseline to zero in the latter portion of the time history. This produces a velocity pulse and ramp-like acceleration with a permanent displacement, as seen in Figure.

Figure 12 also show the separated LFS and HFS acceleration time histories, which are integrated separately to give the resulting velocity and displacement timeseries. The LFS and HFS can also then be recombined to give the total form of velocity and displacements just by adding the waveforms.

The wavelet transform enables the necessary filtering, de-noising and LFS and HFS separation making integration and baseline correction simple.

5.2 Processing horizontal component, TCU068EW

Figure 13 shows the LFS of the EW component using *bior1.3* at level 10 decomposition and after wavelet transforming, integrating and baseline correcting. The fling is apparent in the acceleration and velocity sub-bands followed by the large ramp-like displacement. The wavelet transform locates the optimal fling acceleration sub-band, from which the second

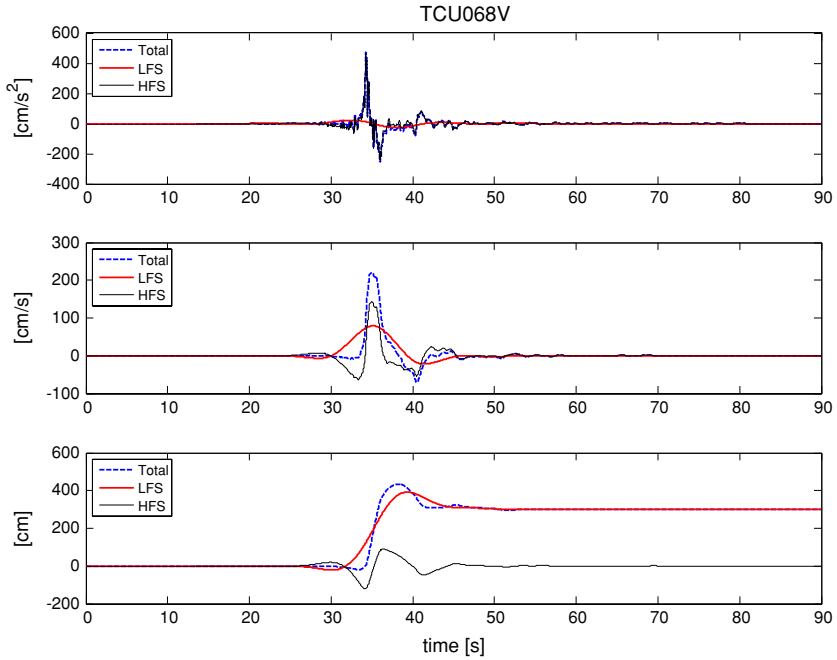


Fig. 12 Comparison of lower and higher frequency sub-bands for TCU068V at level 10, using *bior1.3*

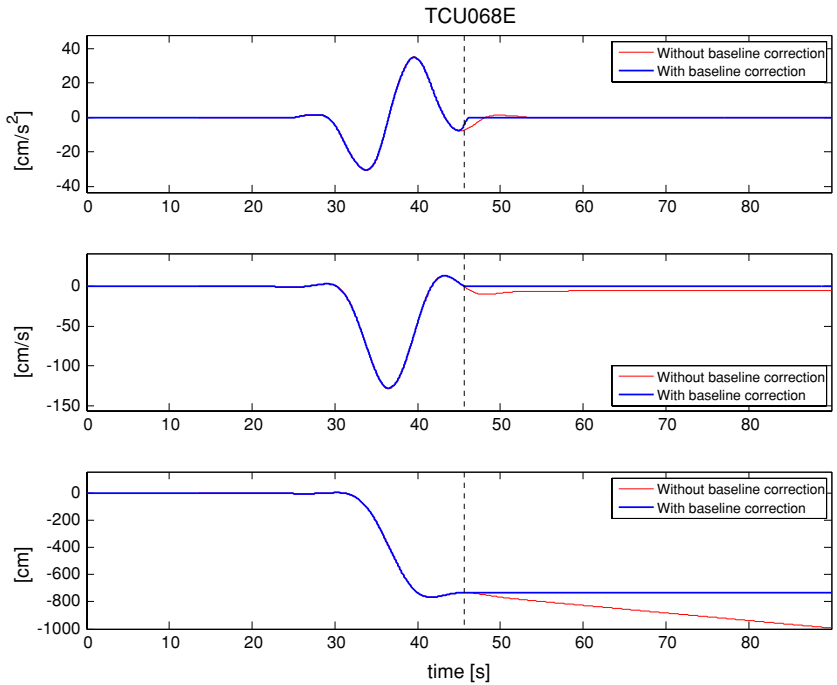


Fig. 13 Baseline correction lower frequency sub-band (LFS) for TCU068EW component obtained at level 10 with *bior1.3*

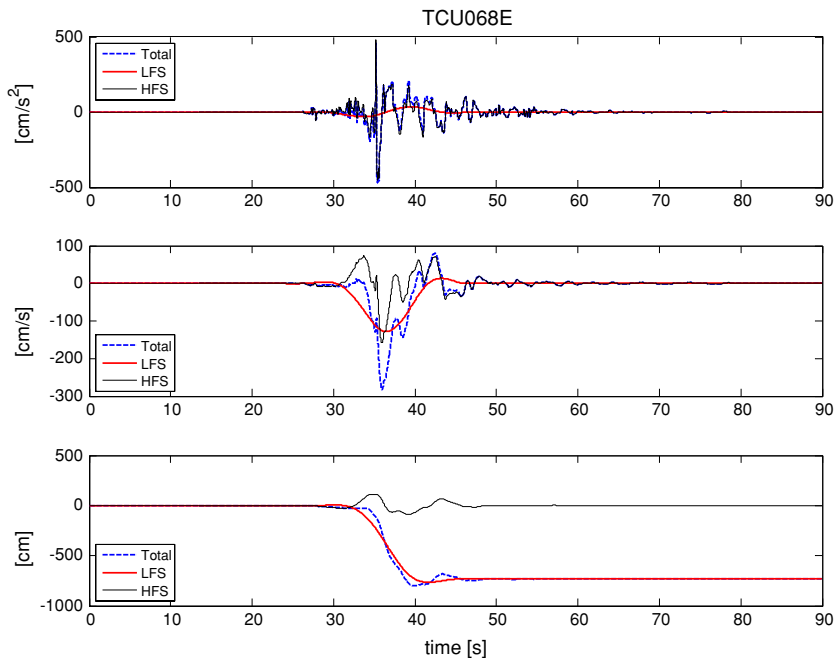


Fig. 14 Comparison of lower and higher frequency sub-bands for TCU068EW obtained at level 10, using *bior1.3*

integration yields the displacement. Figure 14 also shows the HFS acceleration, velocity and displacement timeseries. The combined corrected timeseries are obtained either by adding the LFS and HFS timeseries or by re-integrating the corrected (summed) acceleration. Figure 14 compares the LFS acceleration (fling type A) and the one-sided velocity with that of the HFS. The velocity for the HFS is type B, which gives a displacement recovery in the short period.

In this case and after wavelet transforming, the LFS displacement shows a downward quadratic profile. The mean and residual tilt angles are computed from the optimal quadratic coefficients, Eq. (21), as describe previously. These are given in Table 1.

The Residual displacement is obtained simply by inspection from the end point of LFS displacement timeseries, i.e., at $t_{\text{end}} = 90$ s.

5.3 Processing horizontal component, TCU068NS

Figure 15 shows the LFS obtained by using wavelet *bior1.3* at level 10. In this case the velocity baseline shift in the latter portion of the wavelet-transformed velocity time history, giving rise to a displacement offset nearly 11 m. This is due to the effects of tilt. To correct for the offsets, the baseline procedure described previously is applied.

The net displacement for this event Wu and Wu (2007) and [private communication, Dr Hung-Chie Chiu] was approximately 10 m (vector sum of NS and EW). This was recorded on an A900 instrument installed at the Taiwan strong motion station TCU068. It recorded the Chi-Chi main shock at a distance of 380 m from the fault surface rupture.

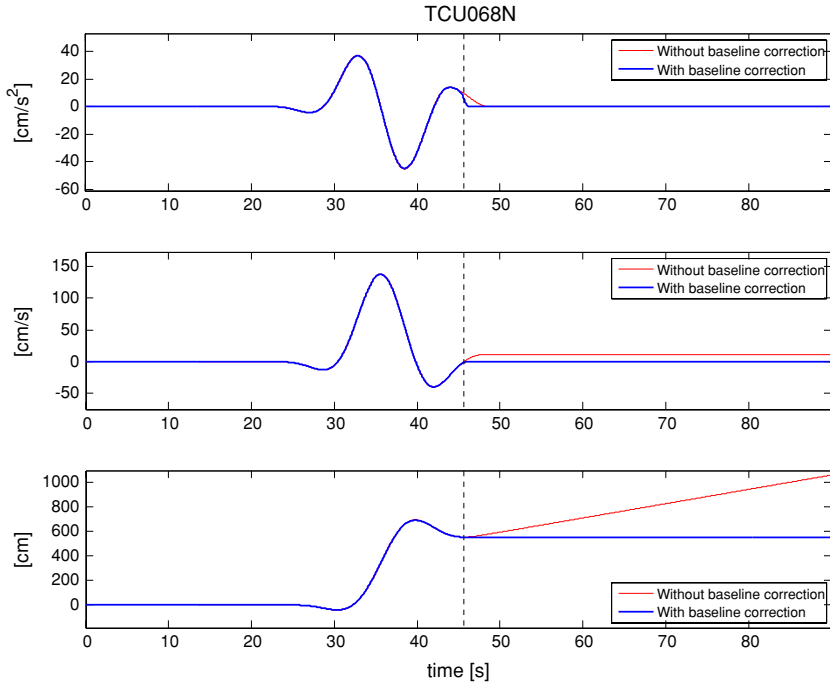


Fig. 15 Baseline correction lower frequency sub-band (LFS) for TCU068NS component obtained at level 10 with *bior1.3*

The vector sum of permanent displacements obtained here is 9.66 m, which is of the correct order.

Figure 16 shows the LFS and HFS acceleration profiles. These demonstrate that the LFS has a sine type A profile, whilst the HFS has a cosine type B profile. The HFS therefore shows local vibrations, which are superimposed on the LFS. Figure also shows the corrected total profile after wavelet transforming, baseline correction and first and second re-integration.

Finally, Fig. 17 shows all the three derived displacement timeseries. It also includes the vector sum of all three components. The vector displacement is defined as $\mathbf{d} = (x_1, x_2, x_3)$. The timeseries of vector displacement magnitude $|\mathbf{d}|$ indicates a maximum total displacement of 11.8 m with a residual (final) displacement of 9.66 m. Figure 18 displays the vector displacement \mathbf{d} including directional information. The direction of the displacement vector is in keeping with the GPS vectors displayed in Wu and Wu (2007).

5.4 Estimates of signal-to-noise ratio (SNR)

It is important to consider the effect of the wavelet-denoising scheme. It is possible to subtract the corrected accelerograms from the raw accelerogram data thus obtaining an estimate of the noise. The power spectrum of this extracted noise is displayed in Fig. 19. This figure also compares the power spectra for the LFS, HFS, corrected data and raw accelerograms. Note that the wavelet denoising scheme extract very little power at the low frequency end of the spectrum. Thus, it does not remove the fling component. This is clearly not the case when employing a low-cut filter.

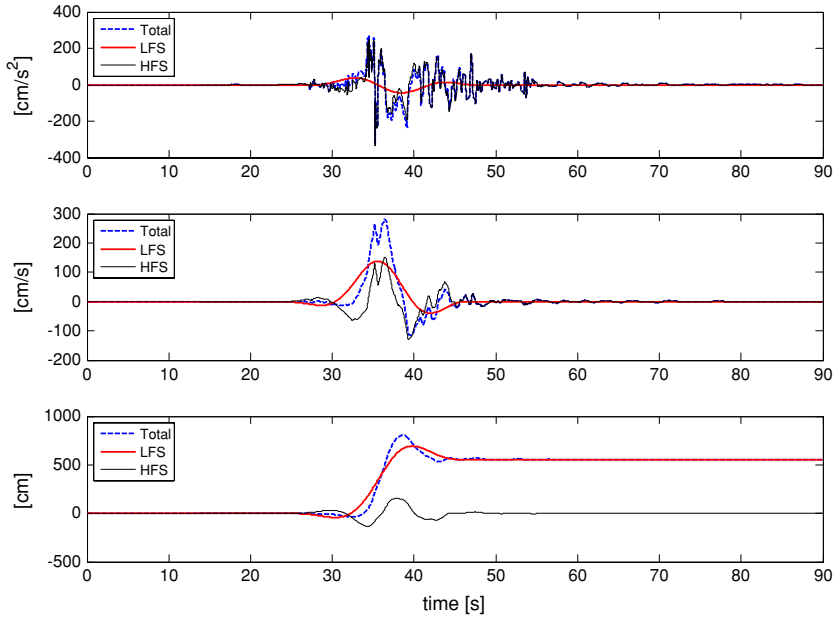


Fig. 16 Comparison of lower and higher frequency sub-bands for TC068NS at level 10, using *bior1.3*

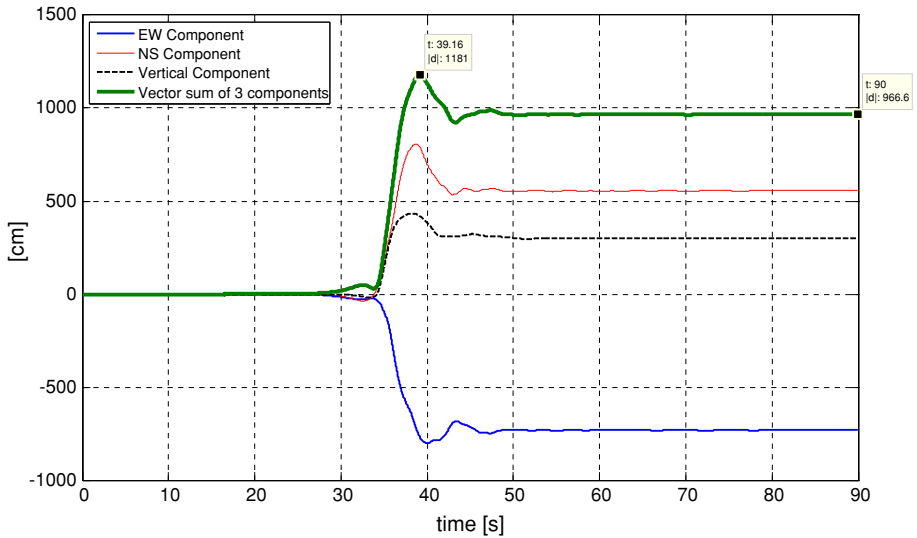


Fig. 17 Comparison of derived displacement timeseries for all three components

The signal-to-noise ratio is an important measure of how clean the raw data was before denoising. The signal-to-noise ratio in this paper is defined by Eq. (22)

$$SNR = 20 \log_{10} (\bar{s}/\bar{\epsilon}) \tag{23}$$

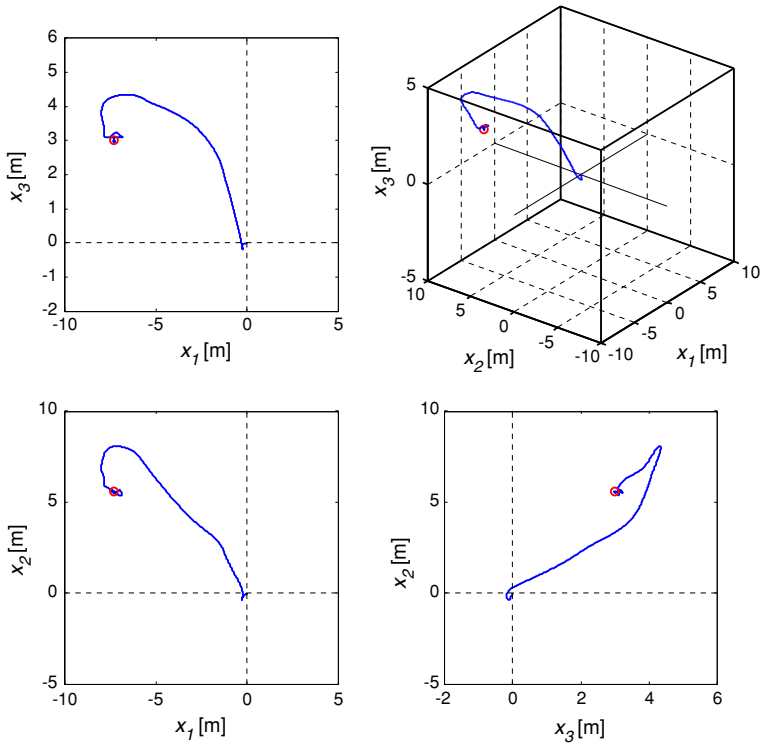


Fig. 18 Resultant ground displacement traces for TCU068 Chi-Chi Event

where \bar{s} is the mean power of the raw (signal) acceleration within bandwidth of 0 to 25 Hz, $\bar{\varepsilon}$ is the mean power of the extracted noise over this same band width. Note that the multitaper method (Coifman and Donoho 1995) or multiple-window method is employed to determine the power spectra and thence these mean power levels. This is a non-parametric method and essentially finds an approximate solution to a Fredholm integral equation of the first kind. The method uses windows defined by Slepian sequences, which essentially allow a reduced variance of the spectral estimate. Table 2 summarizes the SNR for the three components of the Chi-Chi event.

Note a SNR of 40 dB as described in Graizer (2005) seems too optimistic. The SNR of TCU068V is much lower than for the other two components. Again this is a reflection of the fact that the vertical component is insensitive to tilts and other distortions therefore the dispersion is less than for the horizontal components.

6 Discussion on method

The assumption that the LFS displacement offsets are only due to tilt needs some more justification and is presented here. Table 2 demonstrates that the noise power of the horizontal sensors is slightly greater than that of the vertical sensor. Therefore although the noise may behave differently for the three components, the wavelet de-noising performs equally well in cleaning the LFS of most of the noise for all three components.

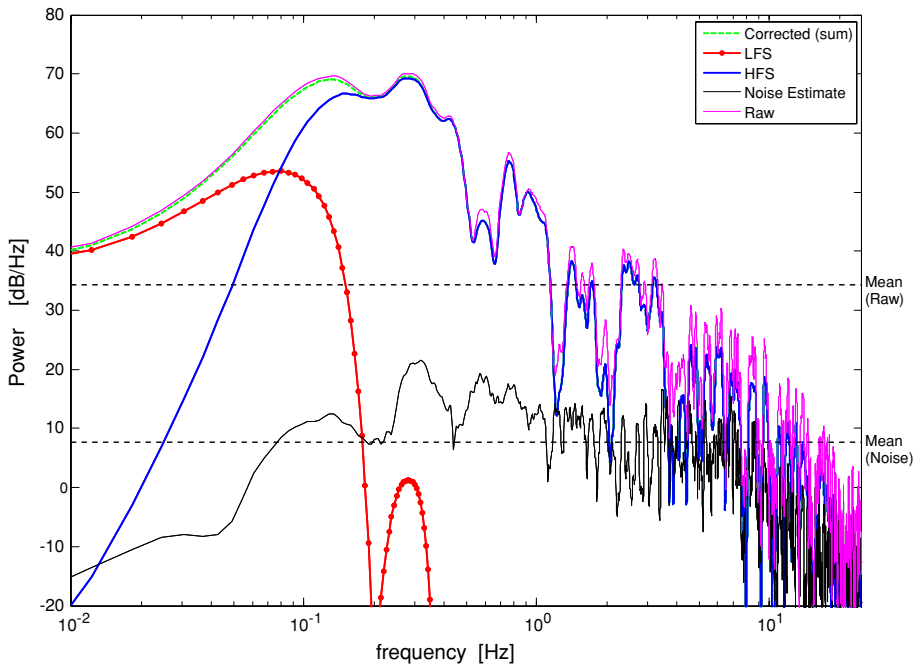


Fig. 19 Comparison of power estimates (multi-taper method) for TCU068V

Table 2 Estimated signal-to-noise ratio (SNR)

	Signal \bar{s} (dB)	Noise $\bar{\epsilon}$ (dB)	SNR (dB)
TCU068EW	40	8.79	31.2
TCU068NS	39.7	8.22	31.5
TCU068V	34.3	7.63	26.7

Indeed correcting the vertical component may be considered superfluous in this case because the baseline corrected profile is almost identical to that without the correction. This shows only a difference in displacement of 13 cm in 300 cm at the end of the record see Fig. 11. It is consistent with Eq. (5), which demonstrates that the vertical sensor is responding to vertical acceleration only and is insensitive to tilt. This difference at the end of the record, (13 cm in 300 cm, i.e., $\sim 4\%$) may indeed be due to noise, but it is very small and not significant in this case. The noise power is indeed greater in the horizontal sensors, but it is only by 1 dB and 0.6 dB with respect to the vertical sensor (see Table 2). The discrepancy in displacement, however, of ~ 4.5 m for the northern component for example, between the wavelet de-noised + baseline corrected and the wavelet de-noised and baseline uncorrected, is far too great to be attributed to the small differences in noise power. If the discrepancy due to noise, in the horizontal components, was of the same order as that for the vertical component we would expect a final displacement offset of 10–20 cm. Similar results are observed for the eastern component, see Fig. 13. Therefore it is concluded that the contribution due to noise can be ignored and that the offset in the LFS displacement is due to tilt.

The values of T_i for the two horizontal components are similar, which indeed is confirmation of good estimation. The value of T_i for the vertical component is significantly different

(~ 10 s difference) from that of the horizontal components. This is a consequence of the fact that baseline correction is automated and therefore applied to the vertical component as well, even though baseline correction may be considered as unnecessary in this case, since the displacement artifact is very small and consistent with Eq. (5), as discussed earlier. The wavelet de-noised + baseline corrected profile and the wavelet de-noised and uncorrected profile are virtually the same as shown in Fig. 11. The deviation in displacement is only slight from 56 s onwards to the end, because tilt has a negligible effect on the accelerometer, see Eq. (5). Therefore in this case, it is safe to ignore this difference in T_i between the vertical sensor and the two horizontal sensors and conclude that the vertical sensor behaves in a manner predicted in theory in Eq. (5); dependant only on translation, and not tilt, which is itself a good result. Therefore the similar T_i 's of the horizontal sensors are confirmation of good estimation, but all three components are evidence of satisfactory performance of the method described in this paper.

7 Summary and conclusions

This paper shows that the wavelet transform and more specifically the wavelet QMF filters, the non-linear scaling with de-noising provide a very reasonable method for automatically correcting seismic events, and provide an alternative to some of the current methods used. In particular the combination of wavelet filtering and de-noising produces lower and higher frequency acceleration sub-bands, which are easily integrated and automatically corrected for baseline shift. In particular the wavelet transform can isolate the fling. The paper focuses on the Chi–Chi 1999 event with data from Lee (2001), which has a wealth of data for analysis. The paper demonstrates that the wavelet transform is a useful tool to apply, not just for seismic correction but also for extracting LFS and HFS time histories from the data as well estimating tilt angles and signal-to-noise ratios. The separation of the data into LFS and HFS makes correction and integration easier. Generally only one time point is required from which to correct for baseline shifts and then to re-integrate to obtain profiles resembling the theoretical fling models. Sometimes, but not in this case, the same automated baseline correction method may need to be applied to the HFS, in particular for events of a lower magnitude. This method has been found to be equally as successful on data from the Icelandic event of 29th May in 2008; an event of a lower magnitude 6.3 and with smaller displacements.

The analysis uses the condition (i) and (ii) extensively, as in Graizer (2005). These essentially set out the framework for obtaining estimates of ground motions due to translation only. In doing so the lower frequency content in particular should give the type A sine model as a basis for approximating as best possible the model fling in the long period. It also uses the type B cosine model for the short period. To comply with condition (i) and (ii) for the lower frequencies, the wavelet transform is used to filter and de-noise and then to integrate the LFS and HFS separately for the velocity and displacement profiles. The object then is to zero the tilts and other distortions in the latter portion of the LFS acceleration time history, then to re-integrate to obtain the velocity and displacement profiles, which resembles the fling type A model.

As an aside the method also lends itself to obtaining estimates of the tilt angles from the lower frequency displacement profile offsets. In this case the results clearly show that the vertical component is insensitive to tilt, in contrast to the two longitudinal components, which are very sensitive to tilt angles. This is similar to the results obtained using event TCU052, 10 km away from event TCU068.

These estimates of tilt angles assume that the noise content of the signal has been successfully removed. So that what we see at the end of the LFS displacement is, by assumption, the influence of ground tilts. It has been shown that noise twice integrated can produce linear/quadratic like displacement profile. Therefore the question as to whether the linear/quadratic function in the latter part of some of the displacement timeseries is in fact due to tilts, should remain open. Without *a priori* information on the noise this seems difficult to answer in the general case. However, it can be said with some certainty that for TCU068, the vertical component behaves in a theoretically consistent manner and points to small displacement artifacts due to noise. The horizontal components also behave consistently, but that the displacement artifacts are too large for the very small differences in noise power between these and the vertical component. Therefore it is concluded that these artifacts must be due to tilt only. It is suspected that for the large magnitude events, this may be the norm, since the deviations due to tilt will subsume those due to noise. However, this needs further work and investigation to determine whether this holds for the general case.

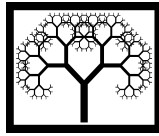
Finally, wavelet filtering and de-noising makes it possible to obtain estimates of the signal-to-noise ratios (SNR) for the seismic components. The SNR, and signal power estimate, for the vertical component is lower than that of the horizontal components, demonstrating again that the vertical component shows less sensitivity to errors due to tilts.

Acknowledgments Deo Gratias. Also thanks to Dr Hung-Chie Chiu, whom I met at the Geneva conference in 2006 and who kindly sent data and seismic profiles for this and other events for comparison and provided invaluable comments in an exchange of emails. I also wish to thank Dr Anton Shterenlikt for his suggestions on noise integration. The contributions from the reviewers are gratefully acknowledged and gave much food for thought and discussion over issues, which needed clarification and explanation.

References

- Abry P (1997) Ondelettes et turbulence, Multirésolutions, algorithmes de décomposition, invariance d'échelles. Diderot Editeur, Paris
- Alexander NA, Chanerley AA, Goorvadoo N (2001) A review of procedures used for the correction of seismic data. In: Proceedings of the eight international conference on civil and structural engineering computing, Vienna, Austria, pp 101–102
- Bertero VV, Herrera RA, Mahin SA (1976) Establishment of design earthquakes—evaluation of present methods. ASHRAE Trans 1:551–580
- Bertero VV, Mahin SA, Herrera RA (1978) Aseismic design implications of near-fault San Fernando earthquake records. Earthq Eng Struc Dyn 6:31–42
- Bolt BA (1971) The San Fernando Valley, California, earthquake of February 9 1971: Data on seismic hazards. Bull Seismol Soc Am 61:501–510
- Bolt BA (1975) The San Fernando earthquake, 1971. Magnitudes, aftershocks, and fault dynamics, vol 196, Chap. 21, Calif. Div. of Mines and Geol., Sacramento
- Boore DM (2001) Effect of baseline corrections on displacements and response spectra for several recordings of the 1999 Chi-Chi, Taiwan, earthquake. Bull Seismol Soc Am 91:1199–1211
- Boore DM, Bommer JJ (2005) Processing of strong-motion accelerograms: needs, options and consequences. Soil Dyn Earthq Eng 25:93–115
- Chanerley AA, Alexander NA (2002) An approach to seismic correction which includes wavelet de-noising. In: Proceedings of the tenth international conference on civil, structural and environmental engineering computing, Prague, Czech Republic, pp 107–108
- Chanerley AA, Alexander NA (2007) Correcting data from an unknown accelerometer using recursive least squares and wavelet de-noising. Comput Struct 85:1679–1692
- Chanerley AA, Alexander NA (2008) Using the total least squares method for seismic correction of recordings from unknown instruments. Adv Eng Softw 39:849–860
- Chen S-M, Loh C-H (2006) Estimates of permanent ground displacements from near-fault, strong-motion accelerograms. In 1st European conference of earthquake engineering & seismology, Geneva

- Coifman R, Donoho DL (1995) Translation invariant de-noising, wavelets and statistics, Lecture Notes in statistics, vol 103. Springer, New York, pp 125–150
- Debauchies I (1992) Ten lectures on wavelets. SIAM, Philadelphia
- Donoho DL (1995) De-noising by soft-thresholding. *IEEE Trans Inf Theory* 41:613–627
- Freund JE (2003) *Mathematical statistics with applications*. 7th edn. Prentice Hall, Englewood Cliffs
- Graizer VM (2005) Effect of tilt on strong motion data processing. *Soil Dyn Earthq Eng* 25:197–204
- Halldorsson B, Mavroeidis GP, Papageorgiou AS (2009) Near-fault and far-field strong ground motion simulation for earthquake engineering applications using the specific barrier model. *J Struct Eng, ASCE* (in press)
- Iwan WD, Moser MA, Peng CY (1985) Some observations on strong-motion earthquake measurement using a digital accelerograph. *Bull Seismol Soc Am* 75:1225–1246
- Lee WHK, Shin TC, Kuo KC, Wu CF (2001) CWB free strong-motion data from the 21st Sept Chi-Chi, Taiwan, Earthquake. *BSSA* 91:1370–1376. CD ROM
- Makris N (1997) Rigidity-plasticity-viscosity: can electrorheological dampers protect base-isolated structures from near-source ground motions?. *Earthq Eng Struct Dyn* 26:571–591
- Makris N, Black C (2003) Dimensional analysis of inelastic structures subjected to near fault ground motions. Earthquake Engineering Research Center, University of California Report No 2003-05
- Trifunac MD (1971) Zero baseline correction of strong-motion accelerograms. *Bull Seismol Soc Am* 61(5):1201–1211
- Trifunac M, Lee V, Todorovska M (1999) Common problems in automatic digitization of strong motion accelerograms. *Soil Dyn Earthq Eng* 18:519–530
- Veletsos AS, Newmark NM, Chelepati CV (1965) Deformation spectra for elastic and elastoplastic systems subjected to ground shock and earthquake motions. In: *Proceedings of 3rd World conference on earthquake engineering*, Wellington, New Zealand, pp 663–682
- Wu Y-M, Wu C-F (2007) Approximate recovery of coseismic deformation from Taiwan strong-motion records. *J Seismol* 11:159–170



On Fling and Baseline Correction using Quadrature Mirror Filters

A.A. Chanerley¹, N.A. Alexander² and B. Halldorsson³

¹University of East London, United Kingdom

²University of Bristol, United Kingdom

³Earthquake Engineering Research Centre, University of Iceland

Abstract

This paper presents a new and alternative method of estimating displacements from seismic acceleration records. The method essentially uses biorthogonal and/or debauchies wavelets in order to denoise the noisy accelerometer data. Wavelets use quadrature mirror filters, these are maximally flat filters and in the case of the biorthogonal filters have linear phase. These are useful properties and when used with a denoising scheme these filters are able to extract the long period fling from the record. The net result is that integration to velocity and to displacement is made easier. Furthermore, the method also enables automatic baseline correction, without having to manually locate suitable time points. The records used in this paper are from the strong motion Chi-Chi 1999 event of magnitude 7.3 and the May 29th 2008 event at Selfoss in Iceland of magnitude 6.3

Keywords: fling, baseline, correction, wavelet, strong motion, filters, denoise, displacement, acceleration, Chi-Chi.

1 Introduction

The problem with obtaining estimates of displacement is that standard filtering methods cannot extract the low frequency displacement from the acceleration time history. This is partly due to baseline shift brought about by integrating noise buried in the time history and partly by integrating distortions due to instrument tilts brought on by the seismic wave perturbing the ground. Usually the correction schemes try to locate time points at which to adjust for baseline shift evident after two integration's of the acceleration time history recorded by the instruments. Therefore schemes such as those proposed by [1,2,3,8,13] are used to correct for baseline shifts. It is also acknowledged that the baseline shift is due to tilt as well as noise [3,13,14,15], though absolute measurements of tilt are not available, this paper

uses a least squares method with which to estimate the residual angles of tilt for the horizontal components.

The seismic correction scheme described in this paper provides an efficient filtering and thresholding method with which to extract permanent ground displacements from the acceleration time histories. Standard filtering methods cannot do this, but the wavelet filters, which are maximally flat when combined with a threshold scheme not only extract the long and short period, but de-noise the time-history thereby improving the signal-to-noise ratio. The correction scheme is applied to the data from the Chi-Chi event 1999, with $M = 7.6$.

2 Wavelet filtering and de-noising

The discrete wavelet transform (DWT) [3] may be considered as an octave-band filter bank, which implements successive low-pass and high-pass decomposition followed by down sampling by a factor of 2. As an example, 4-channel filter bank scheme is shown in Figure (1). The filters used in wavelet filter banks are digital finite impulse response filters (FIR), also called non-recursive filters because the outputs depend only on the inputs and not on previous outputs. Digital equivalents of classical Butterworth, Chebyshev and other classical analogue filters all depend on previous outputs as well as on the inputs.

The method takes the discrete wavelet transform (DWT) [4-9] of a signal, and passes the transform through a threshold [16,17], by removing the data below a certain value and then takes the inverse transform (iDWT), then to reconstruct a de-noised time signal. Reconstruction is the inverse process of decomposition, which up samples by a factor of 2 and applies low-pass and high pass filter banks. Essentially, through decomposition the DWT is able to concentrate most of the energy of the signal into a small number of data, after convoluting and down sampling with the appropriate filter weights depending on the selection of a wavelet basis. The dimensions of the transformed and de-noised data will be large compared to the magnitude of the noise obtained after high pass filtering. Therefore thresholding the wavelet transform will remove the low-amplitude noise in the wavelet domain and the inverse DWT will retrieve the desired signal with little loss of relevant detail.

The diagram of Figure (1) essentially shows how both the low frequency and the higher-frequency components of the signal can be extracted using a wavelet decomposition tree. In this paper a wavelet decomposition tree is implemented, where the resulting low frequency component is further decomposed showing the long period pulse type signal with greater clarity as we move to higher levels of the decomposition tree

2.1 Other Wavelet Properties

Another property of the low and high pass filters is that their frequency responses are mirror images about $\pi/2$, hence they are called quadrature mirror filters (QMF). This is shown in Figures (2) and (3), showing linear phase and that the frequency response mirror images about $\pi/2$. In the case the biorthogonal wavelet(s) (bior1.3) shown these wavelet filters are symmetric and have linear phase, which make them important for the sort of processing necessary for seismic correction. Other wavelets such as symlets are nearly symmetric and have nearly linear phase.

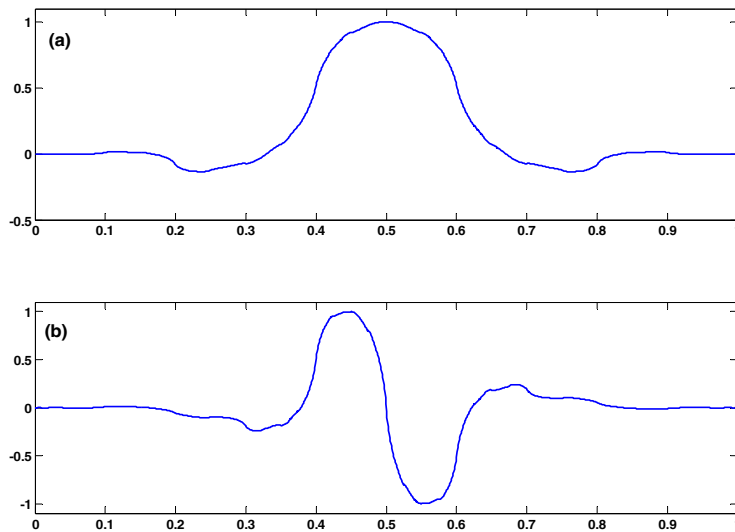


Figure 2: (a) the bior1.3 scaling function and (b) bior1.3 Wavelet

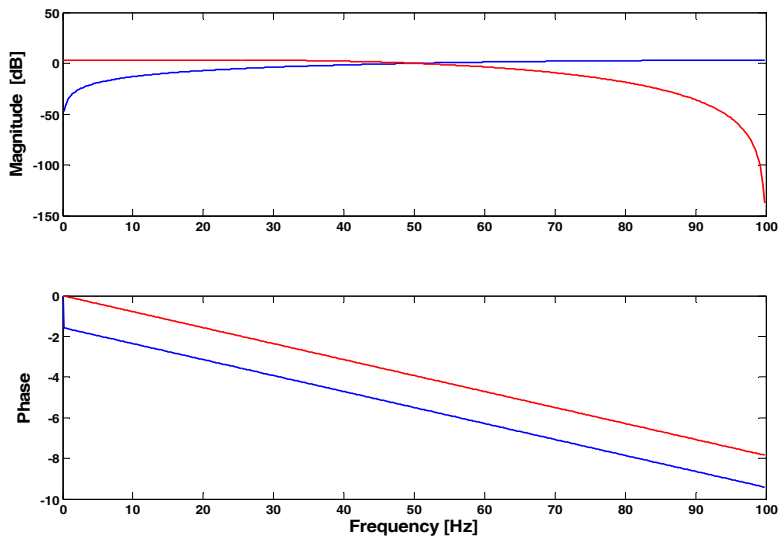


Figure 3: Wavelet bior1.3 associated low pass and high pass filters and their phase. Note that these QMFs are maximally flat

The other factor in this analysis is that we also de-noise the signal by thresholding [17], an essential operation. Basically thresholding involves the setting to zero wavelet coefficients (i.e. the transformed data values), whose absolute values are below a certain threshold. This type of thresholding is called ‘hard’. It leaves discontinuities in a signal, which could lead to unwanted and spurious oscillations. A ‘soft’ threshold scheme [17] on the other hand still removes absolute values below a threshold, but it then gradually sets to zero the discontinuities, in effect smoothing and therefore is a better procedure to apply.

Therefore a soft thresholding scheme is implemented however, with some differences. The wavelet coefficients of the transformed signal remain in their separated sub-bands at a suitable level of decomposition and de-noising is applied to each of the lower frequency sub-bands and the higher frequency sub-bands. This is the usefulness of the wavelet transform and de-noising in this application. Integrating noise twice produces considerable errors, which contribute to baseline shifts in the velocity and quadratic trends in the displacement. Standard filtering methods are not able to remove noise to a sufficient degree. However the wavelet transform with thresholding removes the noise and reveals a cleaned low frequency fling. Further distortions after 1st and 2nd integration are then due to tilts and rotations, which can be corrected relatively easily

3 The low frequency Fling model(s)

Fling is identified in velocity and low frequency acceleration ground pulses. The model fling pulses are related by the following equation (11)

$$\ddot{s}(t) = A \sin\left(\frac{2\pi(t-t_1)}{T}\right), \quad T = t_2 - t_1, \quad t_1 \leq t \leq t_2 \quad (1)$$

for the sine, type A fling model, where, $s(t)$ is the ground displacement time-series, t_1 and t_2 are the start and stop times and T is the duration of the acceleration sine.

For the cosine type B type fling model the expression is similar

$$\ddot{s}(t) = A \cos\left(\frac{2\pi(t-t_1)}{T}\right), \quad T = t_2 - t_1, \quad t_1 \leq t \leq t_2 \quad (2)$$

Integration of the above equations gives the type A and type B profiles for velocity and displacement. These are shown in Figure 4 and Figure 5.

The profile is type A where the acceleration is shown as a sine pulse, leading to a one-sided velocity pulse and ramp-like displacement. The displacement therefore retains its permanency and doesn't recover. The type B cosine profile leads to a two-sided velocity profile where the displacement recovers. The wavelet transform extracts mainly type A profiles in the lower frequency sub-band and type B profiles in the higher frequency sub-band. The latter are summed with the former and give rise to an estimate of the local ground motion.

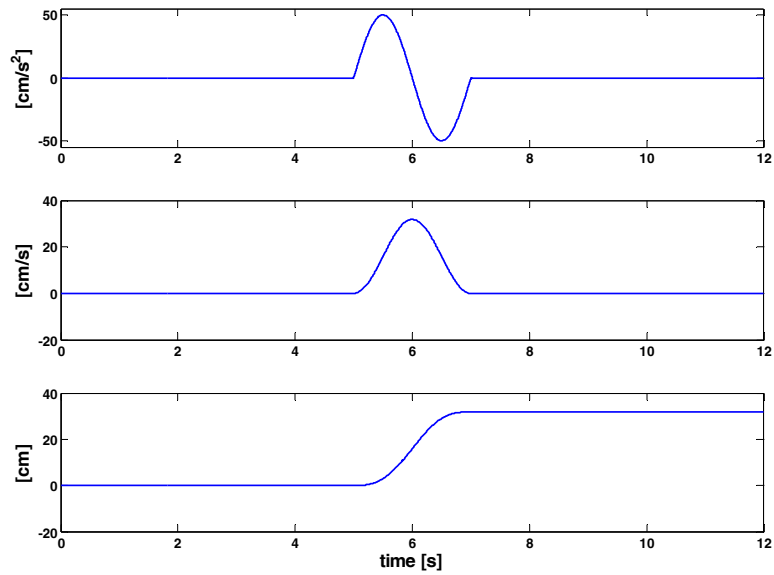


Figure 4: Sine model of type A fling profiles. Type A fling leaves a permanent displacement

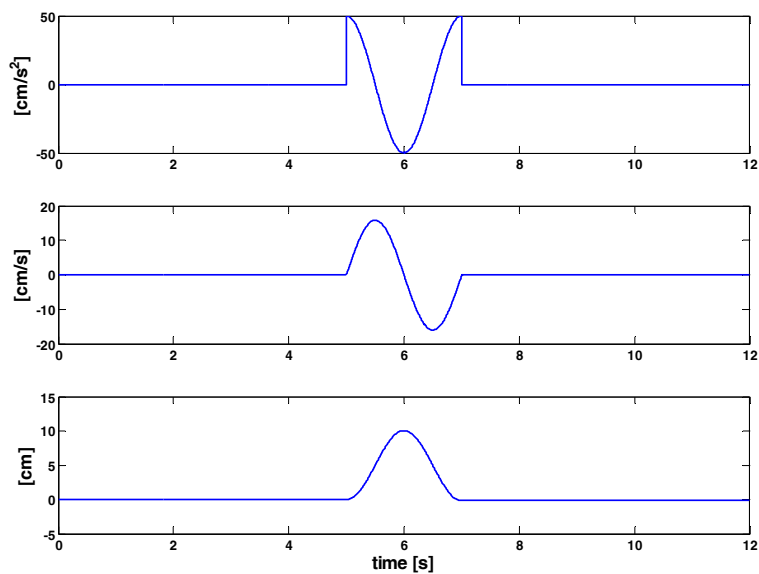


Figure 5: cosine models of type B fling profiles. Type B fling leads to a recovery in displacement

3.1 Correcting for Baseline shift

Baseline shifts [3,10,11,12,15] are a cause of integration problems when integrating from acceleration through to displacement. These are caused by instrument/sensor tilts during the earthquake. They lead to offsets in acceleration, velocity and displacement.

In order to resolve this issue of the baseline shift, the paper invokes the conditions specified in [13], these are repeated below for ease and coherence of presentation.

1. The input ground motion must be purely translational, without any tilting or any other natural distortions.
2. The record must contain clear beginning and ending parts with relatively small amplitudes to allow baseline correction.
3. The signal to noise level of the record must be high enough, at least 40dB.

Condition (1) implies the ideal low frequency model of the acceleration fling(s) shown in Figures (4) and (5). Condition (2) is met after de-noising with the wavelet transform and extracting the low-frequency fling. In order to meet fully condition (1) the extracted low frequency, acceleration time history is zeroed after the sine-like fling and re-integrated to yield the velocity and displacement. Condition (3) requiring a SNR of 40dB is optimistic, the SNR found were much less than that required in [13]. It is shown in this paper that, using only the lower frequency sub-band timeseries extracted by the wavelet transform, it is possible to approximate the pure translational ground motion.

4 Baseline Correction and Estimation of Tilt Angles

Typically, an accelerometer records timeseries a_i or \ddot{a}_i from which an estimate of the ground motion \hat{x}_i , can be obtained through de-convolution. Note that all equations in this section only apply to the horizontal components of the accelerometer.

$$\hat{x}_i = \ddot{x}_i - g\psi_{3-i} - \varepsilon, \quad i \in \{1, 2\} \quad (3)$$

However, it is clear that recorded and obtained estimate \hat{x}_i is not precisely the translational ground acceleration \ddot{x}_i i.e. it is corrupted by the tilt timeseries ψ_{3-i} and the instrument noise timeseries ε , both of which are unknown. In order to obtain the velocity and displacement timeseries we must integrate \hat{x}_i and recognize it is not precisely \ddot{x}_i .

In general, the tilt angles impose a linear error in velocity and quadratic error in displacement after the end of the timeseries. While the instrument noise may produce oscillations of low frequency content that may also be linear/quadratic like after the end of the timeseries. Thus, it is essential that an effective noise reduction strategy is employed to increase the signal to noise ratio. Wavelet de-noising provides such a strategy and is employed to reduce the magnitude of instrument noise. This allows a clearer distinction between errors due to tilts and errors due to noise in derived displacement timeseries. A wavelet based de-noising strategy is far superior to band pass filtering, as it make no assumption as to the frequency content of the noise.

To remove this quadratic from the displacement time series for $t > T_i$ we zero the low frequency sub-band acceleration time series for $t > T_i$. The time T_i is the time at which the low frequency sub-band velocity timeseries returns to zero. A least squares fit of the form in equation (4) is obtained from the displacement timeseries for $t > T_i$. From this optimal quadratic the following estimates of tilt angles, equation (5), are achieved.

$$x = c_2 t^2 + c_1 t + c_0 \quad (4)$$

$$\psi_{3-i}^* = \frac{2c_2}{g}, \quad \bar{\psi}_{3-i} = \frac{c_1}{gT_i} - \psi_{3-i}^* \quad (5)$$

The higher frequency sub-bands for all three components do not require any correction. These reset to zero in the latter portion of the time history after the strong motion and after application of the wavelet transform. This isn't the case for other events in which the same correction is applied to the higher frequencies.

In the result section 5, the *bior1.3* wavelet is used throughout because it has linear phase properties, though other wavelet bases give similar results.

5 Results

5.1 Results for TCU052V

Figure (6) shows the result for the low frequency sub-band of the vertical component for TCU052, with and without baseline correction. It's clear there isn't a great deal of difference between the time histories with and without the correction. Pendulum theory [13] demonstrates that for small angles, the vertical component is insensitive to tilt and responds only to acceleration due to translation. The offset shown in the displacement before correction is 58.6cm (at 278.6cm) at 90sec, and is due to sensor noise.

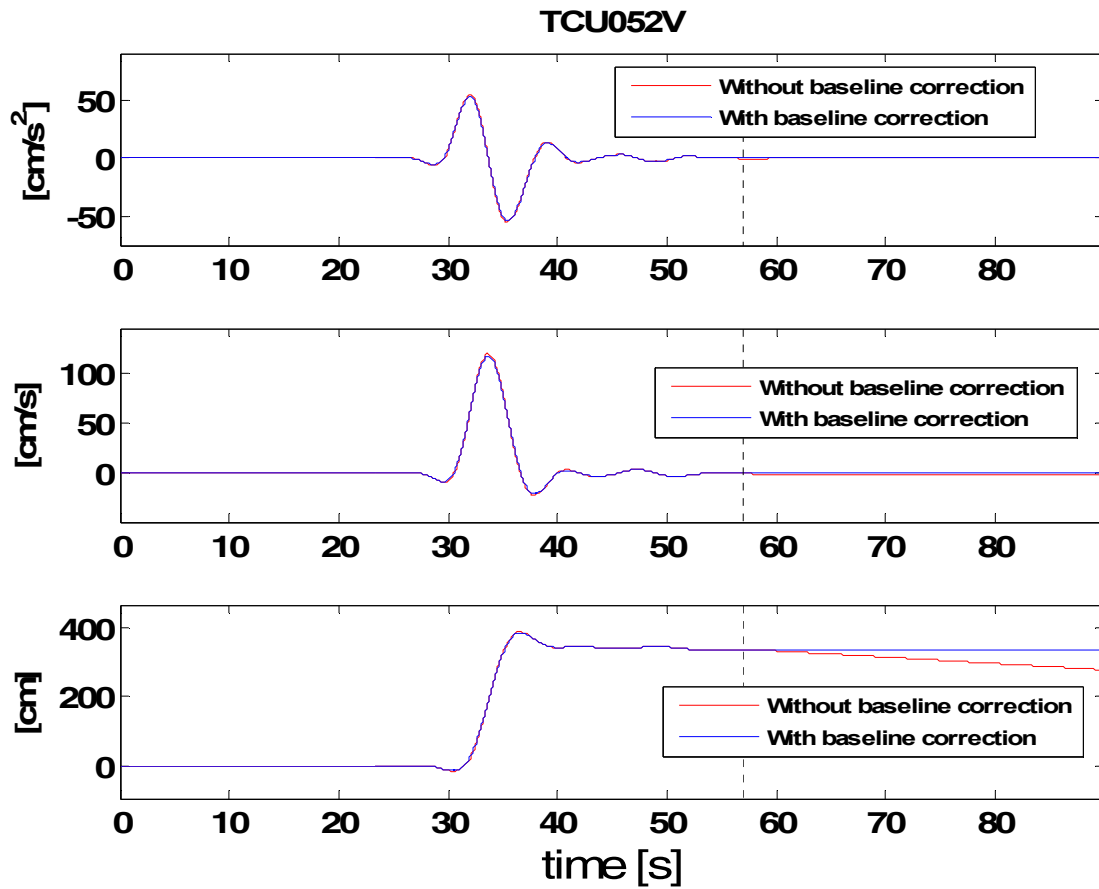


Figure 6: TCU052 low frequency sub-band fling for vertical component at level 9, using the bior 1.3 wavelet

Figure (7) shows the resulting time histories re-integrated from the acceleration after wavelet transforming, de-noising and correcting for baseline shift of $T_i=56.8\text{sec}$, the final displacement is 336.9cm, this compares with 350cm published in [1], and 397.2cm GPS, 2.7km distance.

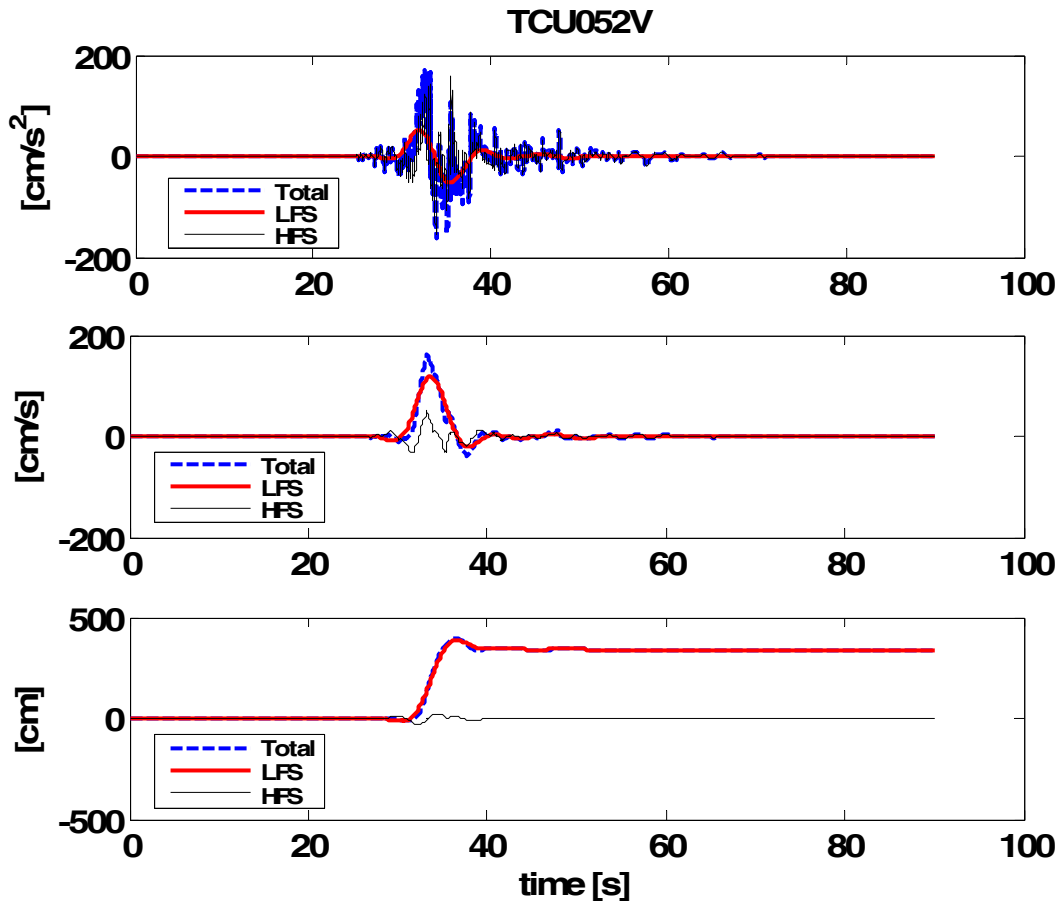


Figure 7: TCU052N comparing the low frequency sub-band (LFS), the higher frequency sub-band (HFS) and the total time history after correction and re-integration from acceleration to displacement

5.2 Results for TCU052N

Figure (8) shows the low-frequency fling for the northern component. Level 10 was selected for this analysis because it gives an acceleration fling with very much less ripple in the latter portion of the time history, therefore is a better approximation to the model fling of Figure (4). Figure (9) shows the low frequency sub-band (LFS) compared with the higher frequency sub-band (HFS) and with the corrected time-history after re-integration. The T_i for this correction is 48.76sec and the final displacement is 625.4cm. This compares with 687.9 obtained by [1] and 845.1cm GPS, 2.7km distance.

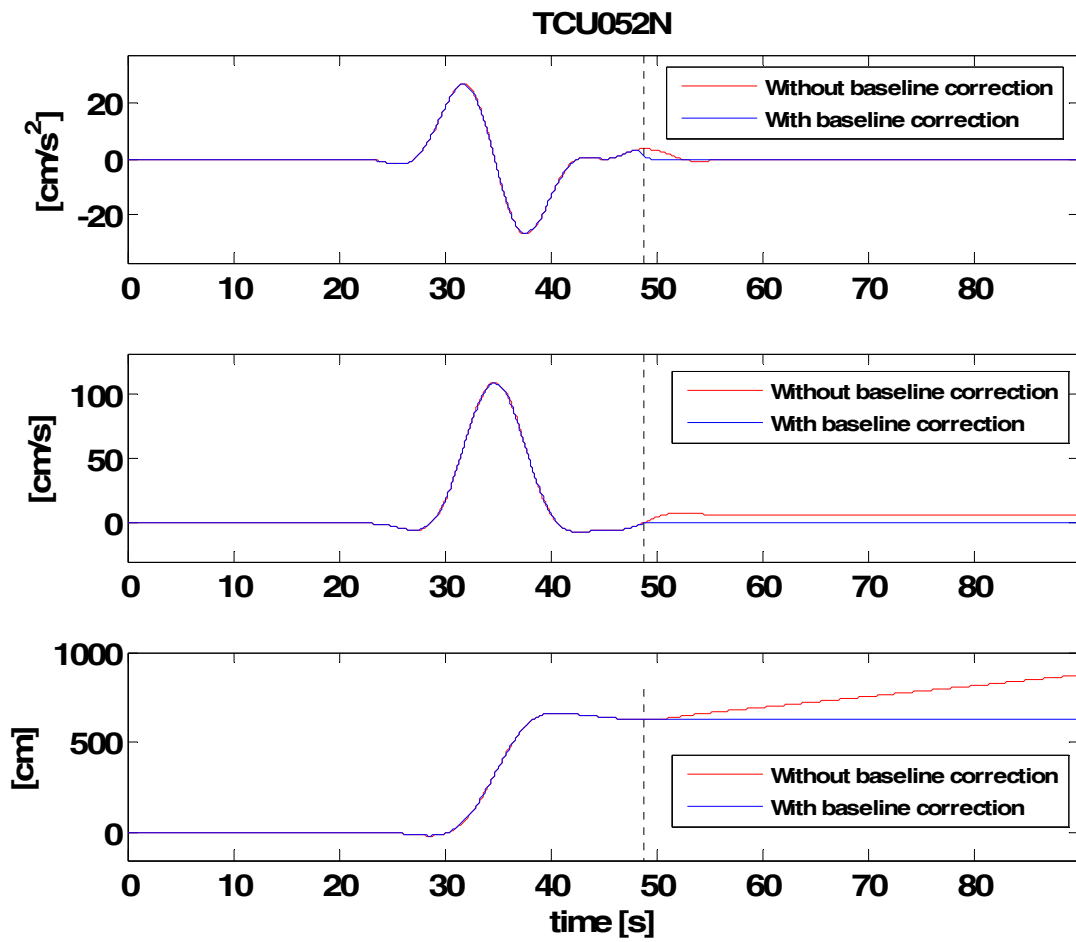


Figure 8: TCU052 low frequency sub-band fling for northern component at level 10, using the *bior 1.3* wavelet

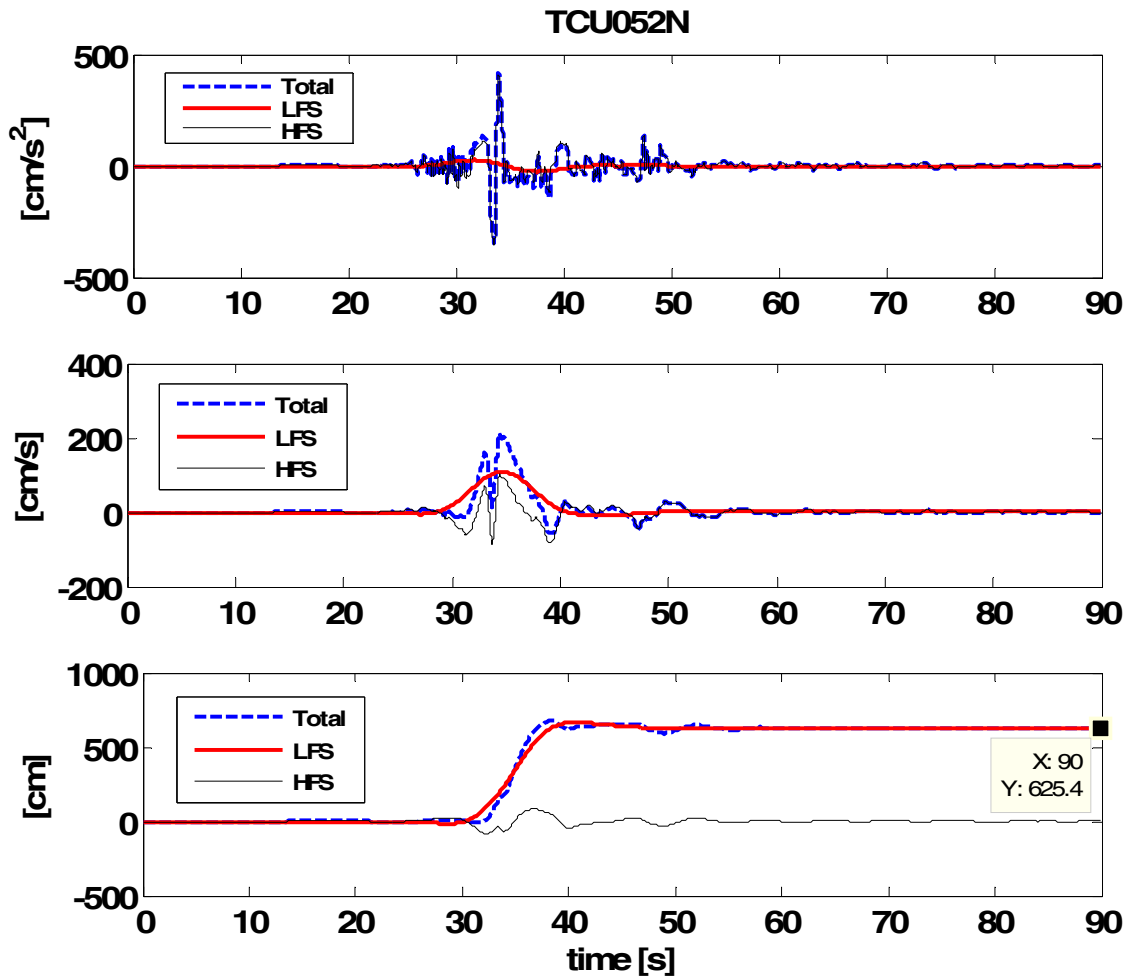


Figure 9: TCU052N comparing the low frequency sub-band (LFS), the higher frequency sub-band (HFS) and the total time history after correction and re-integration from acceleration to displacement.

5.3 Results for TCU052E

Figure (10) below shows the low frequency sub-band fling for the easterly component, at level 10 and using the *bior1.3* wavelet. As for the northerly component level 10 was selected since the acceleration fling was the closest to a model fling, and almost ripple free in the latter half of the low frequency acceleration time history, as shown above. Figure (11) compares the low and high frequency sub-bands and gives the total resultant displacement after correcting the acceleration sub-bands and re-integrating. The T_i for the correction is at 40.05sec and the permanent displacement is at -355.3cm , this compares with -357.7cm published in [1] and -342cm GPS at 2.7km distance.

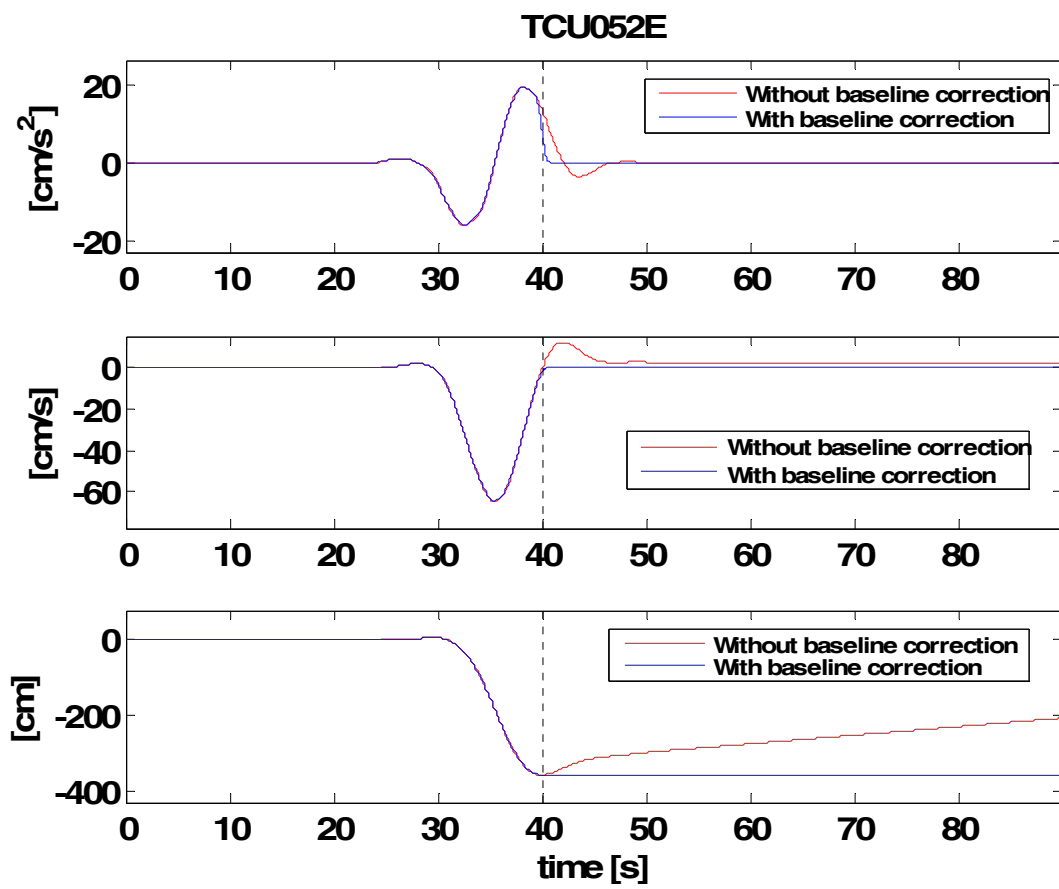


Figure 10: TCU052 low frequency sub-band fling for the easterly component at level 10, using the bior 1.3 wavelet

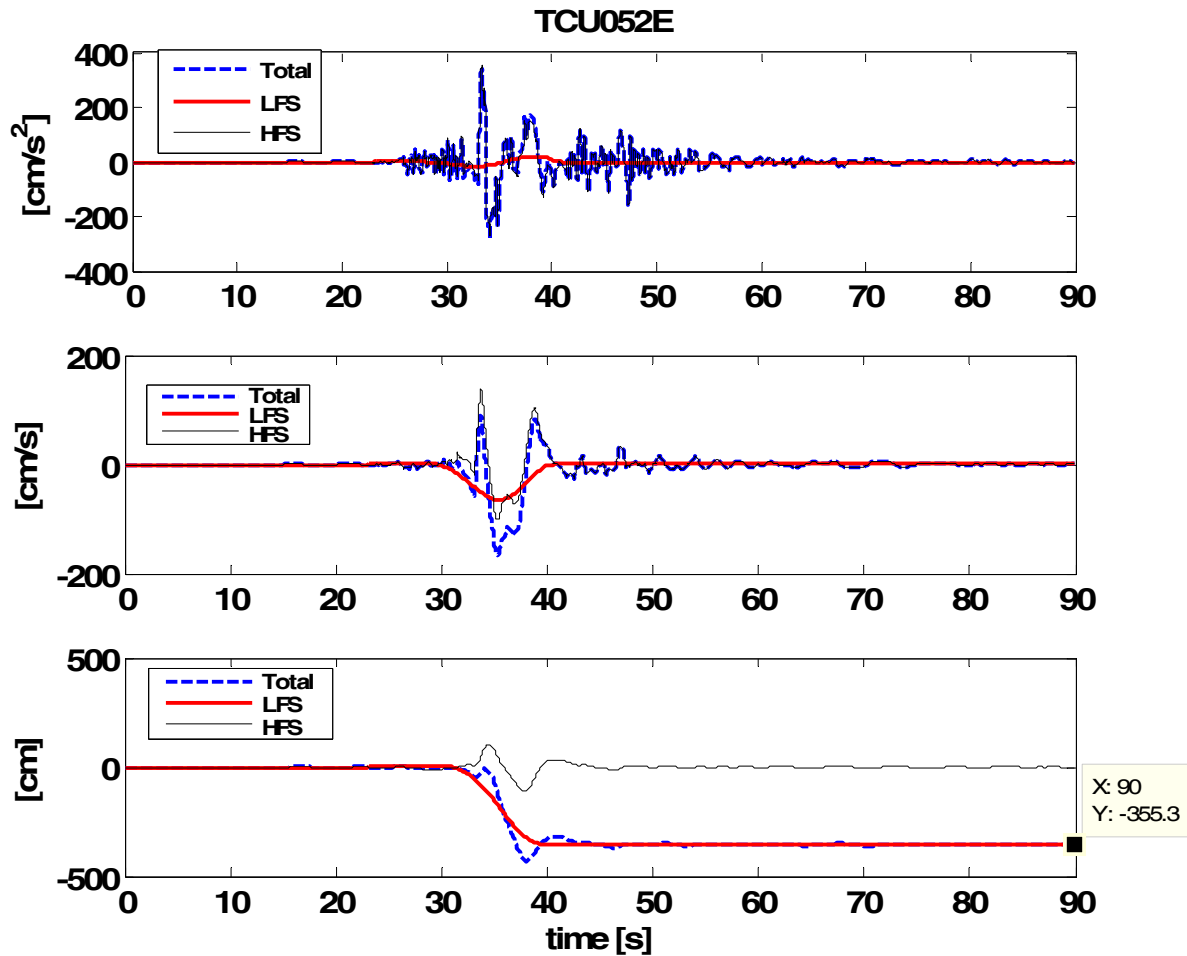


Figure 11: TCU052E comparing the low frequency sub-band (LFS), the higher frequency sub-band (HFS) and the total time history after correction and re-integration from acceleration to displacement.

6 Summary

Table 1 and 2 below summarise the data profile of the TCU052 event. The final residual displacement is 8m. The above displacement results are consistent with those obtained in [1], in which they developed a baseline correction scheme based on the [2]. The method described in this paper uses the wavelet transform, which isolates the low-frequency fling, corrects automatically for baseline shift and re-integrates from acceleration down to displacement. In addition the method determines the mean and residual tilt angles for the horizontal components by least squares fitting the quadratic displacement offset. The method is relatively easy to use and the analysis uses the condition (i) and (ii) extensively, as in [13]. These essentially set out the framework for obtaining estimates of ground motions due to translation only. In doing so the lower frequency content in particular should give

the type A sine model as a basis for approximating as best possible the model fling in the long period. It also uses the type B cosine model for the short period. To comply with condition (i) and (ii) for the lower frequencies, the wavelet transform is used to filter and de-noise and then to integrate the low-frequency sub-band (LFS) and the higher frequency sub-band (HFS) separately for the velocity and displacement profiles. The object then is to zero the tilts and other distortions in the latter portion of the LFS acceleration time history, then to re-integrate to obtain the velocity and displacement profiles, which resembles the fling type A model. This method doesn't supersede any other methods, but presents an alternative, which is quick and easy to use.

Wavelet <i>bior1.3</i>		Baseline e point	Residual disp.	Disp offset	GPS:Wu (2.7km)	Mean tilt	Residual tilt
	i	T_i	$x_i(t_{end})$			$\bar{\psi}_{3-i}$	ψ_{3-i}^*
		[s]	[cm]	[cm]	[cm]	[Deg.]	[Deg.]
TCU052E	1	40.05	-355	150	-342.3:-357.7	0.0051	-0.0024
TCU052N	2	48.76	635	248	845.1:687.9	0.0077	-9.13E-4
TCU052V	3	56.93	337	59	397.2:350.5	-	-

Table 1: Estimated data obtained from corrected Chi-Chi Event.

	Signal \bar{s} (dB)	Noise $\bar{\epsilon}$ (dB)	SNR (dB)
TCU052E	38.8	0.45	38.36
TCU052N	39.1	1.57	37.49
TCU052V	28.2	1.34	26.8

Table 2: Estimated Signal-to-Noise Ratio (SNR)

7 Iceland Event May 29th 2008

On May 29th 2008 an earthquake occurred in Iceland in the Olfus district about 8 km NE of the town of Selfoss. According to the USGS and the EMSC the magnitude of the earthquake was 6.3. The Icelandic Strong Motion Network and the newly installed ICEARRAY network recorded this seismic event. The ICEARRAY is a small aperture array located around the village of Hveragerdi. A total of 13 stations recorded the event and all 39 components have been analysed using the methodology described in this paper, therefore some results are presented.

5.1 Station 1, Component 1 (EW)

Figure (12) shows the low frequency fling is approximately 2 cm/sec/sec producing a velocity pulse, with a peak velocity of approximately 4cm/sec, which gives rise to a displacement of 12.34cm. In this case the acceleration fling is not as smooth as that for the Chi-Chi event, but nevertheless is clearly manifest.

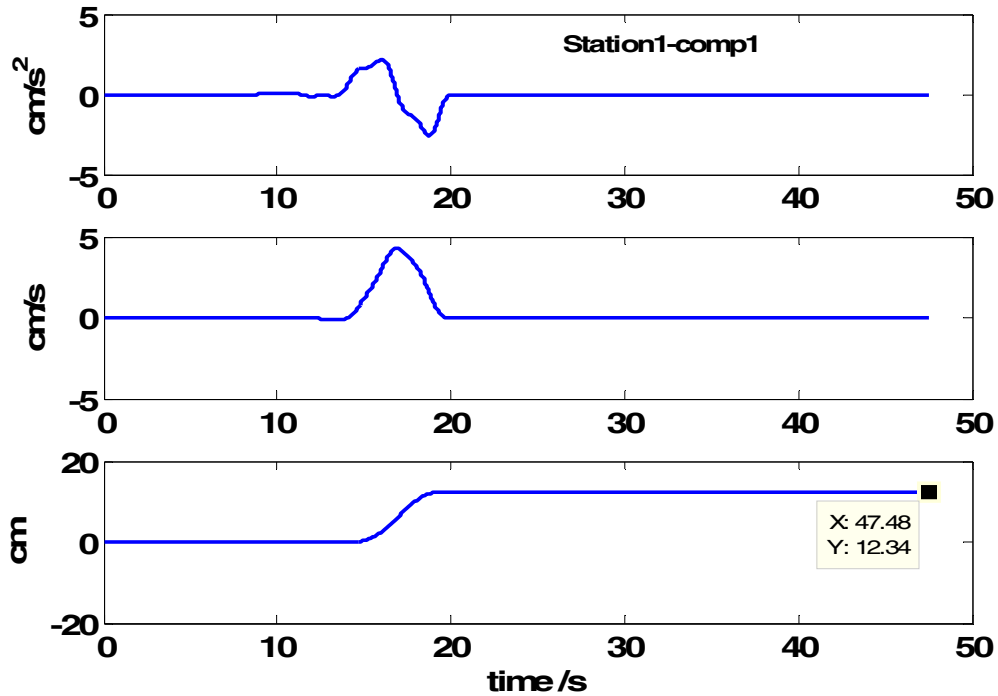


Figure 12: low frequency sub-band (LFS) acceleration fling for the EW component of station 1 and a velocity peak.

Figure (13) shows the low and higher frequency sub-bands after correction and re-integration from acceleration to displacement. The T_i for the correction is at 19.35sec and the permanent displacement is at 12.34cm.

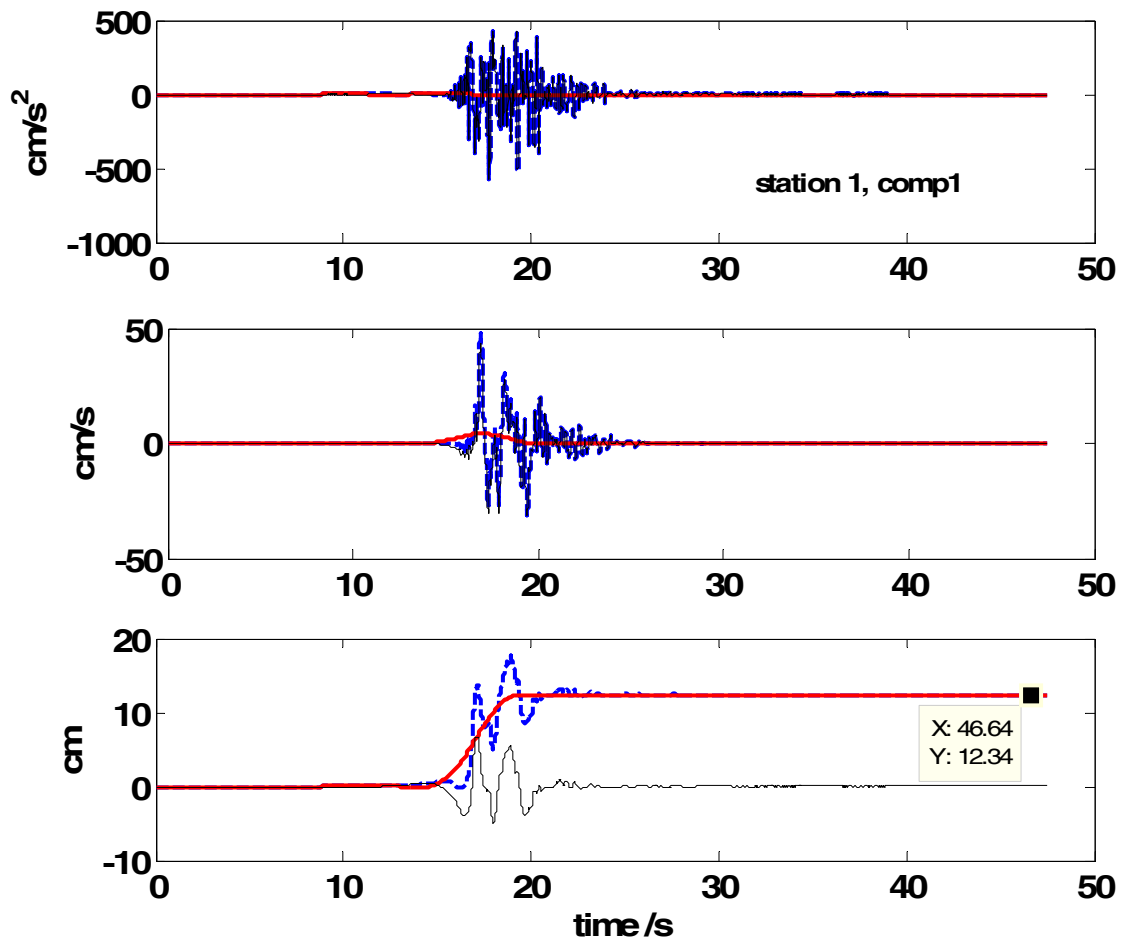


Figure 13: comparing the low frequency sub-band (LFS), the higher frequency sub-band (HFS) and the total time history after correction and re-integration from acceleration to displacement for the EW component.

7.2 Station 1, Component 2 (NS)

Figure (14) shows a –sine type A acceleration fling response with sensors aligned in the opposite direction to the ground movement. The peak fling acceleration is approximately 14cm/sec/sec and the peak velocity pulse is at 10cm/sec, giving rise to a displacement of 13.37cm. Figure (15) shows a comparison of the low and higher frequency components as well as the total acceleration, velocity and displacement. The T_i for the correction is at 18.99sec and the permanent displacement is at 13.37cm., the T_i is consistent with that for the EW component. The resultant motion in a NW direction is approximately 18cm; this is consistent with GPS, which gives an overall displacement of 17cm NW.

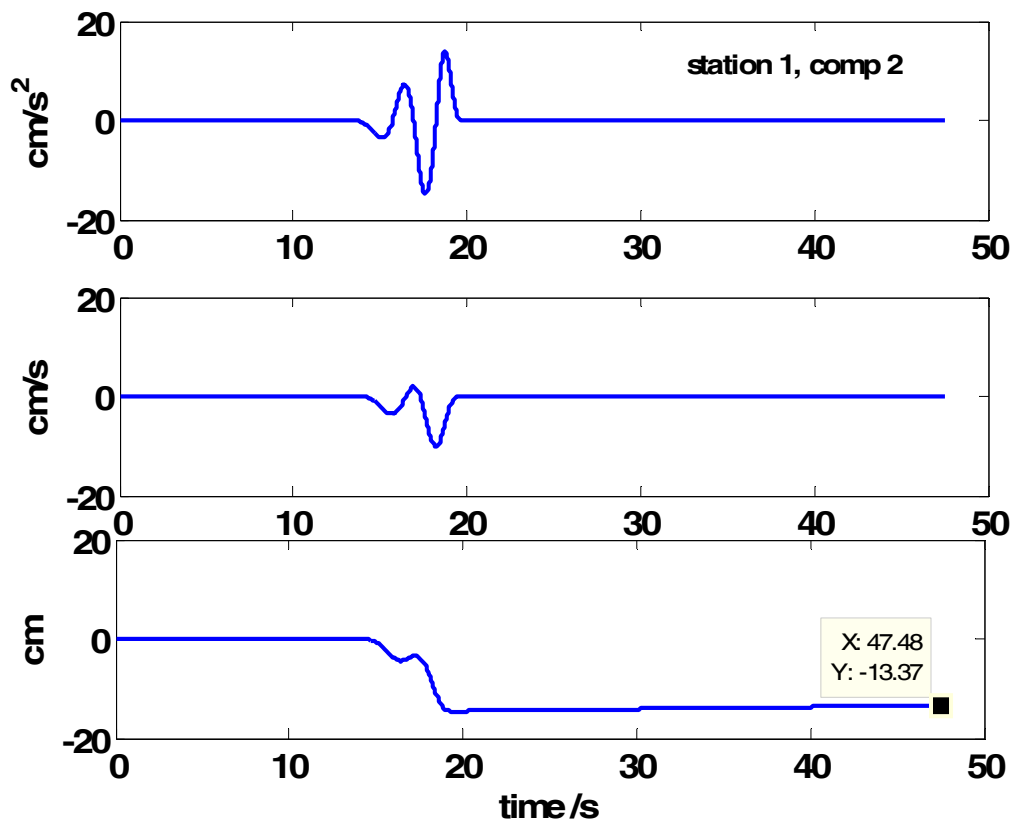


Figure 14: low frequency sub-band (LFS) acceleration fling for the NS component of station 1 showing a (-)sine type A time history

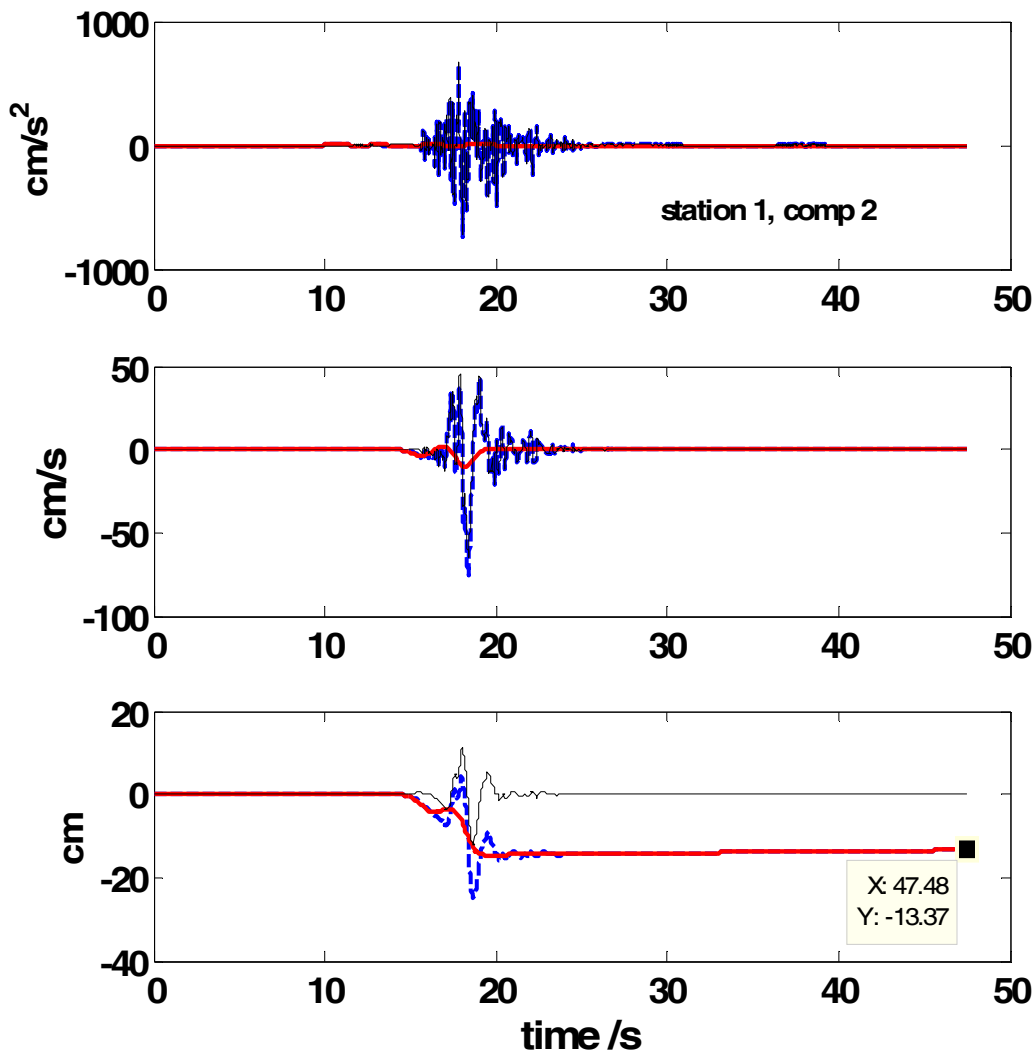


Figure 15: comparing the low frequency sub-band (LFS), the higher frequency sub-band (HFS) and the total time history after correction and re-integration from acceleration to displacement for the NS component.

7.3 Station 1, Component 3 (V)

Figure (16) above shows the low frequency acceleration sine type A fling, which gives a pulse like velocity of 0.6cm/sec and a permanent displacement of 1.2cm. Figure (17) below, shows the low and higher frequency time histories and the resultant after re-integration from acceleration to displacement.

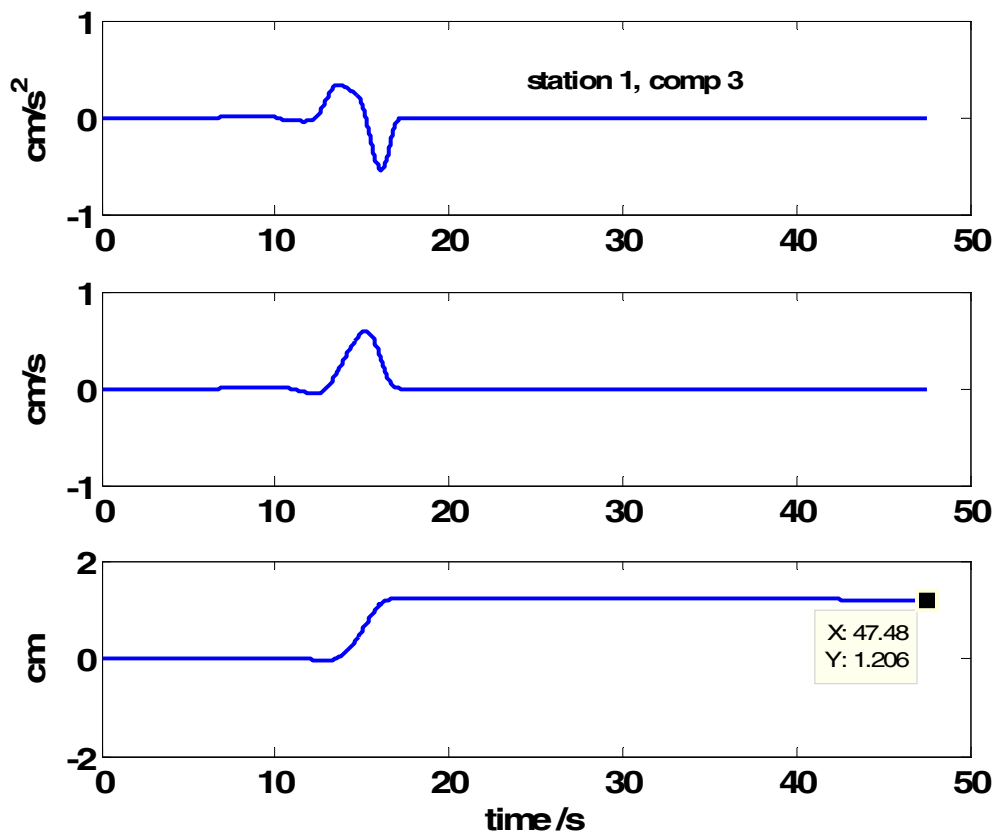


Figure 16: low frequency sub-band (LFS) acceleration fling for the Vertical component of station 1 showing a sine type A time history, with a permanent displacement of 1.2cm

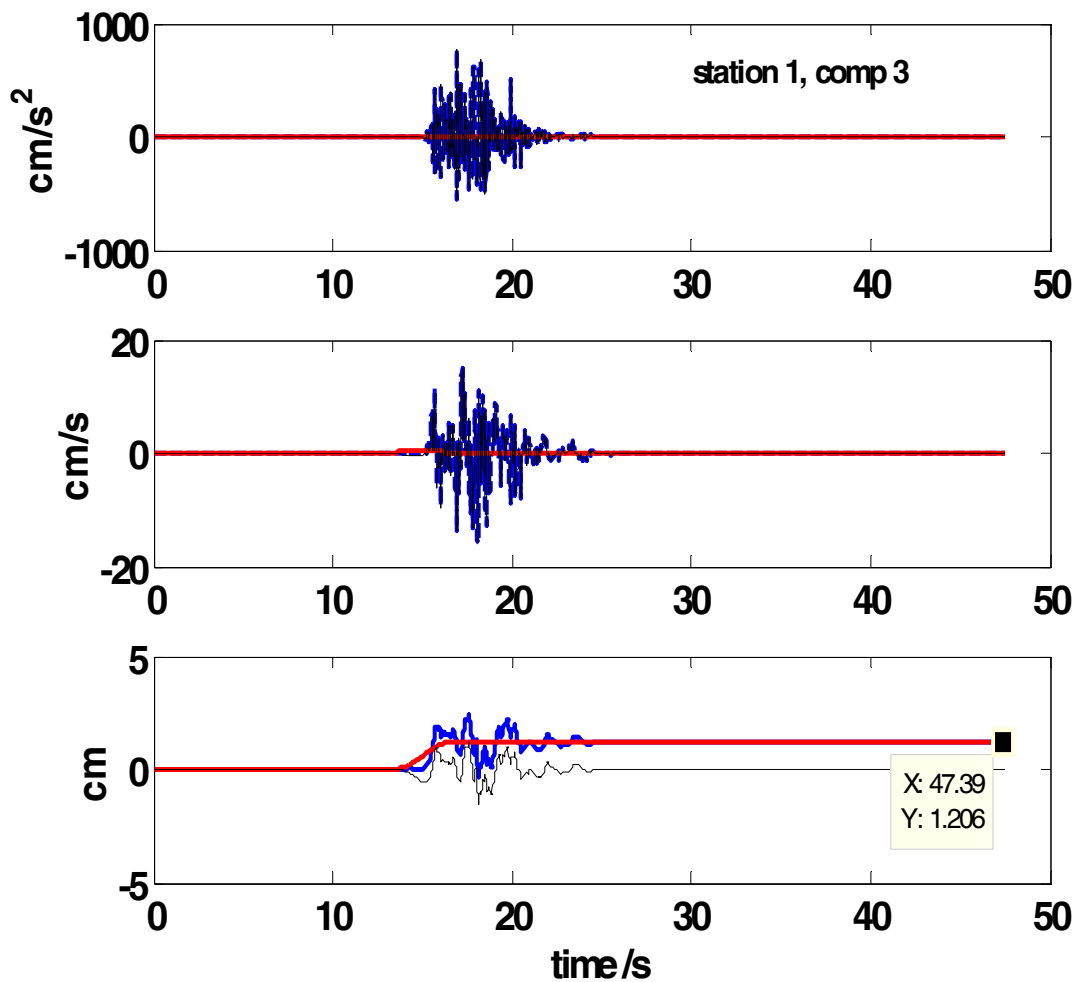


Figure 17: comparing the low frequency sub-band (LFS), the higher frequency sub-band (HFS) and the total time history after correction and re-integration from acceleration to displacement for the Vertical component.

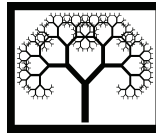
7.4 Summary

The results for horizontal and vertical components are similar for the 11 stations; these make up the ICEARRAY in the village of Hveragerdi. GPS shows that the village moved 17cm NW and most of the results reflect this movement to within a few centimetres. Stations 12 and 13 however, were some way away from the ICEARRAY and their results are not the same with net displacements much less than that experienced in Hveragerdi.

References

- [1] Y.-M. Wu and C.-F. Wu, "Approximate recovery of coseismic deformation from Taiwan strong-motion records," *Journal of Seismology*, vol. 11, pp. 159-70, 2007.
- [2] W. D. Iwan, M. A. Moser, and C. Y. Peng, "Some observations on strong-motion earthquake measurement using a digital accelerograph," *Bulletin of the Seismological Society of America*, vol. 75, pp. 1225-46, 1985.
- [3] D. M. Boore, "Effect of baseline corrections on displacements and response spectra for several recordings of the 1999 Chi-Chi, Taiwan, earthquake," *Bulletin of the Seismological Society of America*, vol. 91, pp. 1199-211, 2001.
- [4] [Daubechies I, Ten Lectures on Wavelets, SIAM, Philadelphia, PA, 1992
- [5] N. A. Alexander, A. A. Chanerley, and N. Goorvadoo, "A review of procedures used for the correction of seismic data," in *Proceedings of the Eight International Conference on Civil and Structural Engineering Computing*, Vienna, Austria, 2001, pp. 101-102.
- [6] A. A. Chanerley and N. A. Alexander, "Correcting data from an unknown accelerometer using recursive least squares and wavelet de-noising," *Computers and Structures*, vol. 85, pp. 1679-1692, 2007.
- [7] A. A. Chanerley and N. A. Alexander, "Using the total least squares method for seismic correction of recordings from unknown instruments," *Advances in Engineering Software*, vol. 39, pp. 849-860, 2008.
- [8] A. A. Chanerley and N. A. Alexander, "An approach to seismic correction which includes wavelet de-noising," in *Proceedings of the Tenth International Conference on Civil, Structural and Environmental Engineering Computing*, Prague, Czech Republic, 2002, pp. 107-108.
- [9] S.-M. Chen and Loh C-H, "Estimates of Permanent Ground Displacements from Near-fault, Strong-Motion Accelerograms," in *1st European Conference of Earthquake Engineering & Seismology*, Geneva, 2006.
- [10] M. Trifunac, V. Lee, and M. Todorovska, "Common problems in automatic digitization of strong motion accelerograms," *SOIL DYNAMICS AND EARTHQUAKE ENGINEERING*, pp. 519-530, 1999.
- [11] M. D. Trifunac, "Zero baseline correction of strong-motion accelerograms," *Bulletin of the Seismological Society of America*, vol. 61, pp. 1201-11, 1971.
- [12] D. M. Boore and J. J. Bommer, "Processing of strong-motion accelerograms: needs, options and consequences," *Soil Dynamics and Earthquake Engineering*, vol. 25, pp. 93-115, 2005.
- [13] V. M. Graizer, "Effect of tilt on strong motion data processing," *Soil Dynamics and Earthquake Engineering*, vol. 25, pp. 197-204, 2005.
- [14] R. Nigbor, "Six-degree-of-freedom ground motion measurement", *Bul. Seism. Soc. America* 84, 1665-1669.
- [15] R Boroschek and D Legrand, "Tilt Motion Effects on the Double-Time Integration of Linear Accelerometers: An Experimental Approach", *Bull. Seism Soc America* 96, 6 pp2072-2089, 2006

- [16] R. Coifman and D. L. Donoho, *Translation Invariant De-Noising, Wavelets and Statistics, Lecture Notes in statistics* vol. 103, pp125-50: Springer-Verlag, 1995.
- [17] D. L. Donoho, "De-noising by soft-thresholding," *IEEE Transactions on Information Theory*, vol. 41, pp. 613-627, 1995.



Automated Baseline Correction, Fling and Displacement Estimates from the Chi-Chi Earthquake using the Wavelet Transform

A.A. Chanerley¹ and N. Alexander²

**¹School of Computing & Technology
University of East London, United Kingdom**

**²Department of Civil Engineering
University of Bristol, United Kingdom**

Abstract

This paper proposes a novel approach using a wavelet-based algorithm for the routine processing of seismic events, baseline correction and displacement and shows that the wavelet transform extracts the acceleration ‘fling’ completely naturally from seismic events. It uses seismic records from the Chi-Chi event and extracts the fling by applying wavelet filter banks for decomposition and reconstruction. Initially the choice of wavelet is based on the shape of the long-period ‘fling’ and in this case the Haar Transform, db1, and db(2) and their associated filter banks seem well suited. These wavelets also give depth of decomposition such that an optimal estimate of ‘fling’ and thus consequent displacement is obtained. Other Wavelet transforms also give good results therefore the method is not transform specific. This method can automatically correct for baseline shifts in the velocity characteristics, to then obtain displacements, but there can be a trade off. Moreover the process is routine and relatively straightforward to implement. The displacements are compared with GPS readings and results using other methods and the initial results are encouraging. In particular the acceleration and velocity ‘fling’ are manifest as the transform runs through the decomposition levels, which lends credibility to this routine method of seismic and baseline correction and displacement estimation. The point to make is that at a particular level of decomposition, the wavelet transform separates the long and short period acceleration sub-bands. It then becomes easier to perform a 1st and 2nd integration separately on the short period but in particular the long period, which identifies acceleration and velocity ‘fling’ and velocity baseline offsets, the latter which can then be corrected.

Keywords: correction, seismic, wavelet transform, integration, Chi-Chi, Abrahamson’s ‘fling’, decomposition, reconstruction.

1 Introduction

Strong ground motions at near-fault sites may contain long period, pulse type waves which induce substantial permanent ground deformation. Standard filtering methods [1] cannot extract such permanent displacements of the ground from acceleration time-histories. Recent work in [2] compares estimates of displacement obtained through 1st and 2nd integration's from the Chi-Chi events with those of GPS readings taken near the sites of the strong-motion recordings. In order to obtain reasonable estimates of displacements a baseline correction procedure has been required. Thus approximate methods have been used in order to correct for baseline shift and then integrate for velocity and integrate again for displacement. The difficulty is that a standard and automated procedure for baseline-shift correction had not hitherto existed. Most of the baseline correction schemes have been based on a two-point scheme proposed in [3] with modifications proposed by [4]. A good corrected displacement history is similar to a ramp function [2] between two points suitably chosen. However, the choice of differing points can lead to considerably different estimates of final displacements.

The wavelet transform has been used [5,7] for de-noising the seismic record prior to de-convoluting the instrument response. The wavelet transform has also been used [6] in order to implement baseline correction scheme and consequent estimates of permanent displacement of some Chi-Chi seismic recordings. The procedure [6] uses a 3-phase approach but is still complicated requiring selection processes at the various phases, but their results compare favourably with GPS readings.

The proposition from this paper is essentially an easy and almost automated operation. It is routine and applies an automated stationary-wavelet procedure to look for the long period, 'fling' in the acceleration and velocity time histories at a suitable decomposition level. The main point to note is that the wavelet transform successively down-samples, convolutes, de-noises and separates the long and short period sub-bands of the acceleration time histories, at each level of decomposition. A threshold scheme removes the resulting coefficients below a certain value and then reconstructs a de-noised time-history from the long and short period de-noised sub-bands, using the inverse wavelet transform.

2 Filter Bank Approach to the Wavelet Transform

The wavelet transform may be considered as a set of complementary low-pass and band-pass filters, which can correlate/convolute and down sample by a factor of 2, a noisy signal by successively applying the filters. Effectively the process decomposes i.e. halves the frequency band each time (hence the name dyadic sampling) creating sub-bands. Each time it applies a low-pass filter bank it decomposes the transition band by a factor of 2 moving to lower sub-band frequencies at each level of decomposition.

A similar argument applies to the band-pass filter banks for the shorter period parts of a signal.

Moreover the method takes the discrete wavelet transform (DWT) [8,12] of a signal, and passes the transform through a threshold [9,12], which de-noises the signal. It removes the coefficients below a certain value and then takes the inverse DWT in order to reconstruct a de-noised time signal. Reconstruction is the inverse process of decomposition, which up samples by a factor of 2 and applies low-pass and high pass filter banks. The DWT is able to concentrate most of the energy of the signal into a small number of wavelet coefficients, after correlating/convoluting and down sampling with the appropriate filter weights depending on the selection of a wavelet basis. In this case the wavelet ‘db1’, (Daubechies (1)) and ‘db2’ (Daubechies (2)) were chosen over other wavelets because they gave a greater depth of decomposition levels, necessary for some of the seismic events and because to some extent they correlate with the acceleration ‘fling’. The dimensions of the wavelet coefficients will be large compared to those of the noise coefficients obtained after high pass filtering. Therefore thresholding or shrinking the wavelet transform will remove the low-amplitude noise in the wavelet domain and the inverse DWT will retrieve the desired signal with little loss of detail. A block diagram of a 1-level, 2-band the operation is shown in Figure (1).

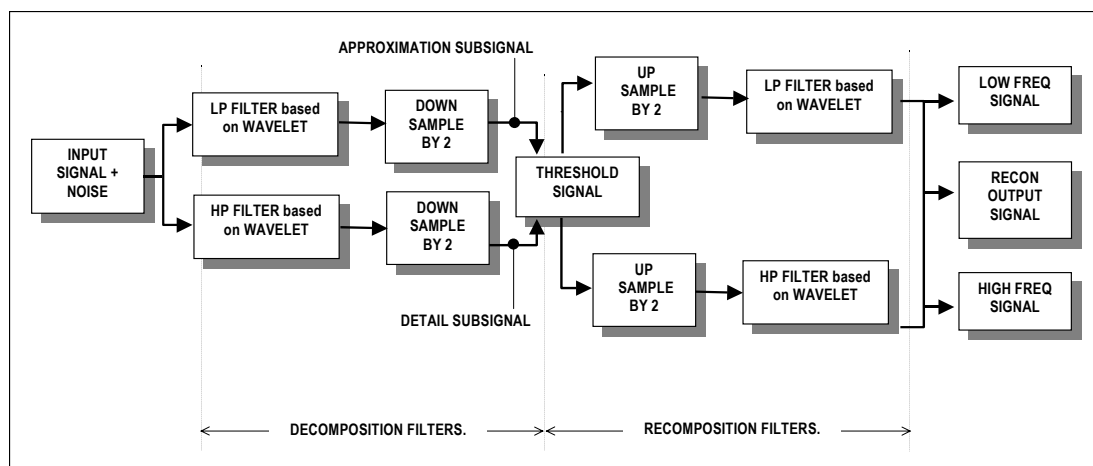


Figure 1: 1-level, 2-band Wavelet de-noising block diagram

However the DWT is not translation invariant and so the implementation in this paper uses the stationary or translation invariant wavelet transform [10,12]. This essentially applies a range of signal shifts to allow for misalignment of the signal and wavelet features, it then averages out the shifts in order to obtain the de-noised signal

The problems with shift-invariance are connected with the alignment between features in the signal and features of the wavelet basis. In particular at discontinuities where Gibbs like phenomena can occur with unwanted oscillations. An approach to surmount this problem is described in [10,12] where it is suggested to forcibly shift the signal, so that it's features change positions in relation to the wavelet basis. Then to un-shift and retrieve the de-noised signal hopefully without any unwanted noise or spurious oscillation i.e.

Average [Shift → De-noise → Un-Shift]

The diagram of Figure 1 shows that both the low frequency and the high-frequency components of the signal can be extracted. It shows only one level of decomposition, but a wavelet decomposition tree is usually implemented, where the resulting low frequency component is further decomposed showing the long period pulse type signal with greater clarity as we move to higher levels of the decomposition tree

3 Selection of Wavelet Basis

In this paper wavelet 'db1', the Haar transform, wavelets 'db2', are selected and mainly used at typical decomposition levels of 10 and 11. The 'db1' Haar transform has a rectangular shape, which correlates with a clipped, long period, "fling" and the wavelet 'db2', has a spiky 'fling' shape. This is shown in Figures (2). Other wavelets also have a shape, which is similar to the seismic waveform for particular events. These therefore and their associated filter banks are well suited to the task and gives good results for the seismic records under investigation.. These give a good 'fling' output of the long-period acceleration and velocity time-history, and a ramp-like displacement time history. Other wavelet bases are also possible and Figure (3) illustrate the point with bi-orthogonal wavelet pairs bior1.3 and bior6.8, showing that reasonable displacements are obtainable by both with only one level of adjustment. Figure (4) uses the Haar wavelet (db1) and db10. The former gives a maximum of 15 levels of decomposition with good results. The Haar wavelet result is consistent with that of [2] and GPS as shown for the vertical component of TCU052 from the B-series of seismic events [11].

Wu & Wu 2007 [2]
disp = 350.5cm

GPS [2]
disp = 397.2cm

Wavelet 'db1'
level = 11, disp = 358.8cm
level = 10, disp = 380.4cm

4 Results

4.1 TCU052 N-component

This component gives a large GPS reading. It shows the onset of a big ‘fling’, shown in Figures (5) and (6). This demonstrates the results of wavelet de-noising and decomposition, followed by the two integrations on TCU052, North component.

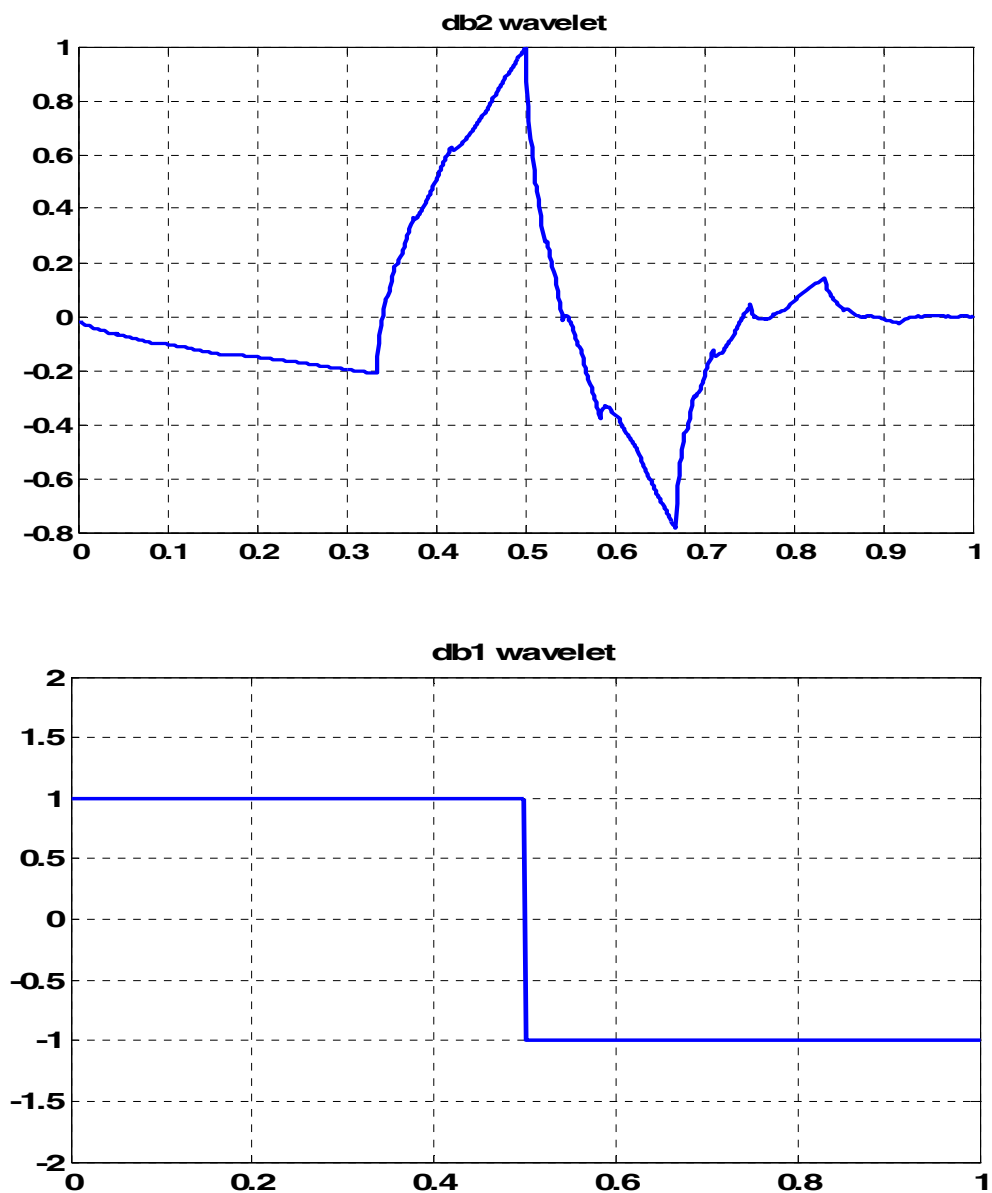


Figure (2) The ‘db2’ wavelet, showing a shape similar to that of a spiky acceleration ‘fling’ and the ‘db1’ wavelet as that of a clipped ‘fling’ shape.

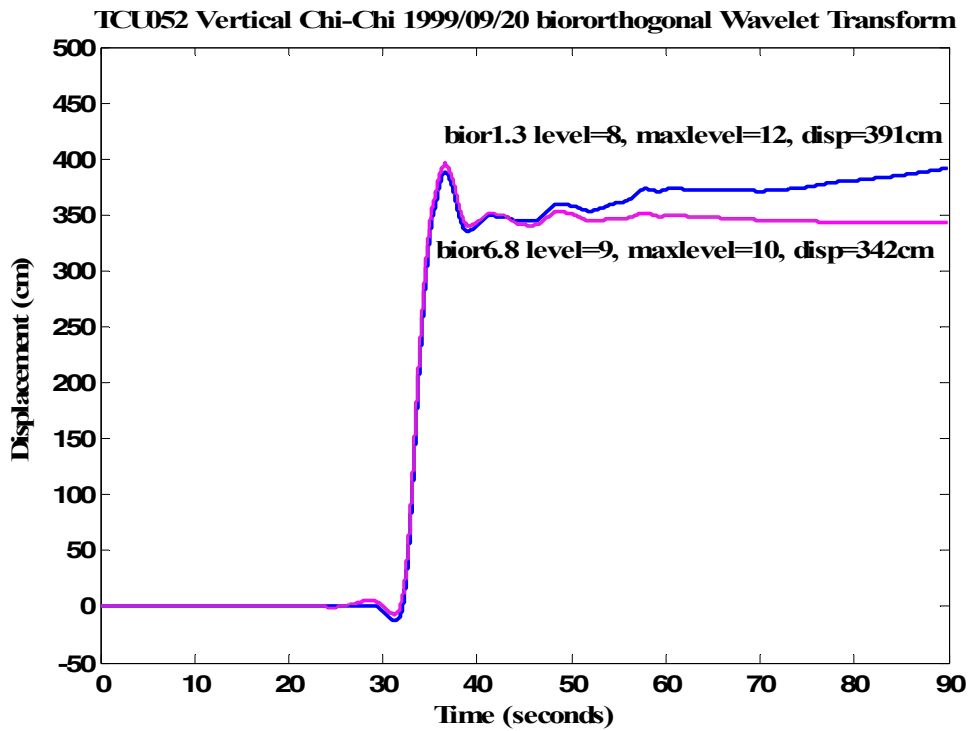


Figure (3) Event TCU052 vertical component using bi-orthogonal wavelets showing displacements with different levels of decomposition

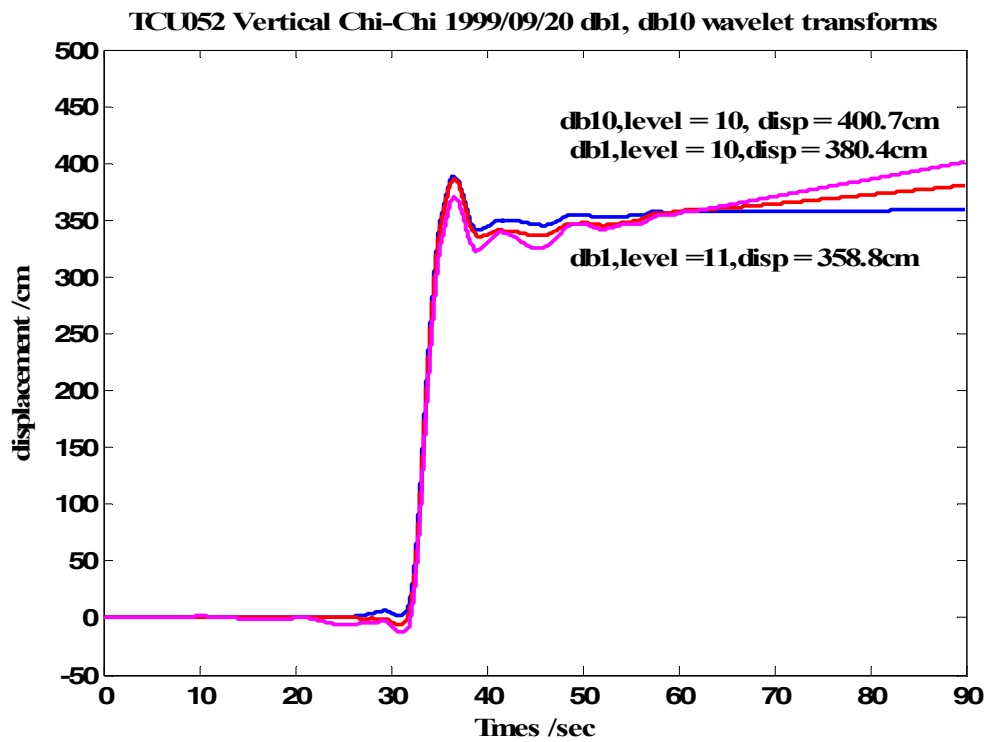


Figure (4) Event TCU052 vertical component using Daubechies wavelets db1 and db10 showing displacements and different levels of decomposition

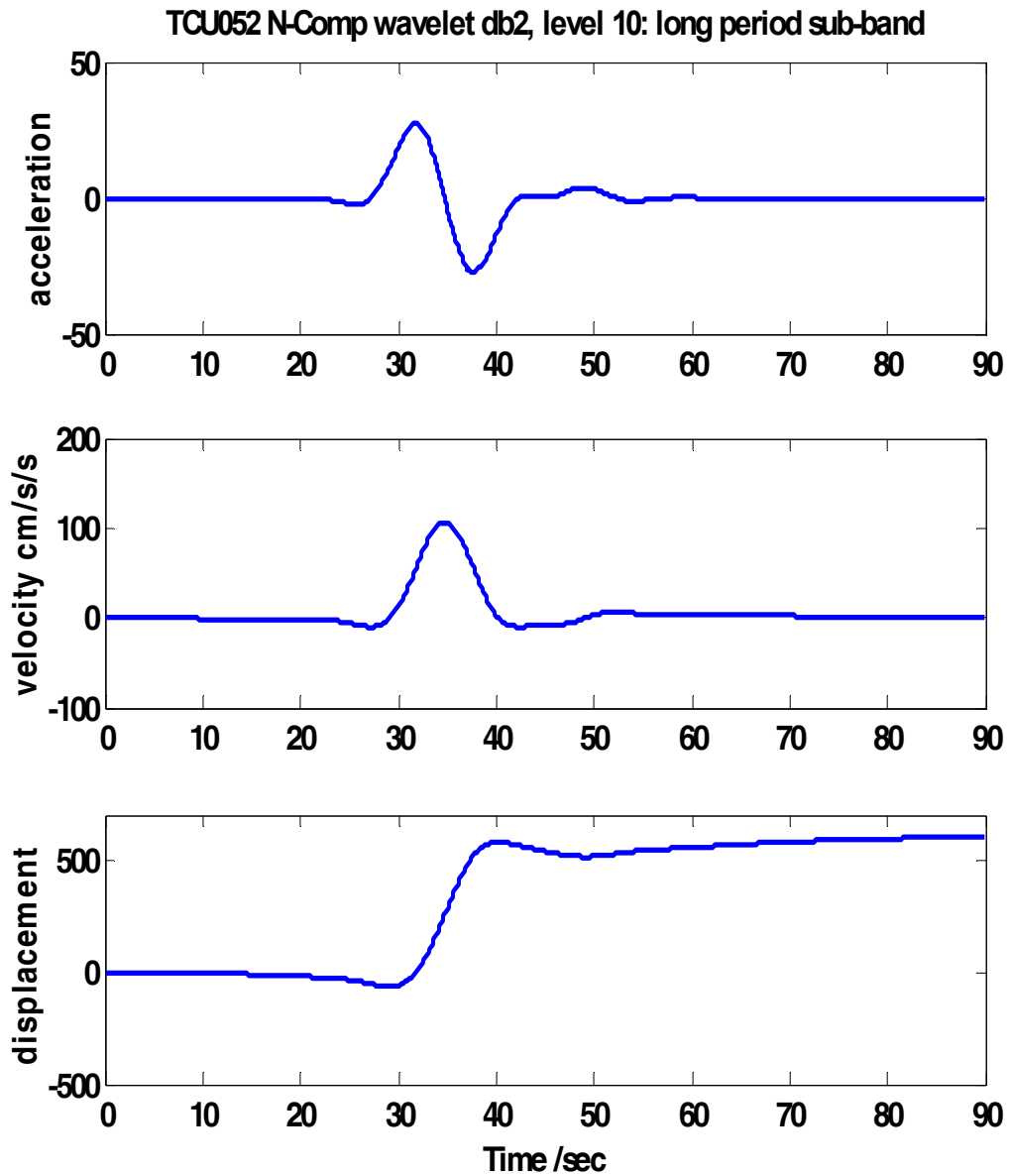


Figure (5) TCU052 N-Component, long period sub-band at level 10, wavelet db2. The acceleration ‘fling’ is symmetric with $\pm 27 \text{ cm/s/s}$, the velocity peak is at 106.6 cm/s and the end displacement is 604 cm . The long period mean was removed from the acceleration

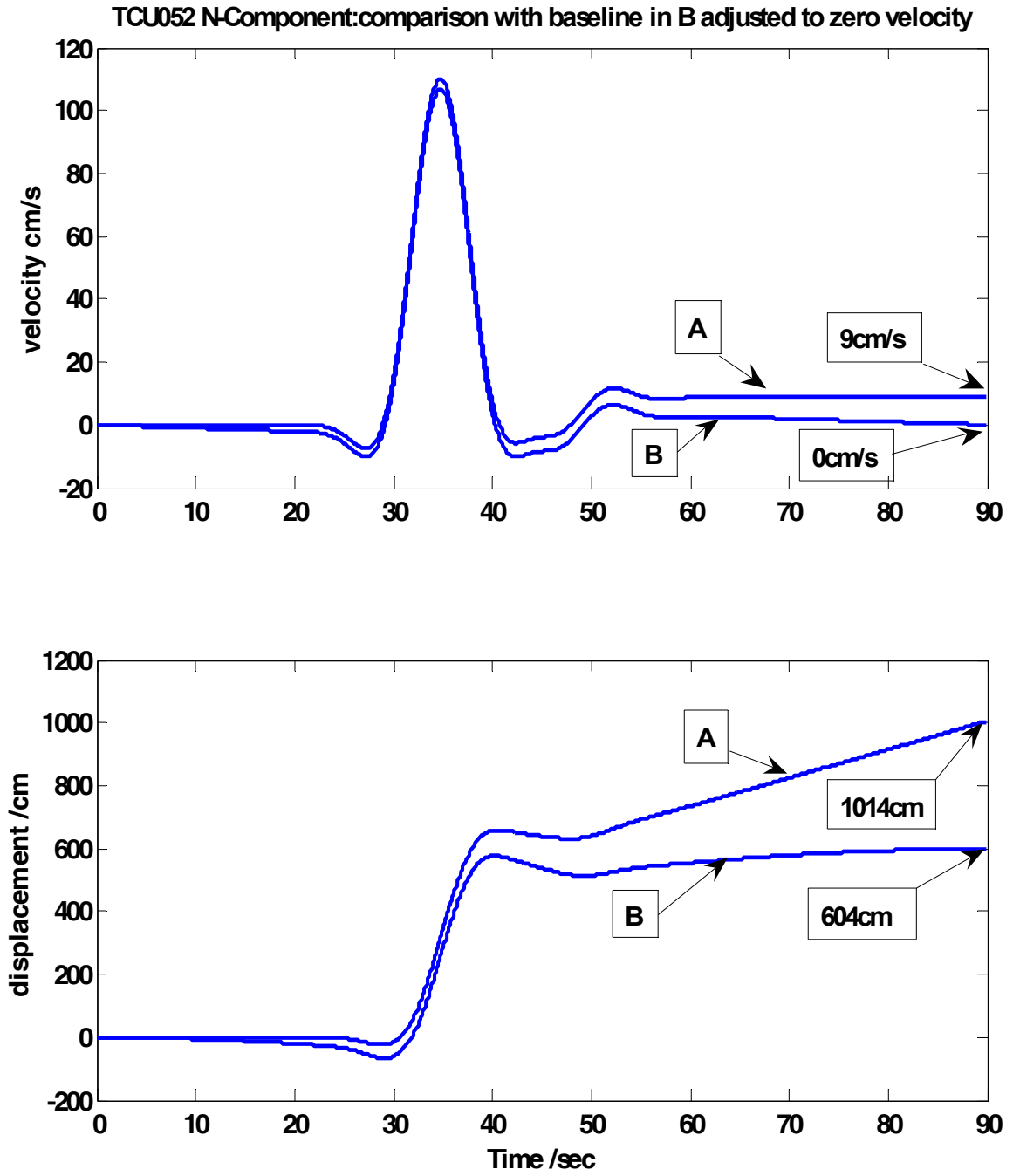


Figure (6) TCU052 N-Component, long period sub-band comparison at level 10, wavelet db2. Velocity plot B has had long period acceleration mean removed for baseline adjustment and so the long period velocity goes to zero. Velocity plot A has only the pre-event mean removed from the original record.

As mentioned earlier the criterion for choosing the db1 or db2 wavelet is its correlation with the shape of the acceleration ‘fling’. In this case decomposition at level 10 shows in Figure (5) such a ‘fling’ in the long period, acceleration and velocity sub-band. The peak velocity is at 106.6cm/s ending at a zero velocity at the end of the 90sec record. The acceleration ‘fling’ is textbook symmetric with peaks at $\pm 27\text{cm/s}^2$. The displacement is at 604cm, which compares with 687.9cm [2] and 845.1cm from a GPS station 2.7km away. In this case the long period acceleration mean was removed, because there was a baseline shift in the long period velocity in the 2nd half of the record, [4] between 50sec and 90sec.

For the purposes of comparison Figure (6) shows the long period record with only the pre-event mean removed from the whole original record [4] without any further baseline processing, plots [A]. This shows an offset in velocity of 9cm/sec over approximately 45sec, which gives rise to shift in displacement of 405sec. Figure (6) also shows the linear velocity trend adding to the final displacement. In plot [B] adjusting the offset for the last portion of the record by removing the long period mean in this automated manner forces the velocity to zero, but produce an offset at the beginning of the record. However, this offset is small and for a much shorter duration, therefore may be neglected where the motion produces large displacements. For example at 19sec the original record shows a zero displacement, whereas after adjusting for zero velocity in the latter record by removing the long-period mean, at 19sec the displacement produced is now -18cm , i.e. 3% of the overall displacement.

Figure (7) compares the long period acceleration, velocity and displacement sub-bands against their total records. These demonstrate that the accelerations need not be very large to produce ramp-like displacements, it is of course the time for which these occur that can make a significant contribution to the displacement. Figure (8) shows the long and short period acceleration sub-bands at level 10 decomposition, followed by the corresponding long and short period velocity sub-bands after 1st integration. Finally Figure (9) shows the corresponding long and short period displacement at level 10 after a 2nd integration.

4.2 TCU052 EW-component

The East component of TCU052 of Figure (10) shows a negative going ‘fling’ in the long period, sub-band velocity profile which reaches a max of -64 cm/sec . The final displacement at 90-sec is -270cm . This compares with a GPS station reading of -342.3 cm and that of [2] of -357.7 cm . In this particular case, the baseline shifts in the latter portion of the velocity by 0.92cm/s and a linear displacement shift of 50cm over 57sec. However, after de-noising with the wavelet transform the long and short period means are removed and the velocity ends at zero. This changes the velocity in the initial portion, from zero to a maximum of -0.2cm/s and the displacement from zero to -2.5cm . The end displacement after the ramp is steady at -270cm for approximately 50secs. These small changes can be ignored. Figure (11) shows the total displacement with the long and short period displacement sub-bands are added together.

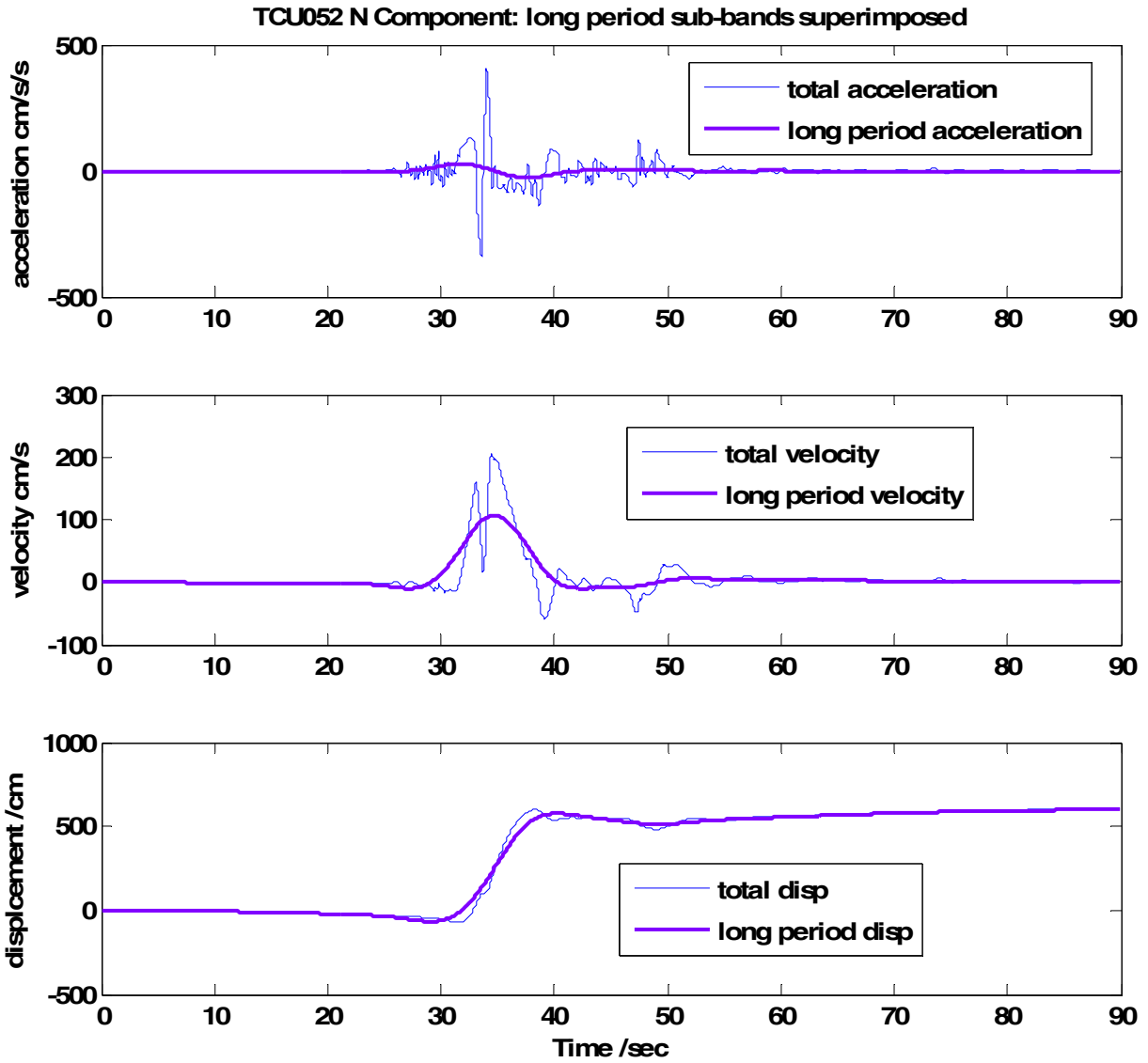
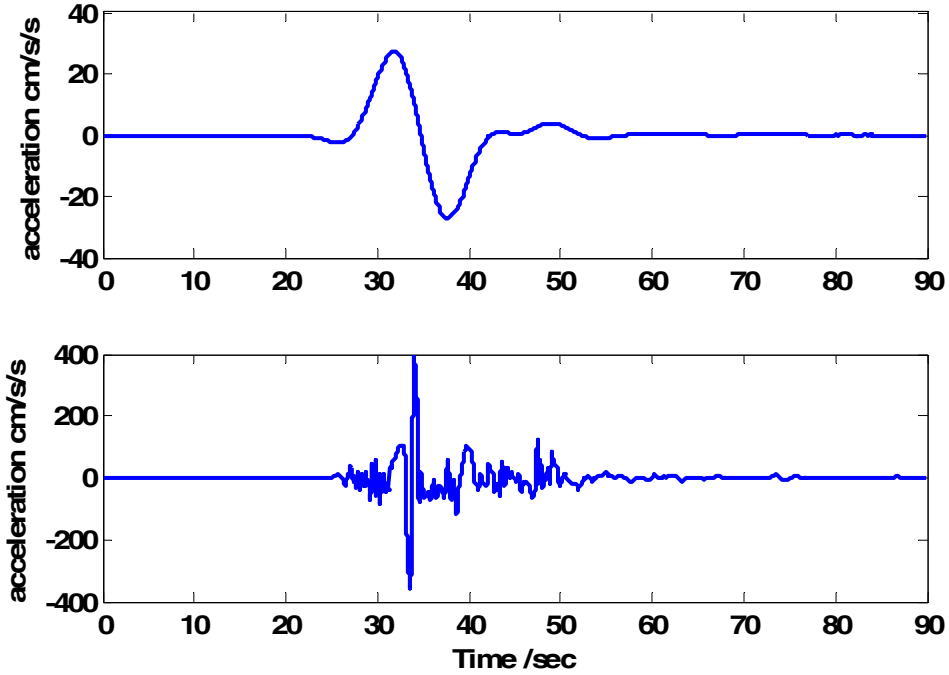


Figure (7) TCU052 N Component, wavelet db2, level 10. The above compares the long period sub-band acceleration, velocity and displacement. It shows the dominance of the small, long period ground acceleration 'fling', giving rise to a 100cm/s-velocity peak and 5m-ramp displacement

TCU052 N Comp: db2, long and short period acceleration sub-bands at level 10



TCU052 N Comp: db2, long and short period velocity sub-bands at level 10

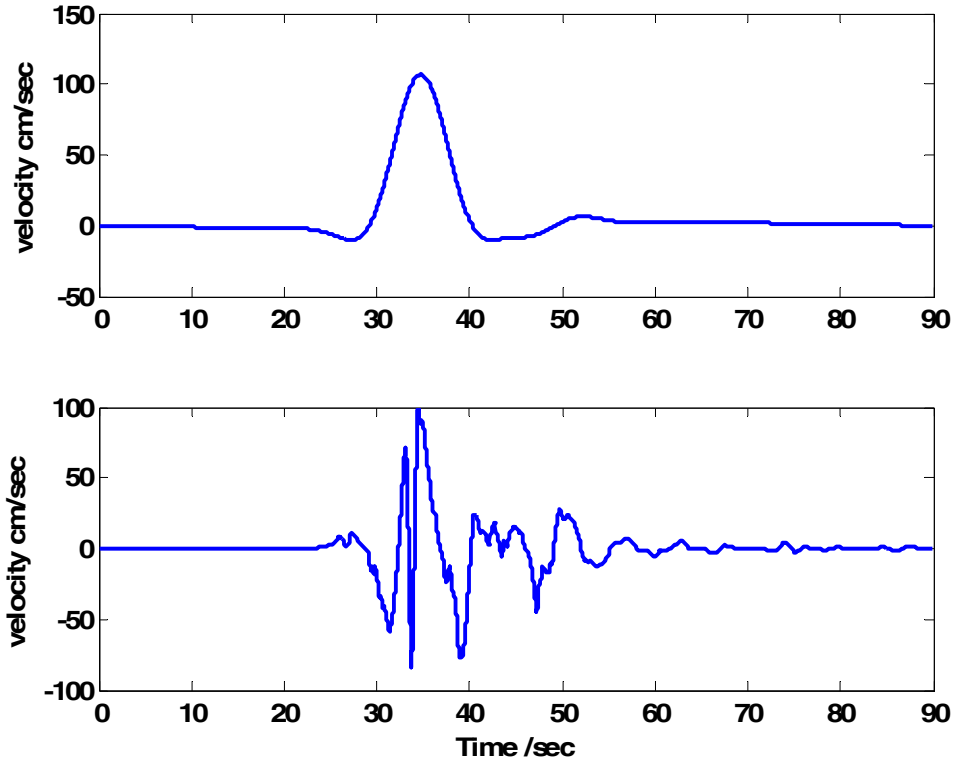


Figure (8) TCU052 N Comp: the top plot shows the long and short period acceleration sub-bands at level 10. The second plots show the corresponding long and short period velocity sub-bands after the 1st integration of the acceleration sub-bands of the top plots

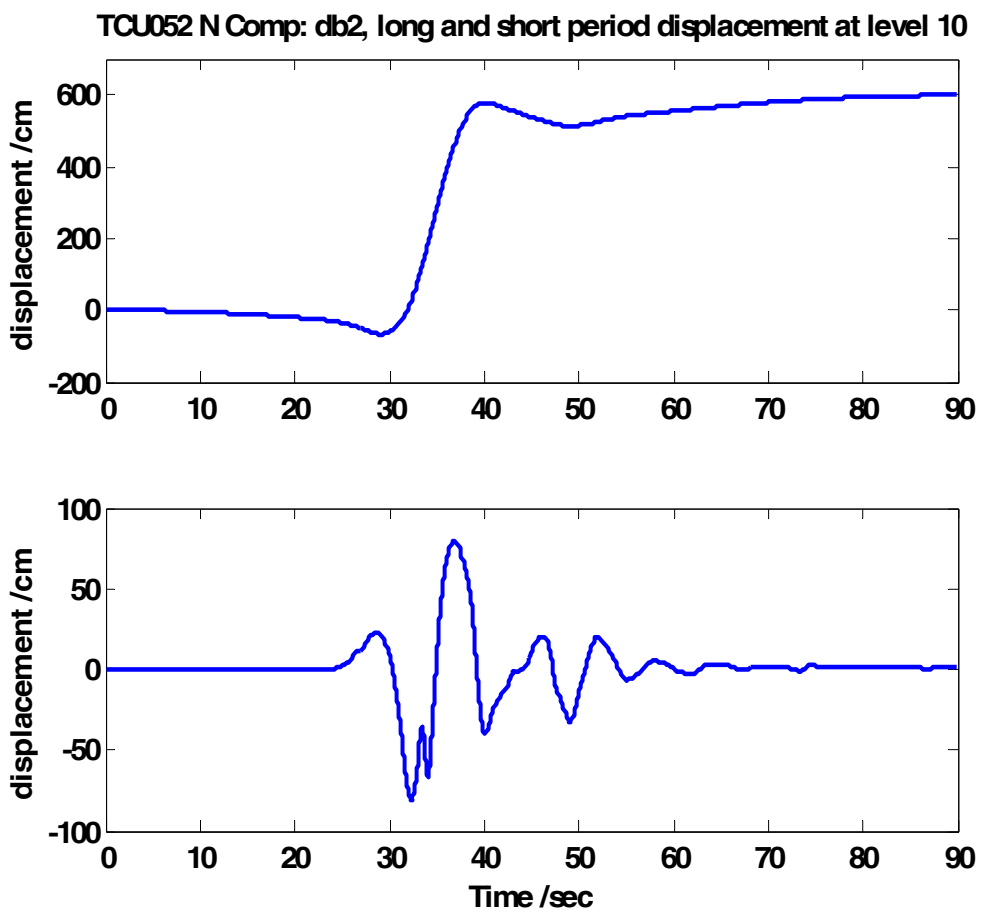


Figure (9) TCU052 N Comp: db2, long and short period displacement at level 10 after integrating (2nd integration) of the velocity sub-bands at level 10.

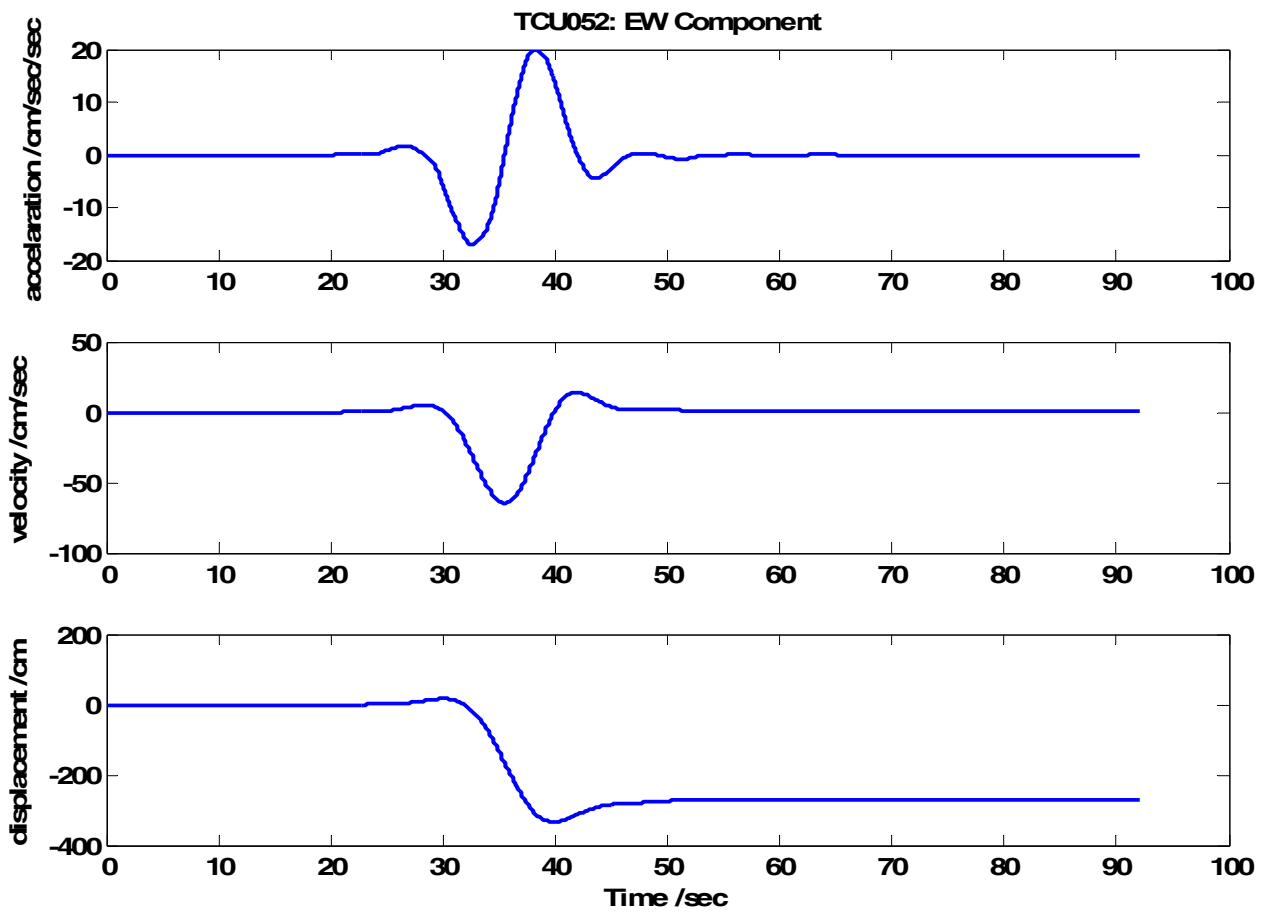


Figure (10) TCU052 EW component, long period sub-band at level 10, showing an acceleration ‘fling’, giving rise to a velocity trough and zero velocity, a displacement ramp and a final displacement of -270cm .

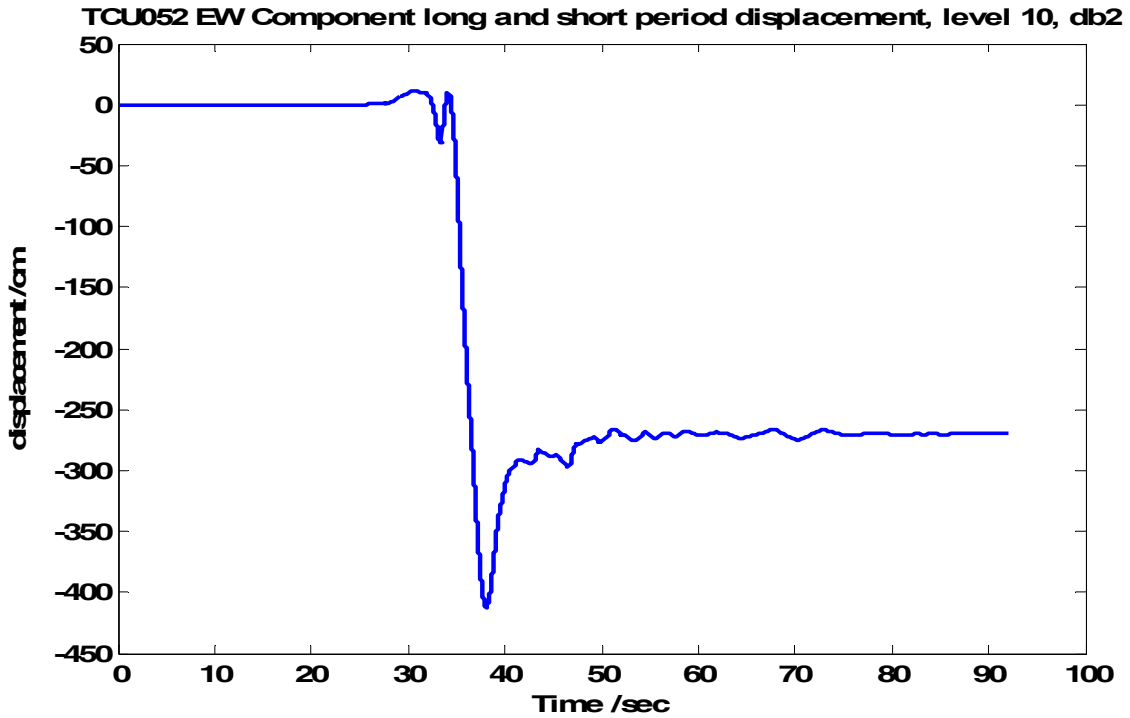


Figure (11) TCU052 EW component: total displacement (-270cm) at level 10, db2 wavelet, long and short period displacement sub-bands added together

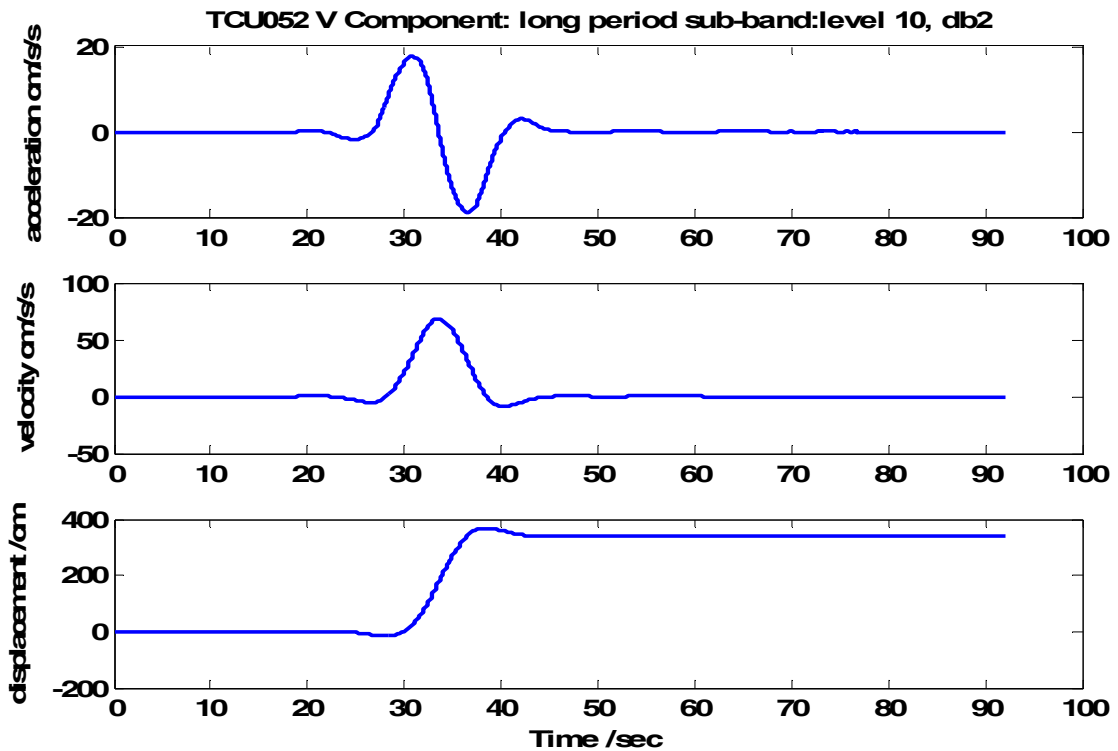


Figure (12) TCU052 V component: long period sub-band, level 10, db2 showing 'fling' and velocity at zero. Displacement at 338cm from 43sec to end of trace.

4.3 TCU052 V-component

The plots in Figures (12) and (13) show a classic almost theoretical ‘fling’ obtained using wavelet ‘db2’ at level 10 on the vertical component of the TCU052 record. The long period ‘fling’ in the acceleration sub-band is clear as is the velocity pulse after integration. The displacement is a classic ramp after the 2nd integration. Figure (13) shows the final displacement from both the long and short period contributions. These are of course added on the assumption that the movements are in the same direction, which may not be the case. The overshoot is due to the short period displacement modulation, the end displacement gives 338cm at 90sec, and the method in [2] gives 350.5cm. It is observed that wavelet ‘db1’ gives a displacement of 350cm, nearer to the GPS reading of 397.2-cm, where the station is 2.7km away. However the acceleration sub-band ‘fling’ is almost theoretical for ‘db2’, hence the preference for its displacement output.

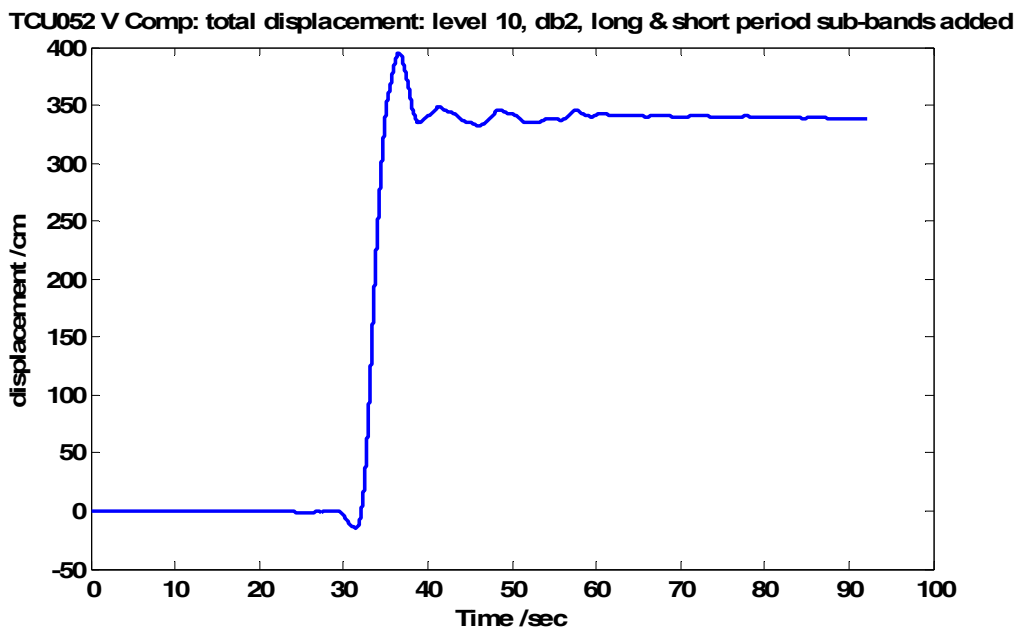


Figure (13) TCU052 V component: total displacement at level 10, db2 wavelet, long and short period displacement sub-bands added together giving a final displacement of 338cm

4.4 Noise Power

Figure (14) shows the noise power spectral plots of TCU052 NS and Vertical components. The EW component noise power spectrum is similar to that of the NS, therefore is not shown. The plots are quite clear in demonstrating that the vertical component has a much smaller noise power than that of the NS and the EW components. It is also clear that the low frequency noise power tends to dominate until approximately 2.5Hz in both the NS and EW components and then reduces considerably. In all 3 cases the noise power is reduced after applying the wavelet

transform, in the NS and EW components the noise averages 0dB after 0.8Hz and then reduces to below 0dB after approximately 2Hz.

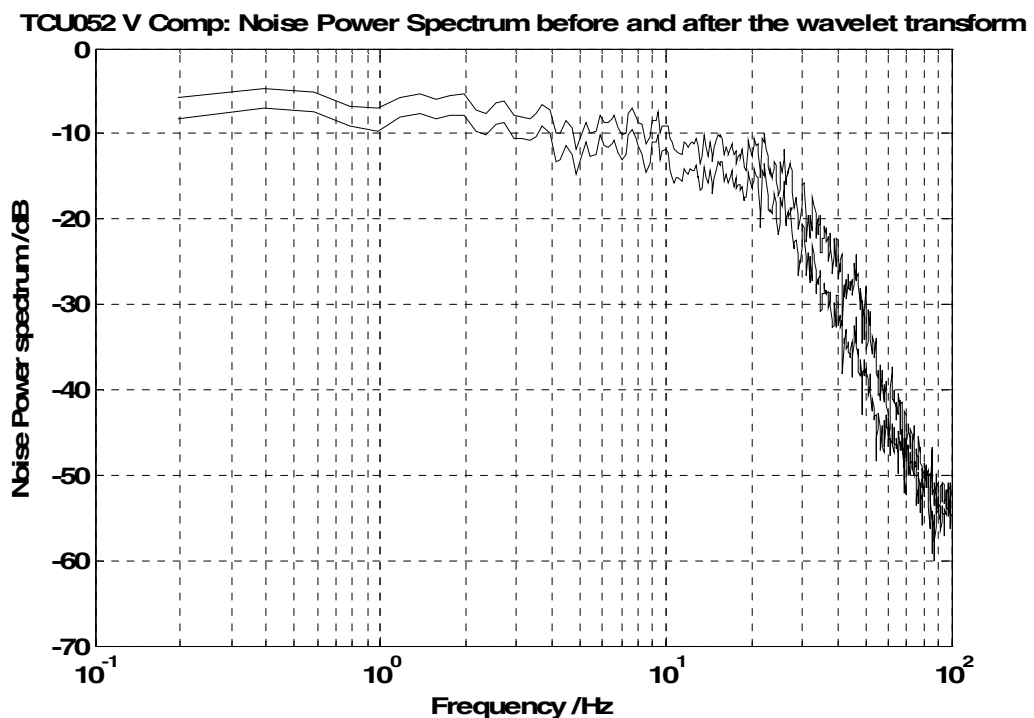
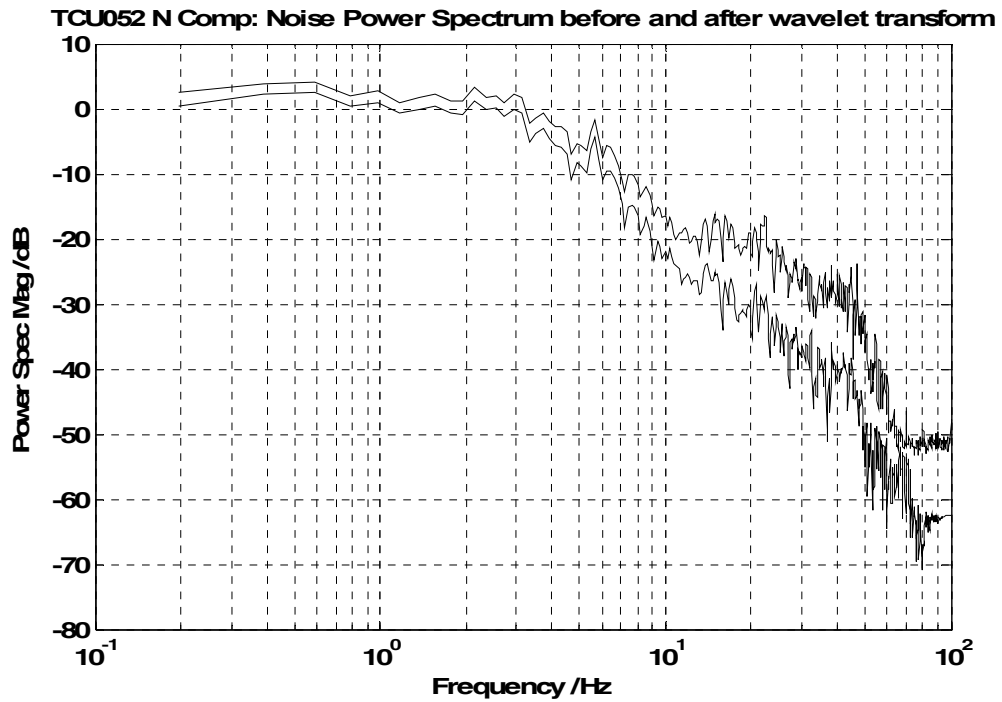


Figure (14) TCU052 N and V Comp: noise power spectrum shows in the North (N) comp a reduction in the noise power at low frequencies by an average of 1.5dB reaching 0dB at 1.1Hz, after applying the wavelet transform. The actual noise power is on average 2.5dB to approximately 2.2Hz. The Vertical (V) component shows a much smaller noise power, on average at -5dB.

5 Summary and Conclusion

The results demonstrate that wavelet transform is well suited in de-noising and analysing the accelerogram from a seismic event and decomposing it down to long and short period sub-bands, from which the sub-band velocity and displacement follows naturally after integration only, without any further processing. In particular the wavelet transform is well suited to identifying the long period ‘fling’ in both the acceleration and velocity, from which the ramp-like displacement is a natural outcome after 2nd integration. The point to make is that at a particular level of decomposition, the wavelet transform can automatically separate the long and short period acceleration sub-bands, as shown in Figure (8). It is then easier to perform a 1st and 2nd integration separately, but on the long period in particular as shown in Figure (8) and (9). This method also identifies acceleration and velocity ‘fling’ and importantly velocity baseline offsets, (Figure (6)) in the latter portions of the long period velocity sub-band. This velocity shift can lead to misleading displacement results, assuming that there isn’t any afterslip in the seismic event. The shift in the latter velocity portion can be corrected by removing the long period mean after applying the wavelet transform, which forces the long period velocity to end at zero. This was the case with the TCU052 NS component and with the EW, but not with the Vertical component. This though may lead to a slight shift in baseline at the beginning of the long period velocity. This was evident in the NS case, but to a much lesser extent in the EW case since its velocity had a small velocity offset. The enforced shift at the beginning is usually for a much shorter time, therefore small changes in displacement at the beginning can be ignored where the overall ground motion leads to large displacements. Alternatively since the baseline offsets in the long period velocity is more easily identified after the wavelet decomposition as described in this paper, the baseline offset can also be corrected by methods due to [2,3,4,6]. The noise floor during the seismic event is shown to be at an average of 2.5dB for the EW and NS components, but much lower for the vertical component.

References

- [1] Trifunac MD, “Zero Baseline Correction of Strong Motion Accelerograms”, *BSSA*, 61, pp 1201-1211
- [2] Wu Y-M., Wu C-F., “Approximate Recovery of Co-Seismic Deformation from Taiwan Strong-Motion Records”, *J. Seismology*, 11:159-170, 2007
- [3] Iwan MD, Moser MA, Peng CY, “Some Observations on Strong-Motion Earthquake Measurements using a Digital Accelerograph”, *BSSA* 75:1222-1246, 1985
- [4] Boore DM, “Effect of Baseline Correction on Displacement and Response Spectra for Several Recordings of the 1999 Chi-Chi, Taiwan, Earthquake,” *BSSA*, 91,5, pp1199-1211, 2001
- [5] Chanerley AA, Alexander NA, “Correcting Data from an Unknown Accelerometer using Recursive Least squares and Wavelet De-noising”, *J. Computers and Structures*, 85, 1679-1692, 2007

- [6] Chen, S-M, Loh C-H, “Estimates of Permanent Ground Displacements from Near-fault, Strong-Motion Accelerograms”, *1st European Conference of Earthquake Engineering & Seismology*”, paper 1631, Geneva, 3-8 Sept, 2006
- [7] Chanerley AA, Alexander NA, “ L_p De-Convolution of Seismic Data using the Iterative Least Squares Method “, *Proc. 8th International Conf on Computational Structures Technolog*, paper 243, Las Palmas, Sept 2006
- [8] Debauchies I, “Ten Lectures on Wavelets”, Philadelphia, PA: *SIAM* 1992
- [9] Donoho DL, “De-Noising by soft Thresholding”, *IEEE Trans. Info. Theory*, 41(3): 613-27, 1995
- [10] Coifman R, Donoho DL, “Translation Invariant De-Noising”, *Wavelets and Statistics, Lecture Notes in statistics*, 103, *Springer-Verlag*, pp. 125-50, 1995
- [11] Lee WHK, Shin TC, Kuo KC, Wu CF, (2001) CWB Free Strong-Motion Data from the 21st Sept Chi-Chi, Taiwan, Earthquake, *BSSA*, 91: 1370-1376 CD ROM
- [12] Burrus C, Gopinath RA, Guo H., “Introduction to Wavelets and Wavelet Transforms”, PHI, 1998